



Technische Universität München

Fakultät für Physik

**Advancements in Monolithic U-Mo Fabrication:
Demonstration of Gradient Foil Fabrication and
Development of a Pilot Physical Vapor
Deposition Process for Full-Size U-Mo Foils**

Bruno Baumeister

Vollständiger Abdruck der von der Fakultät für Physik der Technischen
Universität München zur Erlangung des akademischen Grades eines

Doktors der Naturwissenschaften (Dr. rer. nat.)

genehmigten Dissertation.

Vorsitzender: apl. Prof. Dr. Norbert Kaiser

Prüfer der Dissertation: 1. Prof. Dr. Winfried Petry

2. Prof. Dr. Peter Böni

Die Dissertation wurde am 09.02.2022 bei der Technischen Universität
München eingereicht und durch die Fakultät für Physik
am 04.04.2022 angenommen.

“Things are only impossible until they're not.”

Jean-Luc Picard in Star Trek

ABSTRACT

Within the context of a global initiative to reduce the enrichment of nuclear fuels for research and test reactors, new fuel candidates with significantly higher uranium density must be developed and appropriate fabrication techniques need to be established. For the conversion of the FRM II research reactor and other high-performance research reactors worldwide to a lower enriched fuel element, a monolithic uranium-molybdenum (U-Mo) alloy fuel is the most promising candidate.

In the proposed European fabrication process chain for such fuels, two major advancements must be made towards its further industrialization: (i) the demonstration of fabrication techniques for U-Mo foils with a thickness gradient, necessary to reduce thermal spikes at the edges of fuel plates, and (ii) the development of a pilot PVD coating process for the application of a zirconium interdiffusion barrier between the U-Mo foil and the surrounding aluminum cladding.

Currently, no fabrication process for gradient U-Mo foils is available worldwide. Hence, a comprehensive assessment of possible techniques for a first-of-a-kind fabrication demonstration using non-radioactive surrogate materials was performed, focusing on the achievable precision, surface quality, material efficiency and expected radiological impact. In collaboration with industrial and research partners, numerous gradient foils of stainless steel AISI 316L and titanium alloy Ti-6Al-4V were produced. Hereby, gradient full-size foils (762 mm x 45 mm) conforming to specifications and compatible with the fuel plate fabrication process were produced by classical milling, and the collection of more than 98 % of the generated scraps for recycling was demonstrated. Gradient mini-size foils (82.5 mm x 19 mm) were successfully produced for the first time using additive manufacturing by selective laser melting, and post-production treatments like shot peening and hot isostatic pressing were applied to obtain foils compatible with the plate fabrication process.

On the way towards its industrialization, the pilot PVD coating process for full-size foils follows the previously developed mini-size process at TUM. In parallel to its upscaling to full-size geometry, two key issues of the previous process were successfully resolved within this thesis. The ductility of the coating was significantly improved via an optimized substrate biasing approach, which aims to reduce the re-sputtering effect and structural damages in the deposited Zr layer. Therefore, the newly built PVD coating device was equipped with an unbalanced magnetron type 2 sputtering source, which allows a reduction of the substrate biasing voltage while simultaneously increasing the ion flux towards the substrate. A new substrate holder, which uses spring force to keep the foils flat throughout the coating process, allows the reliable coating of up to 800 mm long full-size substrates. An optimized set of process parameters was developed for this PVD coating device, aiming at the reproducible deposition of at least 8 μm Zr with defect-free adherence and high layer ductility at a high deposition rate. In a joint fabrication study, TUM's pilot PVD coating process and Framatome-CERCA's C2TWP cladding application process were successfully tested and specification-conform half-size plates were produced out of Zr-coated stainless steel substrates.

By these first-of-a-kind demonstration experiments on the fabrication of gradient foils, and by successfully establishing the pilot PVD coating process at TUM's Nuclear Fuel Fabrication and Characterization Laboratory, important advancements of the European fabrication process chain for monolithic U-Mo fuels were accomplished.

KURZZUSAMMENFASSUNG

Im Rahmen weltweiter Bemühungen zur Reduzierung der Anreicherung von Kernbrennstoffen für Forschungs- und Testreaktoren müssen neue Brennstoffkandidaten mit deutlich höherer Uran-Dichte entwickelt und geeignete Fertigungsverfahren geschaffen werden. Für die Umrüstung des Forschungsreaktors FRM II und anderer Hochleistungs-Forschungsreaktoren weltweit auf ein niedriger angereichertes Brennelement ist ein monolithischer Uran-Molybdän (U-Mo) Brennstoff der vielversprechendste Kandidat.

In der Europäischen Prozesskette für die Fertigung solcher Brennstoffe stehen zwei wichtige Weiterentwicklungen auf dem Weg zur Industrialisierung an: (i) die Demonstration von Fertigungsverfahren für U-Mo-Folien mit einem Dickengradienten, welche zur Verringerung von Leistungsspitzen an den Rändern der Brennstoffplatten erforderlich sind, und (ii) die Entwicklung eines Pilot PVD-Beschichtungsprozesses für die Aufbringung einer Zirkonium-Interdiffusionsbarriere zwischen der U-Mo-Folie und dem umgebenden Aluminium-Cladding.

Derzeit ist weltweit kein Fertigungsverfahren für Gradienten U-Mo-Folien verfügbar. Daher wurde zunächst eine umfassende Evaluierung möglicher Techniken für eine erstmalige Fertigungsdemonstration unter Verwendung nicht-radioaktiver Ersatzmaterialien durchgeführt, wobei der Schwerpunkt auf der erreichbaren Präzision, der Oberflächenqualität, der Materialeffizienz und den erwarteten radiologischen Auswirkungen lag. In Zusammenarbeit mit Partnern aus Industrie und Forschung wurden zahlreiche Gradientenfolien aus rostfreiem Stahl AISI 316L und der Titanlegierung Ti-6Al-4V hergestellt. Mittels klassischem Fräsen wurden dabei spezifikationskonforme, mit dem Brennstoffplatten-Herstellungsprozess kompatible full-size Gradientenfolien (762 mm x 45 mm) hergestellt und erfolgreich mehr als 98 % der anfallenden Späne zur Wiederverwendung aufgesammelt. Mini-size Gradientenfolien (82.5 mm x 19 mm) wurden zum ersten Mal erfolgreich mittels additiver Fertigung durch selektives Laserschmelzen hergestellt und anschließend Nachbearbeitungsverfahren wie Kugelstrahlen und heißisostatisches Pressen angewendet, um mit dem Brennstoffplatten-Herstellungsprozess kompatible Folien zu erhalten.

Auf dem Weg zur Industrialisierung folgt der Pilot PVD-Beschichtungsprozess für full-size Folien dem zuvor an der TUM entwickelten mini-size Prozess. Parallel zur Hochskalierung auf full-size Geometrie wurden im Rahmen dieser Arbeit zwei Schlüsselprobleme des vorherigen Prozesses erfolgreich gelöst. Die Duktilität der Zr-Beschichtung wurde durch optimiertes Substrat-Biasing deutlich verbessert, indem der Re-Sputtering-Effekt und die Einbringung von Strukturschäden in die Zr-Schicht reduziert wurden. Zu diesem Zweck wurde die neu gebaute PVD-Beschichtungsanlage mit einer sog. unbalanced magnetron Sputterquelle vom Typ 2 ausgestattet, die eine Reduzierung der Substratvorspannung bei gleichzeitiger Erhöhung des Ionenflusses zum Substrat ermöglicht. Ein neuer Substrathalter, welcher die Folien während des gesamten Prozesses durch Federkraft flach hält, ermöglicht die zuverlässige Beschichtung von bis zu 800 mm langen Substraten. Für diese Beschichtungsanlage wurde ein optimierter Satz von Prozessparametern entwickelt, der auf die reproduzierbare Beschichtung mit mindestens 8 μm Zr, mit fehlerfreier Haftung und hoher Schichtduktilität bei hoher Abscheiderate, abzielt. In einer gemeinsamen Fertigungsstudie wurden der Pilot PVD-Beschichtungsprozess der TUM und der C2TWP-Claddingapplikationsprozess von Framatome-CERCA erfolgreich getestet und spezifikationskonforme half-size Platten aus Zr-beschichteten Edelstahlsubstraten hergestellt.

Mit diesen erstmalig durchgeführten Demonstrationsexperimenten zur Fertigung von Gradientenfolien und der erfolgreichen Etablierung des Pilot PVD-Beschichtungsprozesses im TUM Nuclear Fuel Fabrication and Characterization Laboratory konnten wichtige Fortschritte in der europäischen Prozesskette zur Herstellung monolithischer U-Mo-Brennstoffe erzielt werden.

TABLE OF CONTENTS

1	Introduction	1
1.1	Research Neutron Source FRM II	1
1.2	Enrichment Reduction	2
1.3	Fabrication of Monolithic U-Mo Fuels for FRM II.....	4
1.4	Aim of this Thesis	7
2	Theoretical considerations	9
2.1	Materials Science	9
2.1.1	Interdiffusion	9
2.1.2	Monolithic U-Mo Fuels with Interdiffusion Barrier	12
2.1.3	Surrogate Materials	22
2.2	Fabrication of Flat U-Mo Foils	28
2.3	Interdiffusion Barrier Application	32
2.3.1	Substrate Surface Condition.....	32
2.3.2	Processes	34
2.3.3	Low-Pressure Plasma Physics	36
2.3.4	Sputter Erosion Process	41
2.3.5	Sputter Deposition Process	48
2.3.6	Plasma Cleaning.....	52
2.3.7	Previous Work at FRM II.....	53
3	Experimental Basics	61
3.1	Experimental Infrastructure for PVD coating	61
3.1.1	The HSK3 Device	61
3.1.2	The HSK2 Device	66
3.2	Sample Preparation.....	69
3.2.1	Substrate Preparation for PVD Coating.....	69
3.2.2	Sample Preparation for Characterization	71
3.3	Sample Characterization	74
3.3.1	Microscopy.....	74
3.3.2	Mechanical Characterization	75

4	Fabrication Demonstration of Gradient Foils	77
4.1	Gradient Foil Geometries	77
4.2	Fabrication Processes	80
4.2.1	Process Requirements	80
4.2.2	Milling.....	81
4.2.3	Selective Laser Melting.....	83
4.3	Fabrication Demonstration of Gradient Foils by Milling.....	88
4.3.1	Mini-Size	88
4.3.2	Full-Size	92
4.4	Fabrication Demonstration of Gradient Foils by Selective Laser Melting	96
4.4.1	Fabrication	96
4.4.2	Post-Production Treatments.....	100
4.5	PVD Coating and C2TWP Cladding Application	105
5	Development of the Pilot PVD Coating Process.....	107
5.1	Design Fundamentals for the Pilot PVD Coating Process	107
5.1.1	Requirements	107
5.1.2	Constraints.....	109
5.2	Optimized Substrate Heating for PVD Coating	110
5.2.1	Micro-Size Sample Holder	110
5.2.2	Process Characterization.....	110
5.2.3	Sample Production	113
5.2.4	Sample Characterization	116
5.2.5	Implications on the Full-Size PVD Coating Process.....	122
5.3	Optimized Substrate Biasing for PVD Coating	123
5.3.1	Plasma Enhancement by Static Magnetic Fields	124
5.3.2	Plasma Enhancement by Electron Emission.....	129
5.3.3	Implications on the Full-Size PVD Coating Process.....	136
5.4	The Full-Size PVD Coating Device	137
5.4.1	Chemical Cleaning Equipment	137
5.4.2	Vacuum Chamber Interior Design	137
5.4.3	Substrate Holder.....	138
5.4.4	Sputtering Source	142
5.4.5	Power Supply Units	144
5.4.6	PLC System.....	147
5.4.7	Weighing Equipment.....	148
5.4.8	Trimming Equipment.....	148
5.4.9	Packaging and Sealing Equipment.....	149
5.5	Process Realization and First Results.....	151

5.5.1	Process Flow	152
5.5.2	Process Characterization and Parametrization	154
5.5.3	First Results after C2TWP Cladding Application	170
6	Conclusion	177
6.1	Fabrication Demonstration of Gradient Foils	177
6.1.1	Outlook.....	178
6.2	Development of the Pilot PVD Coating Process	180
6.2.1	Outlook.....	182
Scientific Contributions		i
Bibliography.....		iii
List of Figures		xix
List of Tables		xxv
Danksagung		xxvii

1 INTRODUCTION

This thesis was conducted within the framework of the conversion of the research reactor *FRM II* (Forschungs-Neutronenquelle Heinz Maier-Leibnitz), operated by *TUM* (Technical University of Munich), from its current *HEU* (highly enriched uranium) fuel to a lower enriched fuel. The high-density fuel working group at FRM II is developing new fuel candidates and fabrication techniques to achieve this goal. This thesis deals with advancements in fabrication techniques for lower enriched monolithic *U-Mo* (uranium-molybdenum) fuels, the fuel candidate with the most promising irradiation behavior but also the one with the greatest challenges for fabrication on an industrial scale.

1.1 RESEARCH NEUTRON SOURCE FRM II

To allow a high neutron flux as well as a high neutron brilliance, the FRM II is designed and built with a compact core, using only one single fuel element. Such a fuel element contains 8.1 kg of HEU with 93 at.% uranium-235 and can be operated for a cycle length of typically 60 days. At a comparably small thermal power of 20 MW, a maximum undisturbed thermal neutron flux of $8 \cdot 10^{14}$ n/cm² s builds up in the moderator, approximately 12 cm away from the fuel element. This results in the highest flux-to-power ratio of neutron sources worldwide [1].

Figure 1 shows a cut view of the FRM II core installations. The fuel element is located in a central light water cooling channel, surrounded by a heavy water moderator tank and a light water pool. The control rod moves vertically through the fuel element. Beam tubes guide the generated neutrons to the experimental facilities outside the reactor core.

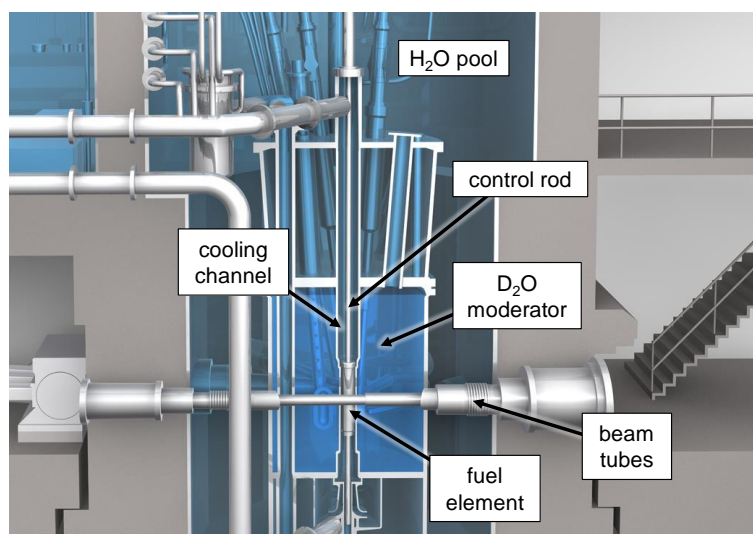


Figure 1: Cut view of the FRM II core installations. The single fuel element is located in the center of the D₂O moderator tank, surrounded by the H₂O pool. After [1].

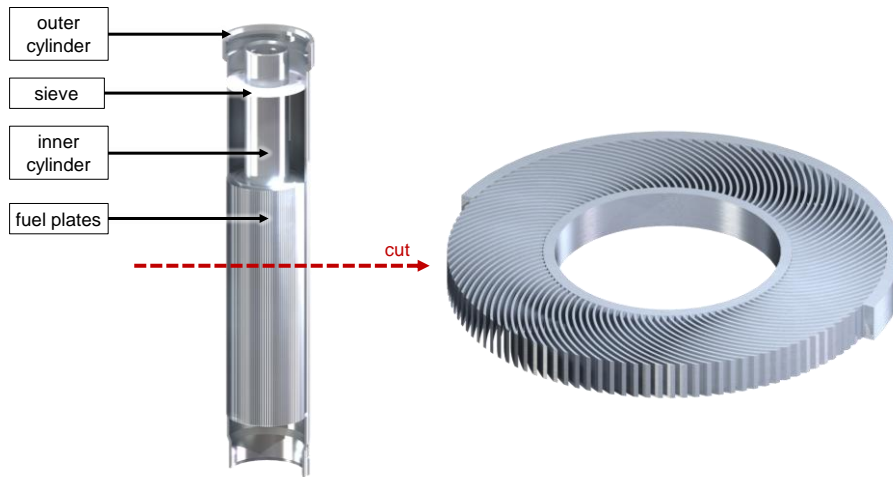


Figure 2: Inner view of the current FRM II fuel element. The control rod moves vertically through the inner cylinder. The 113 involute-shaped fuel plates reside between the inner and the outer cylinder and are cooled by light water, flowing through the equidistant gaps in between. After [2].

As Figure 2 depicts, the fuel element consists of two concentric aluminum alloy (AlMg3) cylinders with radii 65 mm and 114.5 mm, with 113 fuel plates located in between. Before the fuel plates are shaped to the so-called *involute*s, each plate is 720 x 76 mm in size and has a thickness of 1.36 mm. The involute shape of the fuel plates allows a constant cooling channel width of 2.2 mm in between the plates. Each fuel plate contains a 708 x 62.4 mm rectangular core of *disperse* U_3Si_2/Al *cermet*, which incorporates approximately 72 g of uranium. Herein, ceramic U_3Si_2 particles with a maximum diameter of 125 μm are incorporated in a metallic aluminum *matrix*. This 0.60 mm thick fuel *meat* is located in between two 0.38 mm thick aluminum alloy (AlFeNi) plates – the so-called *cladding* – to safely enclose the fuel and the fission products [2].

In the current FRM II fuel plate design shown schematically in Figure 3, the fuel meat consists of two zones. The inner zone with a width of 51.5 mm has the nominal uranium density of 3.0 gU/cm³, which represents a fuel *volume loading* – the volume fraction of fuel particles within the matrix – of ~ 26.5 vol.%. The outer zone with a width of 10.9 mm has a reduced uranium density of 1.5 gU/cm³, representing a fuel volume loading of ~ 13.3 vol.%. Herein, “outer” stands for the side of the fuel plates which is nearer to the D₂O moderator. This density step is required to minimize the radial peak-to-average power density ratio along the arc of the fuel plates due to increased thermal neutron flux at the regions of the fuel element in close proximity to the D₂O moderator tank, which acts as a neutron reflector. Without this density step, thermal spikes would occur at the outer edges of the fuel plates, significantly increasing the cooling requirements for the core [2].

Figure 4 shows the power deposition profile at the end of life of a current FRM II fuel element. As can be seen, more power is deposited at the sides of the fuel plates. The sudden step in the power deposition at a radius of approximately 10.6 cm correlates with the begin of the outer fuel zone with reduced uranium density.

1.2 ENRICHMENT REDUCTION

As part of international efforts to minimize the use of HEU in the nuclear fuel cycle, research reactors operating with HEU fuel – like the FRM II – shall be converted to lower enriched uranium fuel.

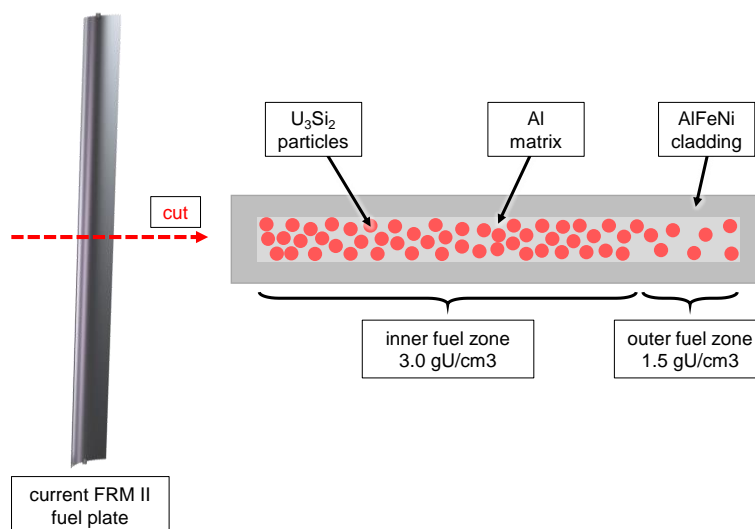


Figure 3: Cut view of a current FRM II fuel plate before involute shaping. To compensate the high thermal neutron flux at the outer side of the fuel element, the uranium density is reduced from 3.0 gU/cm^3 to 1.5 gU/cm^3 in the outer fuel zone.

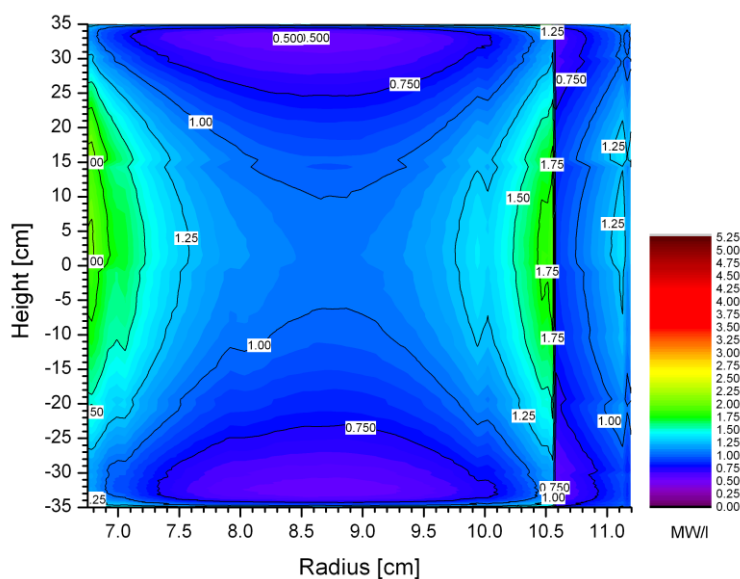


Figure 4: Power deposition in MW/l at the end of life of a current FRM II fuel element. More power is deposited at the sides of the fuel plates due to the locally increased thermal neutron flux. From [2].

In general, the safety, the scientific quality, and the economic viability of the FRM II must not be impaired by the conversion, leading to the following general conditions:

- No negative impact on the (inherent) safety is allowed
- The achievable cycle length must remain at approximately 60 days
- Only marginal losses of the neutron fluxes at the experimental facilities are allowed
- The outer dimensions of the fuel element must remain unchanged

Given these conditions, it becomes clear that the inventory of fissile uranium-235 in the fuel element must remain at least constant, while increasing the amount of non-fissile uranium-238. This is only

achievable by increasing the uranium density within the fuel element. Considering the additional parasitic neutron absorption of uranium-238, it can be estimated that an enrichment reduction by any factor must be overcompensated by a density increase with an even higher factor.

The maximum uranium density can be achieved by using pure uranium with a density of 19.1 gU/cm³ [3] as fuel. However, pure uranium is not a suitable research reactor fuel due to its unstable irradiation behavior. For example, due to its orthorhombic crystal structure, its anisotropic thermal expansion leads to severe fuel deformation under irradiation and thermal cycling [3]. Therefore, research reactor operators, fuel developers and fuel fabricators worldwide are focusing on either increasing the volume loading of existing disperse fuels or the development of entirely new fuel materials. For the former, a volume loading of 50 % is generally considered to be a practical limit for fabrication [4], since the mechanical properties of the fuel core will become more and more dominated by the typically hard and brittle fuel particles. The most promising fuel candidates for research reactor conversion up to date – high-loaded disperse U₃Si₂, disperse and monolithic U-Mo – are depicted in Figure 5. These candidates are either predicted or have already proven to have a stable irradiation behavior and to be able to be fabricated on an industrial scale. Furthermore, they have uranium densities sufficient for the conversion of many research reactors.

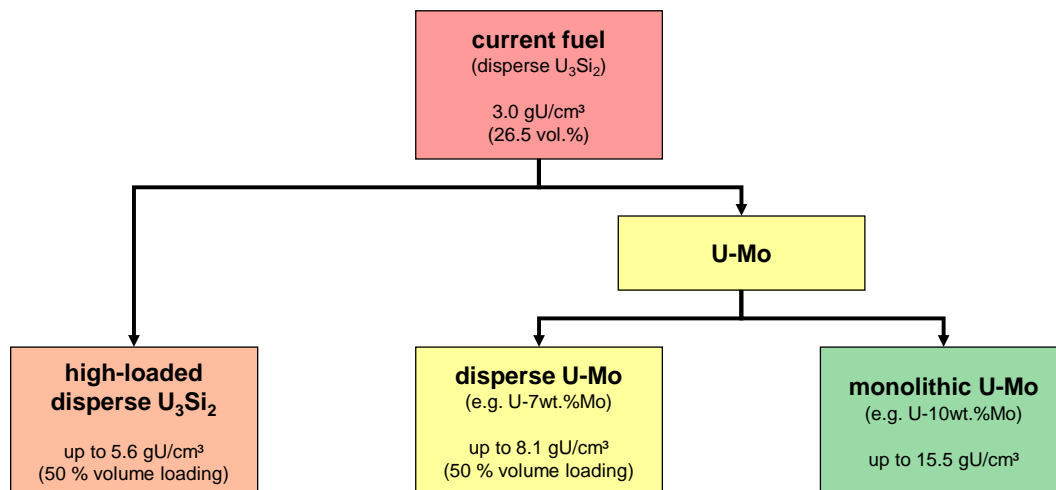


Figure 5: Fuel candidates for the conversion of FRM II. Monolithic U-Mo fuels have the highest uranium density and therefore allow the lowest enrichment. Density data from [3,5].

Within the European HERACLES consortium of fuel developers and fabricators [6], FRM II is engaged in the development of all three fuel candidates. Because monolithic U-Mo allows the highest uranium density of 15.5 gU/cm³ and therefore the lowest enrichment, FRM II focuses its research on this fuel candidate. Here the disperse fuel meat is replaced by a massive metallic U-Mo layer, a so-called *foil*, which is again clad with two aluminum alloy (e.g. AlFeNi) plates. The alloying of uranium with 7 - 10 wt.% molybdenum stabilizes the γ phase of uranium, which has a stable irradiation behavior [7].

1.3 FABRICATION OF MONOLITHIC U-MO FUELS FOR FRM II

Extensive research on fabrication processes for monolithic U-Mo fuels for FRM II and other research reactors is performed in Europe [8–15] and the United States [16–28], among others. Figure 6 schematically shows the proposed European fabrication process for monolithic U-Mo fuel plates.



Figure 6: Proposed European fabrication process for monolithic U-Mo fuel plates. After rolling foils from U-Mo ingots, an interdiffusion barrier is applied by PVD, followed by the cladding application by C2TWP.

This process consists of the following general fabrication steps:

- Alloying and casting of U-Mo ingots
- Rolling of U-Mo foils
- Application of an interdiffusion barrier by PVD
- Application of the cladding by C2TWP

Currently, the proposed process does not include a measure to reproduce the density step of the current disperse U_3Si_2 fuel of FRM II. With monolithic U-Mo, however, maintaining a low radial peak-to-average power density ratio becomes even more important due to the increased uranium density in the fuel. Current research at FRM II proposes one of the following measures to do so, only the latter being dealt with in the context of this thesis:

- An advanced fuel element design with optimized placement of neutron-absorbing materials in the non-fueled parts of the fuel element (“fuel element design approach”) [29]
- A thickness gradient of the U-Mo foils along their width (“gradient foils approach”) [30]

Fabrication of gradient U-Mo Foils

Figure 7 schematically shows a cut view of a potential gradient monolithic fuel plate before involute shaping. Here, also the inner edge of the fuel foil has a reduced thickness to compensate also the higher neutron flux near the central channel of the fuel element.



Figure 7: Cut view of a potential gradient monolithic fuel plate before involute shaping. To compensate higher thermal neutron fluxes at the inner and outer side of the fuel plates, the U-Mo foil has a thickness gradient along its width.

As the fuel material U-Mo is expensive and requires complex safety and security measures during fabrication, handling and transport, the entire fabrication process for such fuels must be well designed. Especially, to reach a maximum material efficiency, the choice and design of the foil fabrication technique is crucial. Framatome-CERCA is developing a European fabrication process for U-Mo foils, based on published experience from the US-American fuel fabrication program [15]. This development currently only aims for flat (non-gradient) U-Mo foils, similar to what is currently being developed at the US-American fuel fabricator *BWXT* (BWX Technologies Inc.) [26–28,31]. Thus, fabrication processes for gradient U-Mo foils still need to be developed.

Interdiffusion barrier coating

In early tests of disperse U-Mo fuels with aluminum matrices [32–34] and tests of monolithic U-Mo fuels with aluminum cladding [35,36], the formation of an amorphous interdiffusion layer between U-Mo and Al was observed under irradiation, as depicted in Figure 8. As gaseous fission products tend to accumulate in this interdiffusion layer, leading to excessive fuel plate swelling and finally plate destruction, this effect was identified as the main reason for the failure of these tests. Thus, it must be avoided in disperse and monolithic U-Mo fuels. For the latter, the placement of a thin interdiffusion barrier, e.g. of zirconium, between the U-Mo foil and the Al cladding was found to block interdiffusion efficiently in numerous irradiation tests [37–39]. This was also verified by heavy-ion irradiation experiments, where the damage from fission products is reproduced by irradiating U-Mo/Zr/Al multilayer samples with iodine ions with kinetic energies of approximately 80 MeV [40–43].

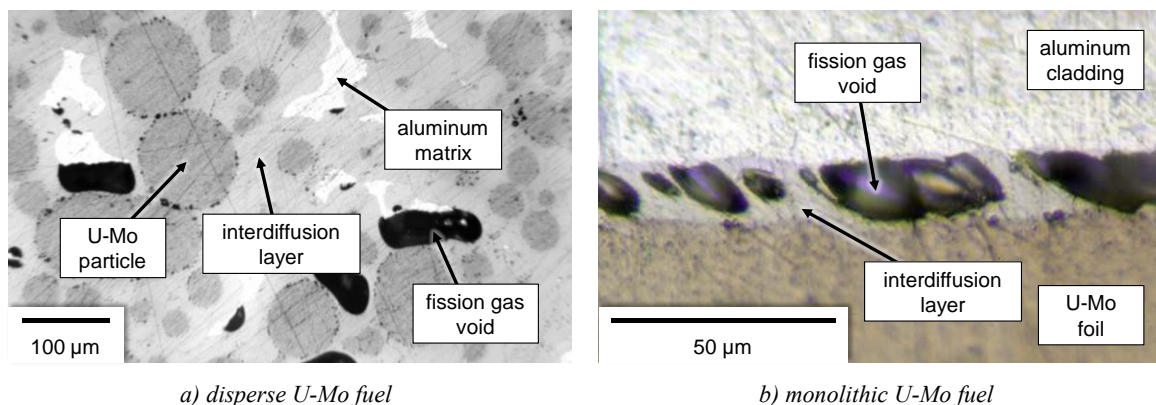


Figure 8: Micrographs of disperse (a) and monolithic (b) U-Mo fuel after irradiation in RERTR-4 and RERTR-8, respectively. An interdiffusion layer between U-Mo and Al has formed and gaseous fission products have accumulated in voids. After [34,36].

While US-American fuel fabricators use a co-rolling process to apply the Zr interdiffusion barrier onto the U-Mo foils during their fabrication by hot-rolling [26–28], TUM is proposing a *PVD* (physical vapor deposition) process to apply a Zr coating onto bare U-Mo foils. In 2011, it was demonstrated that PVD coating of *large-size* U-Mo foils (700 x 62.4 mm) with Zr is technically feasible with an experimental device, the so-called *HSK1* (Handschuhkasten 1) [8]. However, coating adherence deficiencies [9] required a comprehensive investigation of the coating process at a significantly reduced sample size, the so-called *mini-size* geometry (82.5 mm x 19 mm). Thus in 2013, a versatile experimental device – the so-called *HSK3* (Handschuhkasten 3) – was built, which integrated several techniques to improve the coating adherence and its properties. With this device, an experimental mini-size PVD coating process for U-Mo foils with 100% surface coverage and defect-free adherence was developed. However, significant optimization potential was still identified [12,14]. As a next step towards the industrialization, a pilot PVD coating process for *full-size* (762 x 45 mm) U-Mo foils must be developed.

Cladding application

To apply the aluminum cladding to the coated U-Mo foils, US-American fuel fabricators use a *HIP* (hot isostatic pressing) process [19,27,28], whereas the European fuel fabricator Framatome-CERCA uses its proprietary *C2TWP* process [9]. Both processes must ensure a defect-free bonding of the coated U-Mo foil with the Al cladding without large porosities and voids. The development and optimization of the confidential C2TWP process is not part, but is accomplished in the course of this thesis by Framatome-CERCA.

1.4 AIM OF THIS THESIS

The aim of this thesis is to bring forward the European fabrication process for monolithic U-Mo fuels in the key areas of gradient foil fabrication and PVD coating.

Gradient foil fabrication demonstration

No fabrication process for gradient U-Mo foils is currently available worldwide. Thus, this thesis aims at a first-of-a-kind technology demonstration of fabrication processes for such foils and subsequently, fuel plates made thereof.

Initial developments at US National Laboratories to develop such a fabrication process [44,45] for the conversion of the HFIR reactor (Tennessee, USA) were halted, since HFIR has recently shifted its preferred conversion scenario towards high-loaded U_3Si_2 fuel [46]. Also, the research at FRM II is shifting towards advanced fuel element designs which do not necessarily need gradient U-Mo foils. Thus, this topic has recently become less relevant and is dealt with only briefly via the following tasks, treated in the respective sections of the thesis which are given in brackets:

- Evaluation and selection of suitable surrogate materials to avoid the need of using radioactive U-Mo material in first studies (2.1.3).
- Evaluation and selection of suitable fabrication processes for gradient U-Mo foils (4.2).
- Fabrication demonstration of gradient foils from surrogate material in mini-size and full-size geometry (sections 4.3 and 4.4).
- Demonstration of the compatibility of the PVD coating and C2TWP cladding application processes with gradient foils (section 4.5).

Pilot PVD coating process

In 2016, TUM's mini-size PVD coating process and Framatome-CERCA's C2TWP cladding application process were successfully demonstrated by producing the *LEU* (low enriched uranium) fuel plates for the *EMPIrE* irradiation test (European Mini-Plate Irradiation Experiment) in the ATR reactor (Idaho, USA) [12,13,47–50].

For the upcoming European irradiation test *FUTURE-MONO-1* [51], planned in 2023 in the BR2 material test reactor (Belgium), LEU fuel plates shall be fabricated from flat full-size U-Mo foils with a Zr coating applied by a pilot PVD coating process. After this irradiation test, the complete European fabrication process for monolithic U-Mo fuels as proposed in Figure 6 shall be industrialized for the conversion of FRM II and potentially other research reactors.

Thus, this thesis aims at establishing a pilot PVD coating process for such full-size substrates, which are ~ 20 x larger than the mini-size geometry. This process shall incorporate the experience gained from the existing mini-size PVD coating process and its development shall already be focused towards industrialization. This will be accomplished by the following tasks:

- Evaluation of the mini-size process and review of the results from the EMPIrE fabrication campaign (section 2.3.7).
- Definition of design fundamentals for a pilot PVD coating process (section 5.1).
- Conduction of optimization studies (sections 5.2 and 5.3).
- Design, construction and commissioning of a new full-size PVD coating device (section 5.4).
- Realization, characterization and parametrization of the pilot PVD coating process and demonstration using surrogate materials (section 5.5).

2 THEORETICAL CONSIDERATIONS

2.1 MATERIALS SCIENCE

A detailed knowledge of the involved materials and their interaction is crucial when developing and optimizing fuel fabrication processes. Hereby, the relevant materials are the fuel core material U-Mo, the interdiffusion barrier material Zr and the cladding material AlFeNi. To understand the properties and behavior of these materials during fabrication and irradiation, a brief introduction to intermetallic solid-state diffusion is given and the materials' physical, thermal and mechanical properties are described. A surrogate material study was performed to identify materials suitable to replace U-Mo for experiments within this thesis.

2.1.1 INTERDIFFUSION

The topic of solid-state diffusion, together with interdiffusion between different materials, is widely covered in extensive literature. Also, interdiffusion effects in U-Mo fuels have been studied in several publications and theses before. A detailed presentation of the theoretical foundations of diffusion, tailored to fabrication processes for U-Mo fuels, can be found in [14] for example.

Diffusion refers to the transport of atoms in gases, liquids or solid materials. The root cause for diffusion in solids is always a *concentration gradient* $\partial C(x, y, z, t)/\partial r$. *Fick's first law* [52] describes the *diffusive flux of atoms* J along such a concentration gradient as follows:

$$J = -D \nabla C(x, y, z, t) \quad (1)$$

Herein, D is the *diffusion coefficient*. To calculate the variation of the concentration $C(x, y, z, t)$ over time t , *Fick's second law* [52] can be used:

$$\frac{\partial C(x, y, z, t)}{\partial t} = D \Delta C(x, y, z, t) \quad (2)$$

The diffusion coefficient is not constant but depends, among others, on the temperature T according to an Arrhenius [52] equation:

$$D(T) = D_{\infty} e^{-\left(\frac{Q_D}{RT}\right)} \quad (3)$$

Herein, D_{∞} is the theoretical diffusion coefficient at infinite temperature, Q_D is the energy barrier – or *activation energy* – for the diffusion process and R is the universal gas constant. For volumetric diffusion inside individual crystal grains, Q_D generally is high due to the strong inter-atomic binding forces and the small number of crystallographic defects, which could allow atoms to exchange places. For diffusion across grain boundaries, the high number of crystallographic defects and weakened inter-atomic binding forces due to the grain misalignment lead to significantly lower activation energies. The lowest activation

energies can be found for surface diffusion, where practically an infinite number of vacant positions is available for the diffusing atoms and atomic binding forces may be very weak.

The theory given so far only covers the *self-diffusion* of atoms in a homogeneous *single-phase material*, composed of a single chemical element X . The corresponding diffusion coefficient is called *self-diffusion coefficient* D_X^* . For the diffusion of atoms in homogeneous *single-phase mixtures* AB, composed of the chemical elements A and B, the so-called *intrinsic diffusion coefficients* $D_A^I(C_A)$ and $D_B^I(C_B)$ must be considered separately. The intrinsic diffusion coefficient $D_X^I(C_X)$ depends on the respective atomic concentration C_X of the element X inside the mixture and can be estimated from its self-diffusion coefficient D_X^* and its thermodynamic activity coefficient γ_X using *Darken's equations* [53]. Here, Φ is the co-called *thermodynamic factor*.

$$D_X^I(C_X) = D_X^* \left(1 + \frac{\partial \ln \gamma_X}{\partial \ln(C_X)} \right) = D_X^* \Phi \quad (4)$$

Now, if two different materials A (in the α phase) and B (in the β phase) are brought into contact, an interface plane at the position $x_{\alpha\beta}$, the so-called *Matano plane*, is formed and both materials can diffuse into each other across this interface. This *interdiffusion* leads to the mixing of the materials and the formation of concentration profiles $C_A(r)$ and $C_B(r)$ of both elements. At any time, the sum of both concentrations remains constant at every position r :

$$C_A(r) + C_B(r) = \text{const. } \forall r \quad (5)$$

In such a mixture, the so-called *interdiffusion coefficient* for the diffusion of material A can be derived from the intrinsic diffusion coefficients D_A^I and D_B^I using again Darken's equations:

$$D(C_A) = C_A D_B^I + (1 - C_A) D_A^I \quad (6)$$

Due to the different interdiffusion coefficients and concentration profiles of both materials, the position $x_{\alpha\beta}$ of the Matano plane will move over time. This movement obeys a parabolic growth law:

$$x_{\alpha\beta}(t) = \sqrt{2 k_{\alpha\beta} t} \quad (7)$$

Here, $k_{\alpha\beta}$ is the so-called *growth factor*. It depends on the interdiffusion coefficient D_{ij} in the i phase, the concentration gradient K_{ij} in the i phase near the interface and the equilibrium composition C_{ij} at the i side of the interface. A detailed discussion on $k_{\alpha\beta}$ can be found in [54].

$$k_{\alpha\beta} = 2 \left(\frac{(D K)_{\beta\alpha} - (D K)_{\alpha\beta}}{C_{\alpha\beta} - C_{\beta\alpha}} \right)^2 \quad (8)$$

This theory can now be extended to mixtures of two elements A (in the α phase) and B (in the β phase), which form an *intermetallic compound* in the γ phase. As can be seen in Figure 9, a certain time after the two elements are brought into contact in their initial state (a), the γ phase has evolved in between the α and β phase (b). This corresponds to the *isothermal line* at temperature T_0 in the phase diagram (c), from which the concentration profile (d) can be extracted by looking at the concentrations at the single-phase boundaries.

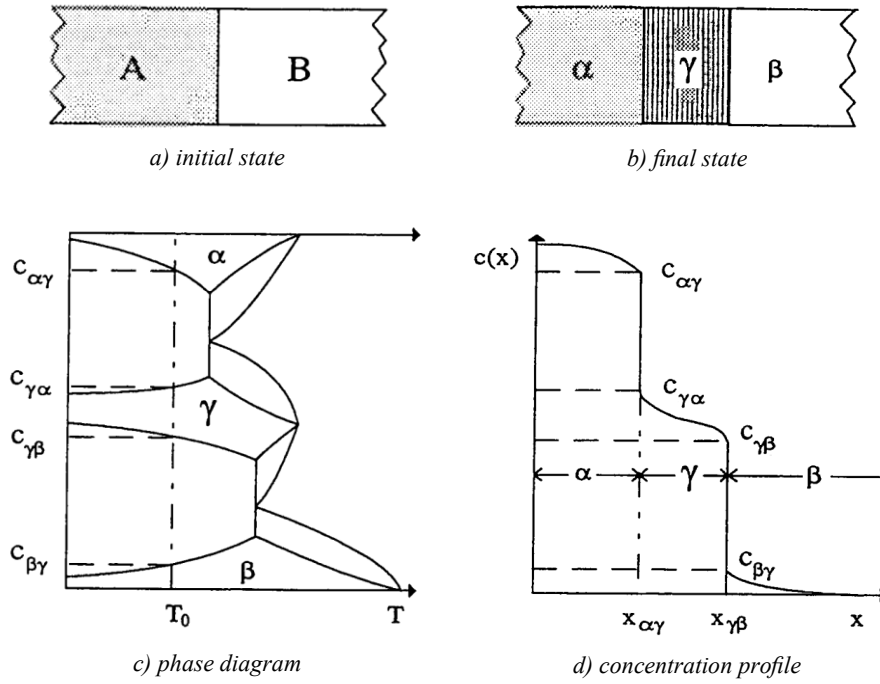


Figure 9: Multi-phase diffusion of elements A and B. When the elements A and B in their respective α and β phases are brought into contact, an intermetallic compound, the γ phase, can be formed. After [55].

Like in the previous case, the interdiffusion coefficients of the different materials at their boundaries can be calculated using equation (6). As shown in [55], the thickness of the intermetallic phase $S_\gamma = x_{\gamma\beta} - x_{\alpha\gamma}$ also obeys a parabolic growth law:

$$S_\gamma(t) = \sqrt{2 k_\gamma t} \quad (9)$$

Again, the growth factor k_γ can be calculated as:

$$k_\gamma = 2 \left[\left(\frac{(D K)_{\beta\gamma} - (D K)_{\gamma\beta}}{C_{\gamma\beta} - C_{\beta\gamma}} \right) - \left(\frac{(D K)_{\gamma\alpha} - (D K)_{\alpha\gamma}}{C_{\alpha\gamma} - C_{\gamma\alpha}} \right) \right]^2 \quad (10)$$

This growth factor can be verified by a diffusion couple experiment, where two pieces of highly polished metal are clamped together for a certain time t at a certain temperature T_0 , typically in an oven. Afterwards, a cross-section of the interface of the two metals is prepared and examined using optical or electron microscopy. From the thickness S_γ of the generated intermetallic phase, the growth factor can be calculated using equation (9). Attention must be paid for certain multi-phase systems, where the intermetallic phase starts to form only after a certain incubation time τ . In this case, equation (9) needs to be expanded as follows:

$$S_\gamma(t) = \sqrt{2 k_\gamma (t - \tau)} \quad (11)$$

As the growth factors k are sums or differences of interdiffusion coefficients, the temperature dependency of k is usually considered following an Arrhenius equation, similar to the temperature dependency of the diffusion coefficients [56]:

$$k(T) = k_{\infty} e^{-\left(\frac{Q_k}{RT}\right)} \quad (12)$$

It must be noted that this assumption is only valid if one of the following conditions is met for the involved diffusion coefficients:

- Dominance of a single diffusion coefficient over the others: $D_{\infty}^i \gg \sum_{j \neq i} D_{\infty}^j$
- Similar activation energies: $E_A^1 \cong E_A^2 \cong E_A^3 \cong \dots$

2.1.2 MONOLITHIC U-MO FUELS WITH INTERDIFFUSION BARRIER

U-Mo as fuel material

Pure uranium can exist in three different phases: the orthorhombic α phase, the tetragonal β phase and the *bcc* (body-centered cubic) γ phase as shown in the phase diagram in Figure 10.

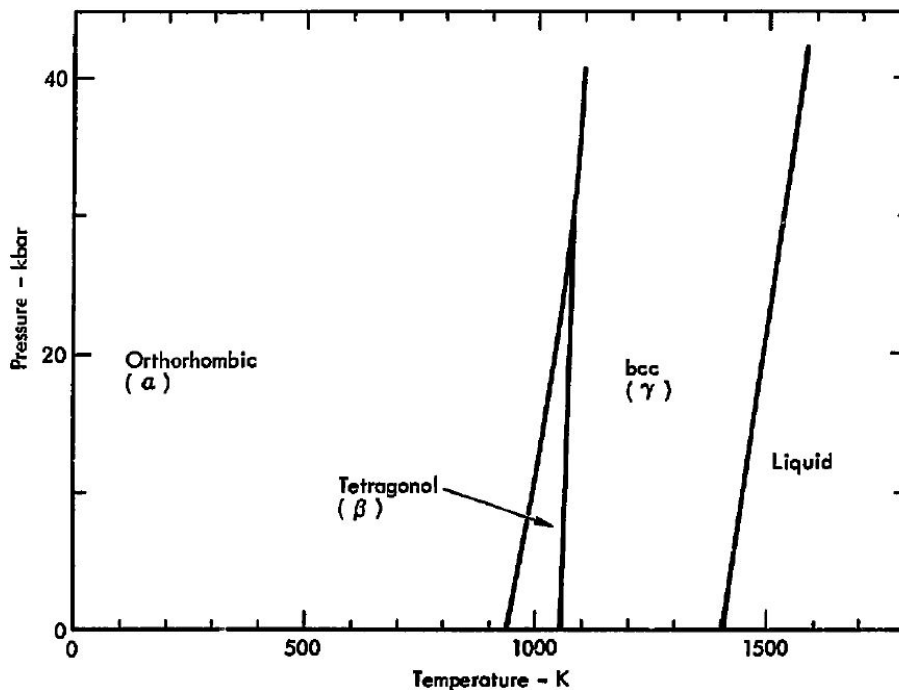


Figure 10: Phase diagram of pure uranium. At atmospheric pressure, the body-centered cubic γ phase only exists at temperatures above 1049 K (776 °C). From [57].

As Table 1 shows, the α and β phase of uranium have anisotropic coefficients of thermal expansion, which leads to macroscopic deformation during thermal cycling. Only the γ phase has an isotropic expansion behavior, making it the only uranium phase usable for research reactor fuels. However, in pure uranium the γ phase is only stable at temperatures above 1049 K. Thus, this high-temperature phase must be stabilized at room temperature, e.g. by rapid cooling after alloying – so-called *quenching*.

This is typically accomplished by alloying uranium with 4d and 5d transition metals from groups IV through VIII. These metals form solid solutions with γ -U in a broad temperature range and thus facilitate quenching the γ phase to room temperature in a metastable thermodynamic state. For example, up to 17 wt.% Mo can be solved in γ -U. An alloy with 10 wt.% molybdenum (U-10wt.%Mo or U-22at.%Mo, respectively) was found to be the best compromise between irradiation stability and uranium density [3,7]. Figure 11 shows the corresponding binary phase diagram of the U-Mo system at molybdenum concentrations between 40 and 100 at.%.

Table 1: Phases of uranium. Only the γ phase has an isotropic thermal expansion behavior and is thus usable as research reactor fuel. Data from [3,58].

	α phase (U) rt	β phase (U) ht1	γ phase (U) ht2
Crystal structure	Orthorhombic	Tetragonal	Body-centered cubic (bcc)
Space group symbol	Cmcm	P42/mnm	Im-3m
Lattice parameters	a = 2.854 Å b = 5.870 Å c = 4.956 Å	a = 10.759 Å b = 10.759 Å c = 5.656 Å	a = 3.474 Å b = 3.474 Å c = 3.474 Å
Coefficients of thermal expansion	$\alpha_a = 35.6 \cdot 10^{-6} / \text{K}$ $\alpha_b = -8.4 \cdot 10^{-6} / \text{K}$ $\alpha_c = 31.6 \cdot 10^{-6} / \text{K}$ (300 - 913 K)	$\alpha_a = 21.2 \cdot 10^{-6} / \text{K}$ $\alpha_b = 21.2 \cdot 10^{-6} / \text{K}$ $\alpha_c = 8.8 \cdot 10^{-6} / \text{K}$	$\alpha_a = 21.6 \cdot 10^{-6} / \text{K}$ $\alpha_b = 21.6 \cdot 10^{-6} / \text{K}$ $\alpha_c = 21.6 \cdot 10^{-6} / \text{K}$ (273 - 1273 K)
Stable temperature	0 K - 941 K	941 K - 1049 K	1049 K - 1405 K

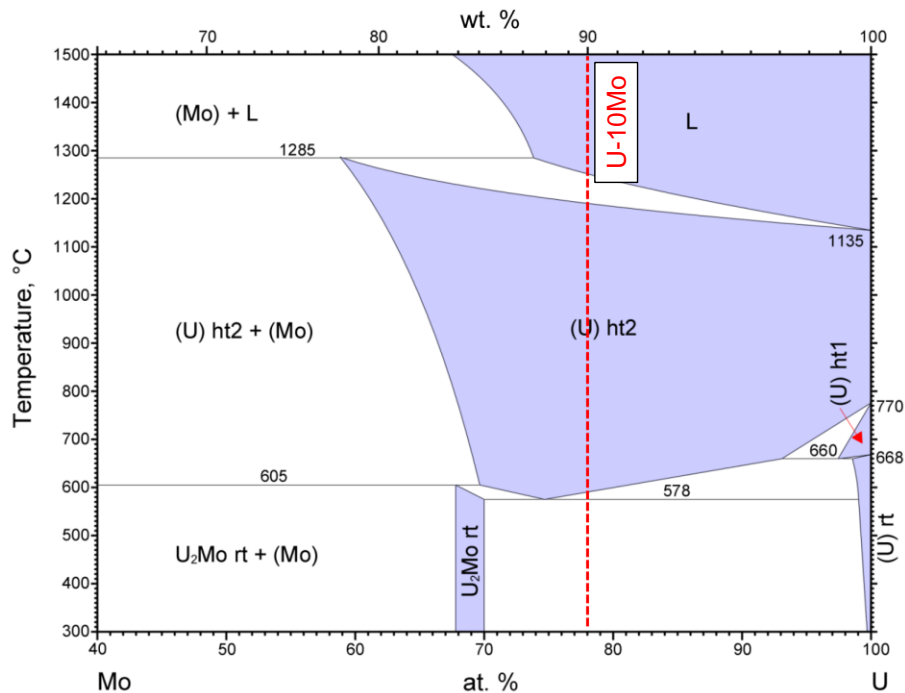


Figure 11: Binary phase diagram of the U-Mo system. The dotted red line indicates the U-10wt.%Mo alloy (U-22at.%Mo). Single-phase areas are drawn in purple, double-phase areas in white. After [59].

Since the γ phase is only metastable at room temperature, a decomposition into the equilibrium phases α -U and δ -U₂Mo (also denoted as U₂Mo rt or γ') is possible, e.g. by annealing at elevated temperatures for a long time. Such decomposition processes are typically expressed in *TTT diagrams* (time-temperature-transformation), which plot the phase composition over time and temperature. As can be seen from Figure 12, the decomposition of the γ phase in U-10wt.%Mo starts after ~ 5 hours of annealing

at ~ 480 °C at the earliest [60,61]. It must be noted that the entire history of processing at elevated temperatures must be considered when estimating the amount of phase decomposition. A single annealing process at 500 °C for 10 hours has the same effect as five sequential annealing processes for 2 hours at the same temperature [60,62].

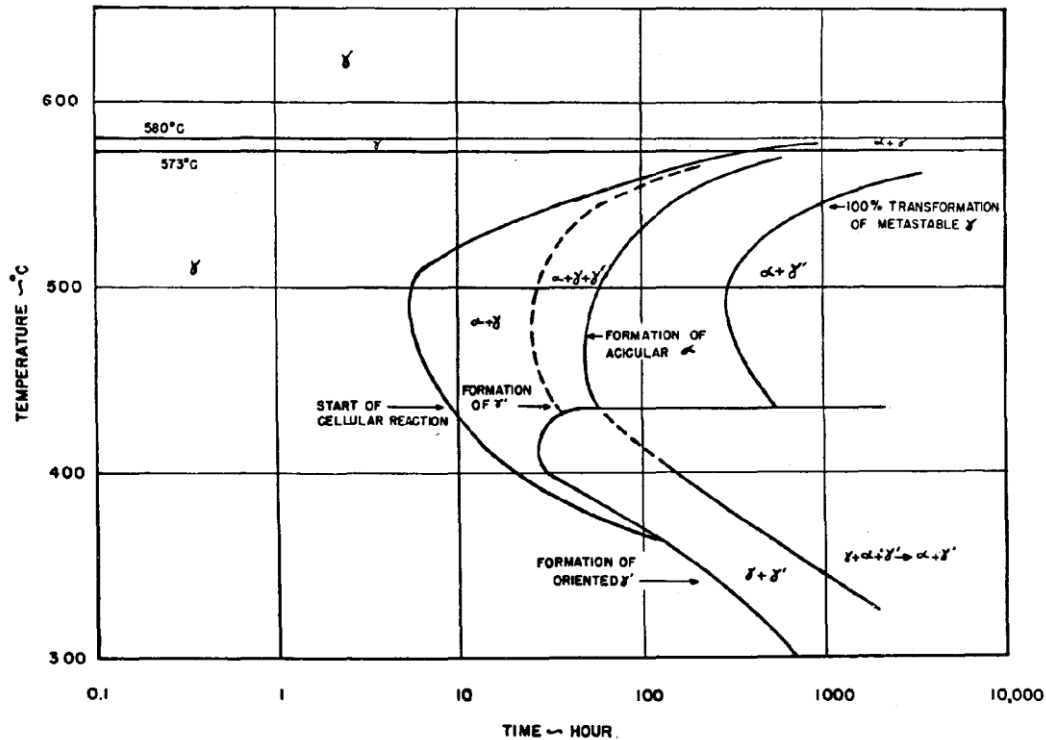


Figure 12: TTT diagram of the U-10wt.%Mo system. The decomposition of the γ phase starts after ~ 5 hours of annealing at ~ 475 °C at the earliest. From [60].

Many factors influence the material properties of U-Mo fuels, i.e. the weight fraction of Mo in the alloy, the fabrication history including thermal treatments as well as the irradiation state. As this thesis deals with the fabrication of monolithic U-10wt.%Mo fuels (hereafter denoted as U-Mo), the material properties in Table 2 are given for unirradiated U-10wt.%Mo foils in the γ phase at room temperature, as produced by the current US-American baseline fabrication process [27,28], where applicable. [3] gives a detailed literature review and discussion of material properties of U-Mo alloys, including the temperature, irradiation and fabrication history dependency of selected properties.

Special care must be taken of the molybdenum homogeneity in U-Mo fuels, as during cooling of ingots or foils, a separation of Mo-rich and Mo-lean phases can occur [63–66]. This can be avoided by introducing a high temperature homogenization step into the fabrication process. Typical homogenization durations are ~ 2 h @ 1000 °C or ~ 9 h @ 900 °C [28,64,65].

Uranium, being a non-precious metal, has a strong tendency for surface oxidation and quickly reacts with atmospheric oxygen to UO_2 (uranium dioxide), and ultimately to the long-term stable form U_3O_8 . After a few minutes at air, the color of freshly cleaned material changes from metallic-grey to yellow-golden and subsequently, after a few days at these conditions, to black. Unlike most other metals, uranium and its alloys do not form a self-passivating oxide layer which stops the further oxidation process. Instead, oxygen can penetrate far inside the material through cracks in the brittle oxide layer and several μm thick oxide layers can be formed [67]. Due to its strong oxidation tendency, uranium

and uranium alloys are considered pyrophoric, i.e. flammable at air atmosphere. This is especially valid for fine powders or other forms with a high surface-to-volume ratio.

Table 2: Material properties of the U-10wt.%Mo alloy. Where applicable, the values are given for unirradiated fuel foils in the γ phase as produced by the US-American fabrication process. If not stated otherwise, all data are given at room temperature. Data from [3,7,68–71].

Property	Value
Lattice parameter	3.416 Å
Density	17.13 g/cm ³
Hardness	285 HV
Elastic modulus	88.3 GPa
Tensile strength	887 MPa
Yield strength	995.9 MPa
Melting temperature	1438 K
Heat capacity @ 100 °C	0.142 kJ/kg K
Thermal conductivity	11.1 W/m K
Thermal expansion (RT - 100 °C)	$11.8 \cdot 10^{-6} /K$

Zr as interdiffusion barrier material

As presented in the introductory chapter, the placement of an interdiffusion barrier between the U-Mo fuel and the Al cladding is proposed to prevent the formation of an unfavorable interdiffusion layer between those materials [37,38,40,42,72]. The selection of an appropriate barrier material must be performed with respect to the following key criteria:

- High thermal conductivity and melting point
- Suppression of the interdiffusion reaction between U-Mo and Al by blocking atomic transport across the barrier
- Low reactivity with the U-Mo fuel and the Al cladding itself
- Irradiation stability of the barrier material and potentially formed intermetallic compounds with U-Mo or Al
- Low absorption cross-section for thermal neutrons
- Compatibility with fuel fabrication and fuel reprocessing processes

In general, refractory metals are considered good candidates [40,73–75]. Refractory metals are body-centered cubic (bcc) elements found in groups IV (Ti, Zr, Hf), V (V, Nb, Ta) and VI (Cr, Mo, W) of the periodic table. They typically have high melting points, high thermal conductivity and low coefficients of thermal expansion [76]. Based on its physical properties, irradiation and interdiffusion behavior as well its compatibility with mechanical fuel fabrication processes such as rolling, Zr was selected as the interdiffusion barrier material in the US-American design for monolithic U-Mo fuel [27,28,74].

Also, molybdenum and tungsten were tested as alternative interdiffusion barrier materials for U-Mo fuels. Following the promising results of [40,77], disperse U-Mo full-size plates with Mo-coated U-Mo particles were part of the *SEMPER-FIDELIS* irradiation test in the BR2 material test reactor. During the *PIE* (post-irradiation examination), a thick interaction layer between the Mo coating and the Al matrix was discovered, which almost fully consumed the Mo coating [78]. Therefore, this coating was discarded for future studies. Based on [79], a study on monolithic U-Mo fuels with a W coating applied by PVD was recently performed at TUM [42,80]. By heavy-ion irradiations, a promising irradiation behavior with almost no U-Mo/W or W/Al interaction was discovered. However, the fabrication of such W-coated U-Mo foils has proven to be difficult due to tungsten's high hardness and brittleness. Thus, further studies on tungsten as alternative interdiffusion barrier material will be performed in the future.

Table 3: Phases of zirconium. At typical process temperatures for fuel fabrication, only the *hcp* α phase occurs. Data from [81,82].

	α phase (Zr) rt	β phase (Zr) ht1
Crystal structure	Hexagonally close-packed (hcp)	Body-centered cubic (bcc)
Space group symbol	P63/mmc	Im-3m
Lattice parameters	a = 3.231 Å b = 3.231 Å c = 5.148 Å	a = 3.609 Å b = 3.609 Å c = 3.609 Å
Coefficients of thermal expansion	$\alpha_a = 7.2 \cdot 10^{-6} /K$ $\alpha_b = 7.2 \cdot 10^{-6} /K$ $\alpha_c = 7.2 \cdot 10^{-6} /K$ (300 - 1125 K)	$\alpha_a = 9.7 \cdot 10^{-6} /K$ $\alpha_b = 9.7 \cdot 10^{-6} /K$ $\alpha_c = 9.7 \cdot 10^{-6} /K$ (1143 - 1600 K)
Stable temperature	0 K - 1136 K	1136 K - 2128 K

As can be seen from the phases of Zr in Table 3, only the *hcp* (hexagonally close-packed) α phase occurs at the typical process temperatures for fuel fabrication. Above 1136 K, the bcc β phase, which is isostructural to γ U, is formed.

Due to the chemical similarity of the neighboring group IV metals Zr and Hf, natural zirconium is always found in a mixture with several wt.% hafnium. Hf is therefore usually not considered to be an impurity to Zr. While not significantly altering the mechanical and thermophysical properties of the material, Hf is a strong neutron absorber, which must be chemically removed from Zr or Zr alloys for nuclear applications [83]. Such processed Zr is called *reactor-grade*.

The mechanical properties of zirconium strongly depend on the purity of the material. Typically, impurity amounts of more than 800 ppm of hydrogen, carbon, nitrogen or oxygen lead to increased hardness and brittleness [76]. For the experiments in this thesis, mostly *industrial-grade* Zr 702 will be used. This grade specifies a Zr+Hf purity of $\geq 99.2\%$ and can contain up to 4.5 wt.% hafnium and 1600 ppm oxygen [84,85]. Table 4 lists the material properties for industrial-grade Zr 702 in an annealed state. It should be noted that, depending on the actual fabrication process, mechanical properties such as hardness can be strongly different. For example, non-annealed Zr samples can reach Vickers hardness values in the range of 200 - 275 HV, depending on their microstructure [86].

Table 4: Material properties of Zr 702. The values are given for bulk material in an annealed state. Data from [84,85].

Property	Value
Density	6.5 g/cm ³
Hardness	150 HV
Elastic modulus	99.3 GPa
Tensile strength	≥ 379 MPa
Yield strength	≥ 207 MPa
Melting temperature	2125 K
Heat capacity	285 J/kg K
Thermal conductivity	22 W/m K
Thermal expansion (RT - 100 °C)	$5.4 \cdot 10^{-6} /K$

Like uranium, zirconium is a pyrophoric non-precious metal which quickly reacts with atmospheric oxygen to form ZrO₂ (zirconium dioxide). This is especially valid for fine powders or other forms with a high surface-to-volume ratio. Zr bulk material tends to self-passivate by a thin and dense ZrO₂ layer, which prevents continuous oxidation.

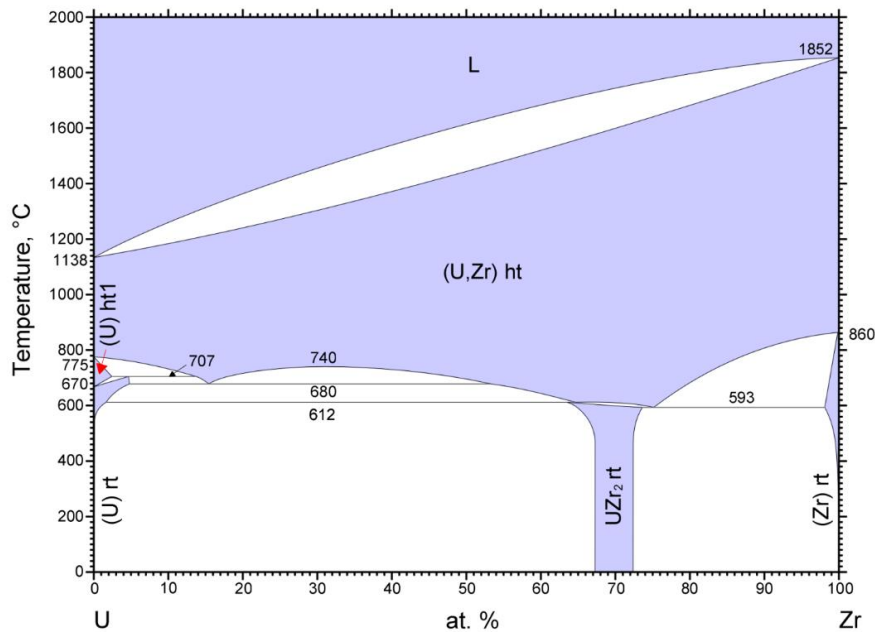


Figure 13: Binary phase diagram of the U-Zr system. At higher temperatures, the Zr β phase allows a single-phase solid solution with the isostructural U γ phase across the entire concentration range. Single-phase areas are drawn in purple, double-phase areas in white. From [59].

Figure 13 and Figure 14 show the binary phase diagrams of the U-Zr and Mo-Zr system, respectively. At low temperatures, the Zr α phase (hcp, denoted as Zr rt) does not allow single-phase systems with the non-isostructural U and Mo phases. At higher temperatures, the Zr β phase (bcc, denoted as Zr ht) is isostructural to the U γ phase (denoted as U ht) and the Mo α phase. Thus, a single-phase solid solution can be formed between β Zr and γ U across the entire concentration range, denoted as (U, Zr) ht. Below 612 °C, UZr_2 starts to separate as an intermetallic phase. Mo, however, can only be solved up to ~ 20 at.% in β Zr and additionally, the intermetallic phase ZrMo_2 can be formed above ~ 200 °C [87].

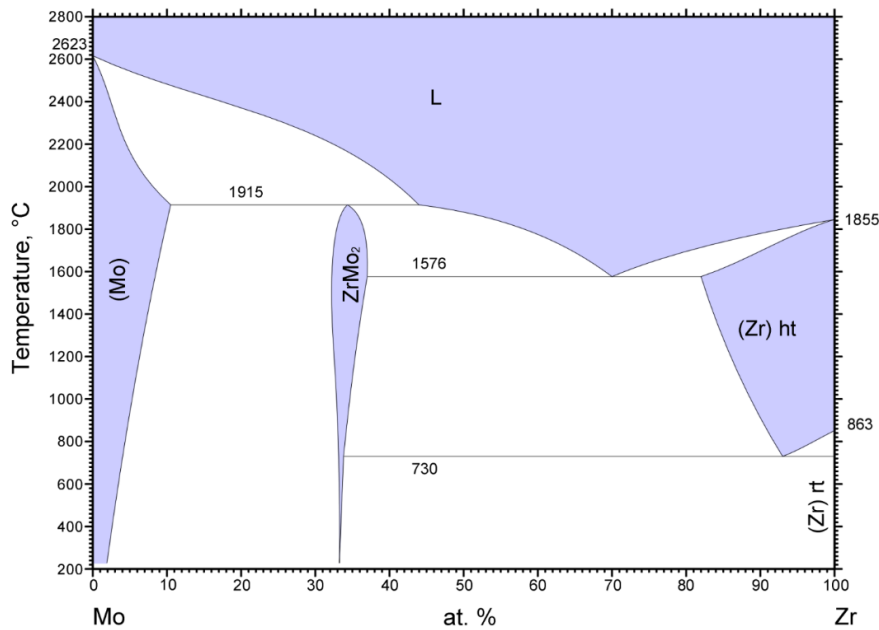


Figure 14: Binary phase diagram of the Mo-Zr system. Only up to ~ 20 at.% Mo can be solved in the Zr β phase before the intermetallic phase ZrMo_2 starts to form. Single-phase areas are drawn in purple, double-phase areas in white. From [59].

For the application of a Zr coating onto U-Mo foils, the three elements U, Mo and Zr need to be considered when studying the interdiffusion behavior. This is displayed in so-called *ternary phase diagrams* in Figure 15. The lower-left side of these diagrams is not of interest for this thesis, as only relatively low Mo concentrations occur in the U-Mo fuel system. The relevant phases at the displayed temperatures are as follows:

- At 1000 °C, a large single-phase area can be found for low Mo concentrations, which includes any mixing ratio of the Zr β and the U γ phase, denoted as (U, Zr) ht. At higher Mo concentrations, the ZrMo_2 phase starts to separate. The remaining space is covered with double-phase areas (drawn in white) and triple-phase areas (drawn in yellow).
- At 700 °C, the U β phase, denoted as (U) htI, as well as the Zr α phase, denoted as (Zr) rt, start to separate at high U respectively Zr concentrations. Thus, the area covered by (U, Zr) ht gets smaller and is interrupted with double-phase areas with the respective U and Zr phases.
- At 600 °C, the U β phase is replaced by the U α phase, denoted as (U) rt. Additionally, the phases U_2Mo , UZr_2 and $\text{U}_6\text{Zr}_3\text{Mo}$ are formed, further reducing the area covered by (U, Zr) ht and introducing further double-phase and triple-phase areas.
- At 500 °C, the $\text{U}_6\text{Zr}_3\text{Mo}$ phase is no longer present but replaced by the $\text{U}_4\text{Zr}_5\text{Mo}$ phase over a wide range of U and Zr concentrations, respectively.

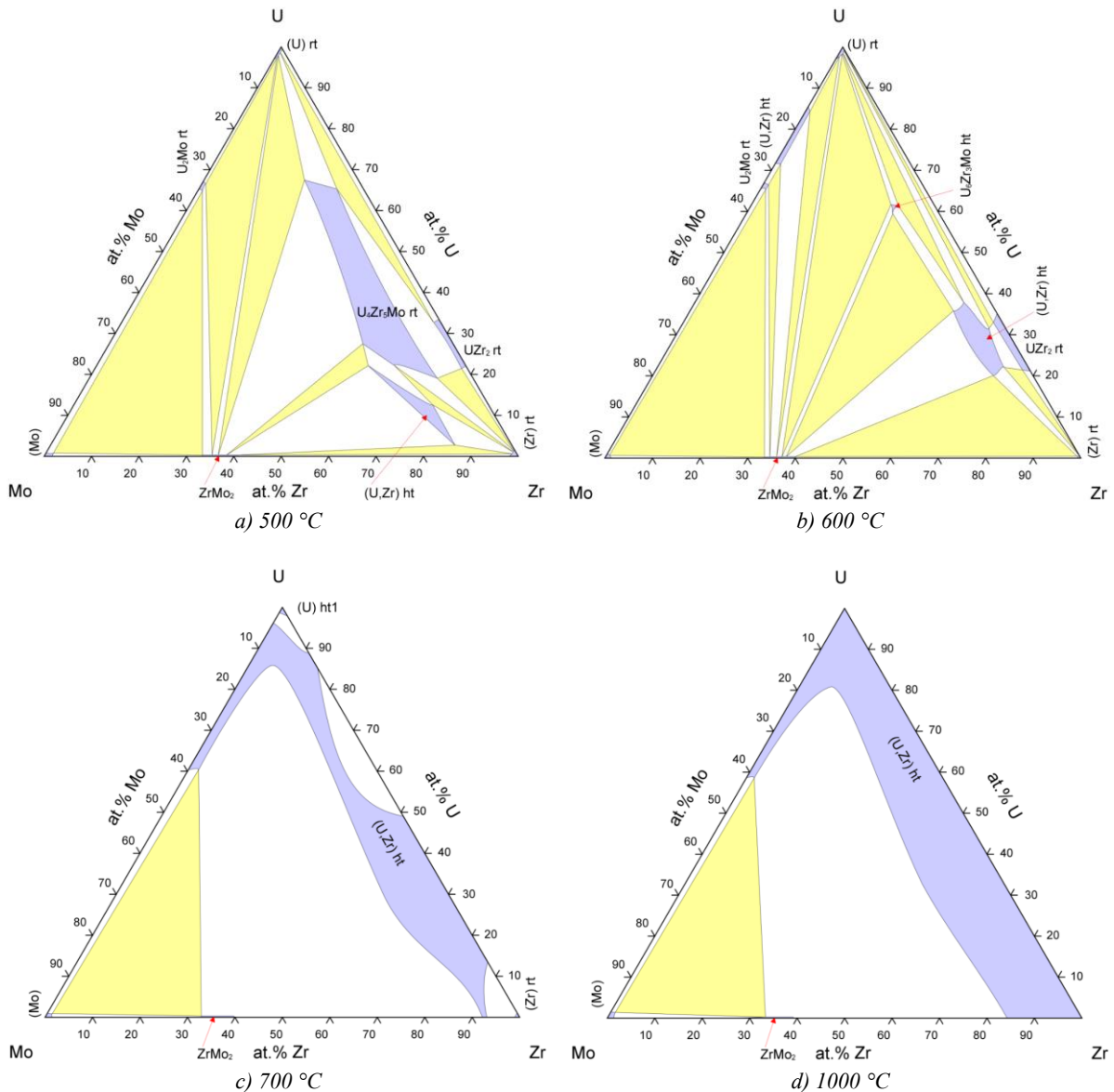


Figure 15: Ternary phase diagrams of the U-Mo-Zr system at 500 °C (a), 600 °C (b), 700 °C (c) and 1000 °C (d). With increasing temperature, the single-phase area of the isostructural Zr β and U γ phases becomes larger. The lower-left side of these diagrams is not of interest for this thesis, as only relatively low Mo concentrations occur in the U-Mo fuel system. Single-phase areas are drawn in purple, double-phase areas in white and triple-phase areas in yellow. From [59].

Figure 16 shows the typical U-Mo/Zr interaction behavior, here produced using polished U-Mo and Zr bulk samples which were clamped together and heated at a certain temperature for several hours. In this experiment, carried out by Huang [88], almost no visible interaction layer forms at 600 °C, even if the samples are kept at this temperature for 960 hours. At 700 °C and above, the diffusion of the bcc U γ phase into Zr stabilizes the newly formed isostructural Zr β phase at the right side of the interface, which therefore now accommodates considerable amounts of U and Mo. Additionally, the ZrMo₂ phase forms at the left side of the interface. The high concentration of Mo in the ZrMo₂ phase leads to a significant Mo depletion in the U-Mo phase and therefore promotes the decomposition of the U γ phase into the U β and finally α phases.

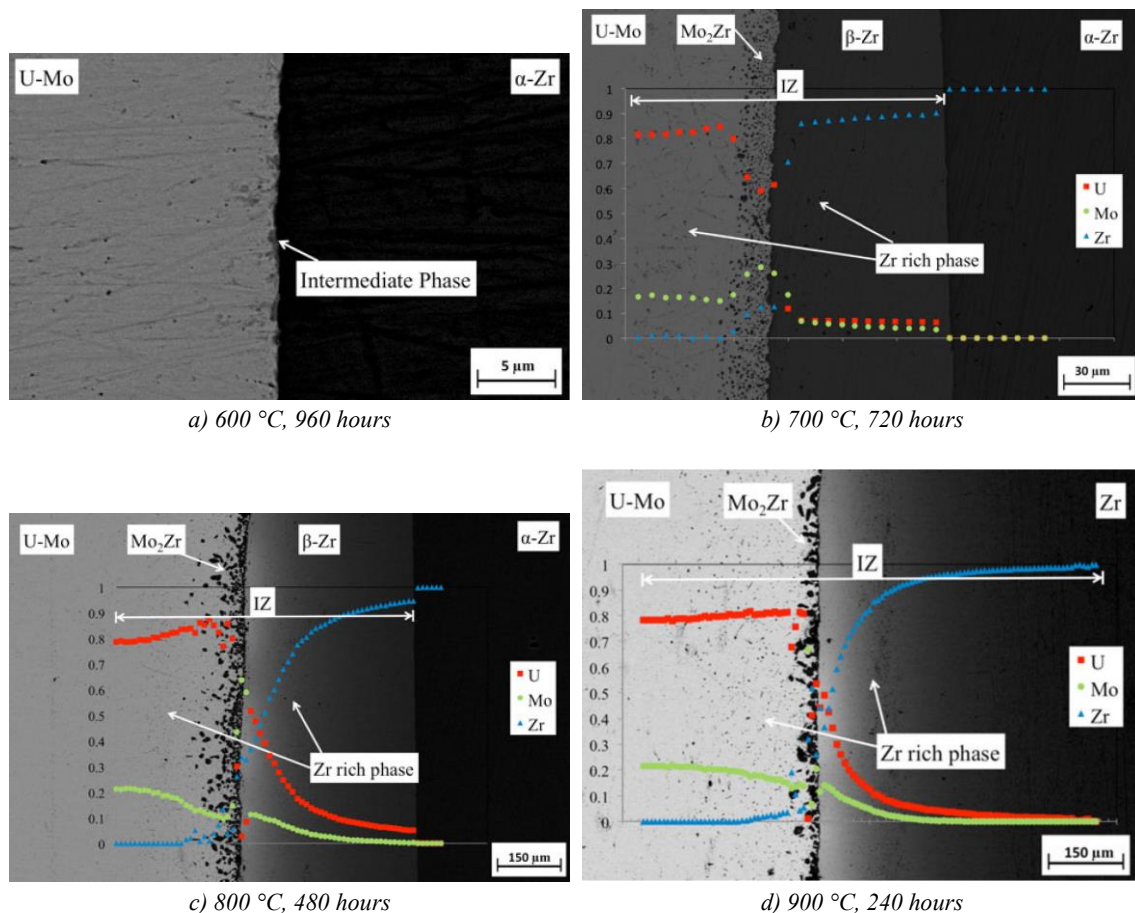


Figure 16: Interaction between clamped bulk U-Mo and Zr samples at various temperatures. While at 600 °C, almost no interaction occurs even after 40 days, several new phases start to form at 700 °C and above. From [88].

AlFeNi as cladding material

AlFeNi is used as cladding material in the current FRM II fuel element. It is typically chosen instead of the more common AGxNE alloys if a higher corrosion resistance is required. Being a Framatome-proprietary alloy for European research reactor fuel, only few material properties of AlFeNi are publicly available, e.g. in [89]. US-American research reactors typically use 6000 series aluminum alloys, e.g. Al-6061. Extensive data about this alloy can be found in [3,7,89,90]. Table 5 lists the specified chemical compositions of these aluminum alloys and Figure 17 shows the ternary phase diagram of the AlFeNi system.

For the fabrication of fuel plates from Zr-coated U-Mo foils, the interface between the Zr coating and the Al cladding remains important. The cladding application process thus needs to be adapted, so that no additional unwanted interdiffusion layers are created, which could potentially diminish the overall fuel performance. Figure 18 shows the phase diagram of the Al-Zr system, which indicates that up to ~ 12 at.% Al can be solved in α -Zr, whereas practically no Zr can be solved in Al. A total of nine different intermetallic phases, ranging from Zr_3Al to $ZrAl_3$, can occur across the entire concentration range. However, only the $ZrAl_3$ and Zr_2Al_3 phases have a positive growth factor and can be observed in the relevant temperature range below 600 °C [91].

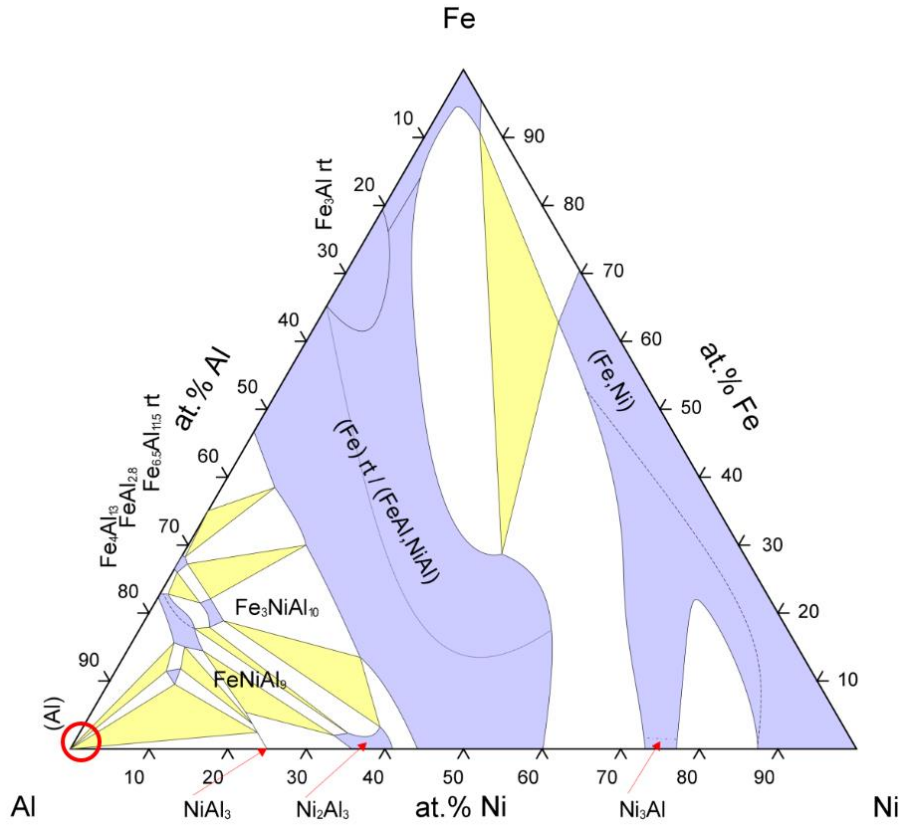


Figure 17: Phase diagram of the Al-Fe-Ni system at room temperature. The red circle in the bottom left corner shows the region of interest for the AlFeNi alloy. Single-phase areas are drawn in purple, double-phase areas in white and triple-phase areas in yellow. From [59].

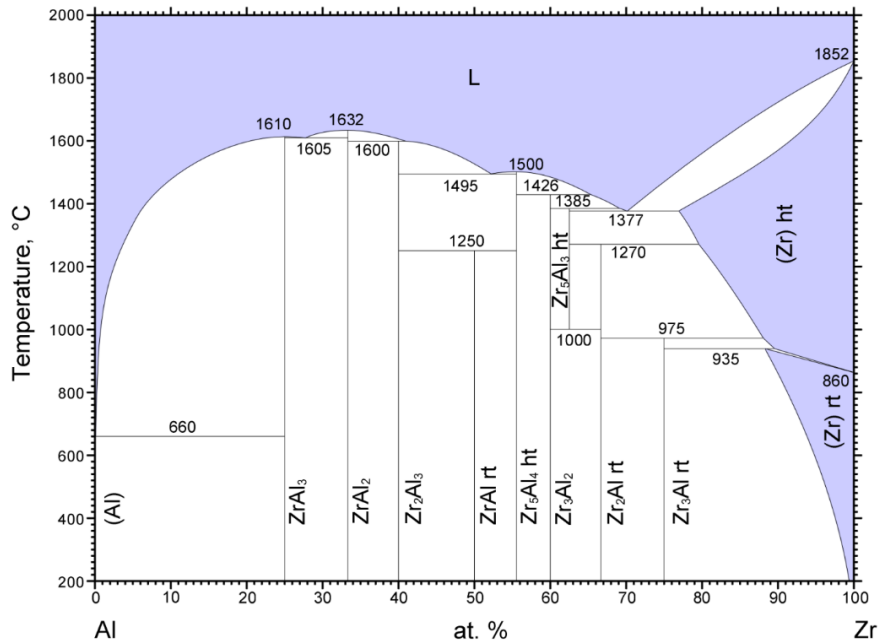


Figure 18: Phase diagram of the Al-Zr system. Only the $ZrAl_3$ and Zr_2Al_3 phases have a positive growth factor and can be observed in the relevant temperature range below 600 °C. Single-phase areas are drawn in purple, double-phase areas in white. From [59].

Table 5: Chemical compositions of selected aluminum cladding alloys. Constituents < 0.8 wt.% are omitted for clearness. Data from [89].

Alloy	Chemical composition
AlFeNi	0.8 - 1.2 wt.% Fe 0.8 - 1.2 wt.% Ni ≤ 1.8 wt.% Fe+Ni 0.8 - 1.2 wt.% Mg rest Al
AG1NE	1.1 - 1.4 wt.% Mg rest Al
AG2NE	1.8 - 2.3 wt.% Mg rest Al
AG3NE	2.5 - 3.0 wt.% Mg rest Al
Al-6061	0.8 - 1.2 wt.% Mg 0.4 - 0.8 wt.% Si rest Al

2.1.3 SURROGATE MATERIALS

Throughout this thesis, several experiments for foil fabrication and foil coating will be performed. To minimize the use of U-Mo in these experiments, a surrogate material must be identified which resembles the properties of the original material as close as possible. This is especially relevant for fabrication demonstration experiments for gradient foils, which will involve subtractive and additive manufacturing processes. There, large amounts of samples will be produced and therefore, a large amount of scraps needs to be dealt with. Below listed are the key criteria for adequate surrogate materials:

- Large similarity of the material properties to U-Mo
- Commercial availability in a wide range of pre-product forms and sizes
- Broad industrial experience on fabrication processes

The specific material properties which were evaluated in the surrogate material study are:

Mechanical properties. For fabrication experiments for gradient foils, the mechanical properties of the original material U-Mo should be met as close as possible to evaluate the feasibility of the fabrication techniques and the quality of the final products. Also, during PVD coating and C2TWP cladding application experiments, the foils can undergo mechanical stress, e.g. due to bending. The evaluated mechanical properties and their units are:

- Density [g/cm³]
- Hardness [HV]
- Elastic modulus [GPa]
- Tensile strength [MPa]
- Yield strength [MPa]

Thermophysical properties. Thermophysical properties are important for a wide range of experiments throughout this thesis, as the foils can be exposed to elevated temperatures during the fabrication, coating and cladding processes. For additive manufacturing techniques, which may include a (partial) melting of the material, also the melting behavior is of interest. The evaluated thermophysical properties and their units are:

- Melting temperature [K]
- Heat capacity [kJ/kg K]
- Heat of fusion [kJ/kg]
- Thermal conductivity [W/m K]
- Thermal expansion [1/K]

Crystal structure and phase behavior. The γ phase of U-Mo is body-centered cubic and can be considered stable, as long as the temperature range $\sim 400 - \sim 575$ °C, where fast γ phase decomposition occurs, is avoided. During fabrication, the fuel can undergo temperature variations from room temperature up to several hundred °C. The surrogate material should therefore also exhibit a cubic crystal structure in a phase which is considered stable up to temperatures of approximately 600 °C.

Magnetism. During PVD coating experiments, the foils will be placed close to a so-called magnetron sputtering source which contains strong permanent magnets to support the coating process. Thus, it is important that the foil does not get attracted by the magnetron sputtering source and the magnetic field lines are not disturbed. This can be accomplished by using materials which are not ferromagnetic at room temperature and only exhibit insignificant paramagnetism and diamagnetism.

Optical absorptance. Additive manufacturing processes may include the (partial) melting of the material in powder form, often by a high-power infrared light source, e.g. a laser with a wavelength close to 1 μm . Thus, the feasibility and efficiency of the process greatly depends on the optical absorptance of the material at this wavelength. When evaluating this material property, special attention must be paid to the surface condition of the material, as it influences the absorptance e.g. by a discoloration due to surface oxidation.

A perfect surrogate material, which resembles all relevant properties of U-Mo, does not exist. Therefore, a compromise needs to be found between similar material properties and the other selection criteria mentioned above. For this compromise, two groups of materials were selected for the surrogate material study: stainless steels and titanium alloys. More precisely, stainless steel grade AISI 316L (also often referred to as X2CrNiMo17-12-2 or 1.4404) and titanium alloy Ti-6Al-4V (also often referred to as ASTM grade 5 or 3.7164) were chosen. Table 6 lists the relevant properties of these materials, if not stated otherwise, at room temperature.

Stainless steels

Stainless steels are iron-based alloys which typically contain considerable amounts of chromium and nickel to improve their corrosion resistance and mechanical properties. Other solutes can include carbon, nitrogen, aluminum, silicon, sulfur, titanium, copper, selenium, niobium, and molybdenum. Their high corrosion and heat resistance makes stainless steels popular for a wide range of applications, including architecture, automotive, medicine and energy. Thus, they are commercially available in various pre-product forms and sizes at comparably low cost. Further, broad fabrication experience with additive and subtractive manufacturing is available [92,93].

Table 6: Results of the U-Mo surrogate material study. If not stated otherwise, all values are given at room temperature. Data from [3,7,68–70,94–104].

Property	U-Mo	Stainless Steel AISI 316L	Titanium alloy Ti-6Al-4V
Density [g/cm ³]	17.13	7.95	4.43
Hardness [HV]	285	152	349
Elastic modulus [GPa]	88.3	193	113.8
Tensile strength [MPa]	887	560	950
Yield strength [MPa]	995.9	235	880
Melting temperature [K]	1438	1400	1660
Heat capacity [kJ/kg K]	0.142	0.500	0.526
Heat of fusion [kJ/kg]	no data	260 - 285	360 - 370
Thermal conductivity [W/m K]	11.1	14.0 - 15.9	6.7
Thermal expansion [10 ⁻⁶ /K] (RT - 100 °C)	11.8	16.0	8.0
Crystal structure	bcc	fcc	hcp+bcc
Ferromagnetism	no	no	no
Optical absorptance @1μm	0.56 - 0.62*	0.64**	0.77***

*) yellow to purple oxidation state; 400 °C

**) pure Fe powder

***) pure Ti powder

Stainless steels can be classified into *martensitic*, *ferritic*, *austenitic* and *duplex* steels, based on whether the dominant phase is *martensite* (body-centered cubic), *ferrite* (body-centered tetragonal), *austenite* (face-centered cubic) or a mixture of austenite and ferrite (duplex steels) [92]. Of these phases, ferrite and martensite are generally considered ferromagnetic, whereas the magnetic permeability of austenite is negligible [105]. Figure 19 exemplarily shows the microstructure of pure austenite as well as with precipitates of martensite and ferrite.

To predict which phases are present in a specific stainless steel alloy, the so-called *Schaeffler diagram* in Figure 20 can be used. To calculate the chromium equivalent of an alloy – the abscissa of a point – the weight concentrations of ferrite-forming solutes are summarized as follows [106]:

$$C_{Cr}^{equiv} = C_{Cr} + C_{Mo} + 1.5 C_{Si} + 0.5 C_{Nb} \quad (13)$$

Similarly, the nickel equivalent – the ordinate of a point – is calculated by summarizing the weight concentrations of the austenite-forming solutes as follows [106]:

$$C_{Ni}^{equiv} = C_{Ni} + 30 C_C + 0.5 C_{Mn} \quad (14)$$

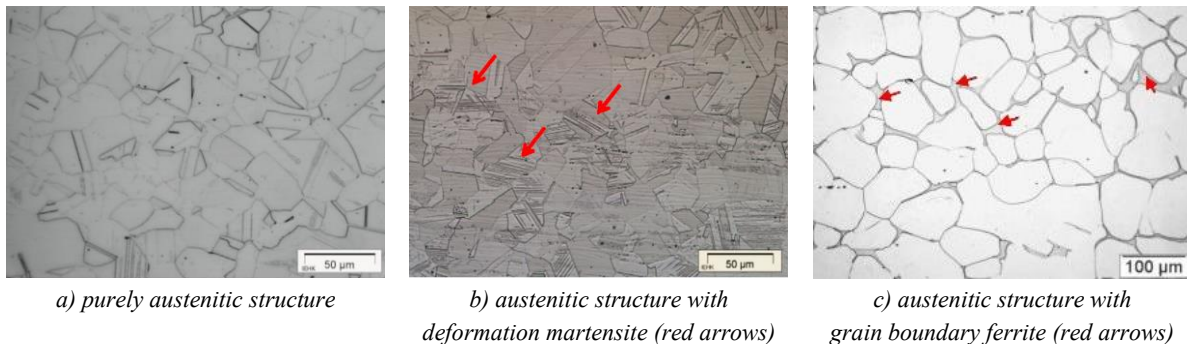


Figure 19: Microstructures of stainless steels. The austenitic structure can contain precipitates of martensite, introduced e.g. by mechanical deformation (b) or ferrite, e.g. at the grain boundaries (c). From [107,108].

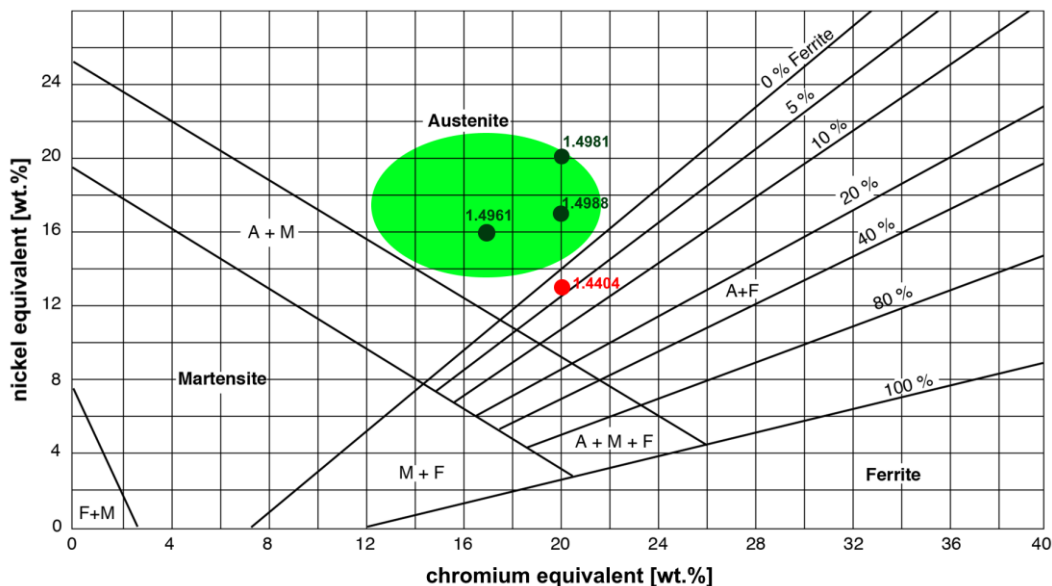


Figure 20: Schaeffler diagram of stainless steels. The green circle indicates purely austenitic steels. The red dot indicates the used alloy 1.4404, which is austenitic with a ferrite amount of less than 5 %. After [109].

Due to the necessity for a non-magnetic single-phase material, only stainless steels with a dominant austenitic phase with little or no other phases are considered. Such so-called *highly heat-resistant* stainless steels, e.g. grades 1.4981, 1.4988 and 1.4961, can be found in the green circle in the Schaeffler diagram. As these steel grades typically are expensive and not commonly used in subtractive and additive manufacturing of small parts, they were rejected as surrogate material. Instead, stainless steel grade 1.4404, or AISI 316L, an austenitic steel with a maximum ferrite amount of 5 %, is chosen as a compromise and marked with a red dot in the Schaeffler diagram. It is a low-carbon steel with added molybdenum, which improves the corrosion resistance remarkably compared to other common types like AISI 304 [92]. It is one of the most common grades of stainless steel and therefore available in a broad range of pre-product forms and sizes at comparably low cost and experience in subtractive and additive manufacturing is widely available. Table 7 gives a typical specification for the chemical composition of stainless steel AISI 316L.

Table 7: Chemical composition of stainless steel AISI 316L. Constituents < 0.8 wt.% are omitted for clearness All values in wt.%. Data from [110].

Constituent	Specification
Cr	16.5 - 18.5 wt.%
Ni	10.0 - 13.0 wt.%
Mo	2.0 - 2.5 wt.%
Mn	2.0 wt.%
Si	1.0 wt.%
Fe	rest

For surface-sensitive applications of stainless steels, like using it as a substrate material for PVD coating, the surface condition plays a key role. DIN EN 10088-2 specifies various standardized conditions for stainless steels available in Europe [111]. Of the conditions listed in this norm, condition “2D” most closely reflects the finishing process route which is applied to U-Mo foils from US-American fabrication. This condition indicates “Cold rolled, heat treated, pickled” with a typical surface roughness R_a of 0.4 - 1.0 μm .

Titanium alloys

Titanium metal is a lightweight material which is known for its high strength and corrosion resistance and therefore is often used in aerospace and industrial processes. In its commercially pure form, also denoted as ASTM titanium grades 1 to 4, it has a comparably low hardness of typically ~ 200 HV [112] and low tensile and yield strengths as low as 240 MPa and 170 MPa, respectively [113]. Therefore, titanium is commonly alloyed with other metals such as aluminum and vanadium for applications where high strength is required. In the form of fine powders, cutting chips or other forms with a high surface-to-volume ratio, titanium and its alloys are considered pyrophoric.

Pure titanium metal undergoes an allotropic phase transition at 882 °C from the low temperature α phase with hcp structure to the high temperature β phase with a bcc structure. By alloying titanium with different additions, the transformation temperature can be altered and a two-phase regime with coexisting α and β phases can be promoted. Elements having a good solubility in the α phase such as Al, O, N and C raise the transformation temperature and are called α stabilizers. In contrast, certain elements decrease the transformation temperature and strengthen the β phase, the so-called β stabilizers like Mo and V [114].

The most commonly used titanium alloy is Ti-6Al-4V, also often referred to as or ASTM grade 5 or 3.7164. It is available in a broad range of pre-product forms and sizes at comparably low cost, yet significantly more expensive than stainless steel. As Ti-6Al-4V is the most common titanium alloy, wide experience is available for subtractive and additive manufacturing. Due to the addition of 6 wt.% aluminum and 4 wt.% vanadium, it is an $\alpha+\beta$ alloy with 5 - 40 vol.% of β phase at room temperature. The general microstructure of the alloy, the β phase fraction and its precipitation state can be defined in a wide range by thermal treatments [115]. Figure 21 gives the phase diagram of Ti-6Al alloys with V addition. It is obvious that the temperature at which the α phase transforms into β depends on the amount

of β -stabilizing V. While the stable phases α and β are typically formed by slow cooling processes, the metastable phases α' (hcp) and α'' (rhombic) can be formed by more rapid cooling. The martensitic α' phase greatly influences the physical and mechanical properties of the alloy due to its high dislocation density and therefore high hardness.

Three different general types of microstructures can be found in a titanium $\alpha+\beta$ alloy: lamellar structures, equiaxed structures and bi-modal structures, which consist of equiaxed α in a lamellar $\alpha+\beta$ matrix. More details on these microstructures as well as the effects on mechanical properties can be found in [115–117].

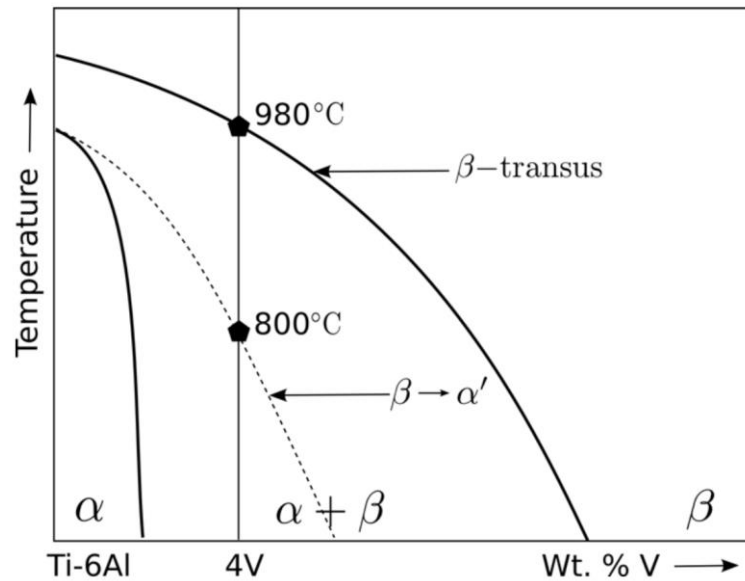


Figure 21: Pseudo-binary phase diagram of Ti-6Al alloys with V addition. Depending on the V content, the β transformation temperature changes. Depending on the thermal treatment applied, the alloy can form the stable phases α and β as well as the metastable phases α' and α'' . From [118].

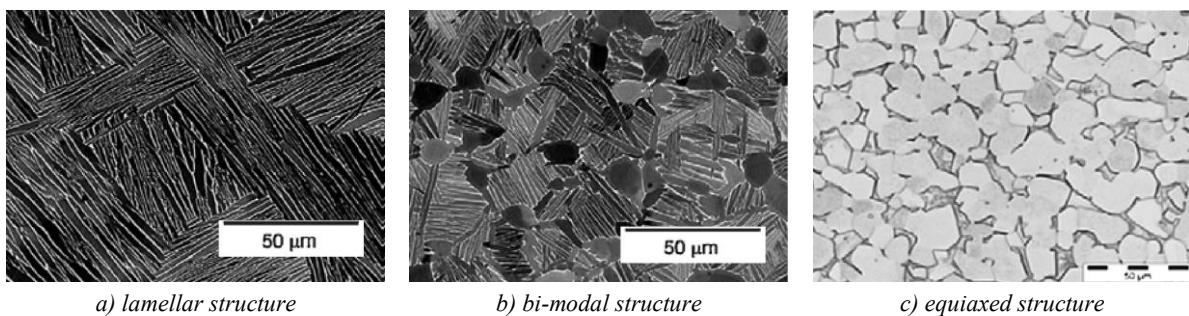


Figure 22: General microstructures of titanium $\alpha+\beta$ alloys. Depending on the processing route, $\alpha+\beta$ alloys can have lamellar (a), bi-modal (b) or equiaxed (c) structures. From [115].

2.2 FABRICATION OF FLAT U-MO FOILS

Since the late 1990s, a fabrication process for flat U-Mo foils is developed as part of the US-American fuel fabrication program. Early research and development of this process took place at various National Laboratories such as *INL* (Idaho National Laboratory), *PNNL* (Pacific Northwest National Laboratory) and *LANL* (Los Alamos National Laboratory). Currently, the so developed *baseline fabrication process* is being industrialized at the US-American fuel fabricator BWXT. Extensive information about these developments and the baseline process can be found in [16–19,21,23,24,26–28]

Since 2019, Framatome-CERCA and TUM are developing a similar European fabrication process for U-Mo foils, which is based on the published experience from the US-American program. Similar to the US-American developments, this fabrication process currently only aims for flat (non-gradient) U-Mo foils [15].

It must be noted that since 2016, the US-American program focuses on U-Mo foils which are pre-coated with Zr using the so-called *co-rolling* technique, described also below. In contrast, the European fuel fabrication program focuses on uncoated, so-called *bare* U-Mo foils, which are coated later with Zr using PVD. As the European fabrication process for bare U-Mo foils is not readily established by the time of this thesis, all experiments requiring U-Mo foils will be performed with bare foils from the US-American fuel fabrication program, kindly supplied to TUM by the US Department of Energy.

Alloying

The first step in the fabrication process for U-Mo foils is to achieve the desired alloy composition, U-10wt.%Mo. Therefore, appropriate amounts of uranium and molybdenum feedstock are alloyed together, typically in vacuum or inert atmosphere at temperatures above 1300 °C using an arc melting device. Hereby, high amounts of energy are introduced into the material by igniting an electrical arc between an electrode and the material to be molten. After the material is cooled down in the melting crucible, several re-melting steps may be performed to improve the homogeneity of the U-Mo alloy.

To achieve a final product – U-Mo foils – with high chemical purity and good mechanical properties, feedstock material with little impurities such as oxygen and carbon must be used, and the material shall be chemically cleaned before alloying to remove surface contamination and oxidation.

Casting

Once the desired alloy composition is achieved in the previous step, the material is cast into one or more rectangular molds. This is typically performed using a vacuum induction melting casting furnace, where the energy is introduced into the material via inductive coupling. After holding the material at a typical temperature of 1300 °C for a short time, the molten metal is released into the mold where it fully cools down and forms the so-called *ingot*.

Again, particular care needs to be taken to ensure a high chemical purity of the final U-Mo foils. For example, mold coatings like graphite, Y₂O₃ (yttria) or Er₂O₃ (erbia), which prevent the material from sticking to the mold, can contaminate the ingot surface and therefore should be removed prior to further processing.

Homogenization

As a next step, the *as-cast* ingot is cleaned to remove surface contamination and cut to the size required for the subsequent rolling steps. The top of the as-cast ingot is usually discarded since unwanted impurities tend to accumulate at the upper side of the castings. The separation of Mo-rich and Mo-lean

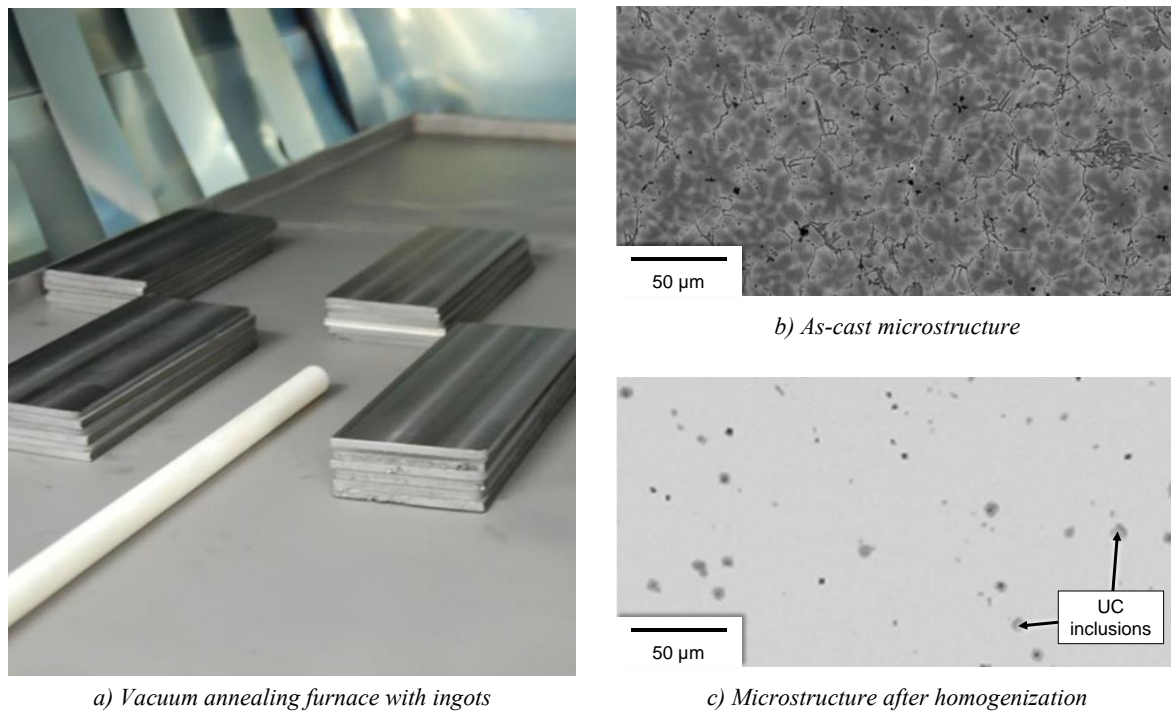


Figure 23: Homogenization of U-Mo ingots. The homogenization step inside a vacuum annealing furnace (a) improves the Mo homogeneity and changes the microstructure from the dendritic as-cast (b) to a homogeneous microstructure (c). Still, some uranium carbide (UC) inclusions can be found in the homogenized ingots. After [3,28]

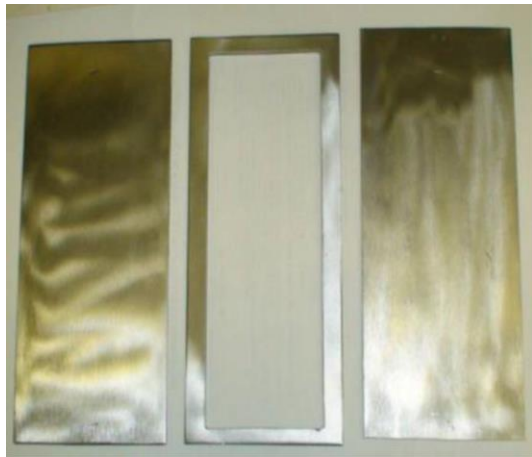
phases, which typically occurs during the ingot cooling, is reduced via a homogenization step prior to the rolling of the ingots. Hereby, the ingots are kept at 890 °C for 144 hours in a vacuum annealing furnace, followed by a quenching step in argon atmosphere. This step ensures a rapid passage of the ingot through the temperature range of fast γ phase decomposition. Argon is used as quenching gas to prevent oxidation of the hot ingots. Figure 23 shows the vacuum annealing furnace as well as electron micrographs showing the as-cast and homogenized microstructure.

Rolling

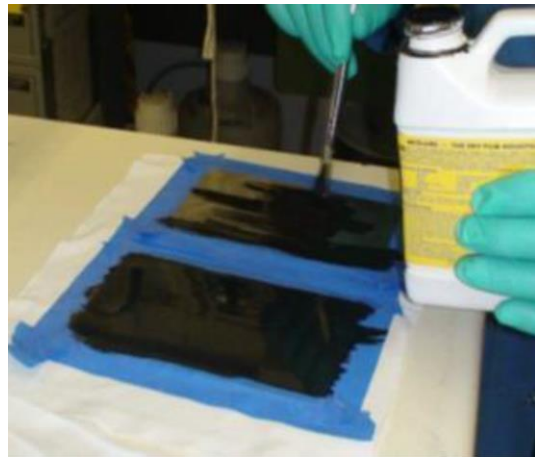
After homogenization, the U-Mo ingots with a typical thickness of 3.5 - 6.35 mm need to be rolled into U-Mo foils, with a thickness tailored to the research reactor they are intended to serve for as fuel core. Typically, the fuel core thickness ranges between 200 μm and 650 μm. The rolling process is divided into two separate steps: hot-rolling at approximately 650 °C, followed by cold-rolling at room temperature.

To avoid oxidation of the U-Mo during hot-rolling, the ingots are encapsulated air-tight into low carbon steel containers – so called *cans* – inside gloveboxes with controlled atmosphere before rolling, as shown in Figure 24. These cans consist of three parts: top plate, picture frame and bottom plate. The top and bottom plates of these cans are coated with a parting agent to facilitate the later removal of the can. After the cleaned ingot is inserted into the picture frame of the can, it is sealed by *TIG* (Tungsten Inert Gas) welding.

If the fabrication of a U-Mo foil pre-coated with Zr by co-rolling is desired, a 250 μm thin polished Zr sheet is spot-welded to the top and bottom plate of the can before the U-Mo ingot is placed in between. During the rolling steps, the thickness of the Zr sheet is reduced to the target thickness of the interdiffusion barrier, typically 25 μm, and a metallic bonding between U-Mo and Zr is established.



a) can components



b) parting agent application



c) can with U-Mo ingot



d) sealed can

Figure 24: Canning process. After fabrication of the can components (a), a parting agent is applied to the top and bottom plate of the can (b) and the U-Mo ingot is inserted into the picture frame (c). The can is finally sealed air-tight using TIG welding (d). From [3,28].

Before hot-rolling of the canned U-Mo ingots, they are pre-heated to 650 °C in a box furnace with air atmosphere, depicted in Figure 25 a, while the rolls of the two-high hot-rolling mill are pre-heated to 80 °C. Once the temperature is reached, the canned ingots are manually inserted into the rolling mill, depicted in Figure 25 b, for typically seven passes with a thickness reduction of ~ 5 - 20 % per pass. In between passes, the ingots are usually re-heated to 650 °C in the pre-heating furnace to compensate the cooling of the ingot during handling and rolling. After hot-rolling, the thickness of the U-Mo foil inside the can is usually ~ 150 % of the final foil thickness.

The main purposes of the canned hot-rolling step are (i) to achieve a large thickness reduction at an elevated temperature and thus reduced tensile strength, and (ii) to achieve a strong metallic bonding between the U-Mo ingot and the Zr sheet, if desired. However, to achieve a good thickness uniformity and surface quality of the foil, a subsequent uncanned cold-rolling step is necessary. Thus, the U-Mo foil is removed from the can and chemically cleaned prior to being cold-rolled in a four-high cold-rolling mill. After typically 10 to 20 passes, the U-Mo foil has reached its target thickness and is called *master foil*.

To avoid surface contamination of the U-Mo foils during the rolling steps, special attention needs to be paid so that the intermittent cleaning processes remove all residues of parting agent and roll lubrication agents from the foils. Further, the temperature of the U-Mo ingots and foils needs to be continuously monitored to minimize the γ phase decomposition.



Figure 25: Hot-Rolling process. The canned U-Mo ingots are pre-heated to 650 °C in a box furnace (a) before they are manually inserted into the hot-rolling mill (b). From [3,28].

Flattening

After cold-rolling, the U-Mo master foils typically exhibit a high waviness due to the cold work built up within the foils. Thus, a thermal flattening step is performed afterwards. Here, up to four master foils are stacked on top of each other and loaded with copper weights inside a vacuum annealing furnace. This stack is kept at 650 °C for 60 minutes inside the furnace, before the furnace is filled with argon to rapidly cool down the foils. At the given temperature and time, no microstructural change of the U-Mo foils is expected.

Sizing

After flattening, the U-Mo master foils are cut to the size required for the subsequent fabrication step, i.e. PVD coating for bare U-Mo foils or cladding application for co-rolled U-Mo foils. As a first step, the cutting to width is performed using a so-called *slitter*, a device with two parallel cylindrical rolls with matching ribs and grooves, which cuts the master foil in one or more highly parallel stripes. As a second step, the stripes are cut to length using either a manually operated benchtop shear or a hydraulic squaring shear.

2.3 INTERDIFFUSION BARRIER APPLICATION

Before bare U-Mo foils can be incorporated into fuel plates, an interdiffusion barrier needs to be applied to the foils – the so-called *substrates*, either in flat or gradient geometry – to prevent the formation of an unwanted interdiffusion layer at the important U-Mo/Al interface during irradiation.

2.3.1 SUBSTRATE SURFACE CONDITION

For the successful application of such an interdiffusion barrier, an appropriate surface condition of the substrate is crucial. Typically, the surface of untreated metallic parts is covered with multiple layers of surface contaminants, chemical reaction products and mechanical deformations, as illustrated in Figure 26. The characteristics and potential removal methods of these layers are:

Deformation layers. The deformation layers can be found directly above the undisturbed bulk structure and are of the same material. Here, a strongly deformed microstructure, either with plastic, elastic, or a combination of both deformations, can be found, which originates from mechanical fabrication processes of the substrate. Typically, these layers altogether are more than 5 μm thick. As those layers consist of unaltered substrate material, the adhesive strength of coatings is comparable to bulk material. However, the irregular microstructure can significantly impact the microstructure of the coating. Thus, it can be favorable to remove this layer to expose the undisturbed bulk material to the coating process. To remove these layers, the deformed material needs to be removed, typically by very gentle mechanical processes. It must be considered that these mechanical processes by themselves can introduce additional deformation into the substrate, thus creating new deformation layers.

Chemical reaction layer. This layer consists of products of chemical reactions between the substrate material and atmospheric constituents, e.g. water vapor, nitrogen or – most prominently for metals – oxygen. Such reaction layers can be self-passivating, meaning that they by themselves can inhibit further reactions once a certain layer thickness, typically 1 - 10 nm, is reached. Otherwise, the reaction layer can reach thicknesses of several μm , often leading to porous and weakly bonded layers. While some chemical reaction layers can be beneficial for a coating process, e.g. as some nm thin transition layer between the substrate and the coating, it is generally favorable to remove all chemical reaction layers and, if needed, create the desired chemical reaction layer in a controlled way. As it is usually not possible to revert the chemical reaction which created this layer, all reacted material needs to be removed from the surface to expose the underlying substrate material to the coating process.

Adsorption layer. The adsorption layer consists of atmospheric constituents which have accumulated at the substrate surface either by chemical or physical bond. These adsorbates, in reaction with the substrate, contribute to the chemical reaction layer. While chemically bonded adsorbates can only form layers of a single atomic layer, physically bonded adsorbates can accumulate to layer thicknesses of 10 nm and more. As adsorption is a reversible process – the reverse process being called desorption – all chemically or physically bonded adsorbates can selectively be removed from the substrate surface by an energy input sufficient to overcome the corresponding bond energy. This is usually necessary for coating processes, as adsorption layers can significantly diminish the adherence of the coatings.

Contamination layer. The outmost surface layer consists of various contaminants, which can originate either from fabrication, transport, handling or storage of the substrate. Such contaminants are typically organic substances, like lubricants, skin grease, volatile components of packaging materials or dust. The contamination layer often is the reason for improper adherence of coatings and thus must be removed in any case. Chemical cleaning agents to remove common contaminants are industrially available.

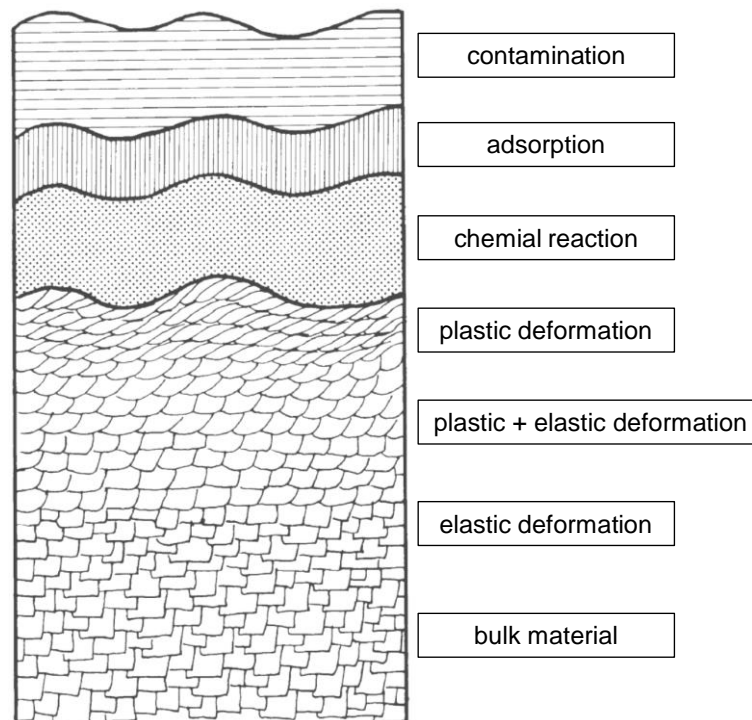


Figure 26: Typical surface structure of untreated metallic parts. The undisturbed bulk material is covered with multiple deformation layers, covered by chemical reaction, adsorption and contamination layers. After [119].

Cleaning and recontamination

It can be concluded that for proper adherence of the interdiffusion barrier, the substrate needs to be free of any contamination, adsorption, reaction, and potentially, deformation layers. The cleaning methods can be categorized as follows:

- Mechanical cleaning by machining, grinding or polishing. These methods allow a material removal on a large scale and thus can remove all surface layers up to the bulk material. However, these processes must be carried out very gently to avoid the introduction of new deformation layers.
- Chemical cleaning by dissolving the adsorption or reaction layers or parts of the substrate material using a suitable chemical reactant.
- Physical cleaning by evaporation, sublimation or bombardment with high-energy particles. Plasma cleaning, a special type of physical cleaning related to PVD, will be discussed in section 2.3.6.

It is inevitable that any workpiece cleaned by one or more of the abovementioned processes is exposed again to a more or less reactive atmosphere after the cleaning process. The reactive species of the atmosphere – mainly O_2 and N_2 – as well as water vapor can quickly form new adsorption and reaction layers. As [14] has demonstrated by calculation, each freshly-cleaned surface exposed to air atmosphere will be fully covered with adsorbates within seconds, even at a reduced gas pressure of 10^{-3} mbar. The only possibilities to extend the time until a full surface coverage is reached are therefore (i) a further reduction of the atmospheric pressure or (ii) the use of a protective gas atmosphere like argon. It was calculated that it takes approximately 5000 seconds until a surface coverage of 90 % is reached in an argon 4.8 atmosphere at $5 \cdot 10^{-3}$ mbar.

2.3.2 PROCESSES

Since the necessity to apply an interdiffusion barrier between the U-Mo foils and the Al cladding was identified in irradiation tests [37–39], processes to accomplish this goal were developed and tested worldwide. The main requirements for such processes are:

- Full coating coverage of the entire U-Mo foil surface on both sides
- Defect-free coating adherence on the entire U-Mo foil surface on both sides
- Achievement of the minimum required coating thickness at every location on the U-Mo foil
- Avoidance of unwanted temperature ranges

Hereby, the minimum required coating thickness depends on the selected interdiffusion barrier material. For the commonly used Zr, a thickness of 25 μm on both sides of the U-Mo foil is proposed for co-rolling in the US-American baseline fabrication process [27,28]. While this thickness originates purely from technical limitations of this process, recent studies [42,120] indicate that a lower Zr thickness in the range of 5 - 8 μm is sufficient to prevent the U-Mo/Al interdiffusion at the fuel-cladding interface.

After the process, the U-Mo foils must still exist in their metastable γ phase. Therefore, the temperature range $\sim 400 - \sim 575$ $^{\circ}\text{C}$, where fast γ phase decomposition occurs, shall be avoided. Further, the formation of interaction layers between U-Mo and Zr shall be prevented, thus temperatures > 650 $^{\circ}\text{C}$ shall be avoided as well.

Co-rolling

The co-rolling process has the advantage of being an integrated process to fabricate U-Mo foils, pre-coated with Zr. However, the following disadvantages have materialized during the development phase, which can limit the applicability and flexibility of the process:

- Possibilities for an independent thickness control of the U-Mo foil and the Zr coating are limited
- The thickness of the Zr coating is highly non-uniform, resulting in a higher average coating thickness necessary to meet the minimum coating thickness requirement at every location on the U-Mo foil
- Co-rolling is not able to apply Zr coatings thinner than 15 μm on average
- Due to the tendency of U-Mo and Zr to form interaction layers at elevated temperatures, thermal treatment possibilities of co-rolled U-Mo foils are limited
- Due to the additional Zr coating, the recycling of rejected co-rolled U-Mo foils is more complex than of bare U-Mo foils
- Co-rolling is not able to apply other promising candidates for interdiffusion barriers, like e.g. tungsten, due to their high hardness and low ductility
- Co-rolling is not able to fabricate U-Mo foils with a thickness gradient

Figure 27 shows an electron micrograph of a U-Mo foil co-rolled with Zr. At higher magnification, a thin continuous interaction layer between the U-Mo foil and the Zr coating can be seen.

Physical vapor deposition (sputtering)

Due to these disadvantages, TUM in cooperation with the French fuel fabricator Framatome-CERCA has developed a European alternative process for the application of interdiffusion barriers: *PVD* (physical vapor deposition), also often referred to as *sputtering*. Since decades, sputtering is a widely used technique to coat work pieces, ranging from small laboratory-scale applications to an industrial scale – e.g. for the fabrication of OLED screens or solar cells.

The main advantages of sputtering, compared to co-rolling, are:

- Coatings of almost any material can be applied to almost any workpiece material
- The coating of work pieces with complex geometries, e.g. a thickness gradient, is possible
- A precise control of the coating thickness is possible, ranging from few nanometers to dozens of micrometers
- The microstructure and adherence of the coating can be adjusted by changing the process parameters
- The temperature of the work piece can be controlled to avoid unwanted interdiffusion with the coating material

Figure 28 shows an electron micrograph of a U-Mo foil PVD-coated with Zr. At higher magnification, no interaction layer between the U-Mo foil and the Zr coating can be seen.

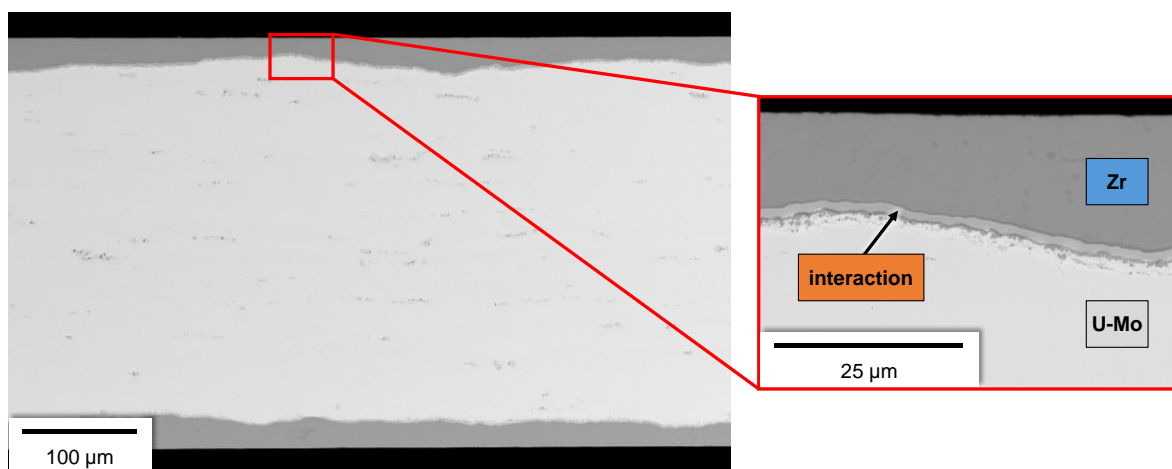


Figure 27: Electron micrograph of a U-Mo foil co-rolled with Zr. While perfect surface coverage and defect-free bonding can be achieved with co-rolling, the coating thickness across the foil surface is highly non-uniform. At higher magnification, a thin continuous interaction layer between the U-Mo foil and the Zr coating can be seen.

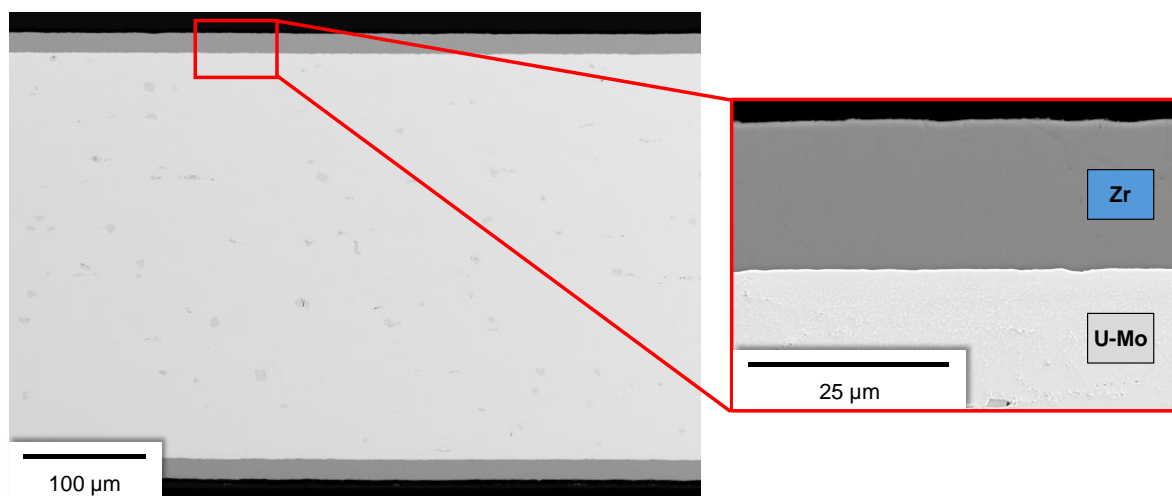


Figure 28: Electron micrograph of a U-Mo foil PVD-coated with Zr. PVD coating allows perfect surface coverage and defect-free bonding together with a very uniform coating thickness across the foil. At higher magnification, no interaction layer between the U-Mo foil and the Zr coating can be seen.

The use of sputtering as a technique for the application of interdiffusion barriers onto monolithic U-Mo foils is challenged by the higher complexity of the process compared to co-rolling, and the experimental work required to identify process parameters which result in coatings with acceptable properties.

The following sections will briefly explain the theoretical background and technical realization of the sputter erosion and deposition process, together with the relevant principles of low-pressure plasmas. For an extensive theoretical description of the sputtering and layer growth processes, tailored to the needs of interdiffusion barrier application for U-Mo foils, reference is made to [14].

Hereby, *sputter erosion* describes the erosion of a material – the so-called *target* made e.g. of zirconium – by its bombardment with energetic particles such as ions. When these particles hit the target surface, target atoms are excited by energy and momentum transfer and can leave the target surface with high velocity. Such free target atoms – an atomic vapor – can condense at the surface of the substrate and form a thin layer of target material. This process is called *sputter deposition*. Figure 29 illustrates the basic principle of this process.

A typical sputtering setup consists of a target, a substrate, and an ion source inside a process chamber with a medium-vacuum partial pressure of a noble gas like argon. In the simplest form of such a setup – *DC* (direct current) sputtering – an electrical field is generated by applying a negative electrical voltage to the target. This electrical field accelerates free electrons, which can ionize gas atoms from the atmosphere and thus ignite a *plasma*, serving as the ion source.

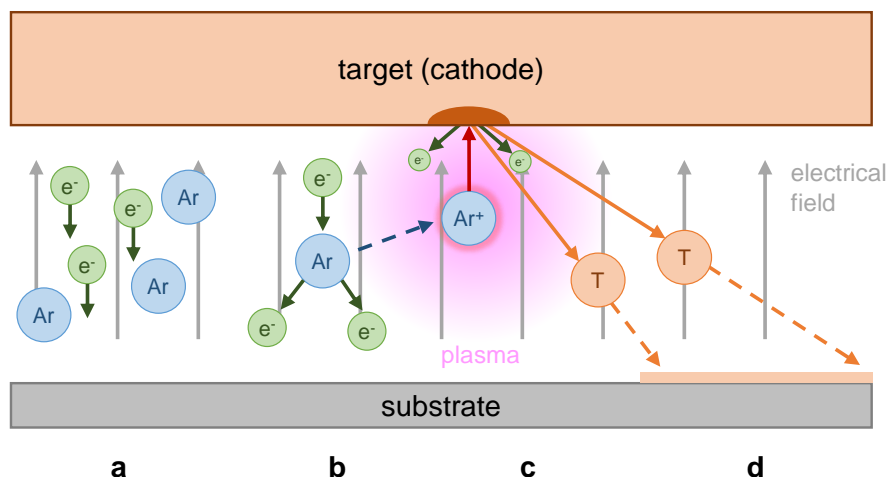


Figure 29: Basic principle of the sputtering process. Free electrons are accelerated (a) and can ionize gas atoms, igniting a plasma (b). Ionized gas atoms from the plasma are accelerated towards the target and can eject target atoms (c). The target atoms can condense at the surface of the substrate (d).

2.3.3 LOW-PRESSURE PLASMA PHYSICS

A plasma is one of the four fundamental states of matter and contains ionized and neutral gas atoms as well as free electrons. In a typical gas under normal atmospheric conditions, the degree of ionization – the density ratio n_i/n_g of ionized gas atoms to all gas atoms – is below 0.1 %, e.g. due to thermal ionization. In contrast, a plasma can reach ionization degrees of $\gg 1$ %, so that it exhibits electromagnetic properties. To ignite and sustain a plasma, a continuous energy supply is required to ionize additional gas atoms and to compensate the energy loss due to ion-electron recombination or radiation. This can either be done by heating the gas, by applying electromagnetic fields, or by an electrostatic field between two electrodes, the so-called *abnormal glow discharge*. In this case, the

energy is supplied by an electrical power supply unit attached to the electrodes. This kind of plasma is called *low-pressure plasma* and is typically generated in atmospheres with a partial pressure in the order of 10^{-2} - 10^{-3} mbar of a noble gas like argon.

Ionization

The ionization of the gas atoms in such a low-pressure plasma dominantly occurs via collisions of accelerated free electrons with neutral gas atoms:



The acceleration of free electrons ($q = -e$) is realized by the electrostatic force F_{el} caused by the electrical field E from the negatively charged target:

$$F_{el} = q E \quad (16)$$

The kinetic energy gain $E_{kin,e}$ of the electrons due to this acceleration is proportional to the potential difference U passed:

$$E_{kin,e} = q U \quad (17)$$

On their way through the plasma, some electrons will collide with argon atoms in the atmosphere. The probability for an argon atom to be ionized at such a collision is proportional to the ionization cross-section σ_i , which can be estimated for single-ionization of argon according to [121]:

$$\sigma_i = 970 \left(\frac{E_{kin,e} - 15.8}{(70 + E_{kin,e})^2} \right) + 0.06 (E_{kin,e} - 15.8)^2 e^{-\frac{E_{kin,e}}{9}} \quad (18)$$

Figure 30 shows the energy-dependence of this cross-section. The maximum value, and therefore the highest probability for ionization is located at an electron energy $E_{kin,e}$ of ~ 100 eV.

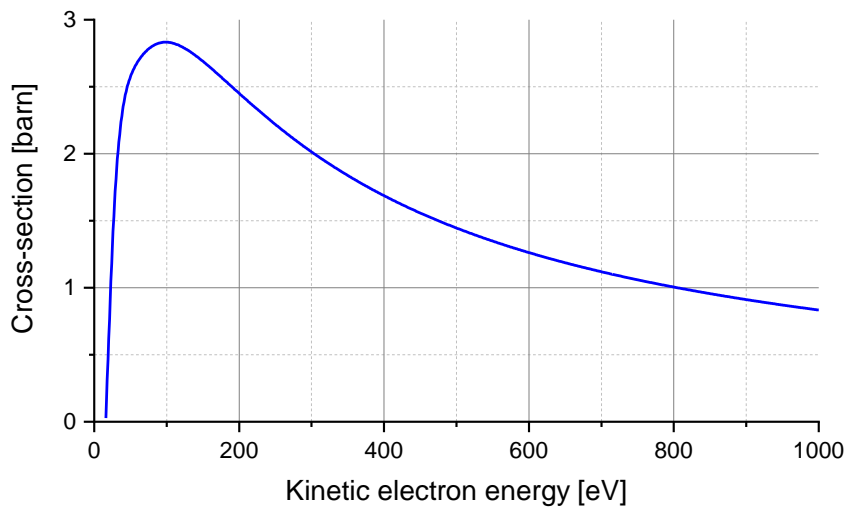


Figure 30: Single-ionization cross-section for collisions of argon atoms with electrons. The highest probability for ionization is located at a kinetic electron energy of ~ 100 eV.

Plasma discharge

Electrons generated by the ionization of gas atoms – so-called *primary electrons* – and electrons released from the bombarded target – so-called *secondary electrons* – are accelerated away from the negatively charged target. Once they have gained sufficient kinetic energy, they can cause further ionizations of the neutral gas atoms. These ions are again accelerated towards the target. This ionization cascade process leads to the ignition of a plasma in a continuous equilibrium state. The ignition point, or *gas break-down point*, is defined by the necessary gas pressure and the electrical potential between the cathodes. The visible light or *glow* is caused by recombination processes of electrons and ions as well as by the de-excitation of gas atoms. If the distance between the cathode and the anode becomes too short, i.e. in the order of magnitude of the mean free path of argon gas atoms λ_{Ar} from equation (19) [122], not enough collisions between electrons and gas atoms can happen and therefore, no plasma can be ignited.

$$\lambda_{Ar} = \frac{6.4 \cdot 10^{-2}}{p_{Ar}} \text{ mm mbar} \quad (19)$$

This effect is commonly used to suppress the ignition of a plasma in unwanted locations in a sputtering device. Hereby, grounded conductive shields – so-called *dark space shields* – are installed close to the parts with cathode potential.

Due to the large mass difference $m_e \ll m_i$ between electrons the ions, the lighter electrons have a much higher mobility in the plasma than the ions. Therefore, the thermal energy of both species is strongly different as well [123]:

$$500 \text{ K} \cong T_i \ll T_e \cong 23200 \text{ K} - 58000 \text{ K} \quad (20)$$

$$50 \text{ meV} \cong k_B T_i \ll k_B T_e \cong 2 \text{ eV} - 5 \text{ eV} \quad (21)$$

As shown simplified in Figure 31, the ignited plasma between the *cathode* (represented by the target) and the *anode* (typically represented by the grounded vacuum chamber walls) contains different electrical potential regimes. Hereby the *plasma potential* V_{pl} depends on the actual realization of the sputtering device, mainly the ratio A_a/A_c of the anode and cathode surface areas. For typical devices, the vacuum chamber walls are significantly larger than the cathode surface area so that $A_a/A_c \gg 1$. Therefore, more highly mobile electrons than ions hit the anode and are thus extracted from the plasma. The resulting excess of positive ions in the plasma leads to a slight positive shift of the plasma potential compared to the *ground potential* V_{gr} , so that usually $V_{pl} > V_{gr}$. In proximity to the cathode and the anode, no plasma is present and the electrical potential drops from the plasma potential V_{pl} to the *cathode potential* V_c and to the *anode potential* $V_a = V_{gr}$, respectively.

In these regimes with strong potential gradients – the so-called *dark spaces* – the acceleration of charged particles occurs in the course of typically a few mm. In the *cathode dark space*, the acceleration voltage U_{CDS} equals the difference between the plasma potential V_{pl} and the cathode potential V_c :

$$U_{CDS} = V_c - V_{pl} \quad (22)$$

The cathode potential V_c results from the voltage U_t applied to the sputtering target via the sputtering power supply unit:

$$U_t = V_{gr} - V_c \quad (23)$$

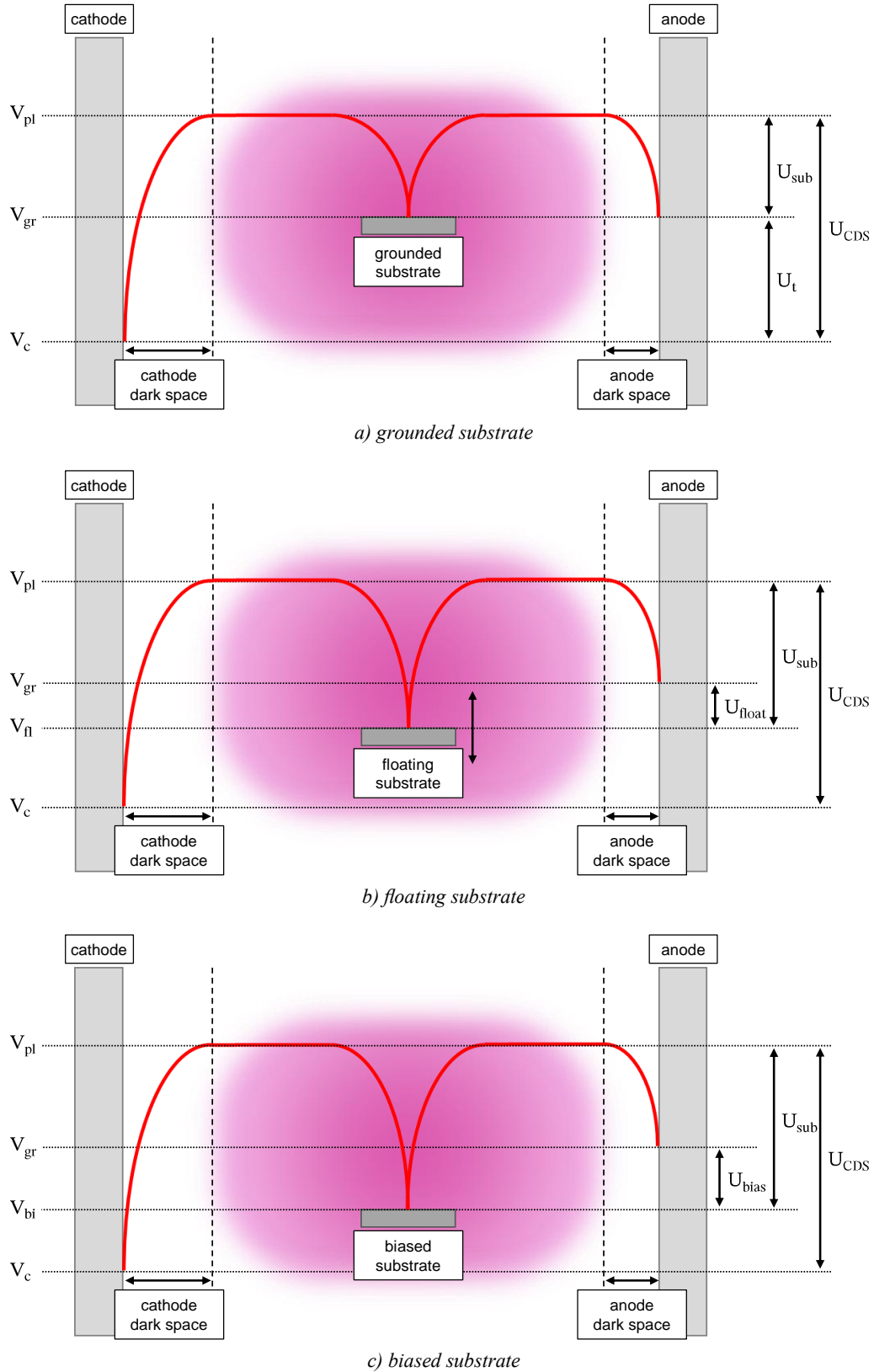


Figure 31: Electrical potential curve for different substrate conditions. In the cathode and anode dark spaces, charged particles are accelerated due to the strong potential gradients but no plasma is present. The substrate can be either on ground potential V_{gr} (a), a varying floating potential V_{fl} (b) or on a specific biasing potential V_{bi} (c). A dark space also develops around the substrate, but is omitted here for simplification. After [124].

To allow the sputter erosion of the target material, the ions from the plasma need to gain enough kinetic energy during their acceleration through the cathode dark space. Assuming no collisions between these ions and neutral gas atoms, the kinetic energy $E_{kin,i}$ of the ions impinging the target is proportional to the cathode dark space voltage U_{CDS} :

$$E_{kin,i} = q_i U_{CDS} \quad (24)$$

As Figure 31 further shows, the substrate can be left or intentionally put on different electrical potentials: the ground potential V_{gr} , the *floating potential* V_{fl} or a specific *biasing potential* V_{bi} . For the latter case, which is often used to modify the properties of the coating, a usually negative *substrate biasing voltage* U_{bias} is applied by a dedicated substrate power supply unit:

$$U_{bias} = V_{bi} - V_{gr} \quad (25)$$

In any case, the potential difference U_{sub} between the plasma potential and the substrate potential determines the amount and the energy of the ions and electrons accelerated towards the substrate [125]:

$$U_{sub} = V_{pl} - V_{gr} \quad \text{for grounded substrates} \quad (26)$$

$$\begin{aligned} U_{sub} &= V_{pl} - V_{fl} \quad \text{for floating substrates} \\ &= (6.7 + \ln m_g) \frac{k_B T_e}{2} \end{aligned} \quad (27)$$

$$U_{sub} = V_{pl} - V_{bi} \quad \text{for biased substrates} \quad (28)$$

As can be seen from equation (27), the floating potential V_{fl} is a characteristic value of the plasma which depends on the atom mass m_g of the work gas and the electron temperature T_e in the plasma.

Figure 32 exemplarily shows a measurement of the substrate current at various substrate potentials [126]. As can be seen, the plasma potential V_{pl} can be deduced by the intersection of the rising flank around 0 V and the electron saturation current. Typical values of the plasma potential in DC sputtering devices are 0 - 20 V [14,127,128]. The measurable substrate current I_{sub} is always the sum of the electron current $I_{sub,e}$ and the ion current $I_{sub,i}$ through the substrate:

$$I_{sub} = I_{sub,e} + I_{sub,i} \quad (29)$$

For $I_{sub} = 0$, both currents are equally great ($I_{sub,e} = -I_{sub,i}$) and the substrate potential equals the floating potential V_{fl} without a connected external substrate power supply unit. In the *mixed bombardment region*, electrons and ions can reach the substrate in varying ratios. If the substrate potential is greater than the plasma potential V_{pl} , all positive ions from the plasma are reflected into the substrate dark space and only electrons can still reach the substrate. This is the case in the *pure electron bombardment region*. The resulting electron saturation current $I_{sub,e}^{sat}$ is shown in equation (30) [129]. Here, n_e is the electron density in the undisturbed plasma close to the substrate and A_{sub} is the surface area of the substrate.

$$I_{sub,e}^{sat} = \frac{1}{4} n_e e \sqrt{\frac{8}{\pi} \frac{k_B T_e}{m_e}} A_{sub} \quad (30)$$

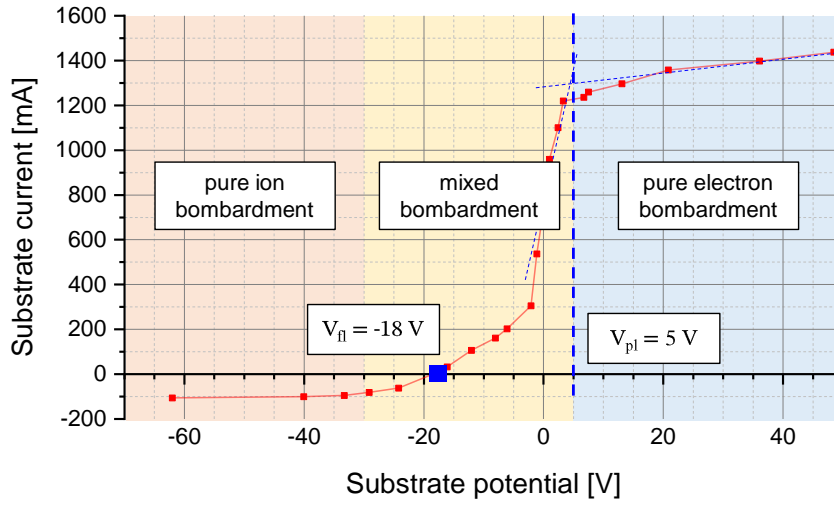


Figure 32: Exemplary measurement of the substrate current at various substrate potentials. By historic definition, the total substrate current – the sum of ion and electron currents – is positive for pure electron currents. Above the plasma potential, only electrons can reach the substrate. Below a certain threshold potential, only ions can reach the substrate. After [126].

If the substrate potential is lower than a certain threshold value $V_{th} = V_{pl} - 2 |V_{fl}|$ [130], no more electrons can reach the substrate, as is the case in the *pure ion bombardment region*. Then, the resulting substrate current equals the ion saturation current $I_{sub,i}^{sat}$ shown in equation (31) [129]. Here, n_i is the ion density in the undisturbed plasma close to the substrate.

$$I_{sub,i}^{sat} = -0.61 n_i e \sqrt{\frac{k_B T_e}{m_i}} A_{sub} \quad (31)$$

Due to the large mass difference of several orders of magnitude of both species, the electron saturation current usually is significantly higher than the ion saturation current [129]:

$$\left| \frac{I_{sub,e}^{sat}}{I_{sub,i}^{sat}} \right| \approx 177 \text{ for argon plasmas} \quad (32)$$

2.3.4 SPUTTER EROSION PROCESS

Once an ionized gas atom with the kinetic energy $E_{kin,i}$ hits the target surface, it transfers a part E_{tr} of its energy to the target atoms according to:

$$E_{tr} = E_{kin,i} \frac{4 m_i m_t}{(m_i + m_t)^2} \cos^2(\vartheta) = E_{kin,i} \Gamma_{i,t} \cos^2(\vartheta) \quad (33)$$

Hereby, m_i and m_t are the masses of the impinging and target atoms and ϑ is the angle of impact with respect to the surface normal. For typical sputtering devices, $\vartheta = 0^\circ$ can be assumed as all electrical field lines end perpendicular to the target surface. $\Gamma_{i,t}$ is the *energy transfer factor*, which defines the maximum transferable energy.

The energy transferred to the target is distributed by a cascade of collisions between the impinging ion and the target atoms. If the energy transferred to a surface atom is higher than its *surface binding energy*

$E_{B,t}$, the atom is ejected from the target surface with a kinetic energy distribution $N(E_{kin,t})$. The maximum possible kinetic energy $E_{kin,t}^{max}$ of the ejected atoms is given as:

$$E_{kin,t}^{max} = \kappa E_{tr}^{max} - E_{B,t} \quad (34)$$

Here, κ is the *energy loss factor* due to the collision cascade in the target material and E_{tr}^{max} is the maximum transferable kinetic energy from the impinging ion to the target atoms. According to [131], the most probable kinetic energy of the ejected atoms $E_{kin,t}^p$ can be estimated as:

$$E_{kin,t}^p \cong \frac{E_{B,t}}{2} \quad (35)$$

Typical values for surface binding energies of metals can be found in [132]. For Zr, $E_{B,t}$ is ~ 6.5 eV, for Mo ~ 7 eV and for W, it is ~ 9 eV.

The rest of the transferred energy is stored in the form of heat or lattice displacements in the target. The impinging ion is either implanted into the target or reflected back into the plasma as a neutral atom.

Sputter yield

An important parameter of sputtering processes is the so-called *sputter yield* Y_S , which gives the amount of ejected (= sputtered) target atoms per impinging ion from the plasma.

$$Y_S = \frac{J_t}{J_i} \quad (36)$$

Here, J_t is the particle flux of sputtered target atoms and J_i is the particle flux of impinging ions. $J_i = I_i/q_i$ can be calculated from the electrical current I_i of impinging ions at the cathode and the total electrical cathode current $I_c = I_i + I_e$, which also includes the electrical current I_e from secondary electron emission:

$$\begin{aligned} I_c &= I_i + I_e = I_i + \gamma_{eff} I_c \\ &\Leftrightarrow \\ I_i &= \frac{I_c}{1 + \gamma_{eff}} \end{aligned} \quad (37)$$

Here, γ_{eff} is effective secondary electron yield per impinging ion. It typically ranges from 0.1 to 1.0 for metallic cathodes [133].

The sputter yield Y_S depends on the mass and energy of the impinging ions, but also on the target material properties, i.e. its melting point and the binding energy of the target atoms. At high ion energies, a sputter yield $Y_S > 1$ is generally possible. [134] calculates the sputter yield for various target materials, ion types and ion energies based on empirical data. Figure 33 shows the sputter yield for U, Nb, Mo, W, Zr and Ti, when bombarded with argon ions with 0 eV to 1000 eV energy. It must be noted that for typical sputtering devices, the energy of the impinging ions is in the range of 200 eV - 400 eV.

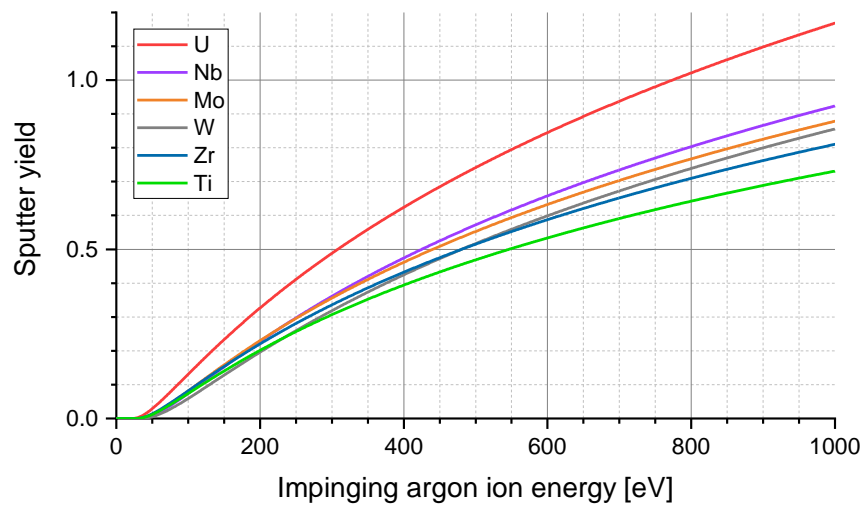


Figure 33: Sputter yield for selected elements and bombardment with argon ions. The sputter yield of zirconium is comparable to other selected refractory metals and is < 0.45 at typical ion energies of < 400 eV. Data from [134].

The sputtered atoms leave the target surface with a specific angular distribution, depending primarily on the energy of the impinging ions. For ion bombardment normal to the target surface, the sputtering rate $R_S(\varphi)$ under the ejection angle φ is estimated by a cosine distribution [135]:

$$R_S(\varphi) \propto \cos^n(\varphi) \quad (38)$$

n is a dimensionless parameter which is > 1 for high ion energies (> 1 keV) and < 1 for lower energies [132]. This is sketched for different ion energies in Figure 34.

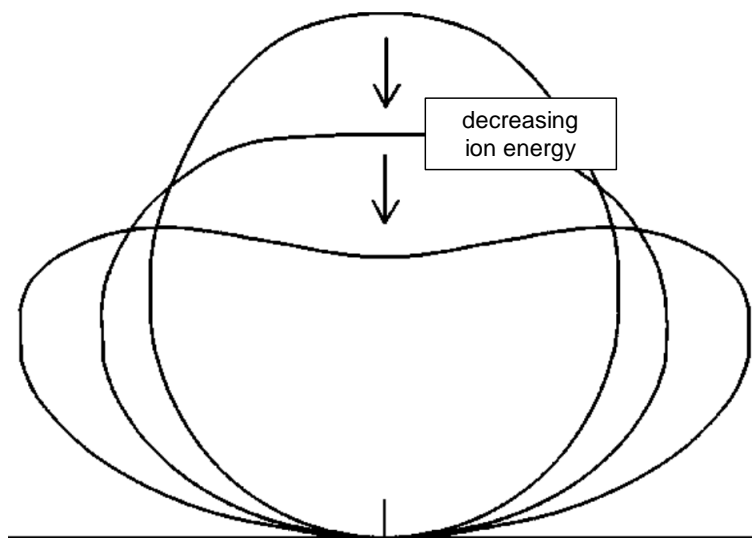


Figure 34: Sketch of the angular distribution of sputtered particles. With decreasing ion energy (shown by arrows), the distribution changes from cosine to heart-shaped. From [136].

On their way from the target to the substrate, the sputtered atoms can undergo collisions with gas atoms from the atmosphere. The probability for such collisions can be estimated via the *mean free path* λ_t of

target atoms in the gas. λ_t of an atom species with atom radius r_t and atom mass m_t , which travels through a gas with pressure p_g , atom diameter r_g and atom mass m_g can be calculated as follows [137]:

$$\lambda_t = \frac{k_B T}{p_g \pi (r_t + r_g)^2 \sqrt{1 + \frac{m_t}{m_g}}} \quad (39)$$

Figure 35 shows the resulting mean free path of selected atom species in argon atmosphere as a function of the pressure. At typical process pressures in the order of 10^{-3} mbar, the mean free path of the sputtered atoms can be as low as 1 mm, which means that collisions with work gas atoms are highly likely. Such collisions can greatly alter the angular distribution of the sputtered atoms and reduce their kinetic energy.

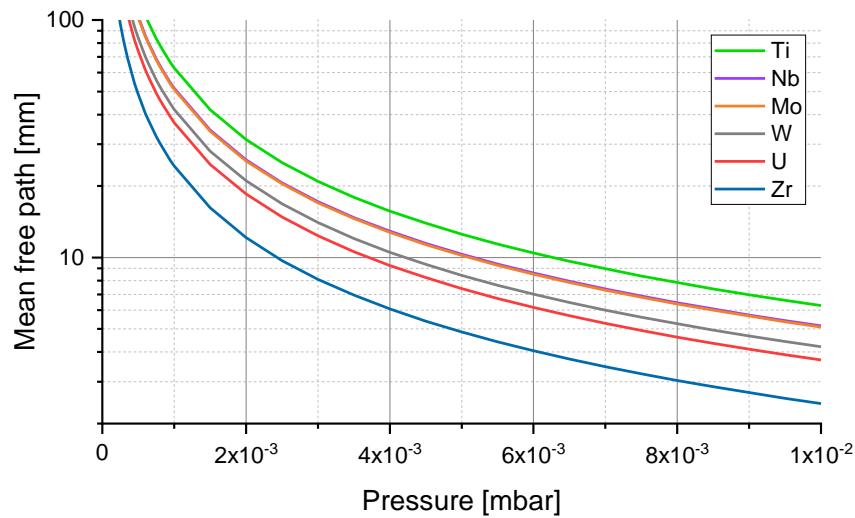


Figure 35: Mean free path of selected atom species in argon atmosphere. At typical process pressures in the order of 10^{-3} mbar, the mean free path of the sputtered atoms can be as low as 1 mm, which means that collisions with work gas atoms are highly likely.

Types of sputtering power supply units

DC. The most common type of *PSUs* (power supply units) for sputtering processes are *DC* (direct current) devices, which produce a constant voltage between their positive and negative outputs. Typically, the negative output is connected to the sputtering target, whereas the positive output is grounded directly at the unit to synchronize the reference potential to the grounded vacuum chamber. The electrical field generated between the target and the grounded vacuum chamber is the energy source for the plasma and accelerates the positive ions towards the cathode. With DC units, the electrical conductivity of the target surface needs to remain high during the target erosion process as otherwise, a static electrical charge up to several kV can build up at the target surface, leading to unwanted arc discharges. Thus, only metallic target materials can be sputtered, and it needs to be ensured that no chemical reaction of the target material with reactive species in the work gas takes place, which eventually leads to the formation of insulating layers, so-called *target poisoning*.

Pulsed-DC. To allow the application of metal oxide or nitride coatings, the metallic target is typically eroded using so-called *reactive sputtering*, where the ejected target atoms undergo a chemical reaction with a reactive species in the work gas, typically oxygen or nitrogen, on their way to the substrate. Attention needs to be paid to avoid target poisoning, where the freshly eroded target surface itself reacts

with the reactive species and forms an insulating layer, which again can lead to the buildup of a static electrical charge. To extend the possible parameter range towards higher concentrations of reactive species in the work gas, a *pulsed-DC* PSU can be used. Here, the phase with negative output voltage, which equals a standard DC unit, is interrupted with short pauses of zero or slightly positive output voltage, to allow a charge decay at the target. Typical pulse frequencies are in the range of 2 - 100 kHz.

RF. To allow also the sputtering of non-conductive targets, an *RF* (radio frequency, 13.56 MHz) PSU is needed. At such high frequencies, the heavy argon ions can no longer follow the variation of the electrical field and the plasma is generated solely from the energy of electrons oscillating in the electrical field. As the target is non-conductive, a negative DC voltage builds up at the target surface from impinging electrons. This voltage itself generates an electrical field which accelerates argon ions from the plasma towards the target and thus leads to its erosion.

Types of sputtering sources

Magnetrons. In so-called *magnetron sputtering sources*, the common type of sputtering sources nowadays, an additional magnetic field B is generated orthogonally to the electrical field. The resulting magnetic force F_{mag} on the moving charged particles in the plasma is thus:

$$F_{mag} = q(v \times B) \quad (40)$$

As this force is always perpendicular to the movement vector v of the charged particles, their kinetic energy does not change. Instead, as the force is also perpendicular to the magnetic field vector B , the particles are forced onto circular trajectories around the magnetic field lines with a specific gyration radius, the so-called *Larmor radius* r_L :

$$r_L = \frac{m |v_{\perp}|}{|q| B} \quad (41)$$

Here, v_{\perp} is the velocity of the particle perpendicular to the magnetic field. The mass of an argon atom is four orders of magnitude higher than the electron mass, so is the radius, and thus the influence of the magnetic field on the argon atoms can be neglected. However, the trajectories of the lighter electrons in the plasma are significantly extended, increasing the collision rate of electrons and argon ions, and thus increasing the ionization density in the plasma. The resulting increased flux of impinging ions J_i to the target leads to an increased sputtering rate, while the process pressure can be reduced by usually one or two orders of magnitude. As a reduction of the process pressure leads to less collisions of ejected target atoms with gas atoms, the energy of the target atoms is also higher when they reach the substrate.

With common permanent magnet or magnetic coil configurations suitable for implementation in a sputtering source, it is not possible to establish a magnetic field with a uniform magnetic field strength across the entire target surface. Therefore, the ionization density near the target surface is non-uniform as well, leading to a non-uniform erosion of the sputtering target.

Typical permanent magnet configurations for sputtering sources are shown in Figure 36. Depending on the relative remanence of the inner and outer magnets, the magnetron is called *balanced* or *unbalanced*. In a balanced magnetron with identical inner and outer magnets, the most common magnet configuration, all magnetic field lines start and end in the magnets. Therefore, most of the electrons are confined in their gyration movement near the target surface (green areas), leading to an intense plasma there and only few escaping electrons, e.g. towards the substrate. In an *unbalanced magnetron type 1*,

the central magnets are stronger than the outer ones so that some magnetic field lines are directed towards the vacuum chamber walls. This configuration, which is only rarely used, drags electrons away from the target and from the substrate, reducing the plasma intensity at both locations. In an *unbalanced magnetron type 2* in contrast, the outer magnets are stronger than the central ones or the central magnet is even replaced by just an iron yoke. Thus, a so-called *Null point* exists where the magnetic field strength B_z in the target surface normal direction is zero. Electrons beyond the Null point are not confined by a gyration movement and can thus escape the plasma towards the substrate (yellow area). This leads to an extension of the plasma towards the substrate and thus increases the substrate ion bombardment, i.e. if a negative substrate biasing voltage is applied. Usually, the chance of electrons escaping the magnetic field is higher, the closer the Null point is to the target surface [138,139].

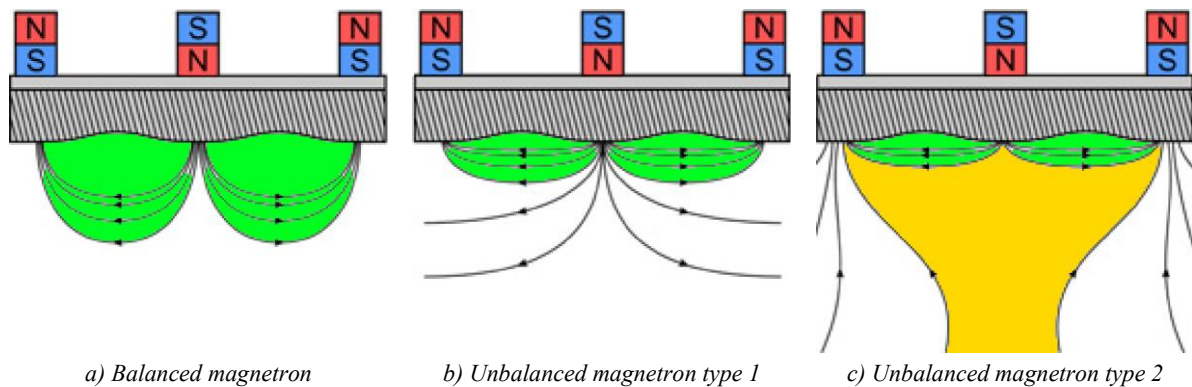


Figure 36: Magnetron configurations. While in a balanced magnetron (a), all magnetic field lines start and end in the magnets, the unclosed magnetic field lines of unbalanced magnetrons either start (c) or end (b) outside of the sputtering source. In the green areas, electrons are confined in their gyration movement around the magnetic field lines. In the yellow areas, electrons can escape the plasma towards the substrate. After [138].

Planar sources. Planar sputtering sources, as shown in Figure 37, are the most common type of sources for laboratory, research and development applications. They are available in a broad range of sizes and shapes and are easy to handle and implement into experimental sputtering devices. They consist of a circular or rectangular target plate which is attached to an array of permanent magnets, both in good thermal contact to cooling water to avoid overheating of the magnets or of the target. By adding ceramic thermal conductors between the target and the cooling block, the high voltage at the target can be electrically insulated from the cooling water if desired. The connections for cooling water and electrical power are typically located outside of the vacuum chamber, as the source is directly attached to a vacuum flange. The major disadvantage of planar sources is that the plasma is not uniform across the target surface but confined to distinct areas below the target due to the magnetic field lines. These areas, which have the highest plasma density and therefore lead to the strongest erosion of the target, are typically shaped like a torus and follow the shape of the permanent magnet array. This leads to the development of characteristic erosion trenches in the target surface, the so-called *racetrack*. This non-uniform erosion limits the maximum possible utilization of the target, as it needs to be replaced once the depth of the racetrack comes close to the target thickness. When this *end-of-life* is reached, typically less than 30 % of the total target material was eroded [138].

Cylindrical sources. To overcome the low target utilization as the major disadvantage of planar sources, cylindrical sources are nowadays most commonly used for large-scale industrial applications. Here, the target consists of a cylindrical hollow tube and the permanent magnets are installed inside the cylinder on a so-called *magnet bar*, which holds the permanent magnets in a stationary position relative to the substrate, as illustrated in Figure 38.

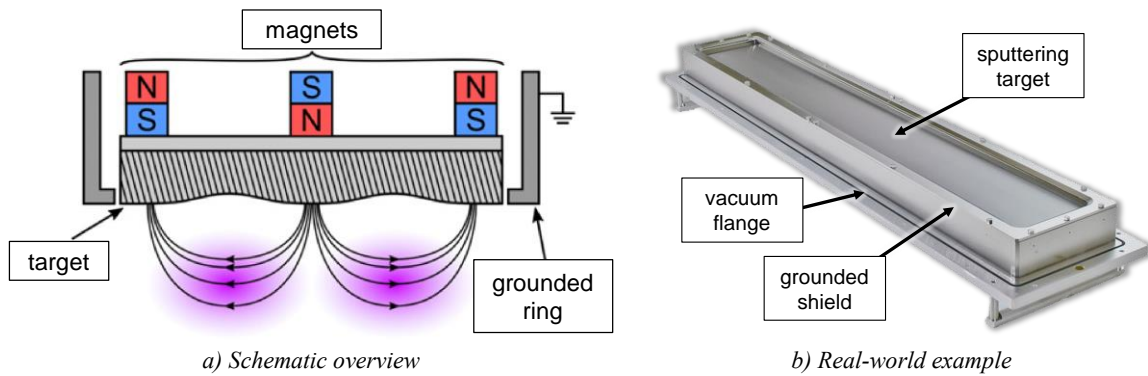


Figure 37: Scheme and example of planar sputtering sources. A flat sputtering target is sitting below fixed permanent magnets. The resulting non-uniform erosion leads to the formation of a characteristic racetrack at the target surface. An optional grounded shield can help to prevent the ignition of a plasma at the sides of the target. After [138,140].

Some sources also allow to rotate the magnet bar itself independent of the target tube to either increase the deposition area of the source or to switch between different deposition areas. Similar to planar sources, all connections e.g. for cooling water and electrical power are typically located outside of the vacuum chamber, as the source is directly attached to a vacuum flange. As the target tube continuously rotates along its length axis, it is uniformly eroded around 360° of the target surface. The heat removal is accomplished by a constant flow of cooling water through the inside of the target tube. Since at a time, only a small portion of the target surface is subject to the energy intake from impinging ions, the maximum allowed electrical sputtering power is substantially higher than for planar targets. The utilization of the target is only limited by the mechanical stability of the thinning tube against the pressure of the cooling water. Maximum utilizations of up to 90 % have been reported [138]. Switching the magnetron between balanced and unbalanced magnet configurations can be done by replacing the magnet bar. The main disadvantage of cylindrical sources is that the target tube can become very heavy and therefore difficult to handle inside vacuum chambers or gloveboxes. Furthermore, the cooling water installation requires great care, as the water is typically at the same electrical potential as the target.

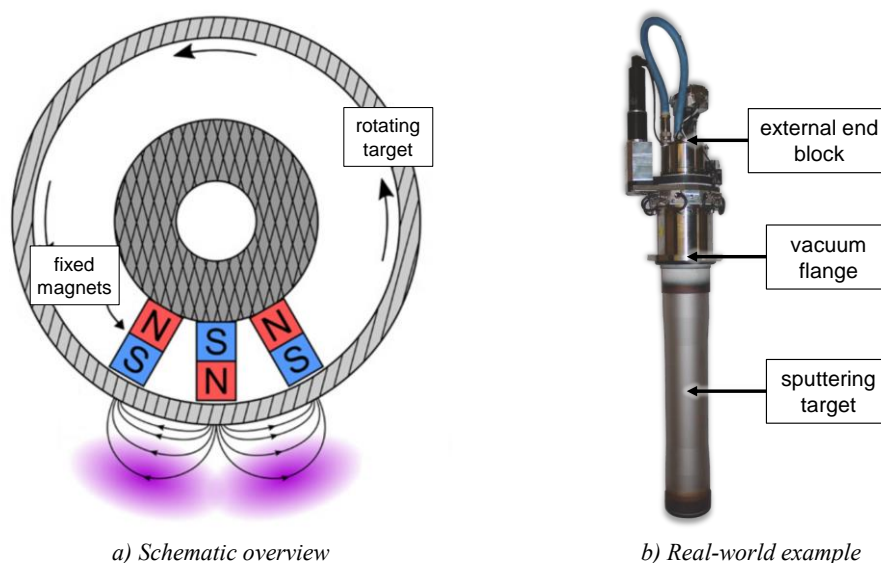


Figure 38: Scheme and example of cylindrical sputtering sources. A cylindrical target tube is rotating around a magnet bar in a stationary position relative to the substrate. The plasma is confined below the permanent magnets. Due to the permanent rotation of the target, it is continuously eroded. After [138,141].

2.3.5 SPUTTER DEPOSITION PROCESS

Sputtered atoms which reach a surface – preferably the substrate – can contribute to the formation of a *deposited layer* of target material on it via multiple steps: *condensation*, *nucleation* and finally, *grain growth*.

Condensation

The deposition of a layer starts with the condensation of atoms from the gas phase on the surface of the substrate. While a fraction of atoms is immediately reflected back into the gas phase or quickly desorbed again, the remaining atoms are initially only weakly bound to the surface via Van-der-Waals force. These so-called *adatoms* can now, under the influence of the lattice potential from the substrate atoms, diffuse across the surface in order to move to the energetically most favorable locations with the highest binding energy. This process is called *surface diffusion*. To allow adatoms to reach such favorable locations, two conditions must be met: the adatoms must have sufficient energy to cross the barriers of the lattice potential, and they must be given enough time to diffuse before additional sputtered atoms condensate on top of them. To conclude, the ability of sputtered atoms to achieve a strong bonding to the substrate is generally higher for high adatom energies and low sputtering rates.

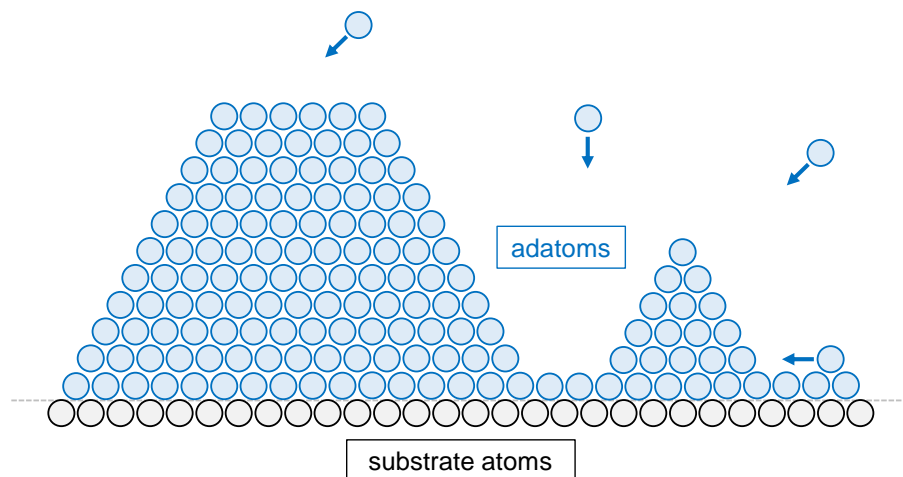


Figure 39: Condensation. Atoms from the gas phase reach the substrate and condensate on the surface as adatoms. These adatoms can diffuse across the surface under the influence of the lattice potential from the substrate atoms.

Nucleation

If condensed adatoms meet on the substrate surface, they can interact with each other and form microscopic crystalline *nuclei*. Those nuclei already exhibit the crystallographic phase and physical properties of the resulting macroscopic deposited layer. Initially, each nucleus has a distinct but random crystal orientation. As the nuclei accommodate more diffusing surface adatoms and atoms from the gas phase, their size will increase until the boundaries of neighboring nuclei meet. These nuclei – now called *grains* – can now interact with each other via their boundaries. For example, atoms can be exchanged between grains by grain boundary migration to achieve the energetically most favorable crystal orientation. The energy required for this migration is defined by the binding energy of an atom in a grain and the energy required to diffuse to the next grain.

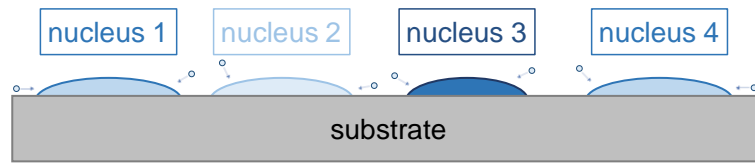


Figure 40: Nucleation. Once adatoms meet each other on the substrate, they can form crystalline nuclei with distinct but random orientation. By the ongoing accommodation of adatoms and atoms from the gas phase, the nuclei grow until their boundaries meet.

Grain growth

By the further accommodation of atoms from the gas phase, the grains continue to grow until the deposition process is stopped. The resulting grain structure of the deposited layer depends mainly on the adatom *mobility* – thus the energy available to the adatoms – and can be classified as structure type A, B, C, D and E, while the adatom mobility increases from structure A to E. The characteristic properties of each structure are explained below [142,143].

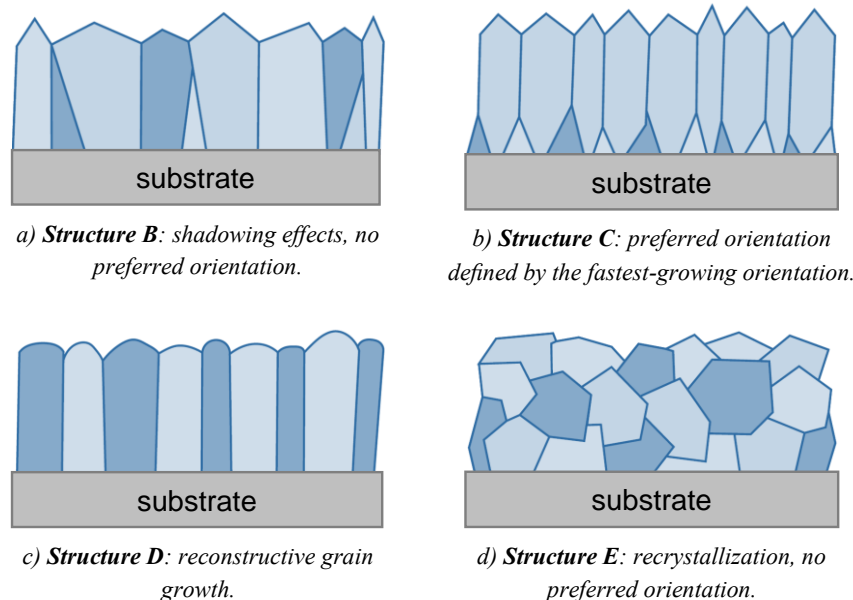


Figure 41: Grain growth structures. Depending on the adatom mobility, the deposited layer can be classified as structure A (lowest energy) to E (highest energy). The structure A, which is characterized by porous, amorphous layers, is not depicted here. After [14].

Structure A. At very low adatom mobilities, structure A is developing. Most of the adatoms are not able to diffuse across the surface of the substrate and thus stick to it typically at the point of impact. This behavior promotes shadowing effects and thus the formation of microscopic voids, leading to a porous layer with low density. The crystal structure is typically amorphous or nanocrystalline, as the nuclei can not accumulate further adatoms due to their missing mobility. Overall, the layers' mechanical properties and their suitability as interdiffusion barrier are considered poor.

Structure B. With slightly increased adatom mobilities, structure B is developing as depicted in Figure 41 a. Due to their higher mobility, adatoms can be accumulated in nuclei and can reach shadowed areas. The resulting layers are thus crystalline – still without preferred orientation – and denser than in structure A. However, as the adatom mobility is still not sufficient to pass across planes or grain boundaries, elevated and bigger grains dominate and can overgrow smaller grains closer to the substrate. The layers'

mechanical properties are typically superior to structure A, however they still exhibit a low ductility and high hardness compared to bulk material.

Structure C. By further increasing the adatom mobility, structure C is developing as depicted in Figure 41 b. The mobility now allows a diffusion of adatoms across the entire surface including planes and grain boundaries, and the resulting grain structure is defined by the growth rate of the respective crystallographic planes. Thus, the initially random grain orientation close to the substrate changes once the grains meet each other and preferentially orientated grains start to overgrow others. The density and hardness of the resulting layers come closer to the respective bulk material properties.

Structure D. At even higher adatom mobilities, structure D is developing as depicted in Figure 41 c. Here, the adatom mobility is sufficient for two-dimensional restructuring grain growth and thus, the initially random grain orientations are fully merged into a grain structure with highly preferred orientation. The grain structure is significantly coarser than in structures A to C and the width of the grains can reach the order of the layer thickness, depending on the adatom mobility. The density of the resulting layers matches the bulk material density, the hardness is significantly reduced, and the ductility is improved.

Structure E. At very high adatom mobilities, structure E is developing as depicted in Figure 41 d. In such systems, sufficient energy is not only available to the adatoms but also to the incorporated layer atoms, so that a three-dimensional restructuring grain growth is possible. Thus, a full restructuring of the entire deposited layer is possible and an entirely randomly orientated grain structure is observed. The properties of the resulting layer match the properties of annealed bulk material and thus are generally superior to all other structures.

Layer properties

It was shown that the adatom mobility is the main factor which influences the structure and properties of the deposited layer. The adatom mobility depends on the energy available to the adatoms, which is delivered mainly from the following energy sources:

Energy of the target atoms. The kinetic energy $\langle E_{kin,t} \rangle$ of sputtered target atoms which hit the substrate surface is directly available to these atoms or other adatoms. Typical values for the kinetic energy of metallic atoms leaving the target are in the range of 3 - 20 eV [14]. However, energy losses can occur by collisions of these atoms with other atoms on their way from the target to the substrate. Therefore, their energy contribution can be increased by decreasing the number of collisions, i.e. reducing the process pressure or the target-substrate distance.

Energy of the backscattered gas atoms. During the bombardment of the target with ionized gas atoms, a significant portion of these atoms is backscattered towards the substrate. The kinetic energy $\langle E_{kin,BS} \rangle$ of such a gas atom can be estimated as follows [14]:

$$\langle E_{kin,BS} \rangle = e U_c \left(\frac{m_t - m_g}{775} \right)^{1.26} \quad (42)$$

To estimate the effective energy contribution per sputtered target atom, this energy needs to be put in relation to the sputtering yield of the respective target material:

$$\langle E_{kin,BS}^{eff} \rangle = \frac{1}{Y_S} \langle E_{kin,BS} \rangle \quad (43)$$

Like target atoms, the backscattered gas atoms can collide with other atoms on their way to the substrate. Thus, their energy contribution can similarly be increased by a reduction of the process pressure or the target-substrate distance.

Energy of ions bombarding the substrate. When ions from the plasma are accelerated towards the substrate, e.g. by a negative substrate biasing voltage U_{bias} , their kinetic energy gain $\langle E_{kin,i} \rangle$ on the way through the substrate dark space is proportional to the electrical potential difference $U_{sub} = V_{pl} - U_{bias}$. Their effective energy contribution per deposited target atom is estimated as follows [14]:

$$\langle E_{kin,i}^{eff} \rangle = q_i U_{sub} \frac{J_i}{J_t} \frac{4 m_i m_t}{(m_i + m_t)^2} = q_i |U_{bias}| R_i \Gamma_{i,t} \quad (44)$$

Here, the reasonable assumption $U_{sub} \approx |U_{bias}|$ is made for high substrate biasing voltages $|U_{bias}| \gg |V_{pl}|$, since the plasma potential is not usually known. This energy contribution can be increased by an increase of the substrate biasing voltage $|U_{bias}|$ or the flux ratio $R_i = J_i/J_t$ of impinging ions to target atoms on the substrate.

Thermal energy of the substrate. The substrate temperature T_s defines the thermal energy $\langle E_{th} \rangle$ available to the adatoms as follows:

$$\langle E_{th} \rangle = \frac{3}{2} k_B T_s \quad (45)$$

Thus, this energy contribution can be increased by heating the substrate during the coating process.

As the exact determination of these energies is hardly possible in practical applications, *structure zone diagrams* [144,145] are typically used to estimate the effect of certain process parameters on the resulting layer structure. The most common structure zone diagram nowadays was created by Anders in 2010 [146] and is shown in Figure 42.

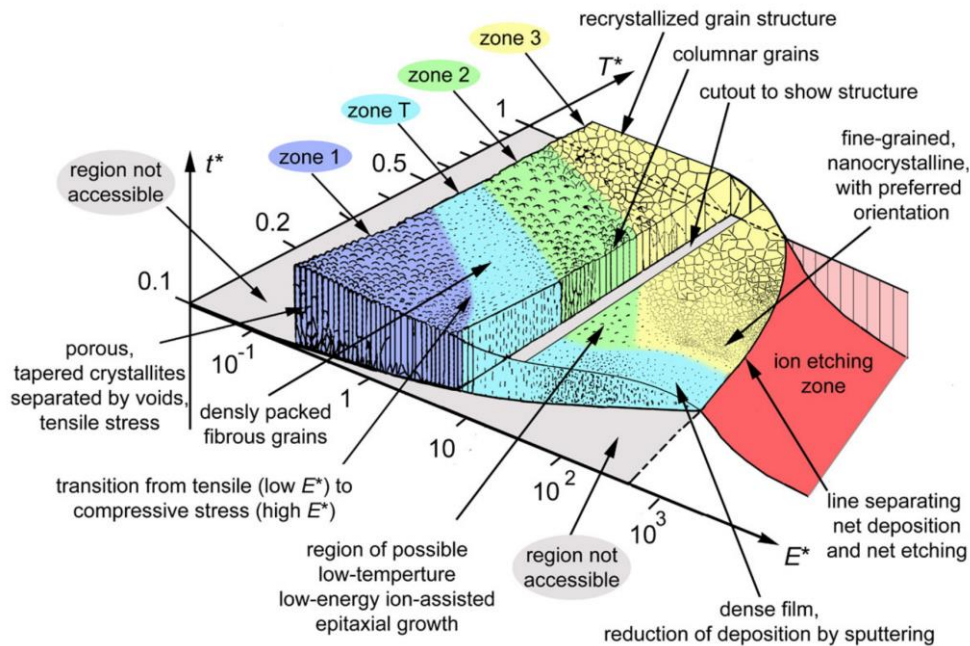


Figure 42: Anders structure zone diagram. The layer structure can generally be influenced by changing the generalized temperature T^* of the substrate or by increasing the normalized kinetic energy E^* of impinging particles. From [146].

In his diagram, Anders displays the resulting layer structure independent of the used apparatus and considers the energy intake of the substrate, e.g. by ion bombardment or by additional substrate heating. The two horizontal axes T^* – the *generalized temperature* – and E^* – the *normalized energy* – are defined as described below. This description already takes into account several corrections applied by Steyer [14] together with Anders regarding the energy transfer between heavy target atoms and light gas atoms as well as regarding the share of the adatom energy across various particle species hitting the substrate.

The generalized temperature T^* in equation (46) extends the homologous temperature $T_h = T_s/T_m$ of earlier structure zone diagrams [145] by a potential temperature T_{pot} , which estimates the energy contribution of impinging particles to the adatom mobility. Here, T_s and T_m are the substrate temperature and the melting temperature of the target material, respectively. The term in brackets shares the energy input $E_{pot,\kappa}$ from the condensation or neutralization of impinging particle species κ , weighted by their particle flux J_κ , across typically $N_{heat,\kappa} \cong 300$ atoms affected by the impinging particles. For standard DC sputtering with balanced magnetrons, the additional effect of T_{pot} on the generalized temperature can typically be neglected, whereas an increase of T^* by up to 20 % can be reached in processes with high fluxes of ionized gas or target atoms towards the substrate.

$$T^* = T_h + T_{pot} = \frac{T_s}{T_m} + \frac{1}{k_B T_m} \left[\frac{\sum_\kappa \frac{E_{pot,\kappa} J_\kappa}{N_{heat,\kappa}}}{\sum_\kappa J_\kappa} \right] \quad (46)$$

The normalized energy E^* in equation (47) sums up the transferred kinetic energy $E_{kin,\kappa} \Gamma_{\kappa,t}$ of the impinging particle species κ , weighted by their particle flux J_κ and normalized by the factor $10 E_{m,t}$, where $E_{m,t}$ represents the heat of fusion of the target material. Special note must be taken, as the energy sum is divided only by the flux J_κ^{layer} of impinging particle species which contribute to the formation of a layer, i.e. neutral or ionized target atoms. With standard DC sputtering using balanced magnetrons, E^* typically does not exceed 1 under the assumption of full thermalization of the sputtered atoms. By a reduction of collisions, or by additional energy input to the substrate, e.g. from a high ion flux due to substrate biasing, values of $E^* \geq 50$ are accessible though.

$$E^* = \frac{\sum_\kappa E_{kin,\kappa} \Gamma_{\kappa,t} J_\kappa}{10 E_{m,t} \sum_\kappa J_\kappa^{layer}} \quad (47)$$

The vertical axis of the Anders diagram indicates the net layer growth or – in case of extreme values of E^* – the re-evaporation of the deposited layer due to the re-sputtering effect at very high impinging ion energies and fluxes.

2.3.6 PLASMA CLEANING

As discussed before, a properly cleaned substrate contributes to the deposition of a layer with good adherence and the desired properties. A promising technique for a physical cleaning process, which can be performed in the same process chamber directly before sputter deposition, is so-called *plasma cleaning*. Here, a dedicated plasma is ignited close to the substrate surface at a medium-vacuum partial pressure of a noble gas like argon. Different physical cleaning processes can be initiated [147–150]:

Electron bombardment. By applying a positive substrate voltage, electrons from the plasma are attracted to the substrate. These electrons can promote desorption processes or break certain chemical

bonds of non-volatile contaminants, which then can be evaporated in the vacuum. Additionally, these electrons can contribute to a substantial warming of the substrate and thus further promote evaporation processes.

Ion bombardment. By applying a negative substrate voltage, positive ions from the plasma are attracted to the substrate. For low ion energies $E_i < 30$ eV, the cleaning effect is comparable to the effect of electron bombardment. In contrast, ions with higher kinetic energy $E_i > 30$ eV can cause a substantial erosion of the substrate by sputtering – analogous to the erosion of a sputtering target. This so-called *ion etching* process is theoretically able to remove any type of surface contaminants, chemical reaction products and mechanical deformations layer by layer. However, as this process is usually not assisted by a magnetron, the processing times are long and thus, only very few nm to μm can be removed from the substrate surface. As the surface is roughened and open chemical bonds are created by the erosion of substrate material, this process is considered to be highly beneficial for the adherence of layers from subsequent sputter deposition.

UV radiation. By the ionization of gas atoms in the plasma, highly energetic photons in the UV range are created. These photons also reach the substrate and can – like electrons – break certain organic contaminants and thus promote their evaporation from the substrate surface.

2.3.7 PREVIOUS WORK AT FRM II

HSK1

First efforts of TUM to apply an interdiffusion barrier onto U-Mo foils date back to the year 2008. At this time, a demonstration tabletop PVD coating device followed by a large-size device – hereafter referred to as *HSK1* (Handschuhkasten 1) – were designed and built mostly using self-manufactured components [8]. The process chamber of the HSK1 PVD coating device was placed inside an argon glovebox to prevent the U-Mo foils and the deposited layers from oxidation. The device was capable of depositing various metallic interdiffusion barriers such as Zr and Ti onto U-Mo foils with up to 700 mm x 62.4 mm. The substrate was laid flat onto a substrate holder plate, located centrally below a rectangular planar sputtering source. Figure 43 shows schematic views of the process chamber and the glovebox.

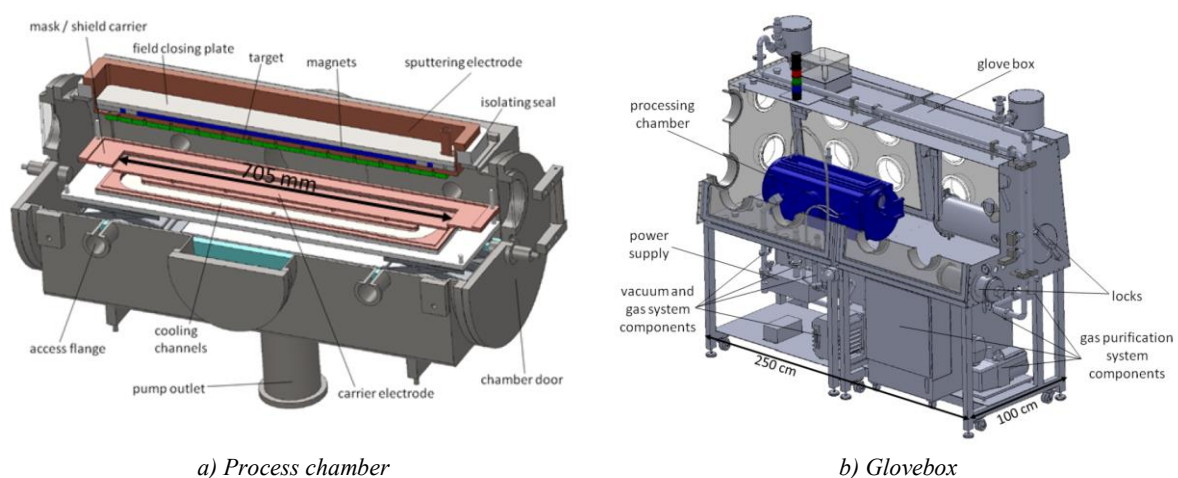


Figure 43: Schematic views of the HSK1 PVD coating device. The process chamber (a) was placed inside an argon glovebox (b) to protect the U-Mo foils and deposited layers from oxidation. The device was capable of depositing various metallic interdiffusion barriers onto U-Mo foils with up to 700 mm x 62.4 mm. From [8].

Figure 44 exemplarily shows Zr-coated U-Mo foils from HSK1. By simple visual inspection and microscopy, the foils met all specifications such as layer thickness, uniformity and adherence. However, after some days of storage at laboratory atmosphere, the samples exhibited large areas of coating delamination, which were confirmed also by electron micrographs of relevant cross-sections [8,9,151].

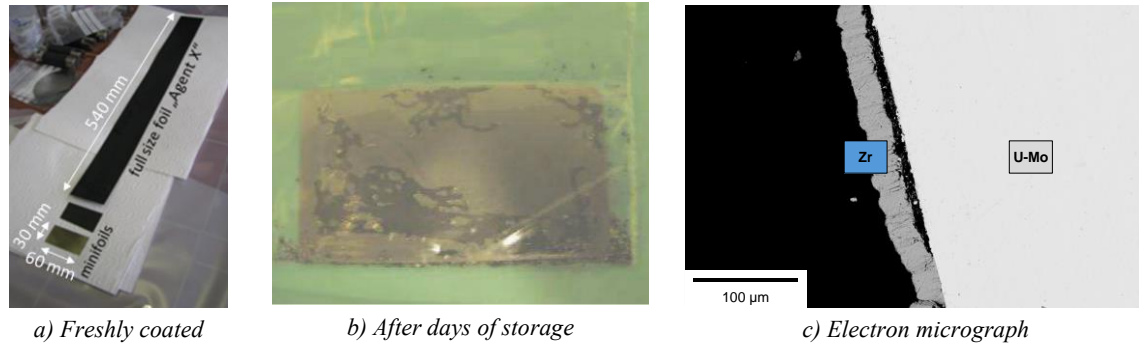


Figure 44: Zr-coated U-Mo foils from HSK1. While freshly coated foils appeared to be in excellent condition (a), delaminations of the coating occurred after some days of storage (b) which were confirmed using electron micrographs of cross-sections (c). From [8,9,151].

Consequently, U-Mo foils with Zr coating applied by the HSK1 device failed reproducibly in *UT* (ultrasonic transmission) testing after the C2TWP cladding application process at Framatome-CERCA, as shown in Figure 45. In comparison, U-Mo foils supplied by INL with a co-rolled Zr coating successfully passed UT testing after C2TWP [9]. In UT testing, the transmission rate is an indicator for the adherence between multiple layers, thus blue regions indicate adherence failures.

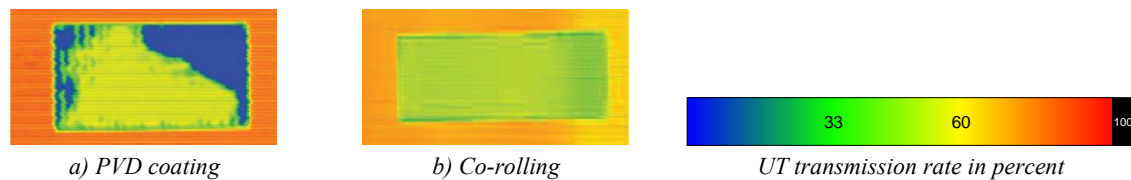


Figure 45: UT test results of Zr-coated U-Mo foils from HSK1 after C2TWP cladding application. Adherence deficiencies become evident for PVD-coated foils (a) but not for co-rolled foils (b). The transmission rate is an indicator for the adherence between multiple layers, thus blue regions indicate adherence failures. From [9].

HSK3

As a consequence, a comprehensive failure analysis was carried out, which in 2013 led to the design and construction of an experimental PVD device capable of depositing interdiffusion barriers onto U-Mo foils in the mini-size geometry (82.5 mm x 19 mm) [14]. This device will be hereafter referred to as *HSK3* (Handschuhkasten 3) and will be described in detail in section 3.1.1. Advancing from HSK1, it is built using customized components from research-focused commercial suppliers and integrates the following techniques to adjust the process parameters with the aim to improve the coating adherence and layer properties:

- Plasma cleaning of the substrate
- Application of a biasing voltage to the substrate
- Radiation heating and/or water cooling of the substrate
- Free adjustment of the target-substrate distance

Similar to HSK1, the substrate is laid flat onto a substrate holder plate located centrally below a rectangular planar sputtering source. The process chamber is again placed inside an argon glovebox to

protect the U-Mo foils and deposited layers from oxidation. Additionally, a dedicated argon glovebox for the chemical cleaning of U-Mo foils prior to coating is directly attached. Figure 46 shows the process chamber as well as both gloveboxes of the HSK3 PVD coating device.

With the abovementioned advances from HSK1, the HSK3 device is capable of applying defect-free Zr coatings with 100 % surface coverage onto U-Mo foils, as depicted in Figure 47. In optimization studies of this mini-size PVD coating process in combination with the C2TWP cladding application process, both have proven to be able to successfully fabricate mini-size demonstration fuel plates with no adherence deficiencies visible in UT testing.

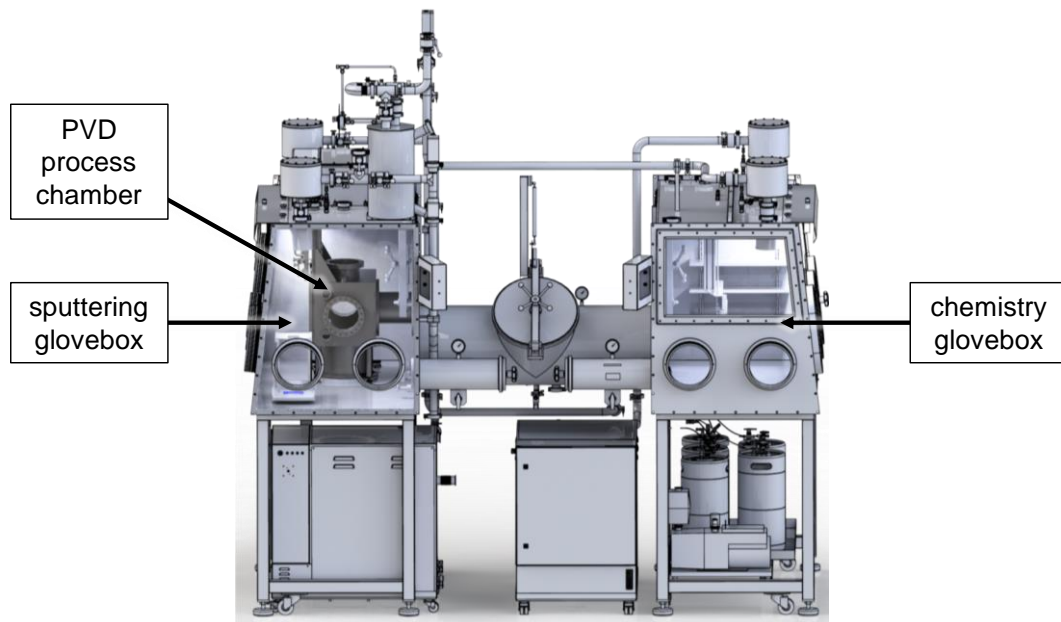


Figure 46: Schematic view of the HSK3 PVD coating device. The PVD process chamber is placed inside an argon glovebox to protect the U-Mo foils and deposited layers from oxidation. This sputtering glovebox is connected to a dedicated chemistry glovebox for the chemical cleaning of U-Mo foils. The device is capable of depositing interdiffusion barriers onto U-Mo foils with up to 82.5 mm x 19 mm. After [12].

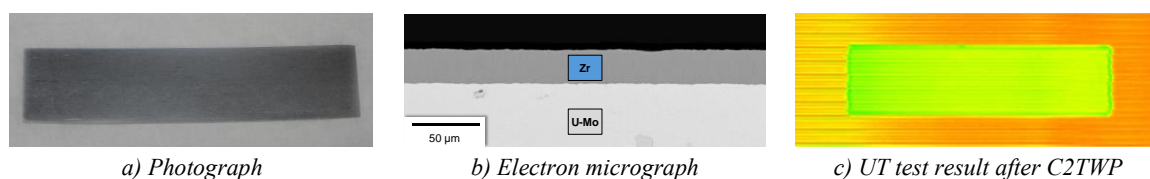


Figure 47: Zr-coated mini-size U-Mo foils from HSK3. No delaminations of the deposited layer were observed on the foils (a), which was confirmed also by electron micrographs (b). After C2TWP cladding application, no adherence deficiencies were identified (c). After [12].

Review of the EMPIRE fabrication campaign

Due to the promising results of TUM's mini-size PVD coating process and the high confidence in the C2TWP cladding application process at Framatome-CERCA, both processes were designated to fabricate LEU fuel plates for the EMPIRE irradiation test in 2016 [12,47–50]. Prior to this fabrication campaign, optimization studies were conducted using stainless steel and depleted uranium U-Mo foils

to find the best combination of process parameters for both processes. The PVD process generally consisted of the following steps:

1. Chemical pre-cleaning and de-oxidation of the substrate by immersion in a mixture of alkaline cleaner and hydrogen peroxide in the chemistry glovebox for 5 minutes
2. Plasma cleaning of side one of the substrate inside the HSK3 PVD process chamber for 15 minutes at a process pressure of ~ 0.4 mbar argon and a substrate voltage of - 800 V
3. Deposition of ~ 25 μm of reactor-grade Zr on side one of the substrate using DC magnetron sputtering with a sputtering power of 300 W and a substrate biasing voltage of - 300 V at a target-substrate distance of 30 mm and a process pressure of $\sim 5 \cdot 10^{-3}$ mbar argon
4. Repetition of steps 2 and 3 on side two of the substrate.

For the EMPIrE irradiation test, a total of four specification-conform LEU fuel plates were fabricated from seven bare mini-size LEU U-Mo foils supplied by BWXT. Three rejects were identified by UT testing, which were attributed either to inner defects in the U-Mo foil such as large uranium carbide inclusions or to large gaps between the U-Mo foil and the Al cladding, as illustrated in Figure 48 [152].

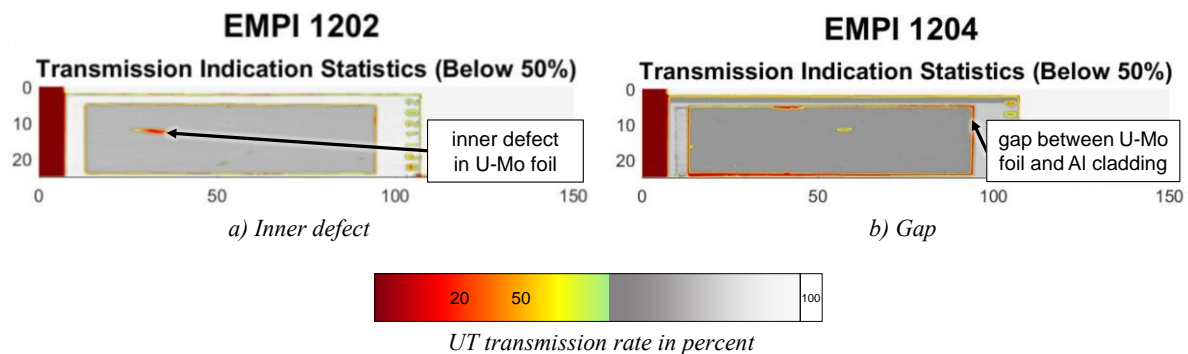


Figure 48: UT test results of rejected EMPIrE fuel plates. Out of seven fabricated fuel plates, three rejects were identified by UT testing. The failures were attributed to inner defects in the U-Mo foil (a) or to large gaps between the U-Mo foil and the Al cladding (b). After [152].

To better understand the interplay between PVD and C2TWP, and to optimize both processes for the future, detailed fabrication studies and destructive examination of several fuel plates from these studies as well as of rejected EMPIrE LEU fuel plates [13,14,153–157] were performed. In these studies, emphasis was put on the U-Mo/Zr interface, especially the potential formation of interaction layers as well as structural changes to the Zr layer following the cladding application. Further, the occurrence, size and shape of gaps between the U-Mo foil and the Al cladding was investigated. The main observations from these studies are described hereafter.

Cracks in the Zr coating. Thin, 5 - 10 μm wide cracks were repeatedly found in the Zr coating perpendicular to the length direction of the U-Mo foil. This length direction corresponds to the C2TWP process direction, along which directional mechanical stresses are applied to the U-Mo foils as shown in Figure 49. Figure 50 shows typical destructive examination results at the depicted sample location.

By polarized light microscopy as well as by an extensive microstructural study using electron-backscatter diffraction (EBSD) carried out by [157], a fine-grained microstructure of the Zr layer was found, as shown in Figure 50 d and e. This microstructure is assumed to be the main cause for brittleness and thus for the formation of the cracks. This assumption is supported by Vickers hardness measurements, which give 266 ± 7 HV0.01 for the Zr layer and only 138 ± 9 HV1 for the utilized reactor-grade Zr sputtering target [13,153].

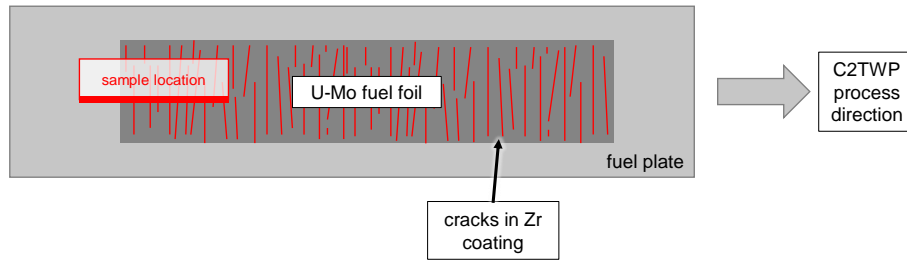


Figure 49: Cracks in the Zr coating introduced by the C2TWP process. Due to directional mechanical stresses applied to the Zr-coated U-Mo foils during C2TWP, cracks are introduced in the Zr coating. Destructive examination results of the depicted sample region can be found in Figure 50.

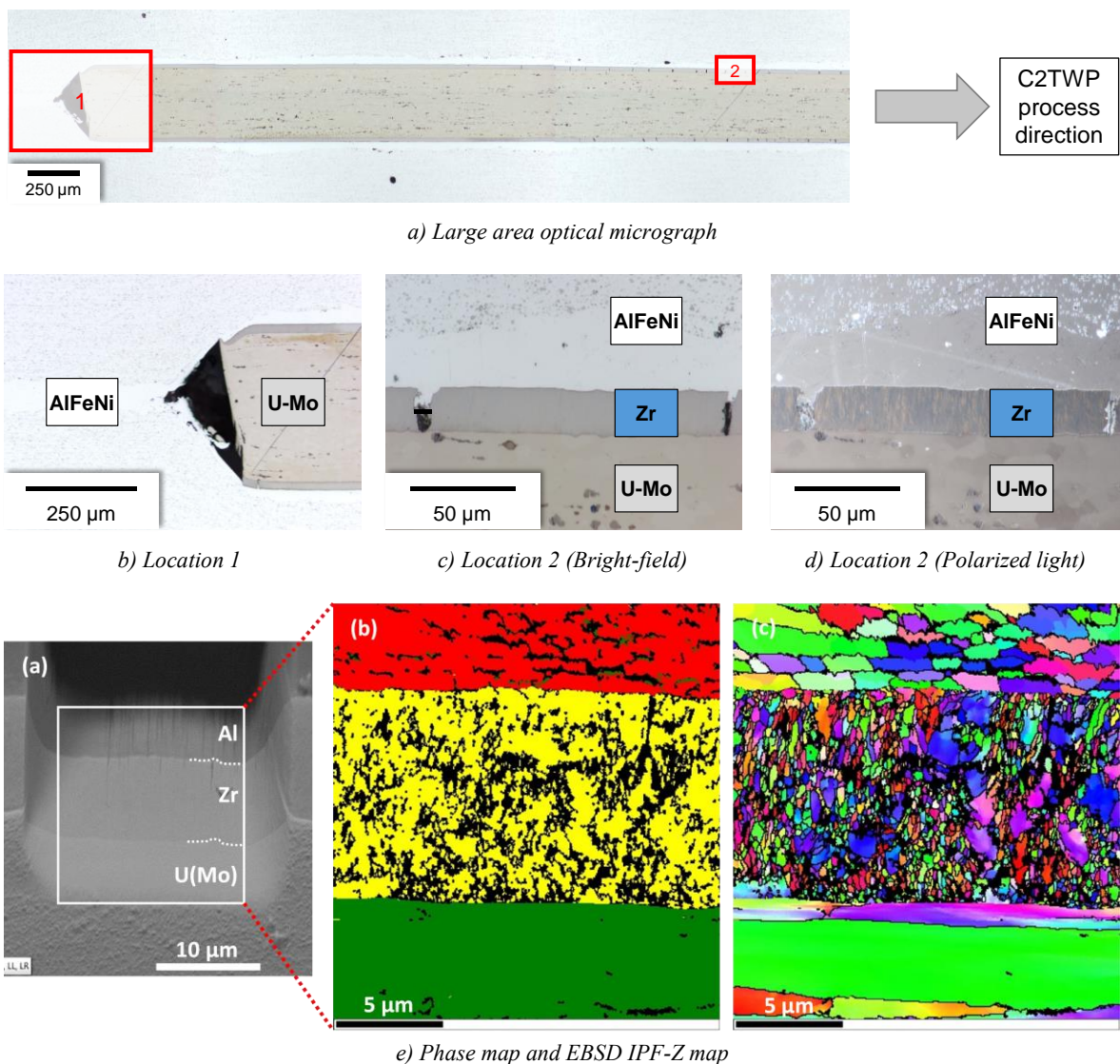


Figure 50: Typical destructive examination results of monolithic U-Mo fuel plates. The typically 5 - 10 μm wide cracks in the Zr coating (c) likely result from a fine-grained Zr layer microstructure (d, e). The gap between the U-Mo foil and the Al cladding (b) can solely be eliminated by Framatome-CERCA. Optical micrographs after [153], phase and EBSD map from [157].

Gaps between U-Mo foil and Al cladding. The gap between the U-Mo foil and the Al cladding which was found in some fuel plates by UT testing, as displayed e.g. in Figure 48 b, could be confirmed also by optical microscopy of cross-sections, as shown in Figure 50 b. The length of this gap typically is in the order of 100 - 200 μm and its maximum height corresponds to the thickness of the U-Mo foil. The elimination of this gap is possible only at Framatome-CERCA by modifications of the C2TWP cladding application process.

Bending of the substrates. After the application of the Zr coating to the first side of the substrate, a notable central upwards bending of the foil, as seen in an extreme example in Figure 51, was observed. The extent of this bending increases with increasing coating thickness and it starts to appear at a thickness of less than 10 μm on mini-size substrates. After the application of the Zr coating to the second side of the substrate, the bending usually disappears.

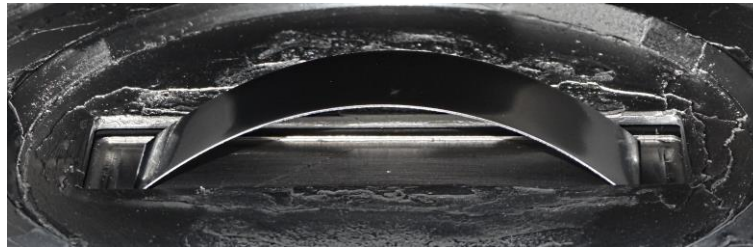


Figure 51: Bending of a mini-size stainless steel substrate with 50 μm single-sided Zr coating. When coated on only one side with Zr, the substrates develop a notable central upwards bending. From [14].

Recommendations for the pilot PVD coating process

Following these results, two major remaining issues of the mini-size PVD coating process were identified, which need to be resolved during its upscaling to full-size geometry and before its industrialization:

- The formation of cracks in the Zr coating during the C2TWP cladding application process, as these cracks can deteriorate its effect as an interdiffusion barrier during irradiation.
- The bending of the substrates after single-sided Zr coating application, as it can deteriorate the coating uniformity, complicate the manual handling of the substrates, or even make the coating of large full-size substrates impossible.

It is proposed to eliminate the cracking of the Zr coating either by reducing the directional mechanical stresses in the cladding application process or by increasing the ductility of the deposited Zr layer. As the former strategy can solely be followed by Framatome-CERCA and might not be technically feasible at all, the latter strategy will be followed via optimizations to the PVD coating process. The following technical approaches for such optimizations seem possible:

Optimized heating. In early fabrication studies with the HSK3 device, samples which were additionally heated during the PVD coating process showed a deposited Zr layer in growth structure type C or higher, but with much larger grains and better mechanical properties, compared to samples with substrate biasing. However, substrate heating was discarded for the EMPIrE fabrication campaign due to a large temperature uncertainty during the coating process and the unwanted formation of significant interaction layers between the U-Mo foil and the Zr coating. Thus, a possibility to eliminate the cracking of the Zr coating during C2TWP would be to increase its ductility via an optimized substrate heating approach at

a defined optimum substrate temperature and with a highly precise temperature control to avoid unwanted temperature ranges. This approach will be presented in section 5.2.

Optimized biasing. In the EMPIrE fabrication campaign, the application of a substrate biasing voltage has shown to be a suitable method to influence the properties of the deposited Zr layer. However, a comparably high substrate biasing voltage of - 300 V was necessary to achieve proper adherence of the coating. While this high voltage led also to a sufficiently high substrate ion flux, the bombardment of the substrate with such high-energy ions also led to a significant re-sputtering of the deposited layer, the introduction of structural damages, and thus to the creation of many new crystallization nuclei. Hence, the high substrate biasing voltage is assumed to be the main cause for the fine-grained microstructure, and thus the brittleness of the Zr layer. Consequentially, a possible way to increase the layer ductility would be to stimulate the growth of larger grains by reducing the nuclei formation rate, i.e. by reducing the energy of the ions bombarding the substrate. Hence, the substrate biasing voltage shall be reduced to a significantly lower value of ~ 100 V or less. At the same time, the energy contribution of impinging ions according to equation (44) must be maintained to preserve the necessary adatom mobility for the deposition of dense and defect-free layers in growth structure type C or higher. Thus, the ion flux to the substrate must be increased in return. Possibilities to accomplish this will be studied in section 5.3.

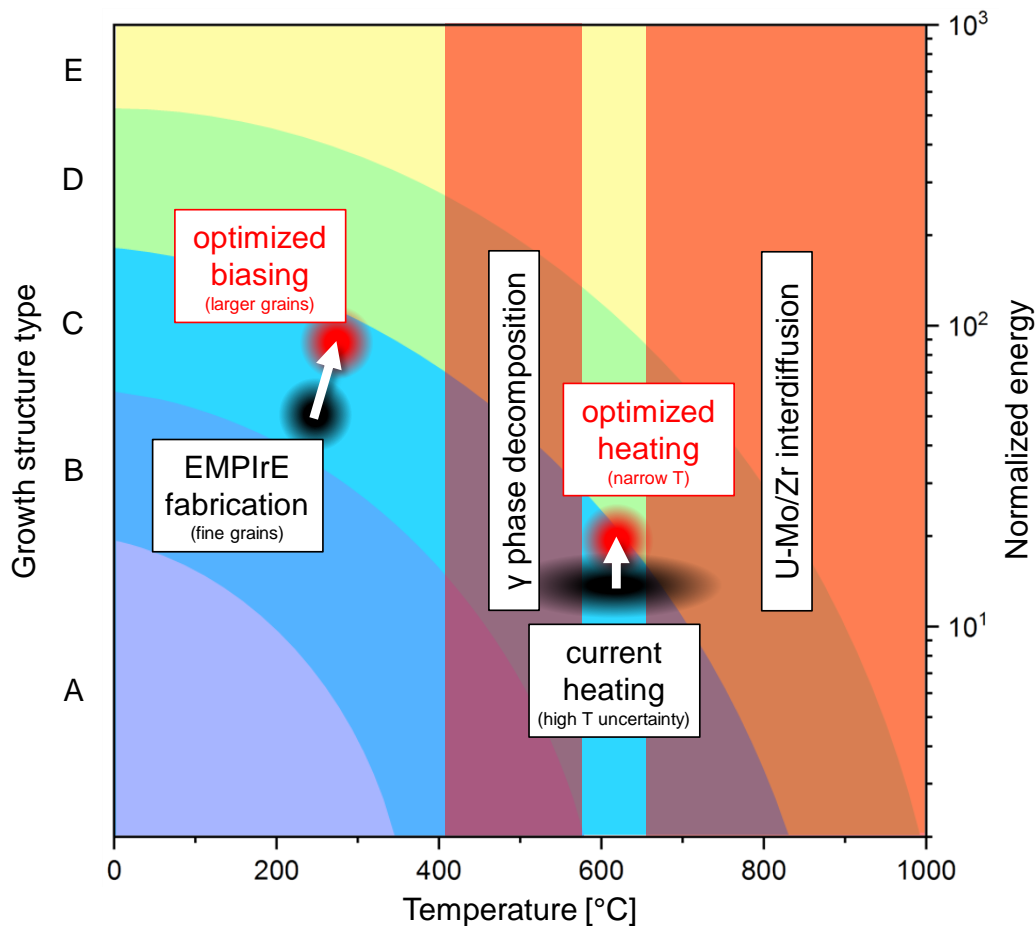


Figure 52: Optimized substrate heating and biasing approaches. While it was possible to reach the growth structure type C with a substrate biasing approach during the EMPIrE fabrication campaign, the fine-grained microstructure of the deposited Zr layer presumably led to its cracking during cladding application. To increase the coating ductility, optimized substrate heating and biasing approaches seem possible. The color code matches the Anders diagram in Figure 42.

Figure 52 summarizes the optimized substrate heating and biasing approaches graphically in an adapted structure zone diagram for the PVD coating of U-Mo foils with Zr. The optimized biasing approach does not need to change the growth structure type – however the growth of larger grains shall be stimulated to improve the ductility of the deposited layer. An optimized heating approach as well does not need to significantly change the growth structure type – however an optimum substrate temperature needs to be found and a more precise control of the substrate temperature is necessary to avoid U-Mo γ phase decomposition at $\sim 400 - \sim 575$ °C and the formation of U-Mo/Zr interaction layers at > 650 °C.

The biasing technique is generally preferred over the heating approach. On one hand, the long heating and cooling times of the substrate before and after the PVD coating process extend the overall processing time and therefore hinder the process industrialization. On the other hand, the biasing technique allows a significantly better process reproducibility, as it is independent of the surface structure of the substrate foils. This structure, which can be strongly different across various fabrication batches of U-Mo foils, has a considerable influence on the surface emissivity and therefore the reachable substrate temperature during heating. However, experiments on substrate heating will be performed to evaluate the reachable growth structure types of the deposited layer as a function of the substrate temperature and thus to potentially identify an optimum substrate temperature for an optimized substrate heating approach.

The substrate bending after single-sided Zr coating application was not considered a major issue for the EMPIrE fabrication campaign in mini-size geometry, since the amount of bending did not negatively influence the PVD and C2TWP processes. In this thesis, which aims at developing a pilot PVD coating process for full-size U-Mo foils, this issue needs to be addressed since the extent of bending is expected to increase with the substrate size. The following approaches to reduce this effect seem possible:

Optimization of PVD process parameters. The relevant literature [132,158,159] suggests changes to the process parameters such as working gas pressure or sputtering power to reduce inner stresses in the coating. Since previous experiments following these suggestions with the mini-size process failed [14], the probability of success of further attempts is considered low. However, the realization of this approach is rather simple and additional experimental studies will be performed.

Reduction of the coating thickness. As the extent of bending increases with increasing coating thickness, an obvious approach would be to reduce the thickness. While the minimum required value of ~ 25 μm on both sides in the EMPIrE fabrication campaign was chosen with the only intent to reproduce the target thickness of co-rolled layers, recent studies [42,120] indicate that a lower thickness in the range of 5 - 8 μm is sufficient to efficiently prevent the U-Mo/Al interdiffusion. Therefore, experimental studies with such thinner Zr coatings will be performed.

Fixing of the substrate. If both abovementioned approaches fail to reduce the bending of the substrates to an acceptable extent, the substrates could be fixed to the substrate holder during the PVD coating process to keep them forcefully flat, e.g. by a mechanical clamp or by an adhesive interlayer. Clamped areas of the substrate, which will thus be shadowed from the Zr particle flux, must be trimmed off afterwards because full surface coverage on both sides is required. Since the bare U-Mo foils are cut from larger master foils before PVD coating, the material loss from this clamping approach could still be kept low if the clamping area is kept small.

Simultaneous coating of both sides. As the bending of the substrates usually disappears when both sides are coated, the simultaneous coating of both sides presents another possible approach to solve this issue. However, this would require a strongly different device design compared to the previous HSK1 and HSK3 PVD coating devices, including two sputtering sources and a substrate holder design capable of holding the substrate flat in between them.

3 EXPERIMENTAL BASICS

3.1 EXPERIMENTAL INFRASTRUCTURE FOR PVD COATING

All experiments and sample production campaigns with PVD are performed in TUM's Nuclear Fuel Fabrication and Characterization Laboratory in the *IAZ* (Industrielles Anwenderzentrum) building at the FRM II site. This laboratory is licensed according to § 9 *AtG* (Atomgesetz) to openly handle uranium up to an enrichment of 50 % U-235 and up to total mass of 150 g U-235. The laboratory provides all experiments three-phase electrical power, cooling water with adjustable inlet temperature and pressure, pressurized air as well as argon, nitrogen and a gas mixture of 4 % hydrogen and 96 % argon.

Two gloveboxes suitable for PVD coating experiments are installed in the laboratory: the HSK3 device which hosts the experimental mini-size PVD coating process and the *HSK2* (Handschuhkasten 2) device, which will be used in this thesis to implement the pilot PVD coating process.

3.1.1 THE HSK3 DEVICE

The HSK3 device was commissioned in 2013 and its design is based on a comprehensive failure analysis of the previous HSK1 PVD coating device. A full description of the HSK3 device and the scientific background for its conception can be found in [14].

Chemistry glovebox

The chemistry glovebox of HSK3, shown in Figure 53, is a nuclear glovebox according to DIN 25412 [160], procured from M. Braun Inertgas-Systeme GmbH. It allows to perform the necessary wet-chemical cleaning steps of bare U-Mo foils in a high-purity argon atmosphere to prevent the foils from re-oxidation. Therefore, the glovebox is equipped with an M. Braun MB 200 G gas purification system [161] with two purification reactors to reduce the oxygen and water vapor content to less than 1 *ppm* (parts per million) in a negative pressure of up to - 10 mbar. To absorb corrosive or harmful fumes of chemicals before they enter the purification system, an active carbon filter can be switched on optionally. To protect the stainless steel glovebox body from corrosion, its inner side is entirely coated with a PTFE film. To avoid the need to transfer the necessary chemicals into the glovebox for each cleaning process, it is equipped with an integrated chemical supply system which can be filled with various etchants, solvents and distilled water.

Sputtering glovebox

The sputtering glovebox of HSK3, shown in Figure 54, is connected to the chemistry glovebox via a transfer load-lock, which allows the transfer of samples between both gloveboxes without contact to the laboratory atmosphere. It is also a nuclear glovebox according to DIN 25412 [160], procured from M. Braun Inertgas-Systeme GmbH. It accommodates a vacuum chamber as PVD process chamber in a high-purity argon atmosphere to prevent cleaned and coated U-Mo foils from re-oxidation. Therefore, the glovebox is equipped with an M. Braun MB 20 G gas purification system [161] with one purification

reactor to reduce the oxygen and water vapor content to less than 1 ppm in a negative pressure of up to - 10 mbar. All connections of the PVD process chamber can either be routed through the glovebox to the laboratory atmosphere or are directly accessible from the outside. For weighing the samples before and after coating, a high-precision scale is installed in the glovebox. Further, a welding tongs for hermetical sealing of leak-tight aluminum-plastic composite bags is available for the packaging of coated U-Mo foils in inert atmosphere.

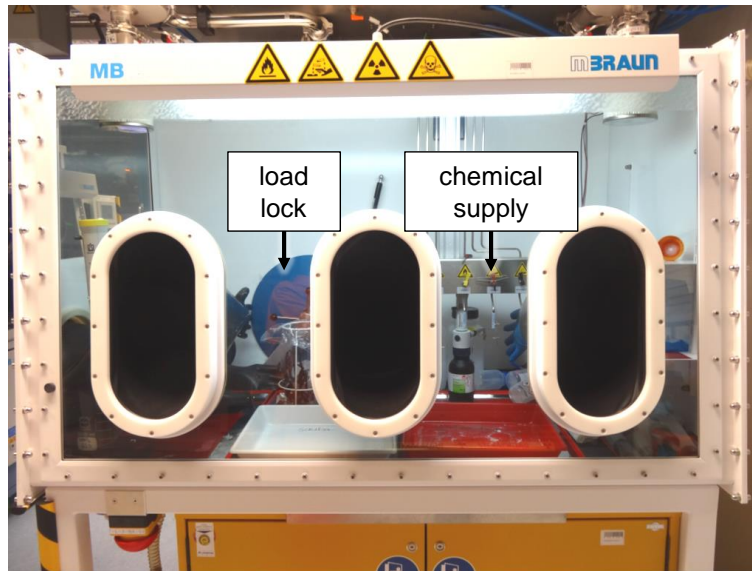


Figure 53: The HSK3 chemistry glovebox. In this glovebox, the necessary wet-chemical cleaning steps of bare U-Mo foils can be performed in a high-purity argon atmosphere. After [14].

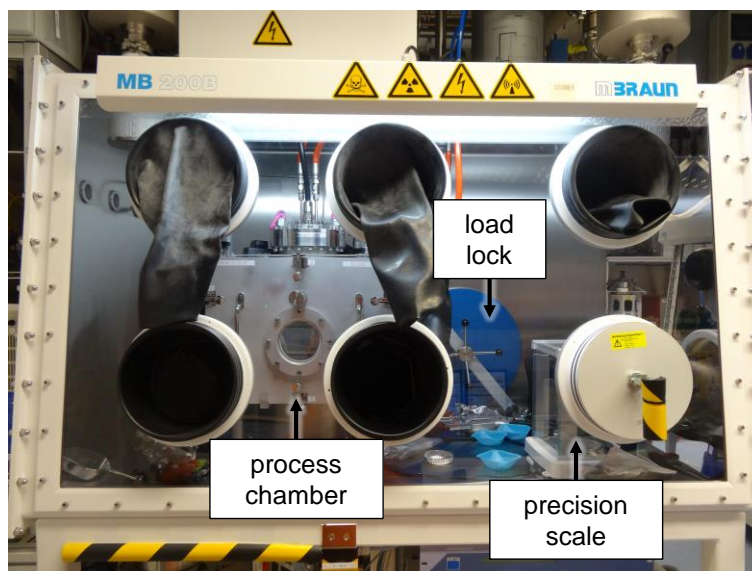


Figure 54: The HSK3 sputtering glovebox. This glovebox accommodates a vacuum chamber as PVD process chamber in a high-purity argon atmosphere to prevent cleaned and coated U-Mo foils from re-oxidation. After [14].

Vacuum and gas supply system

The PVD process chamber inside the sputtering glovebox is a customized vacuum chamber made of stainless steel from VACOM Vakuum Komponenten & Messtechnik GmbH. It has flanges of *CF* (compact flange) type to connect the sputtering source at the top, the substrate holder at the bottom and the vacuum system at the back side as well as various flanges of *CF* or *KF* (Kleinflansch) type to connect the gas inlet or other auxiliary components. The front door of the chamber can be entirely moved upwards by a wire rope hoist for maximum reachability of the installed components inside, as shown in Figure 55.

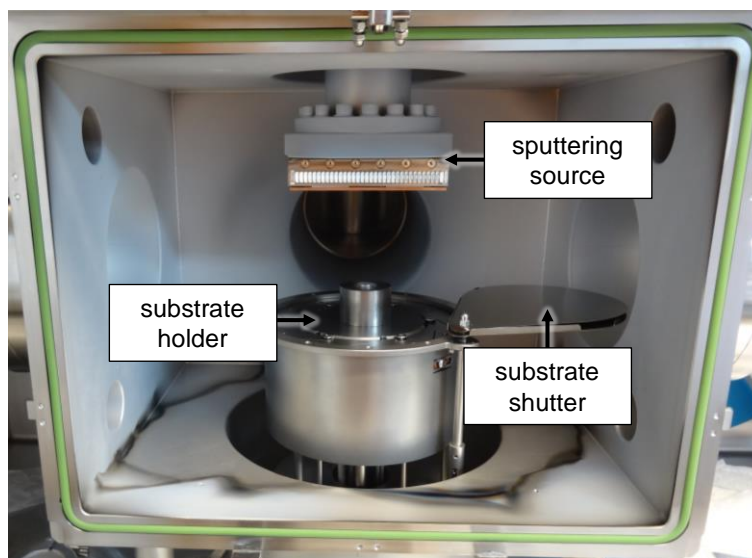


Figure 55: The HSK3 vacuum chamber. The sputtering source (displayed here without dark space shielding) is mounted at the top of the vacuum chamber, above the substrate holder. After [162].

The vacuum in the chamber is established by a combination of a Leybold TRIVAC D 65 B [163] rotary vane pump as backing pump and a Leybold TURBOVAC MAG W 1300 iP [164] turbomolecular pump, which together are able to achieve a base pressure of less than 10^{-7} mbar. After the evacuation, the plasma cleaning and sputtering process pressures in the order of 10^{-1} - 10^{-3} mbar are established by partially closing the valves before pumps and by regulating the inlet flow of the gases argon, argon with 4 % H_2 (up to 3000 ml/min both) and nitrogen (up to 30 ml/min) using three Bronkhorst F-201CS [165] MFCs (mass flow controllers). By activating multiple MFCs at the same time, also a mixture of these gases can be used. For venting the system, a hand-operated venting valve to the glovebox can be opened. The pressure in the chamber is measured using two pressure gauges: a Leybold CERAVAC CTR 100 N precision pressure gauge [166] directly attached to the chamber, capable of measuring three orders of magnitude in mbar, and a Leybold PENNINGVAC PTR 90 N [167] wide range pressure gauge outside the glovebox, capable of measuring twelve orders of magnitude in mbar. Figure 56 schematically shows the vacuum and gas supply system of HSK3.

Sputtering source

Since it was not possible to use a standard commercial sputtering source for the mini-size PVD coating process, a customized design was developed at TUM and fabricated by Reuter Technologie GmbH. It is a strongly balanced magnetron source able to sputter rectangular targets with dimensions of 120-122 mm x 54 mm x 10 mm made of metal or non-conductive materials.

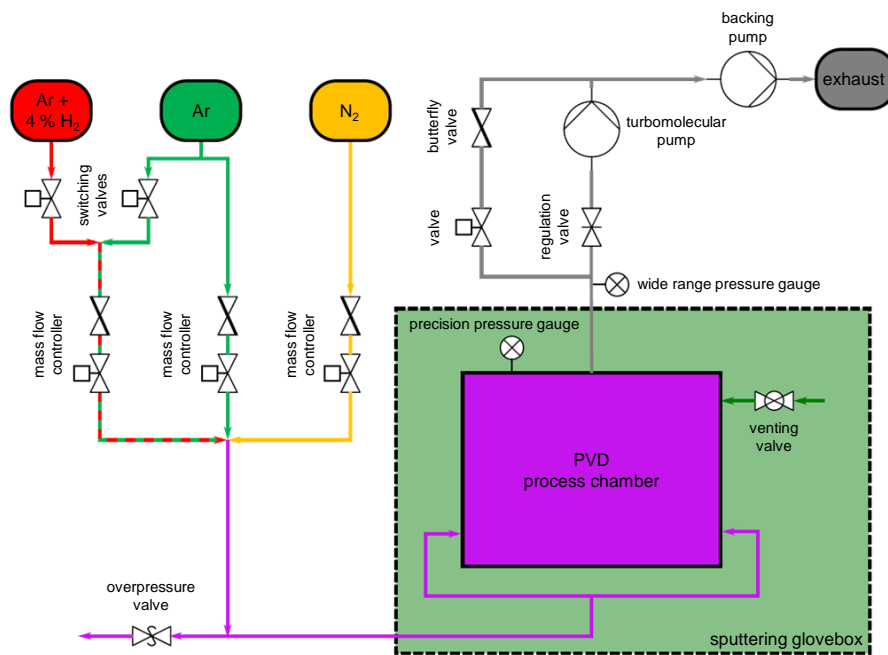


Figure 56: The HSK3 vacuum and gas supply system. The PVD process chamber is evacuated with a turbomolecular and a backing pump. The inlet gas can be chosen from argon, argon with 4 % H₂, nitrogen, or a mixture thereof. After [14].

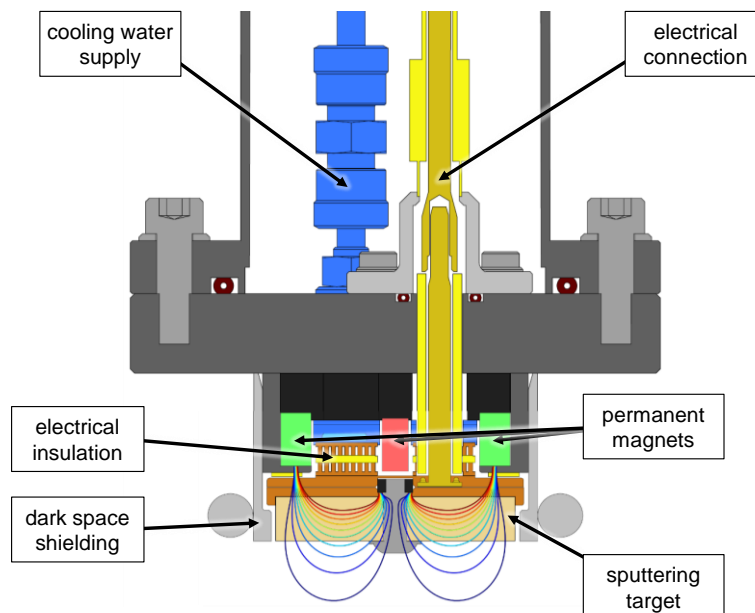


Figure 57: Sectional view of the sputtering source of HSK3 with magnetic field lines. The cooling water is electrically insulated from the sputtering target, which is attached to the source by magnetic force. The magnetic field lines are typical for a strongly balanced magnetron. After [14].

To mount the sputtering target into the source, it is screwed into a copper tray with an iron bar at the backside, which is attached to the base plate of the source by magnetic force. As this force by itself is not able to ensure a good thermal contact, thermal grease is applied to the interfaces between the target

and the copper tray and between the copper tray and the base plate. To avoid a direct electrical contact between the grounded stainless steel cooling water channels and the copper base plate at high voltage, the water channels are separated from the base plate by an *AlN* (aluminum nitride) plate. AlN is known to have an excellent thermal conductivity while being a strong electrical insulator. Figure 57 shows a sectional view of the sputtering source with all major details of the design. Being a sputtering source designed for research and development activities, no focus was put on the material efficiency. Therefore, the maximum achievable target utilization was measured to be approximately 25 % [162], a typical value for such sputtering sources. The sputtering source is successfully tested at a continuous sputtering power of 1000 W for DC and RF sputtering, provided either by a Trumpf Hüttinger TruPlasma DC 3002 DC [168] PSU or a Trumpf Hüttinger PFG-RF 1000 RF [169] PSU. All connections for electrical power and cooling water are accessible from inside the glovebox and need to be routed to the outside for the connection with the power supply units and the laboratory infrastructure.

Substrate holder

The substrate holder of the HSK3 device is located below the sputtering source in direct line-of-sight of the sputtering target. All its actuators and connectors, like e.g. electrical power and cooling water, are directly accessible from the outside of the glovebox. It is a customized version of the EpiCentre deposition stage [170] from UHV design Inc.. For the plasma cleaning and PVD coating process, the substrate is placed flat centrally onto a round molybdenum plate with 100 mm diameter. To ensure 100 % surface coverage, no additional clamping or other obstructive structures are in contact with the substrate. However, to avoid the unwanted coating of the Mo plate and other components of the substrate holder, an aperture ring is placed on top of the substrate. By a manual drive, the distance between the substrate and the sputtering target can be adjusted from 5 - 105 mm.

To allow the additional heating of the substrate and the application of a biasing voltage, a complex design of radiation heating elements, electrical connections, water cooling channels and electrical insulators is required. The key features of this design are shown in a sectional view of the substrate holder in Figure 58. By a complex electrical routing from the high voltage connector outside the glovebox to the Mo plate, a biasing voltage up to - 1200 V can be applied to the substrate while the copper heat sink remains grounded. This voltage is supplied by a Trumpf Hüttinger TruPlasma Bias 3003 [171] DC PSU with up to 3000 W. It can be operated in a high-voltage mode up to - 1200 V for plasma cleaning operations or in a low-voltage mode up to - 300 V for biasing operations. By a radiation heater element placed directly below the Mo plate, substrate temperatures of up to 1000 °C are achievable with only little warming of surrounding components. This heater element is powered by a HeidenPower HEA-PS8080-120 2U [172] DC PSU with up to 3000 W. To cover a wide range of achievable substrate temperatures, the Mo plate can be chosen from three types: (i) a *biasing plate* with strong thermal contact to the heat sink, (ii) a *heating plate* with weak thermal contact to the heat sink, and (iii) a *high-temperature plate* with weak thermal contact to the heat sink and two rectangular cut-outs below the substrate. This high-temperature plate allows substrate temperatures of up to 1000 °C by a direct line-of-sight between the radiation heater element and the substrate. Even though two thermocouples are installed in the substrate holder – one inside the radiation heater element and one inside the Mo plate carrier ring – no precise measurement of the substrate temperature itself is possible. Models to simulate the substrate temperature based on the heating power deliver an uncertainty of the substrate temperature of more than ± 50 °C [14]. To avoid the unwanted layer deposition on the substrate during sputtering target cleaning, the entire surface of the substrate holder can be protected by a swivel-mounted substrate shutter actuated by a pressurized air drive.

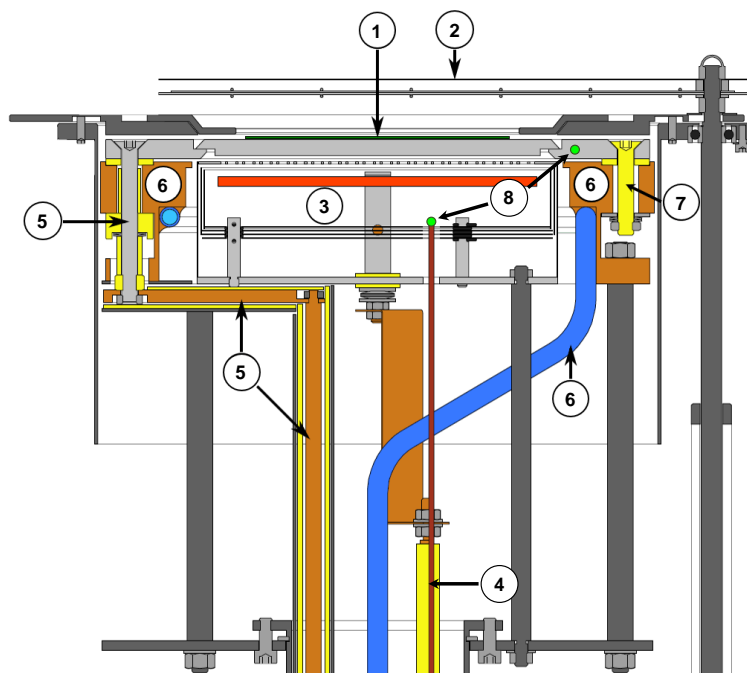


Figure 58: Sectional view of the substrate holder of HSK3. The substrate (1) is loosely placed onto a Mo plate and can be protected by a swivel-mounted substrate shutter (2). To allow substrate heating and biasing, a complex design of radiation heating elements (3), electrical connections (4, 5), water cooling (6) and electrical insulators (7) is required. Two thermocouples (8) allow the measurement of the substrate holder temperature. After [14].

Safety and device control

Since the HSK3 device is placed in a nuclear environment, the protection of the operators and the prevention of unintended release of radioactivity are important safety goals. Therefore, the device is connected to the laboratories' emergency stop system, which automatically stops any ongoing process in the PVD process chamber, shuts down the device and all power supply units and interrupts the cooling water supply in the event of e.g. water leakage, errors of the glovebox gas purification system or cooling water supply or by manually pressing an emergency stop button. Therefore, all valves are designed as *NC* (normally closed).

The PVD coating process and all related process steps, such as e.g. plasma cleaning, pre-heating, biasing and cooling, are entirely controlled and monitored by a BECKHOFF TwinCAT *PLC* (Programmable Logic Controller) system with an electrical cabinet for all analog and digital I/O terminals as well as all digital bus systems of the connected devices. By a *GUI* (graphical user interface), the operator can either set all device parameters manually or preprogram a process recipe with all parameters, which is then automatically executed by the system. At any point in the process – no matter if it is controlled manually or automatically from a preprogrammed recipe – the system monitors critical process parameters like the flow of cooling water and the pressure in the vacuum chamber and subsequently can prohibit the execution of process steps which can be harmful to the device or the operator.

3.1.2 THE HSK2 DEVICE

The pilot PVD coating process, which is developed within this thesis and will be described in detail in section 5, shall be developed using the existing glovebox and vacuum equipment of the HSK2 device.

Glovebox

The HSK2 glovebox is a nuclear glovebox according to DIN 25412 [160], manufactured by GS GLOVEBOX Systemtechnik GmbH. Figure 59 gives a detailed overview of the glovebox and its features. It is able to maintain a high-purity argon atmosphere with less than 1 ppm oxygen and water vapor in a negative pressure of up to - 10 mbar due to a GS M-Line gas purification system [173] with two purification reactors. The gas purification system is connected to the box via two HEPA H13 [174] particle filters to prevent its contamination. The usable inner space of the glovebox is 2489 mm wide, 1200 mm high and between 1200 mm (at the bottom) and 775 mm (at the top) deep. A total of 26 glove ports with 217 mm diameter each, equipped with DIN EN ISO 21420 [175] 0.6 mm thick butyl gloves allows the manual access of all inner installations. The media connections of inner installations can be routed to the outside atmosphere via a total of 18 KF flanges on top and on the sides of the glovebox. The glovebox is equipped with two transfer locks: a main transfer lock with 1000 mm usable inner length and 400 mm usable inner diameter for transferring large components and a small transfer lock with 440 mm usable inner length and 150 mm usable inner diameter for transferring tools and smaller parts in and out of the glovebox. A vacuum chamber is installed centrally in the glovebox, with a directly attached vacuum system outside of the glovebox.

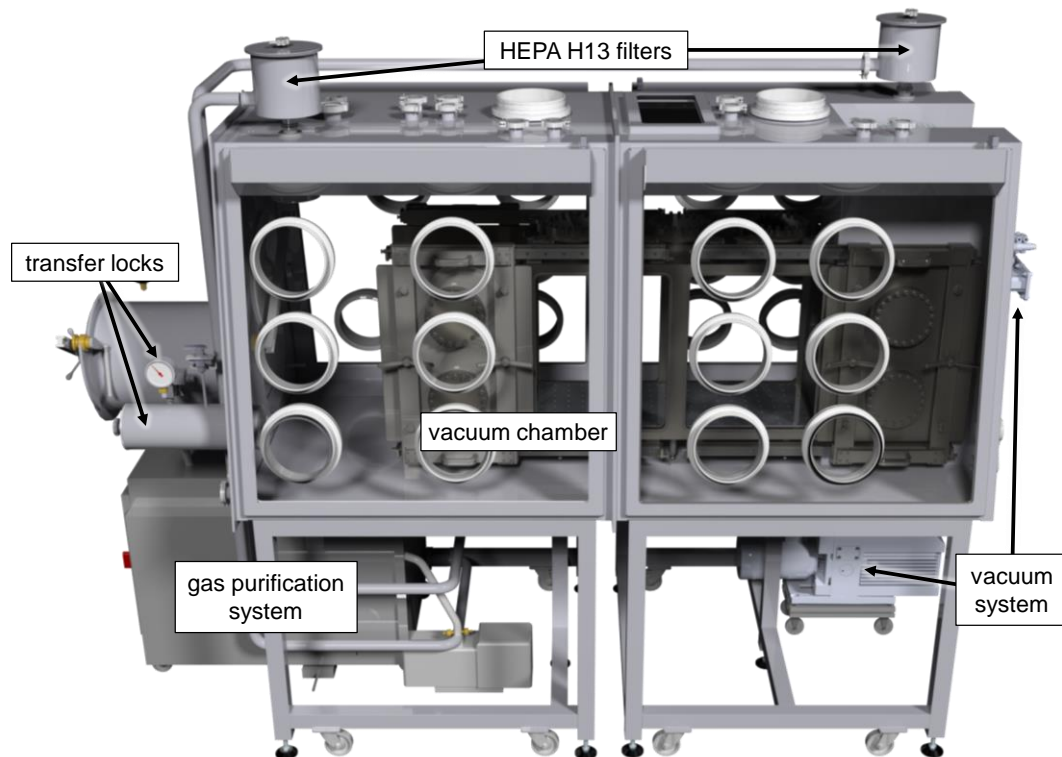


Figure 59: The HSK2 glovebox. The atmosphere is maintained by a two-reactor gas purification system, connected to the box via two HEPA H13 filters. Two transfer locks allow the transport of materials in and out. The installed vacuum chamber is directly connected the vacuum system outside of the glovebox.

Vacuum and gas system

The stainless steel vacuum chamber is a custom design, manufactured by Pink GmbH Vakuumtechnik. Figure 60 gives a detailed overview of the chamber and its features. Its usable inner space is 1000 mm wide, 560 mm high and 400 mm deep. To achieve maximum flexibility for installations, plates with 160 M8 threaded holes each are installed on the inside bottom and ceiling. Access to the inside of the

vacuum chamber is possible through four sliding doors on the long sides of the chamber as well as a swinging door at the front side. The proper closing of all doors is monitored digitally via IFM 5390 inductive position sensors [176]. A total of 13 CF160 flanges is available on the doors and on the top, together with 12 KF40 flanges on the top. The vacuum system outside of the glovebox is directly connected via a CF200 flange on the back side of the vacuum chamber.

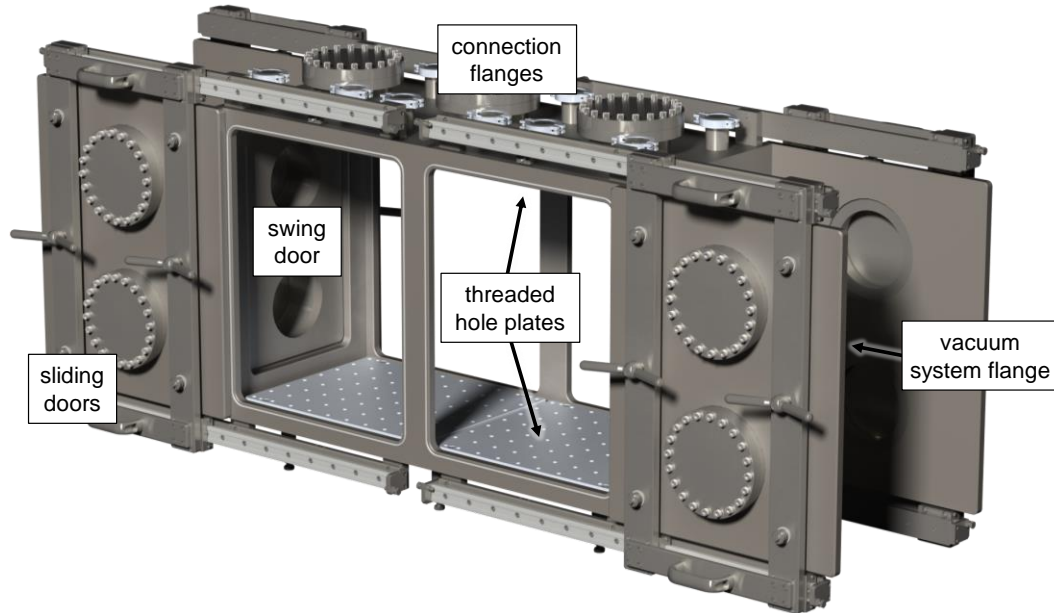


Figure 60: The HSK2 vacuum chamber. The chamber has four sliding doors (1) on the sides and a swinging door (2) on the front. A total of 13 CF160 flanges is available on the doors (3) and on the top (4), together with 12 KF40 flanges on the top (5). The vacuum system is directly connected via a CF200 flange on the back side of the vacuum chamber (6). For maximum flexibility for installations, the floor and ceiling of the chamber are equipped with M8 threaded plates (7).

Similar to the HSK3 device, the vacuum in the chamber is established by a combination of a Leybold TRIVAC D 65 B [163] rotary vane pump as backing pump and a Leybold TURBOVAC MAG W 1300 iP [164] turbomolecular pump, which together are able to achieve a base pressure of less than 10^{-7} mbar. After the evacuation, the plasma cleaning and sputtering process pressures in the order of 10^{-1} - 10^{-3} mbar are established by partially closing the valves before pumps and by regulating the inlet flow of the inlet gases argon (up to 3000 ml/min) and nitrogen (up to 30 ml/min) using two Bronkhorst F-201CS [165] MFCs. For venting the system, two hand-operated venting valves to the glovebox can be opened. The pressure in the chamber is measured using two pressure gauges: a Leybold CERAVAC CTR 100 N precision pressure gauge [166] directly attached to the chamber, capable of measuring three orders of magnitude in mbar, and a Leybold PENNINGVAC PTR 90 N [167] wide range pressure gauge outside the glovebox, capable of measuring twelve orders of magnitude in mbar. The entire vacuum system is optimized towards low leak rates of atmospheric contaminations such as oxygen. Therefore, the vacuum seals which are in contact to the outside of the glovebox are realized using copper seal rings whenever possible. The KF40 vacuum seals inside the glovebox can though be realized using standard rubber seals, since the entire vacuum chamber is located in the high-purity argon atmosphere of the glovebox. Figure 61 schematically shows the vacuum and gas supply system of HSK2.

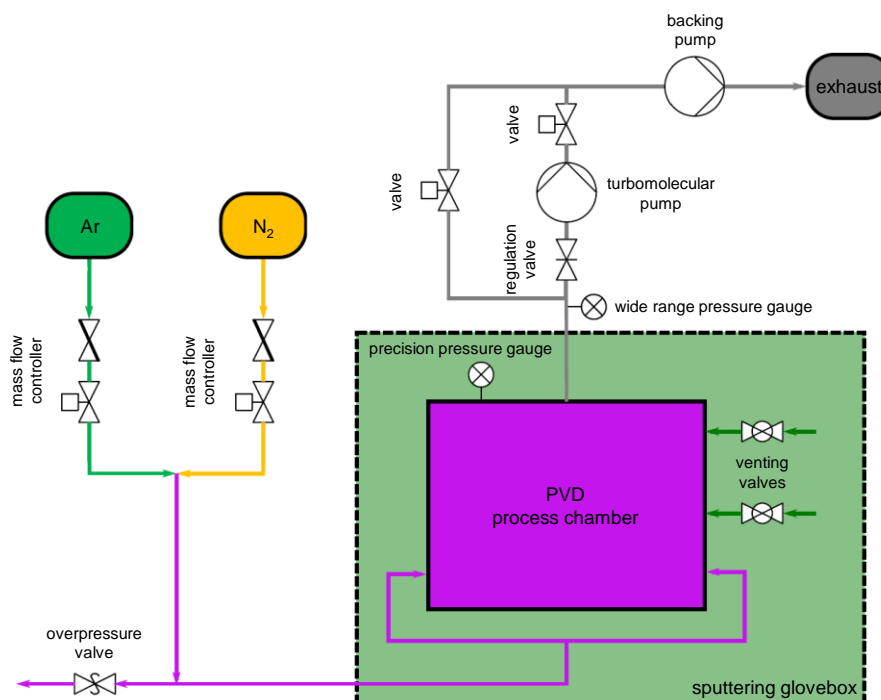


Figure 61: The HSK2 vacuum and gas supply system. The PVD process chamber is evacuated with a turbomolecular and a backing pump. The inlet gas can be chosen from argon, nitrogen, or a mixture thereof.

3.2 SAMPLE PREPARATION

To ensure repeatability of PVD coating and gradient foil fabrication experiments as well as comparability of the samples produced thereby, the use of standardized methods is essential.

3.2.1 SUBSTRATE PREPARATION FOR PVD COATING

The surface of substrates is typically covered with potentially unwanted layers, which can prevent the proper adherence of PVD coatings and thus, the removal of such layers is crucial. Mechanical methods such as grinding and polishing are generally not preferred, as they by themselves can introduce additional damage to the substrate. Instead, the following chemical cleaning methods were developed to prepare the substrates for the PVD coating process.

Chemical cleaning of flat stainless steel substrates

Flat stainless steel substrates for PVD coating experiments are purchased from scientific supply companies such as Goodfellow GmbH. At the suppliers, the material is cut to the final size, chemically cleaned and packaged in between individual sheets of clean paper or cardboard to avoid contamination or touching of substrates. Therefore, only a gentle cleaning procedure is applied to such substrates to remove light contaminants such as dust or fingerprints before they are transferred into the PVD coating devices.

Once removed from packaging, the stainless steel substrates are laid onto a lint-free tissue on the laboratory workbench and wiped in straight lines with a lint-free cloth, soaked in undenatured ethanol. The substrates are dried afterwards by blowing them with dry argon from the laboratory media supply.

Chemical cleaning of gradient substrates

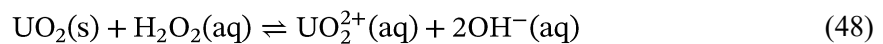
Gradient substrates from stainless steel or titanium alloys are fabricated at workshops or laboratories, which usually do not respect the surface cleanliness requirements of PVD coating processes. During their fabrication, the substrates may get in contact with cooling lubricants, water, grease, dust and fingerprints. Further, samples fabricated by selective laser melting can exhibit a very rough surface with many cavities, which requires additional effort to remove adhering contaminants. Therefore, the following thorough cleaning procedure is applied to all gradient substrates.

First, 50 ml of the cleaning solution, containing 3 vol.% of the industrial alkaline cleaning agent SurTec 138 [177], 0.1 vol.% of the industrial detergent SurTec 089 [178] and 96.9 vol.% distilled water, is prepared in a suitable glass vessel. Then, the gradient foils are immersed into this solution inside an ultrasonic bath with 130 kHz. After 10 minutes, the foils are removed and transferred into a second glass vessel with distilled water, where they are immersed for 1 minute inside the same ultrasonic bath. The last step is repeated once before the substrates are placed on a lint-free tissue and dried by blowing with dry argon from the laboratory media supply. To remove any remaining adhering water or humidity from the potentially rough surfaces, the gradient foils are further dried for 10 minutes in the fine vacuum of the transfer lock of the PVD coating devices.

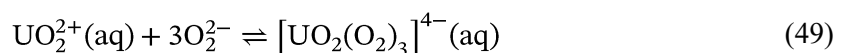
Chemical cleaning of U-Mo substrates

U-Mo substrates are procured from the US-American fuel fabricator BWXT, who has specialized on the fabrication of co-rolled U-Mo foils. Therefore, the surface cleanliness requirements of PVD coating process are usually not respected. The fabrication process of bare U-Mo foils involves the direct contact of the U-Mo material with various potential contaminants such as graphite, parting agents and vacuum pump oil. Further, the applied heat treatments lead to the formation of uranium oxide layers on the surface of the U-Mo foils. Therefore, a thorough cleaning procedure is required to remove surface contaminants from the fabrication process as well as the uranium oxide layer.

The most commonly used approach to dissolve uranium oxides is the immersion in HNO₃ (nitric acid) [179]. While this technique is efficient in removing uranium oxides, it also strongly attacks the surface of the bulk U-Mo, leaving a rugged surface [67]. Therefore, an alternative cleaning solution with H₂O₂ (hydrogen peroxide) in an alkaline environment was developed [10,67]. The cleaning effect of this solution is based on the oxidation of UO₂ (uranium oxide) by H₂O₂ to form the soluble uranyl cation UO₂²⁺:



While in neutral solutions, the ongoing oxidation reactions produce the hardly soluble UO₄ (uranium peroxide), an alkaline environment promotes the formation of easily soluble hydroxo and peroxy compounds:



Compared to nitric acid, this cleaning solution only lightly attacks the underlying bulk U-Mo and therefore, the reoxidation speed is reduced significantly.

Further studies and optimizations [11] have led to the cleaning process which will be used within this thesis. Here, H₂O₂ is combined with the industrial alkaline cleaning agent SurTec 138 [177]. Besides KOH (potassium hydroxide) as alkaline component, it contains various phosphates and salts of organic acids and therefore allows the removal of fatty, organic contaminants. The ideal mixture for the U-Mo

cleaning solution was found to be 15 vol.% SurTec 138, 10 vol.% H₂O₂ (30 vol.% concentrated) and 75 vol.% distilled water.

The cleaning solution is prepared in a suitable glass vessel and the substrates are immersed into this solution under continuous stirring. After 5 minutes the substrates are checked visually by eye and, if their surface appears metallic-silver, transferred into a second glass vessel with distilled water, where they are immersed again for 1 minute under continuous stirring. The last step is repeated once before the substrates are placed on a lint-free tissue and dried by blowing with dry argon from the laboratory media supply.

3.2.2 SAMPLE PREPARATION FOR CHARACTERIZATION

From the samples produced within this thesis, essential information can be gathered via microscopy of cross-sections. Examples are the characterization of the deposited Zr layer or the dimensional and microstructural analysis of gradient foils.

Zr-coated samples

Figure 62 schematically shows the preparation process for Zr-coated samples. In this thesis, such samples range from micro-size (10.3 mm x 9.5 mm) to full-size (762 mm x 45 mm) geometry. For most sizes, only a small portion of the samples can therefore be reasonably prepared for the characterization of the deposited Zr layer. Once the location of the cross-section of interest is identified, the sample is sectioned into smaller pieces until the cross-section of interest is fully exposed. To avoid strong microstructural damage to the samples due to deformation, the sectioning process starts with the removal of the large non-interesting areas by rough methods such as hand shearing and ends with gentle methods such as slow turning cutting discs. The exposed sample piece is then vertically mounted into a cylindrical mold with 30 or 40 mm diameter, which is filled with a transparent epoxy resin such as Struers EpoFix. After the curing time of the epoxy resin has passed, it is removed from the mold and grinded and polished using the semi-automatic grinding and polishing machine ATM Saphir 520. By optical microscopy, the preparation quality is checked after each grinding and polishing step until the desired quality level is reached and the preparation is finished. For the preparation of stainless steel and U-Mo samples with Zr coating, the grinding and polishing recipe in Table 8 was developed. The utilized discs, sample pressing forces and preparation times are given for 30 mm mounts and shall be seen as a general recommendation which may be altered during the sample preparation process as needed.

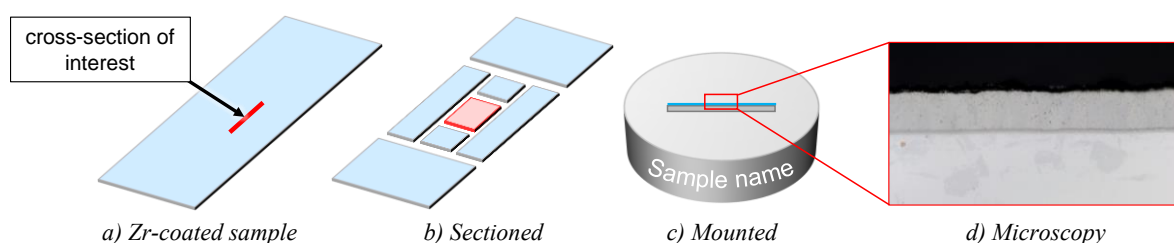


Figure 62: Preparation of Zr-coated samples. From the sample (a), the cross-section of interest is exposed by sectioning (b) and mounted into transparent epoxy resin (c). By microscopy of the cross-section (d), the deposited Zr layers can be characterized.

Table 8: Grinding and polishing recipe for Zr-coated samples. The utilized discs, sample pressing forces and preparation times shall be seen as a general recommendation which may be altered during the sample preparation process as needed.

Step	Grinding/ polishing surface	Lubricant/ suspension	Time [min]	Pressing force [N]	Rotation* speed [rpm]
Plane grinding (back side)	Bonded diamonds #220 grit e.g. Struers MD-Piano	Distilled water	As needed	20	300 →→
Plane grinding	Bonded diamonds #220 grit e.g. Struers MD-Piano	Distilled water	As needed**	20	300 →→
Fine grinding	Composite material e.g. Struers MD-Largo	9 µm diamond suspension	5 - 10	20	150 →→
Diamond polishing 1	Composite e.g. Struers MD-Largo	3 µm diamond suspension	3 - 5	15	150 →→
Diamond polishing 2	Satin-woven silk e.g. Struers MD-Dur	3 µm diamond suspension	3 - 5	15	150 →→
Diamond polishing 3	Satin-woven silk e.g. Struers MD-Dur	1 µm diamond suspension	2 - 3	10	150 →→
Oxide polishing	Porous neoprene e.g. Struers MD-Chem	0.04-0.25 µm colloidal silica	1 - 2	8	150 →←

*) The arrows indicate the respective rotation directions of the sample head and the grinding/polishing disc

**) To remove the areas damaged by sectioning, at least 3 mm of material is removed before continuing with fine grinding

Gradient foil samples

Figure 63 schematically shows the preparation process for mini-size (82.5 mm x 19 mm) gradient foil samples. Usually, multiple cross-section samples of the entire width need to be taken from each gradient foil to assess the fabrication quality. Therefore, the foil is sectioned into three equidistant equal parts to expose one cross-section at the bottom and two cross-sections in the middle of the foil. To avoid strong microstructural damage to the samples due to deformation, the sectioning process is conducted gently e.g. with slow turning cutting discs. Similar to Zr-coated samples, the foil pieces are then vertically mounted into a cylindrical mold with 30 or 40 mm diameter, which is filled with a transparent epoxy resin such as Struers EpoFix. After the curing time of the epoxy resin has passed, it is removed from the mold and grinded and polished using the semi-automatic grinding and polishing machine ATM Saphir 520. By optical microscopy, the preparation quality is checked after each grinding and polishing step until the desired quality level is reached and the preparation is finished.

A recipe similar to the grinding and polishing recipe for Zr-coated samples in Table 8 is used. Since the gradient foil samples usually are not coated with Zr, it is slightly modified:

- The diamond polishing 3 step is not performed.
- The polishing surface for the diamond polishing 2 step is changed to satin-woven acetate, e.g. Struers MD-Dac.

For the preparation of gradient foil samples with Zr coating, the sample preparation recipe for Zr-coated samples is used.

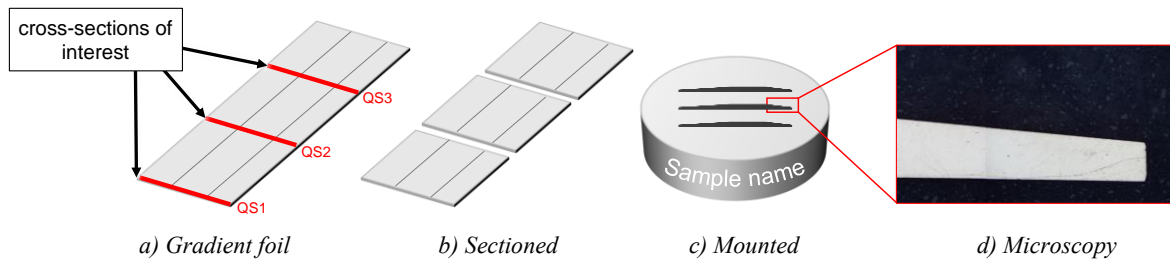


Figure 63: Preparation of gradient foil samples. The foil (a) is sectioned into three equal parts (b) to expose the cross-sections of interest. The sections are then mounted into transparent epoxy resin (c). By microscopy of the cross-sections (d), the shape and microstructure of the sample can be characterized.

Color etching. For the evaluation of the fabrication quality of gradient foils, the microstructure of these samples is important. As the sample preparation recipe described before is not able to reveal the grain structure of stainless steels, a color etching step is applied to these samples. From the many etching procedures given in the literature for austenitic stainless steels [180], the Beraha II color etching is chosen as it gives a strong grain contrast. First, 100 ml of the Beraha II stock solution, usually made of 800 ml distilled water, 400 ml hydrochloric acid (HCl) and 48 g ammonium bifluoride ($(\text{NH}_4)\text{HF}_2$), are mixed with 1 - 2 g of potassium metabisulfite ($\text{K}_2\text{S}_2\text{O}_5$) to produce the etching solution. Then, the polished cross-section is immersed into the solution for 1 - 2 minutes while continuously moving the sample. Afterwards, the sample is thoroughly rinsed with distilled water and dried with dry argon from the laboratory media supply. Figure 64 shows an example of a high-alloy steel etched with Beraha II.

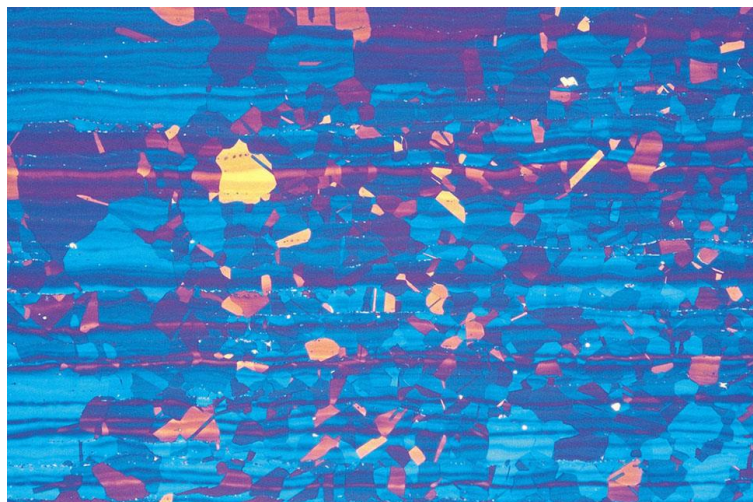


Figure 64: High-alloy steel etched with Beraha II. The color etching reveals the grain structure as well as alloy segregations in the form of horizontal bands. From [180].

3.3 SAMPLE CHARACTERIZATION

After their preparation, the samples can be characterized by various microscopy techniques or by mechanical methods.

3.3.1 MICROSCOPY

The most important tools to characterize the samples are microscopy techniques. Here, the main aspects of interest are the geometry, (micro-)structure, phase composition and the occurrence of interaction layers.

Optical microscopy

For the sample analyses and for the evaluation of the sample preparation quality after each step, an Olympus BX51M optical materialographic microscope, capable of bright-field, dark-field, polarized light and differential interference contrast (DIC) up to 100 x magnification is used. While for most microscopy tasks, the bright-field contrast is sufficient to analyze e.g. the structure of the samples, the dark-field contrast can be used to reveal scratches and pores and polarized light or DIC can be helpful to reveal the microstructure. Figure 65 gives examples of the different contrasts using a Zr-coated U-Mo sample with AlFeNi cladding. Further detailed information on optical microscopy can be found in [181].

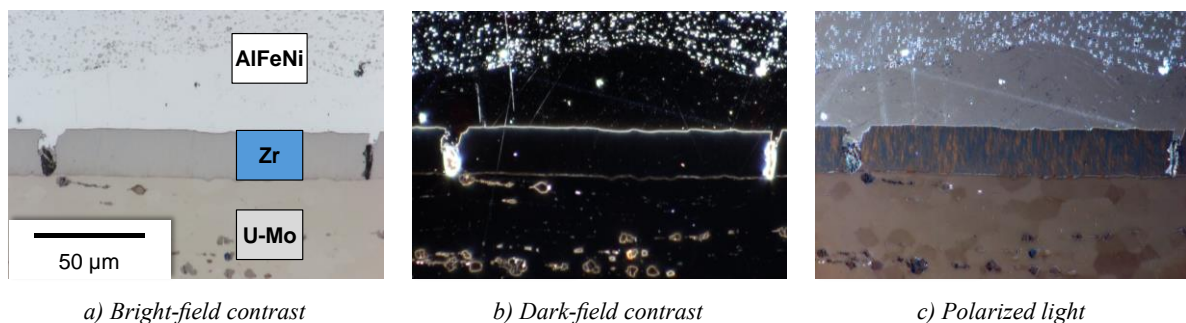


Figure 65: Exemplary optical micrographs of a Zr-coated U-Mo sample with AlFeNi cladding. Dark-field contrast (b) and polarized light (c) can reveal features such as scratches or microstructure, which are not visible with standard bright-field contrast (a). Micrographs from [153].

Scanning electron microscopy

To reach higher magnifications than optical microscopy and to gather additional information on the sample composition, SEM (scanning electron microscopy) is a valuable tool. For this thesis, a ZEISS evo MA 25, equipped with a tungsten cathode, SE (secondary electron) and BSE (backscatter electron) detectors as well as a Thermo Fisher UltraDry EDX (energy-dispersive x-ray) detector is used. The mostly used BSE detector, when operated in composition mode, gives an elemental contrast and heavy elements appear brighter than light elements. With the EDX detector, the identification and quantization of chemical elements is possible. Figure 66 gives examples of the SE and BSE detectors' contrast as well as an exemplary EDX line scan across a U-Mo/Zr interface without an interaction layer. Further detailed information on scanning electron microscopy can be found in [182].

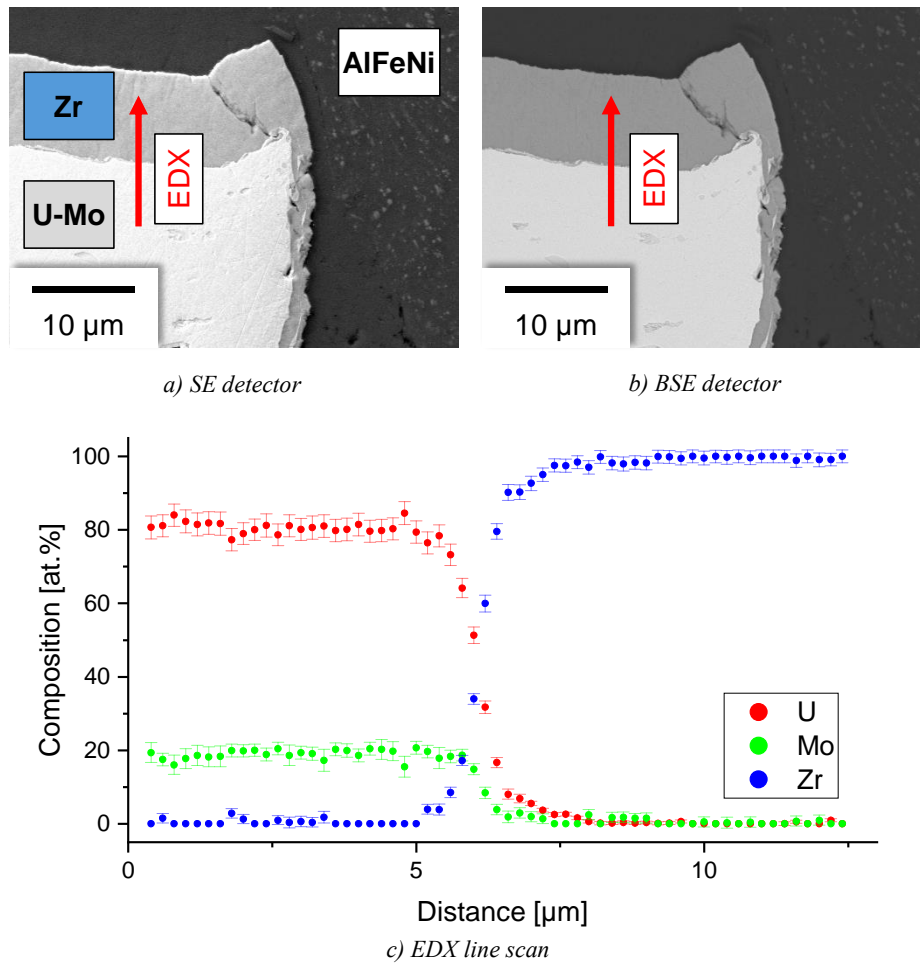


Figure 66: Exemplary SEM micrographs of a Zr-coated U-Mo sample with AlFeNi cladding. While the SE detector gives mostly a topography contrast (a), the BSE detector gives an elemental contrast (b). The EDX line scan (c) reveals the elemental composition profile (e.g. in at.%) along the red line.

3.3.2 MECHANICAL CHARACTERIZATION

The mechanical properties of deposited Zr layers as well as of gradient foils are important for the development of these fabrication processes. Therefore, a valuable tool within this thesis is the hardness measurement using the Vickers method. The result of such hardness testing methods can further give hints on the ductility, strength and wear-resistance of materials. Additionally, the ductility of Zr layers is tested directly using a specially developed bending method.

Vickers hardness testing

The hardness is defined as a material's resistance against the impression of a hard indenter into a softer material. The Vickers hardness testing method is a standardized method according to DIN EN ISO 6507 and is commonly used for hardness testing of metals and coatings [183,184]. Hereby, a pyramidal indenter of a hard material – typically diamond – is pressed onto the surface of the sample with a defined force. From the average diameter d of the indentation, measured using an optical microscope, and the pressing force F , the Vickers hardness HV is calculated as follows:

$$HV = 0.1891 \frac{F}{d^2} \quad (50)$$

The hardness always must be denoted together with the applied load in kilopond. While higher loads lead to larger indentations and therefore simplify the measurement of the diameter, the load shall be set as small as possible for thin structures. Within this thesis, the Vickers hardness testing method is performed on cross-sections using the Struers DuraScan 20 Vickers hardness tester. The device is operated at its lowest possible load of HV0.01 for deposited Zr layers and at HV1 for bulk materials.

Also, according to the DIN EN ISO 6507 standard, the measurement locations shall be at least 2.5 x their diameter away from the edge of the sample. Hardness values of Zr layers, where the diameter of the indentation is close to the layer thickness, shall thus only be seen as qualitative assessments and not as absolute values. Figure 67 exemplarily shows the result of a Vickers hardness test of a hard Zr layer deposited by PVD.

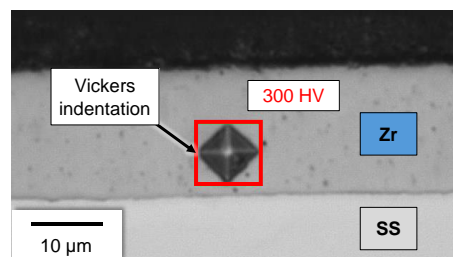


Figure 67: Vickers hardness test of a Zr layer deposited by PVD. The indentation is close to the edge of the sample and the hardness value shall only be seen as qualitative.

Ductility testing by bending

To simulate the behavior of Zr coatings under tensile mechanical stress, as it is expected during the C2TWP cladding application process, their ductility is tested directly. Hereby, sections along the length or width of a Zr-coated substrate are bent twice by 90 degrees around a defined radius of 3 mm. Similar to the sample preparation processes described before, the bent samples are mounted in epoxy resin, grinded and polished until the cross-section can be examined by microscopy. The compressive and tensile stresses induced into the deposited Zr layer by this bending test are assumed to be significantly higher than the stresses from the cladding application process. Thus, if a sample passes the test with little or no crack formation, no cracking of the Zr coating is expected during C2TWP.

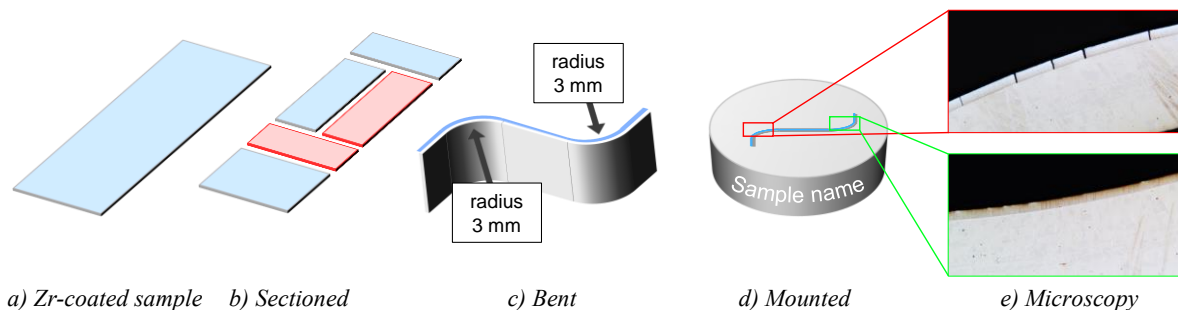


Figure 68: Preparation of bending test samples. The samples (a) are sectioned along their length or width (b) and bent twice by 90 degrees around a radius of 3 mm (c) to introduce compressive and tensile stresses into the Zr layer. After mounting (d), grinding and polishing, the cross-section can be examined by microscopy (e). Micrographs from [14].

4 FABRICATION DEMONSTRATION OF GRADIENT FOILS

A measure to reproduce the density step of the current disperse U_3Si_2 fuel of FRM II is required for its conversion to a lower enrichment using monolithic U-Mo fuel. One of the proposed methods to do so is to use U-Mo foils with a thickness gradient along their width – gradient foils – instead of flat U-Mo foils inside the fuel plates.

As no fabrication process for such gradient U-Mo foils is currently available worldwide, a first-of-a-kind demonstration of the fabrication of such gradient foils and fuel plates made thereof was performed using surrogate materials.

4.1 GRADIENT FOIL GEOMETRIES

Gradient full-size geometry

From neutronic and thermal-hydraulic calculations, a preliminary design for gradient U-Mo foils for the conversion of FRM II, which also features a reduced thickness at the inner side of the foils to compensate the high neutron flux near the central channel of the fuel element, was proposed by Breitzkreutz [30]. To be compatible with the full-size fuel geometry of European irradiation tests (762 mm x 45 mm), it was scaled to this geometry and Figure 69 shows the resulting preliminary gradient full-size geometry. The geometrical tolerances of the foils were set to match the tolerances in the current FRM II fuel element, adapted to monolithic U-Mo.

Gradient mini-size geometry

A gradient full-size U-Mo foil in this preliminary geometry has a total mass of 316.0 g. When fabricating such a gradient foil out of a flat foil with rectangular cross-section, the material loss would be 36.4 g or approximately 10 %. Therefore, to reduce cost and material usage and to facilitate the early experiments, this geometry was scaled down to a gradient mini-size geometry, while keeping the gradient angles of 2.74° at the long gradient and 4.83° at the short gradient, respectively. Hereby, mini-size corresponds to the typical fuel geometry of mini-size irradiation tests like EMPIrE (82.5 mm x 19 mm). Figure 70 shows the resulting preliminary gradient mini-size geometry.

Material loss calculation

Table 9 shows the expected volume and mass of nominal gradient full-size and mini-size U-Mo foils. Additionally, the volume and mass of corresponding nominal flat U-Mo foils with rectangular cross-section are given, together with the estimated material loss when fabricating the gradient foils out of flat foils. As can be seen about 10 % of the material must be removed to fabricate a gradient full-size foil. For the gradient mini-size geometry, the material loss is about 24 % due to the smaller foil width in

relation to the gradients. This table underlines the fact that material efficiency and potential material recovery measures are key factors when considering fabrication processes for gradient U-Mo foils.

Table 9: Material loss calculation for the gradient full-size and mini-size foil geometries. The values were calculated from the geometries in Figure 69 and Figure 70.

Nominal geometry	Gradient U-Mo foil		Corresponding flat U-Mo foil		Material loss
	Volume	U-Mo mass	Volume	U-Mo mass	
Full-size	18.45 cm ³	316.0 g	20.57 cm ³	352.4 g	36.4 g (~ 10 %)
Mini-size	0.71 cm ³	12.2 g	0.94 cm ³	16.1 g	3.9 g (~ 24 %)

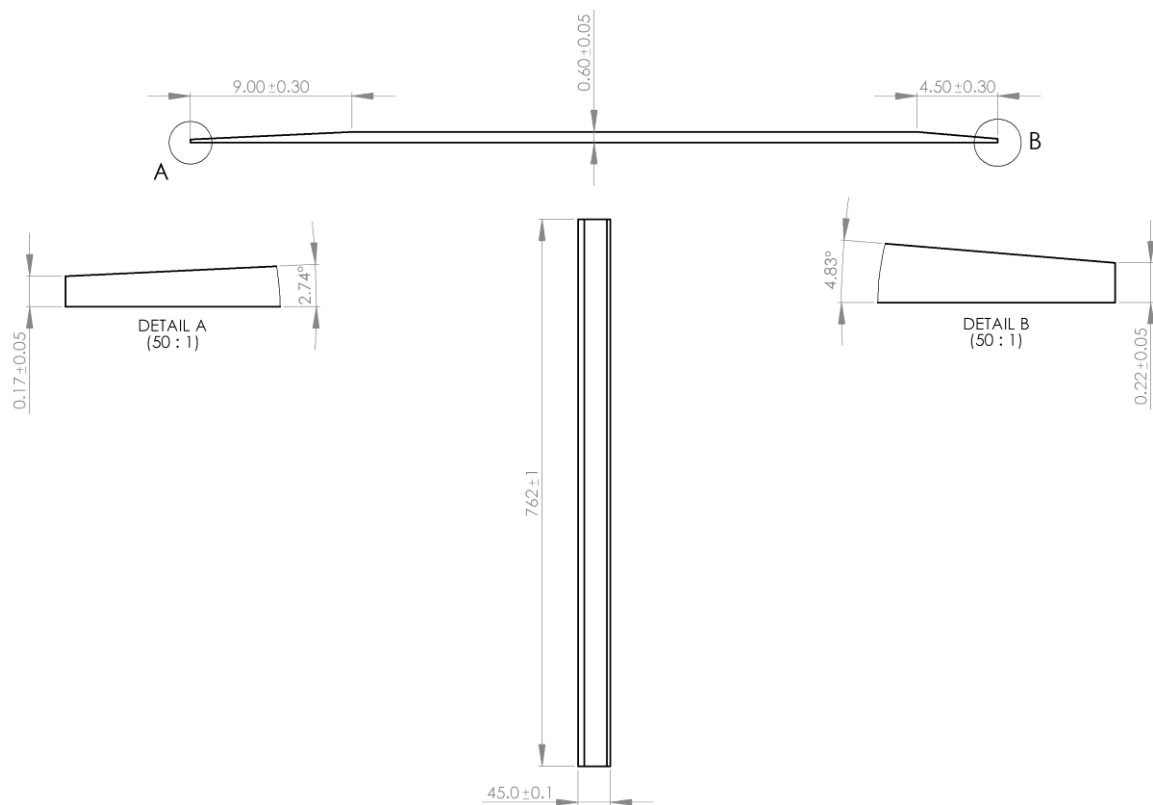


Figure 69: Preliminary gradient full-size geometry. This design is derived from neutronic calculations for gradient U-Mo foils for the conversion of FRM II [30]. All dimensions in mm.

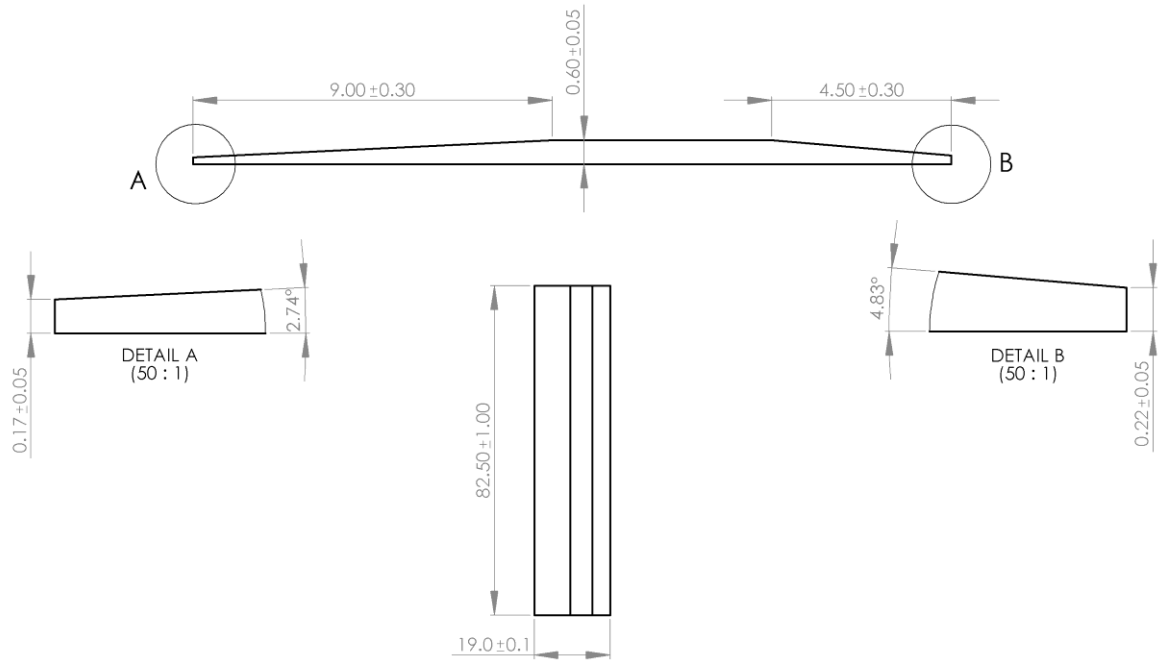


Figure 70: Preliminary gradient mini-size geometry. This design is derived from the full-size geometry in Figure 69. All dimensions in mm.

4.2 FABRICATION PROCESSES

4.2.1 PROCESS REQUIREMENTS

A fabrication process for gradient U-Mo foils must meet certain requirements to be suitable for the industrial fabrication of monolithic U-Mo fuels for research reactors:

Precision. The process must be able to reach the tolerances given in the drawings in Figure 69 and Figure 70. These tolerances are based on the tolerances in the current FRM II fuel element. It can be expected that the tolerance requirements for future FRM II fuel plates using monolithic U-Mo will be similar or stricter than the current ones.

Compatibility. The gradient foils fabricated by the process must be compatible with the subsequent fabrication steps of PVD coating and C2TWP cladding application. If needed, adaptations or optimizations of these processes for gradient foils are acceptable.

Material efficiency. Due to the use of the expensive material U-Mo, it is crucial to reduce the material loss of any fabrication step to an absolute minimum.

Scrap handling. If any U-Mo scraps are produced during the fabrication process of a gradient foil, it should be possible to reuse or recycle these scraps. This requirement especially implies that the scraps should exist in a form which easily allows their collection and, ideally, direct reuse for the same process. If a direct reuse is not possible, it should be possible to insert these scraps into a previous process step, e.g. as raw material for the casting of U-Mo ingots.

Safety and health aspects. Due to the pyrophoricity of U-Mo, especially in forms with high surface-to-volume ratio like fine powders or cutting chips, particular care needs to be taken to avoid metal fires during the fabrication process. Additionally, the direct physical contact of the process operating personnel with radioactive material must be avoided to reduce the risk of incorporation. Such protection against metal fire and incorporation can typically be accomplished by setting up the process in a glovebox with a controlled inert atmosphere. This, however, implies that the process must be compatible with such an inert atmosphere and be implementable into a glovebox.

Criticality. As the process will later be used to fabricate U-Mo foils from enriched uranium, it must be ensured that no nuclear criticality events can occur. This implies that no critical mass of fissile uranium-235 can be accumulated and that the use of neutron moderators like water in proximity to the U-Mo material should be reduced to an absolute minimum.

Figure 71 shows general categories and examples of possible processes to fabricate gradient U-Mo foils: *subtractive manufacturing*, *additive manufacturing* and *forming*. Since forming processes like pilger rolling [44] and extrusion [45] were already developed up to a certain extent at US National Laboratories for the fabrication of gradient foils for the conversion of HFIR, this thesis will focus on the two former categories.

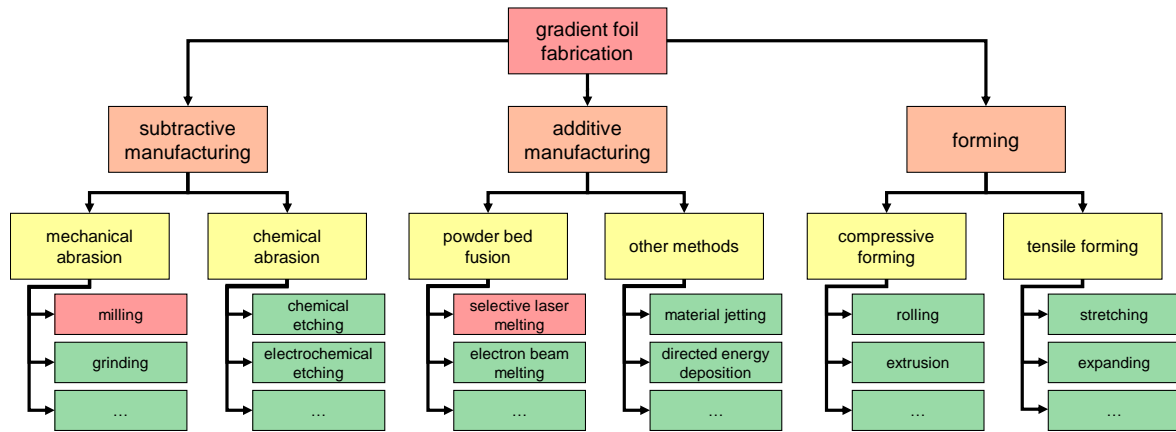


Figure 71: Categories and examples of fabrication processes for gradient foils. Out of the possible processes, this thesis will demonstrate the fabrication of gradient foils using milling and selective laser melting (highlighted in red).

4.2.2 MILLING

The first method investigated to achieve the gradient foil geometries is subtractive manufacturing, i.e. the removal of excessive material from flat foils with rectangular cross-section, as shown in Figure 72.

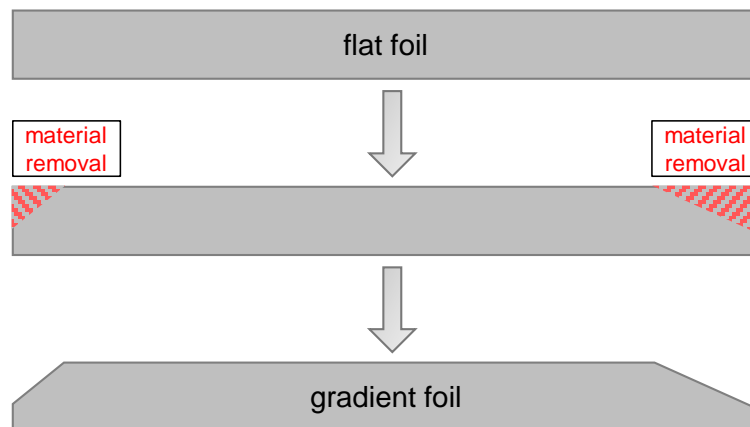


Figure 72: Sketch of subtractive manufacturing processes. Starting from flat foils with rectangular cross-section, the gradient foil geometry is achieved by removing excessive material at the edges.

Subtractive manufacturing processes can be divided into processes with mechanical and chemical abrasion. As the material removal due to chemical reactions is highly specific to the material used, no meaningful evaluation of these processes can be performed using surrogate materials. From the wide variety of mechanical abrasion processes, classical milling was selected as the process of choice for this thesis. Milling is a common industrial process for the fabrication of parts from single units to mass fabrication. By a thorough process planning, trained personnel and by using well-calibrated precision milling machines, the specification-conform fabrication of small to large complex parts with tight tolerances is possible from almost any material, especially metals. So-called *CNC* (computerized numerical control) milling machines, which are commonly found at industrial fabricators, allow the fully automatic fabrication of parts without any physical contact of the personnel with the part. In the following, a brief description of the milling process is given up to an extent necessary to assess the suitability of this process for the fabrication of gradient U-Mo foils and to understand the subsequent

demonstration experiments. A complete description of the milling process can be found in the relevant literature, for example in [185].

By milling, material is removed from a work piece by forcefully bringing it into contact with a cutting tool at a certain *cutting depth*, as shown schematically in Figure 73. The *wedge* – the sharp edge of the cutting tool – penetrates into the material of the work piece and first deforms it elastically. After reaching the yield point, the actual cutting process takes place at the *shear plane* by plastic deformation and the material is sheared off from the work piece under the *shearing angle*, so that a *cutting chip* is generated. As shown exemplarily for steel in the figure, high temperatures up to several hundred °C can occur in the cutting tool but also at the shear plane of the work piece and in the cutting chip. By a high speed of motion of the cutting wedges – usually generated by a continuous rotation of a cutting tool with multiple cutting wedges – and by continuously moving the work piece in relation to the cutting tool at a high *feed rate*, the fast removal of large amounts of material is possible.

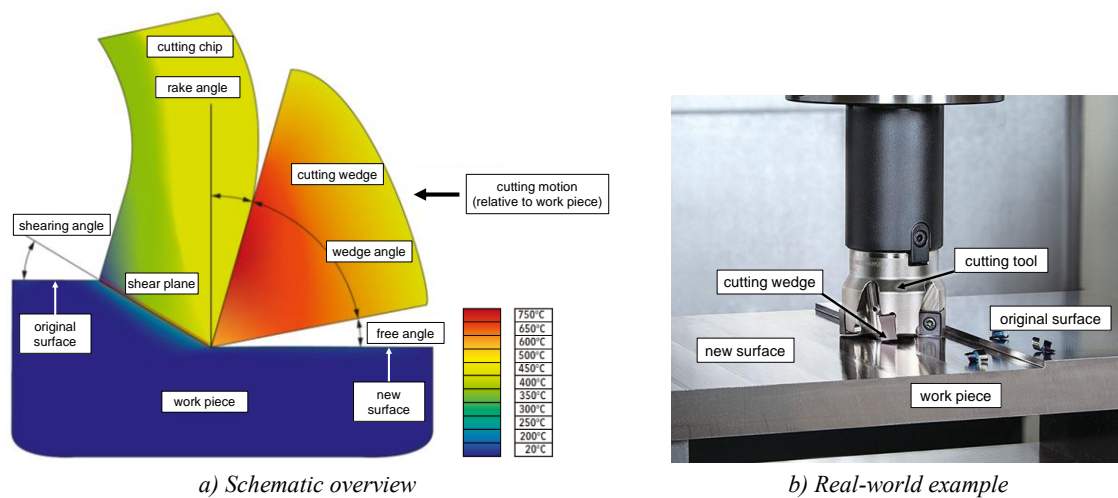


Figure 73: Scheme and example of the milling process of steel parts. The cutting wedge penetrates into the work piece and removes material by shearing it off. A new surface, lower than the original surface, is created. After [186,187].

The two most common general forms of milling are *peripheral milling* and *face milling*, as depicted in Figure 74. By peripheral milling, the material of the work piece is removed by the cutting wedges on the sides of the rotating cutting tool cylinder and the feed motion of the work piece can be parallel or antiparallel to the rotation direction. By face milling, in contrast, the rotational axis of the cutting tool cylinder is in the normal direction of the work piece surface. For the generation of plane surfaces, like it is required for the fabrication of gradient foils, face milling is usually the method of choice.

For the fabrication of a specific part, the planning of the milling process and its associated parameters plays a crucial role. Via an iterative process, the process input parameters such as the geometry and material of the cutting tool, its rotation speed, the work piece feed rate, the cutting depth and the cutting path are optimized until the final product meets the pre-defined requirements such as geometrical accuracy and finish quality of the cut surfaces. Furthermore, the wear of the cutting tool, the form and size of cutting chips as well as economic and process time provisions need to be considered.

To reduce the friction between the cutting tool and the work piece, and therefore to reduce their temperatures and to extend the service life of the cutting tool, a cooling lubricant – usually consisting mainly of water and lubricating oils – can be continuously applied. Such a cooling lubricant can also support the washing away of chips, absorb fine dust and improve the geometrical accuracy and finish quality of the cut surfaces.

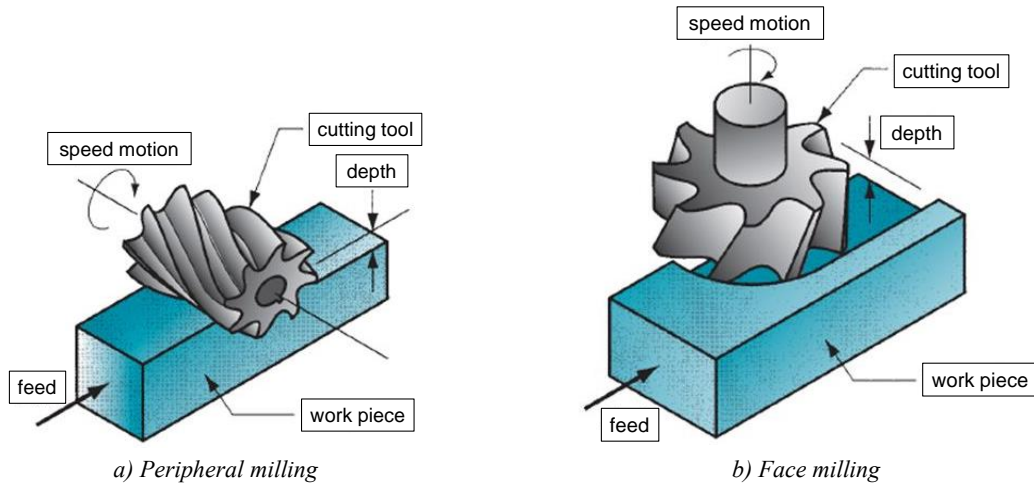


Figure 74: Schematic view of the two most common general forms of milling. While the work piece is continuously moved under the rotating tool at a defined feed rate, the material removal can be either performed by the sides of the cutter (a) or by its face (b). After [188].

In industrial milling processes of inexpensive standard materials, the collection and recycling of scraps – the produced cutting chips – is usually not considered since the cost of these additional operations usually exceeds the cost of the lost material. However, for the milling of costly materials like U-Mo, customized housings can be built around the work piece to collect most of the scraps. As the cutting chips undergo strong plastic deformation and can reach temperatures of several hundred °C, their microstructure is usually strongly different and – depending on the material – oxide layers can be formed. Thus, a chemical cleaning of the scraps should be performed prior to their reuse or recycling.

4.2.3 SELECTIVE LASER MELTING

Another method investigated to achieve the gradient foil geometries is additive manufacturing. Hereby, small parts of the desired material in either liquid, solid or powder form are subsequently added together onto a build plate, from where the final part is later removed. This is illustrated in Figure 75.

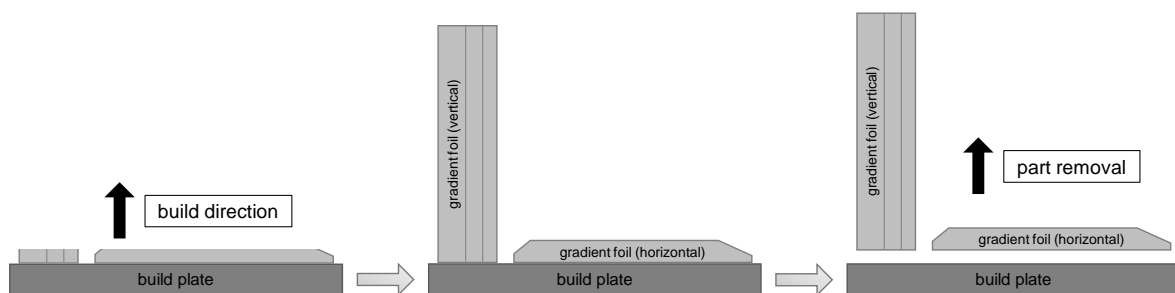


Figure 75: Sketch of additive manufacturing processes. The desired material is subsequently added together onto a build plate before the final part is removed from it.

There are many ways to categorize additive manufacturing processes, e.g. by the physical form of the source material or by the type of energy to add the material together. A comprehensive overview of the various additive manufacturing processes can be found in [189]. The most common and well-understood process types for metals are powder bed fusion processes, where the part is built by selectively melting fine powder, layer by layer, using typically either a laser or an electron beam. Hereby, the smallest achievable feature size, i.e. the smallest tolerance, is limited by the diameter of the powder particles and by the size of the melting spot. Due to its significant precision advantage compared to *EBM* (electron

beam melting), this thesis will focus on *SLM* (selective laser melting), the most common powder bed fusion process available today. In parallel, the fuel fabricator Framatome-CERCA together with *UTBM* (Université de Technologie de Belfort-Montbéliard) recently have conducted feasibility studies of the SLM process with the final material U-Mo [190]. In the following, a brief description of the SLM process is given up to an extent necessary to assess the suitability of this process for the fabrication of gradient U-Mo foils and to understand the subsequent demonstration experiments. A complete description of the SLM process can be found in the relevant literature, for example in [189,191].

As shown schematically in Figure 76, an SLM device generally consists of an infrared laser source and scanning mirrors to deflect the laser beam to the areas to be molten, a build platform, one or more feed cartridges with the metal powder, and a levelling roller or rake to apply a thin layer of powder after each layer. Optionally, the entire powder bed can be pre-heated, e.g. via an infrared heater. Once the SLM device is set up properly, the build process runs entirely automatic. First, the 3D geometry of the part to be built is divided vertically into thin a few 10 μm thick slices by the software of the SLM device. Then, a thin layer of powder is applied to the base plate and the laser beam locally melts the shape of the first slice, fusing it to the build plate where it immediately re-solidifies. In a continuous process of usually several thousand passes, the build platform is then lowered a few 10 μm , another thin layer of powder is applied on top of the powder bed and the next slice is built in the same way.

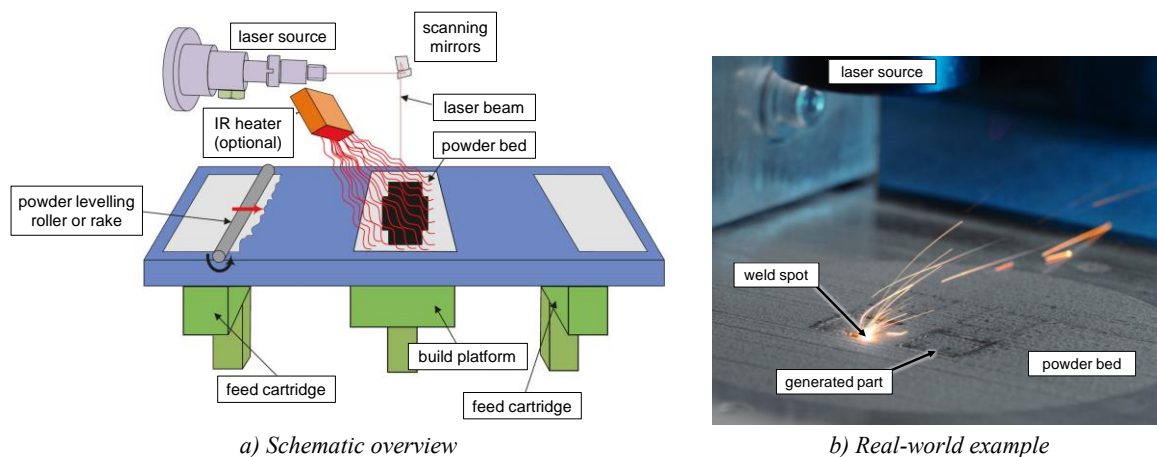


Figure 76: Scheme and example of the SLM process. On the surface of a metal powder bed, a laser beam locally melts the powder to generate a thin slice of solid metal. After each pass, the build platform is slightly lowered, a thin layer of new powder is applied, and the melting process is repeated so that the slices are welded together. After [189].

The shape of each individual slice is usually scanned in a pattern of straight lines, in which the powder is fused together by the energy introduced by the laser beam, as shown in Figure 77 a. This process is called *hatching*. The melting path consists of a central *fusion zone*, where the material is entirely molten and fused together, surrounded by a *heat-affected zone*, which gets warmed by radiation or heat conduction, but not or only partially molten. To fuse the individual slices together, the depth of the *melt pool*, which is shown in Figure 77 b, is higher than the thickness of the powder layer, so that the previously solidified layers below are partially re-molten as well.

Once the build process of a part is finished, usually after several hours of unattended device operation, the build plate is removed from the powder bed and any adhering powder is brushed off carefully. Because the part is firmly fused to the build plate or a carrier structure, it needs to be removed from it by an appropriate technique, like e.g. the commonly used wire spark erosion.

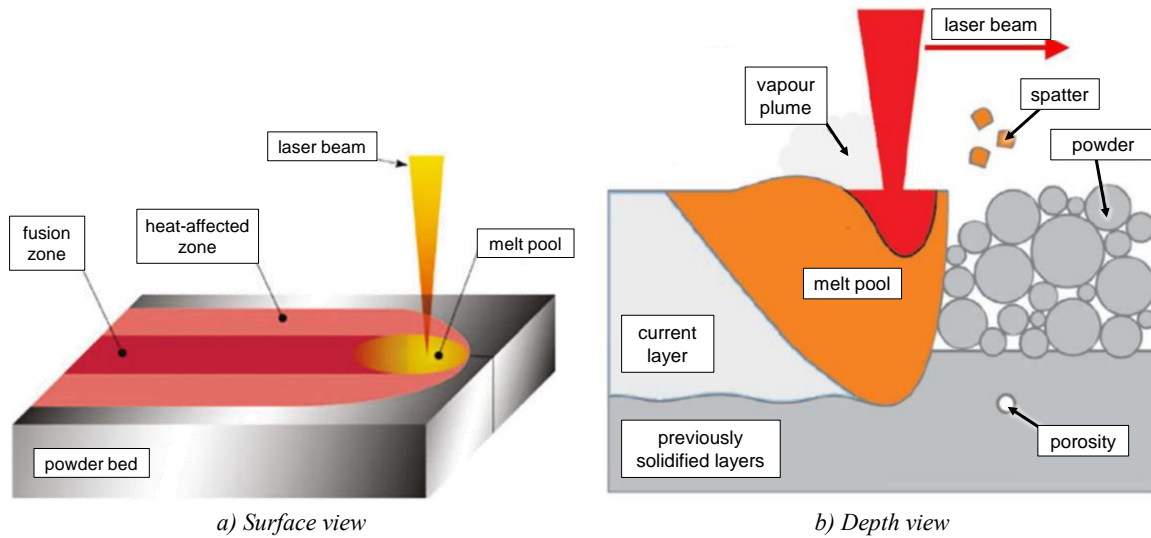


Figure 77: Schematic view of the laser melting process. The laser beam is directed in straight lines across the powder bed and leaves traces of solidified metal behind (a). The so-generated layers are fused together with the previously solidified layers by partially re-melting them as well (b). After [191,192].

The success of an SLM process and the quality of the final part, i.e. its porosity, surface roughness, microstructure and material homogeneity, and therefore its mechanical and physical properties, are defined by many input parameters. This includes the general build setup, the properties of the metal powder and process-specific parameters. For example, the orientation of the part on the base plate as well as the potential use of support and carrier structures around and below the part greatly influence, if a build process can be completed successfully or is aborted prematurely, e.g. due to a rupture of the part. Also, the shape and size distribution of the metal powder as well as its material properties, like e.g. its thermal conductivity, melting point, heat of fusion and optical absorptance need to be considered. The process-specific parameters such as the power, scan speed and spot size of the laser, the slice thickness and the distance in between individual melting paths are usually pre-defined for each material by the manufacturer of the SLM device and thus do not need to be altered for most applications. However, when building parts with a special geometry or from a special material, the pre-defined parameters usually need to be changed or an entirely new set of parameters needs to be developed.

In case the quality of the final part does not meet the pre-defined requirements, even with optimized process parameters, the application of post-production treatments is a common method to improve the quality and ultimately achieve a specification-conform part. The most common techniques, which will also be used within this thesis, are:

Abrasive blasting or shot peening. *Abrasive blasting*, as shown schematically in Figure 78 a, is a common post-production treatment for additively manufactured parts, which aims at removing surface contaminants and sticking powder particles as well as at smoothing the surface. Hereby, a stream of abrasive material is propelled under high pressure, e.g. by compressed air, against the surface of the part, where substantial amounts of material can thus be removed. Alternatively, *shot peening* can be used, as shown schematically in Figure 78 b. By this cold working process, the surface of the part is modified by plastic deformation from impinging spheric metallic or glass particles, which are similarly propelled under high pressure. Due to the roundness of the particles, the surface is smoothed not by abrasion but by compressing the material and pressing in adhering powder particles. Obviously, this process introduces compressive residual stresses into the surface, which may even be beneficial for some

applications. More information on shot peening and its use for additively manufactured parts can be found in [193,194].

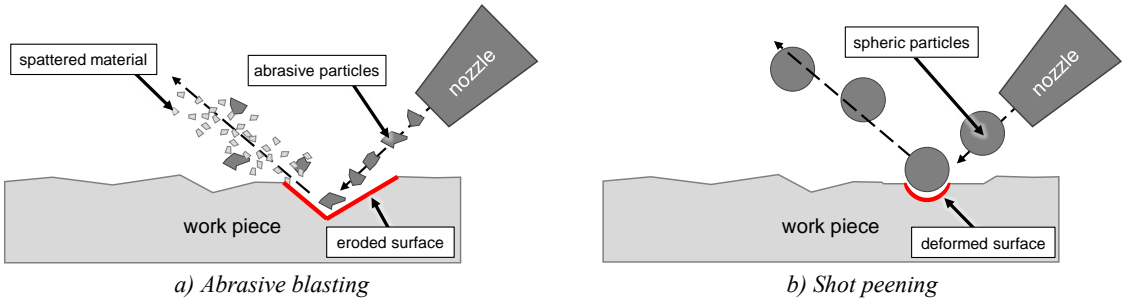


Figure 78: Schematic views of abrasive blasting and shot peening. While abrasive blasting aims at smoothing the surface via removing material by abrasive particles (a), shot peening aims at smoothing the surface solely via plastic deformation (b).

Hot Isostatic Pressing. To reduce inner porosities and to modify the microstructure of additively manufactured parts, *HIP* (hot isostatic pressing) is a common post-production treatment. Hereby, the parts are inserted into a pressure-resistant vessel, which is then heated and filled with an inert gas under high pressure. By the combined application of high temperatures and high external isostatic pressures to the part, inner porosities are eliminated via plastic deformation, creep and diffusion bonding. If the process time and temperature are set high enough, the process can also lead to a full recrystallization of the grain structure, resembling then the microstructure of annealed bulk material. Figure 79 schematically depicts a HIP device. More information on the effects of HIP on stainless steel parts built by SLM can be found in [195].

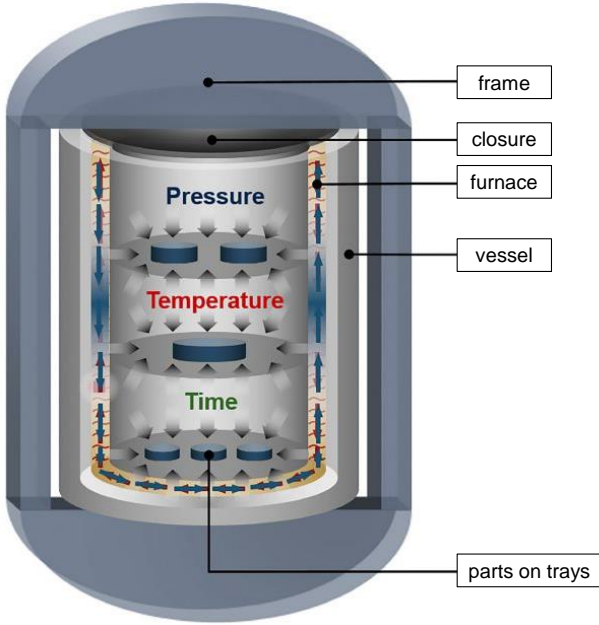


Figure 79: Schematic view of a HIP device. The parts are inserted into a high-pressure vessel, where they are kept at high temperature and high external pressure for a certain amount of time. After [196].

In theory, the SLM process has a material efficiency of 100 %, since only the powder material necessary to build the part is molten together and the powder from the powder bed can be reused. In reality though, many non-neglectable sources of material loss need to be considered. For example, some powder

particles may get sucked into the filters of the ventilation system of the build chamber or may spatter or even get vaporized at the point of impact of the laser beam. Also, some powder particles typically adhere to the surface of the built part or may be partly sintered together in the heat-affected zone of the melting path. The mechanical removal of the part from the base plate as well as potential abrasive post-production treatments can furthermore decrease the material efficiency. A detailed classification and quantitative investigation of the various material losses in SLM processes can be found in [197].

4.3 FABRICATION DEMONSTRATION OF GRADIENT FOILS BY MILLING

The fabrication of gradient foils by milling was demonstrated in mini-size and full-size geometry using the surrogate materials stainless steel AISI 316L and titanium alloy Ti-6Al-4V.

The mini-size fabrication study aimed at demonstrating that the fabrication of gradient foils out of flat foils is technically feasible using commercial milling equipment. The produced samples were characterized in detail to evaluate their surface and geometrical quality as well as the microstructure.

The full-size fabrication study aimed at an upscaling of the mini-size process, while collecting the cutting chips and also including the more challenging material Ti-6Al-4V, which resembles the mechanical properties of U-Mo more closely than stainless steel.

4.3.1 MINI-SIZE

For the mini-size fabrication study, 100 flat foils of stainless steel AISI 316L were procured from Goodfellow GmbH with nominal dimensions of 82.5 ± 1 mm x 19.0 ± 0.1 mm x 0.60 ± 0.05 mm. Assuming the bulk materials' density, the nominal mass of such foils is 7.477 ± 0.192 g. Before milling, the flat foils were measured using a caliper to confirm that they are within the geometrical tolerances claimed by the supplier. On the 48 foils, which were finally used to fabricate gradient foils, average dimensions of 82.59 mm x 18.98 mm x 0.64 mm were measured. The average length and width thus only deviate ~ 0.1 % from the nominal values and a small systematic over-thickness of ~ 6.7 % was found.

Fabrication

The milling process was performed in cooperation with the industrial partner H-TEC Präzisionstechnik GmbH (Grambach/Graz, Austria) at their workshop. As illustrated schematically in Figure 80, the flat foils are held by vacuum on a custom-built substrate holder, which features two inclined foil support surfaces at the respective gradient angles 4.83° (for the short gradient) and 2.74° (for the long gradient). Due to the pre-defined gradient angles, only three linear movement axes of the work table are necessary to mill both gradients into the foils and a commercial 3-axis CNC machining center can be used.

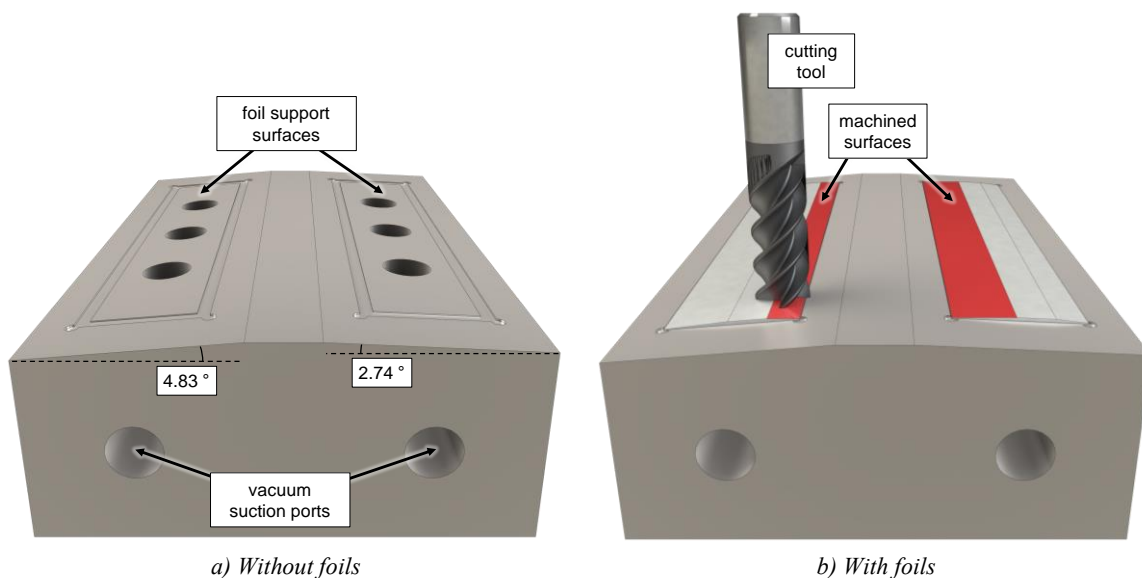


Figure 80: Substrate holder for milling of gradient mini-size foils. The foil support surfaces are inclined at the respective gradient angles 4.83° and 2.74° . The substrate holder is screwed to the work table of a 3-axis CNC machining center.

Via an iterative process, the fabrication parameters were optimized to improve the precision and uniformity of the milled gradients as well as the robustness of the process against failures. Finally, a face mill cutting tool with carbide cutting wedges and a diameter of 20 mm at a rotation speed of 3000 min^{-1} was used and the feed rate was set to 200 mm/min. To mill with the greatest care possible, cooling lubricant was used and the milling of each gradient was performed in two passes, each of them at half of the required cutting depth. Using this parameter set, a total of 48 gradient mini-size foils were fabricated. Two of them slipped out of the substrate holder during milling, presumably due to fluttering and insufficient vacuum suction, and were thus rejected.

Figure 81 shows the mass distribution of the 46 fabricated gradient foils and the original flat foils. By dimensional inspection using a caliper and a measurement microscope, eight of the gradient foils were found to exceed the tolerance of $4.50 \pm 0.30 \text{ mm}$ on the width of the short gradient. The reason for this result is explained in Figure 82. The gradient angles are very small and pre-defined by the substrate holder design, and the foil thickness at the gradient edges is pre-defined as well. Thus, any over-thickness of the flat foils automatically increases the width of the gradients, possibly exceeding the tolerances.

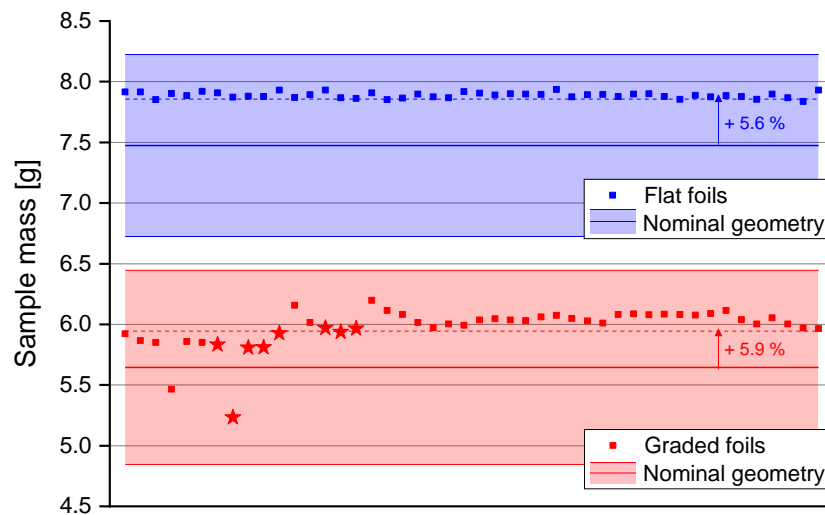


Figure 81: Mass distribution of the gradient mini-size stainless steel foils (milling). While still being within the geometrical tolerances claimed by the supplier, the flat foils show a small systematic over-thickness and are therefore on average 5.6 % heavier than the nominal geometry. Out of the 46 fabricated gradient foils, eight are out of geometrical tolerances (marked with a ★).

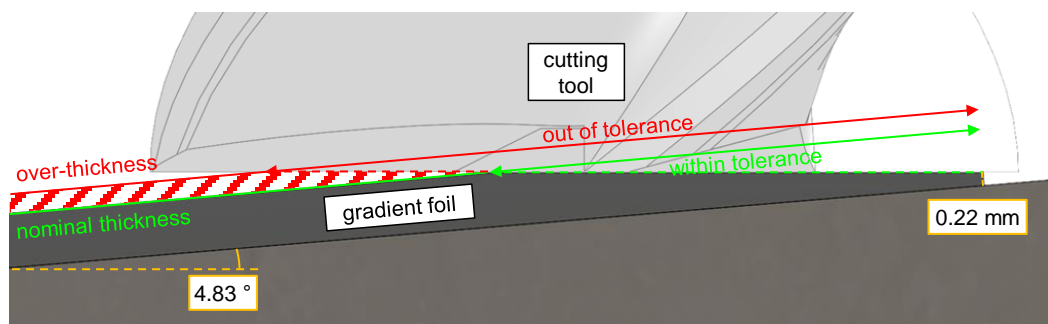


Figure 82: Graphical explanation for the gradient widths being out of tolerance. The gradient angles are very small and pre-defined, and the foil thickness at the gradient edges is pre-defined as well (marked in yellow). Thus, any over-thickness of the flat foils automatically increases the width of the gradients, possibly exceeding the tolerances.

Characterization

Figure 83 exemplarily shows a gradient mini-size stainless steel foil, fabricated by milling. The foil visually appears in good condition with no notable geometrical or other defects. The original surface in the middle as well as both machined surfaces at the gradients appear very regular and shiny. At the machined surfaces, a typical regularly curved milling pattern is visible.



Figure 83: Gradient mini-size stainless steel foil (milling). Both the original and the machined surfaces appear very regular and shiny. The thickness gradients are clearly visible by eye.

This visual appearance is confirmed by surface optical microscopy, as shown exemplarily in Figure 84. The original surface in the middle of the foil exhibits a typical rolling pattern and some dark spots, which presumably are inclusions from the fabrication process. The machined surface shows a regularly curved milling pattern, which results from the material removal by the cutting wedges.

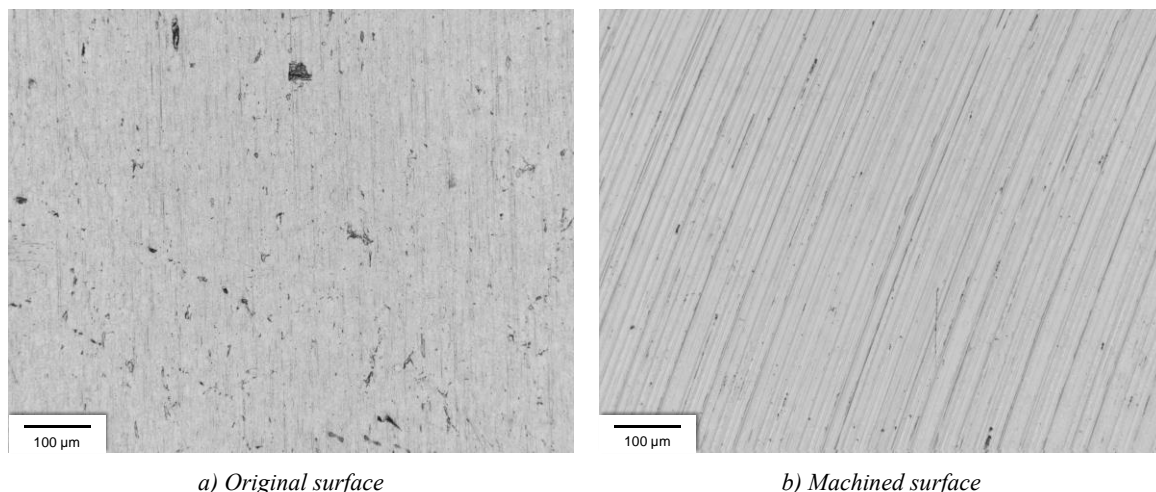


Figure 84: Exemplary surface optical micrographs of gradient mini-size stainless steel foils (milling). The original surface shows a typical rolling pattern and some dark spots, whereas the machined surface shows a regularly curved milling pattern.

Exemplary cross-sections were prepared and the geometrical quality of the foils, the shape of the edges as well as the microstructure were evaluated. Figure 85 shows the cross-sections QS1, QS2 and QS3 at different locations on the same foil. The overview micrographs look very similar without notable defects or geometrical deviations. The edges are free of burrs, chamfers or roundings and the foil thickness at the gradient edges is within the tolerances. At the unmachined middle section, the small systematic over-thickness of the original flat foils is confirmed. By a Beraha II etching of another sample, depicted in Figure 86, a typical but fine-grained austenitic microstructure is revealed throughout the entire cross-section. At the machined gradients, precipitates of martensite in the form of short black stripes are found, which presumably originate from mechanical deformation by the milling process. The martensite precipitates in the center of the foil were found similarly also on original flat foils, hence they do not result from the milling process.

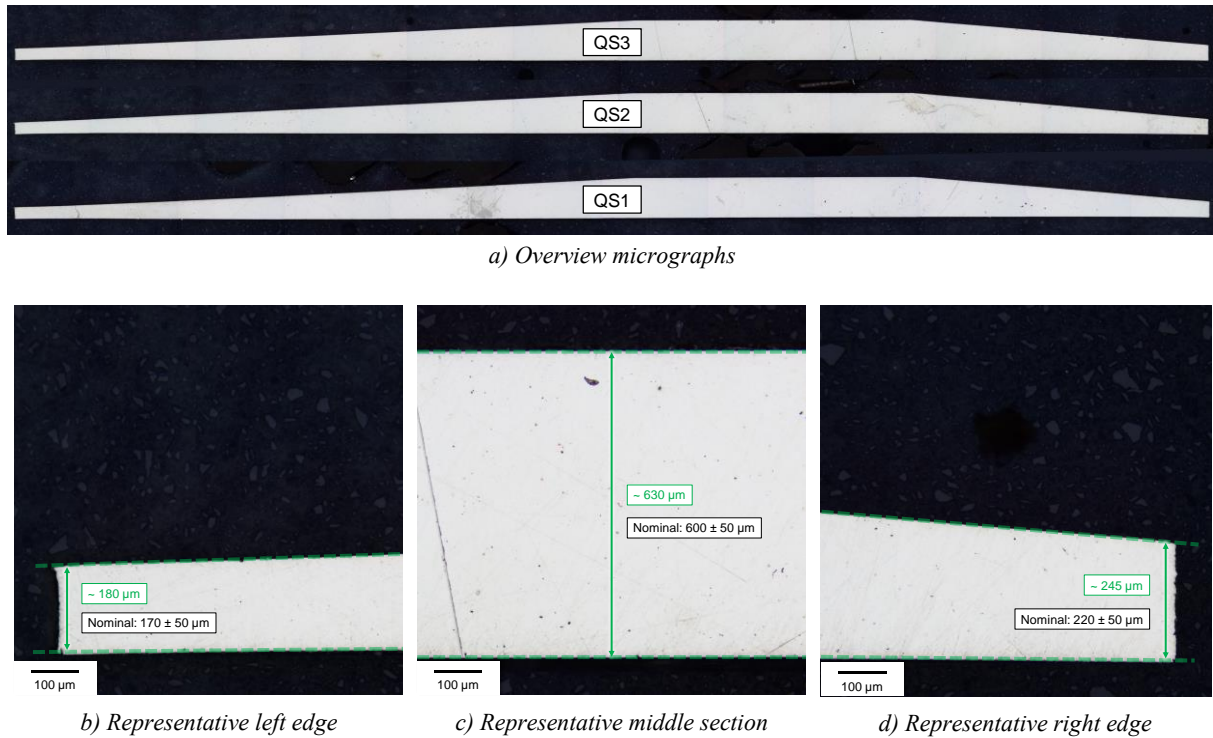


Figure 85: Exemplary cross-sectional optical micrographs of gradient mini-size stainless foils (milling). The three overview micrographs appear very similar without notable defects or geometrical deviations (a). The edges (b, d) are free of burrs, chamfers or roundings and the foil thickness at both gradient edges is within the tolerances. At the unmachined middle section (c), the small systematic over-thickness of the flat foils is confirmed.

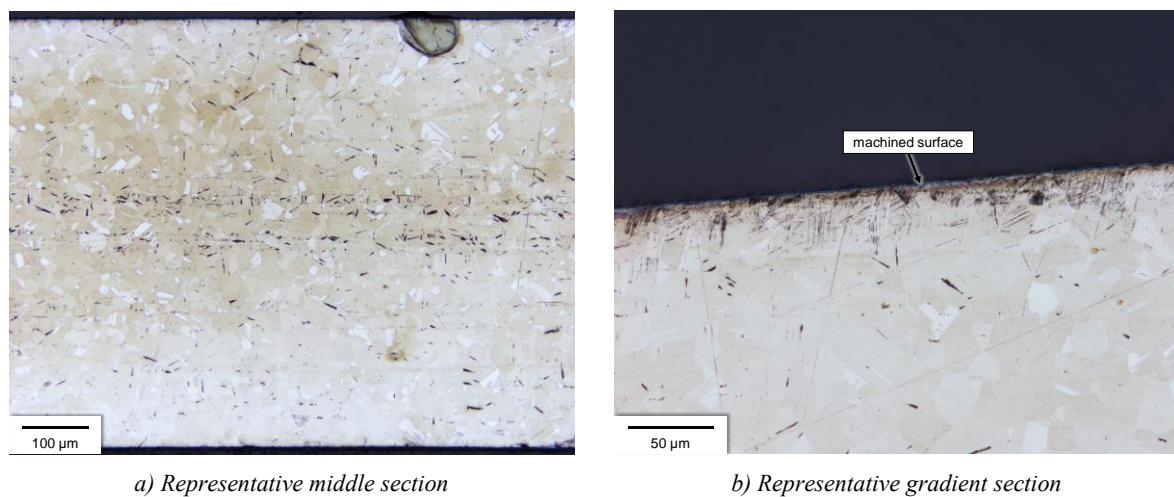


Figure 86: Exemplary cross-sectional optical micrographs of gradient mini-size stainless foils (milling), etched with Beraha II. A typical but fine-grained austenitic microstructure is revealed throughout the entire cross-section. In the center of the foil (a), as well as at the machined gradients (b), precipitates of martensite in the form of short black stripes are found.

4.3.2 FULL-SIZE

Based on the promising results and the experience gained from the mini-size fabrication study, a subsequent full-size fabrication study was performed again in cooperation with H-TEC Präzisionstechnik GmbH. To avoid process failures from fluttering or slipping foils, they are now clamped down via a massive stainless steel bar, screwed to the foil support surface. To be able to collect the cutting chips, the use of cooling lubricant is omitted and the entire substrate holder is fully encapsulated by an aluminum chip collection enclosure. The cutting tool is moving within a small slit in the lid, as depicted in Figure 87. This substrate holder design makes the use of a 5-axis CNC machining center necessary, which is able to horizontally tilt the entire assembly to the respective gradient angles.

After the milling of each gradient, the chip collection enclosure is opened and the chips are swept into antistatic plastic containers using a fine brush. By weighing the foils before and after milling, and by weighing the plastic containers with and without the cutting chips, the chip collection rate can be calculated. After the fabrication of each foil, the enclosure is thoroughly cleaned by wiping it with ethanol-soaked tissues.

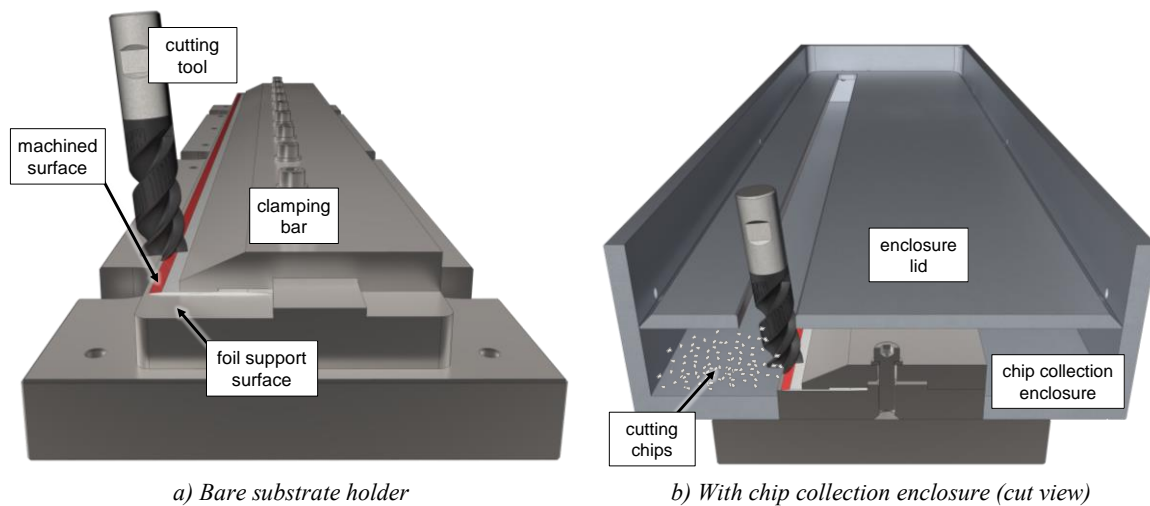


Figure 87: Substrate holder for milling of gradient full-size foils. The foils are clamped to the support surface via a massive stainless steel bar (a). The substrate holder is fully encapsulated by an aluminum chip collection enclosure, with a small slit in the lid for the cutting tool (b). The entire assembly is screwed to the work table of a 5-axis CNC machining center.

Again, the fabrication parameters were optimized to improve the precision and uniformity of the milled gradients. Finally, a face mill cutting tool with carbide cutting wedges and a diameter of 20 mm at a rotation speed of 800 min^{-1} was used and the feed rate was set to 80 mm/min. Each gradient was milled in a single pass with the full cutting depth. Using this parameter set, a total of 24 gradient full-size foils were fabricated, 13 of stainless steel AISI 316L and 11 of titanium alloy Ti-6Al-4V.

After fabrication, all foils were inspected dimensionally using a 3D coordinate measuring machine and no destructive characterization was performed.

Stainless steel AISI 316L

40 flat foils of stainless steel AISI 316L were procured from A.L.L. Lasertechnik GmbH with nominal dimensions of $762 \pm 1 \text{ mm} \times 45 \pm 0.1 \text{ mm} \times 0.60 \pm 0.025 \text{ mm}$. Assuming the bulk materials' density, the nominal mass of such foils is $163.563 \pm 7.393 \text{ g}$. Before milling, the flat foils were measured using a caliper to confirm that they are within the geometrical tolerances claimed by the supplier. On the 13

foils, which were finally used to fabricate specification-conform gradient foils, average dimensions of 761.893 mm x 44.935 mm x 0.594 mm were measured. Therefore, the average length is $\sim 0.01\%$ smaller, the average width is $\sim 0.1\%$ smaller, and the average thickness is $\sim 1\%$ smaller than the respective nominal values.

Figure 88 shows the mass distribution of the 13 fabricated gradient foils and the original flat foils. By dimensional inspection using the 3D coordinate measuring machine, all gradient foils were found to be within the geometrical tolerances.

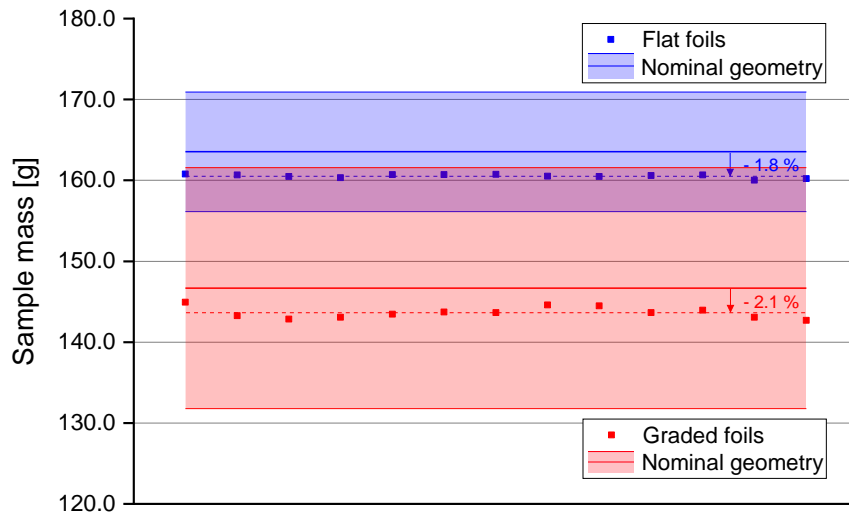


Figure 88: Mass distribution of the gradient full-size stainless steel foils (milling). While still being within the geometrical tolerances claimed by the supplier, the flat foils show a small systematic under-thickness and are therefore on average 1.8 % lighter than the nominal geometry.

Figure 89 exemplarily shows a gradient full-size stainless steel foil, fabricated by milling. It visually appears in good condition with no notable geometrical or other defects. The original surface in the middle as well as both machined surfaces at the gradients appear very regular and shiny. The cutting chips are curly and typically some mm long, without any visible oxidation or discoloration. On average, 16.819 g of cutting chips were collected from each foil, which corresponds to $\sim 98.5\%$ of the removed material.



Figure 89: Gradient full-size stainless steel foil (milling). Both the original and the machined surfaces appear very regular and shiny. The thickness gradients are clearly visible by eye. The cutting chips are curly, shiny, and typically some mm long.

Titanium alloy Ti-6Al-4V

Sheets of titanium alloy Ti-6Al-4V were procured from WHS Sondermetalle e.K. with a nominal thickness of 0.60 ± 0.05 mm. These sheets were cut to size at A.L.L. Lasertechnik GmbH, yielding 40 flat foils with nominal dimensions of 762 ± 1 mm x 45 ± 0.1 mm x 0.60 ± 0.05 mm. Assuming the bulk materials' density, the nominal mass of such foils is 91.143 ± 7.917 g. Before milling, the flat foils were measured using a caliper to confirm that they are within the geometrical tolerances claimed by the suppliers. On the 11 foils, which were finally used to fabricate gradient foils, average dimensions of 762.016 mm x 44.930 mm x 0.630 mm were measured. The average length and width thus only deviate $< 0.2\%$ from the nominal values and a small systematic over-thickness of $\sim 5\%$ was found.

Figure 90 shows the mass distribution of the 11 fabricated gradient foils and the original flat foils. By dimensional inspection using the 3D coordinate measuring machine, all gradient foils were found to be out of the geometrical tolerances. More precisely, the widths of the short and/or long gradients exceeded their tolerances of 4.50 ± 0.30 mm and 9.00 ± 0.30 mm, respectively. The reason for this result is similar to the mini-size fabrication study: due to the very small and pre-defined gradient angles and the determination of the foil thickness at the gradient edges, a small over-thickness of the flat foils can substantially increase the width of the gradients, possibly exceeding the tolerances.

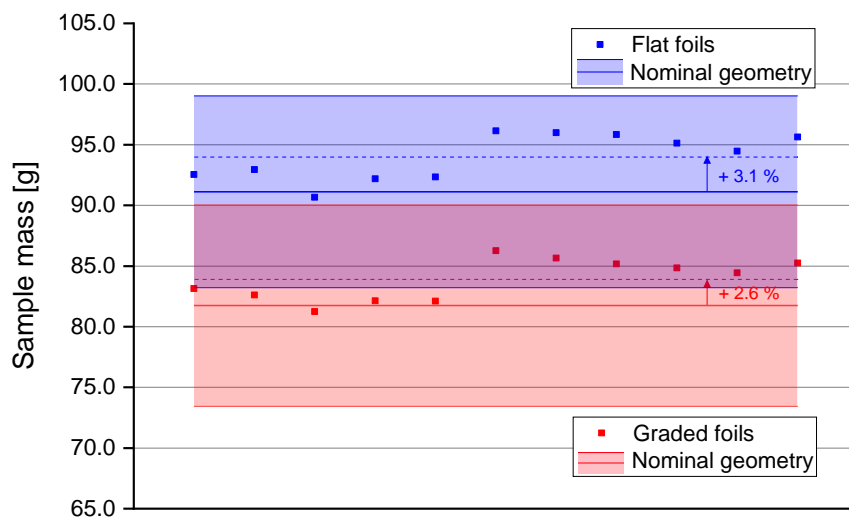
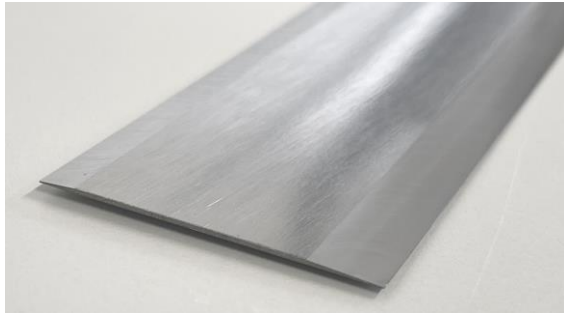


Figure 90: Mass distribution of the gradient full-size titanium alloy foils (milling). While still being within the geometrical tolerances claimed by the supplier, the flat foils on average show a small over-thickness and are therefore on average 3.1 % heavier than the nominal geometry.

Figure 91 exemplarily shows a gradient full-size titanium alloy foil, fabricated by milling. The foil visually appears in good condition with no notable geometrical defects. The original surface in the middle as well as both machined surfaces at the gradients appear very regular and shiny, with a slight brushed texture at the original surface. The cutting chips are curly and typically some mm long. Despite the pyrophoricity of the used titanium alloy and the omission of a cooling lubricant, no sparks were observed during the milling process. Consequently, no visible oxidation or discoloration is found on the cutting chips. On average, 10.072 g of cutting chips were collected from each foil, which corresponds to $\sim 99.2\%$ of the removed material.



a) Gradient foil (close-up view)



b) Cutting chips

Figure 91: Gradient full-size titanium alloy foil (milling). Both the original and the machined surfaces appear very regular and shiny. The thickness gradients are clearly visible by eye. The cutting chips are curly, shiny, and typically some mm long.

4.4 FABRICATION DEMONSTRATION OF GRADIENT FOILS BY SELECTIVE LASER MELTING

The fabrication of gradient foils by SLM was demonstrated in mini-size geometry with the surrogate material stainless steel AISI 316L in cooperation with Laserzentrum Nord GmbH (Hamburg, Germany) – now Fraunhofer Research Institution for Additive Manufacturing Technologies (IAPT). The aim of this study was to find out if the gradient foil geometry can be reliably fabricated using commercial SLM equipment and commercial stainless steel powder. Furthermore, it was evaluated if post-production treatments are necessary to achieve samples with acceptable surface and geometrical quality and with the desired austenitic microstructure.

Due to the poor availability of sufficiently large SLM equipment by the time of this work, no fabrication experiments for full-size gradient foils were performed.

4.4.1 FABRICATION

Using a Concept Laser m2 cusing SLM device [198], two experiments were carried out with the device's default process parameters for stainless steel AISI 316L and using Concept Laser CL 20ES stainless steel powder [199] – a Concept Laser proprietary powder with spherical particles $< 150 \mu\text{m}$, which resembles the chemical composition of AISI 316L. The upper surface of the stainless steel build plate was sandblasted prior to the SLM process to ensure a good bonding with the fabricated parts. The SLM device did not allow the heating of the powder bed before or during the process.

In the initial scoping experiment, depicted in Figure 92 a, the gradient mini-size geometry (“reference geometry”) as well as several modifications of this geometry were tested to explore the feasibility of fabricating wider and thinner foils as well as the possible necessity for lateral support structures. It was found that the fabrication of the reference geometry as well as a $\sim 15\%$ thinner geometry is feasible without lateral support structures (marked in green). In fact, it was found that the $400 \mu\text{m}$ wide bonding bridges between the gradient foils and the optionally tested support structures (marked in yellow) have ruptured during the SLM process and were thus useless. The fabrication of wider geometries with foil widths up to 59 mm was not successful even with massively bonded support structures, as the gradient foils started to bend inside the powder bed during their fabrication due to inner stresses and thus, the subsequently molten layers could not attach to the previous layers anymore (marked in red).

Based on these results, the fabrication experiment was set up with an equidistant rectangular grid of 5×6 equal parts in reference geometry without any support structures, as shown in Figure 92 b. The parts were rotated slightly around the vertical axis to improve the spread of fresh powder by the rake after the melting of each layer. After the SLM process, the gradient foils were removed from the build plate by wire spark erosion, followed by a dimensional inspection using a caliper. The average size of the gradient foils was measured to be $82.22 \text{ mm} \times 18.81 \text{ mm}$, thus only deviating on average $< 1.0\%$ from the nominal values. The thickness could not be reliably measured due to the rough surface. Figure 93 shows the mass distribution of the 30 fabricated gradient foils, which are on average $\sim 11.4\%$ lighter than the nominal geometry. Since the length and width of the foils deviate only slightly from the nominal values, it is assumed that this mass deviation results either from a small systematic under-thickness or inner porosities.

Figure 94 exemplarily shows a gradient mini-size stainless steel foil, fabricated by SLM. The foils show a regular but rough surface and thus, the thickness gradients are only barely visible by eye. No notable geometrical or other defects were observed.

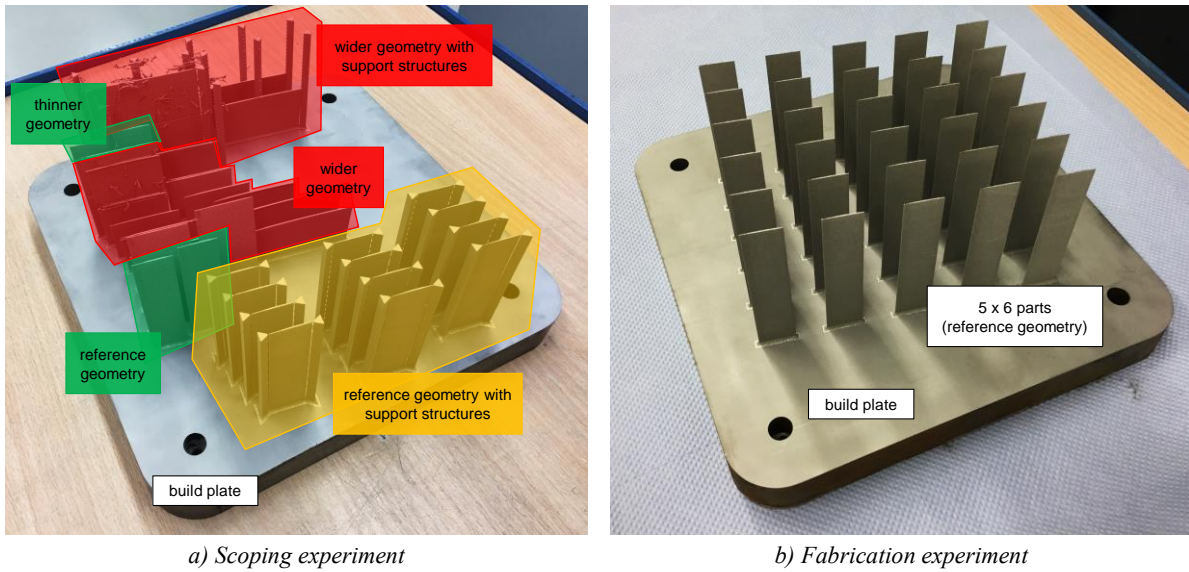


Figure 92: Results of the SLM fabrication experiments. After scoping various geometries and support structures in a first experiment (a), a total of 30 gradient mini-size foils were fabricated successfully without any support structures (b).



Figure 93: Mass distribution of the gradient mini-size stainless steel foils (SLM). Due to either systematic geometrical deviations or inner porosities, the gradient foils are on average $\sim 11.4\%$ lighter than the nominal geometry.



Figure 94: Gradient mini-size stainless steel foil (SLM). The foils show a regular but rough surface, and the thickness gradients are barely visible by eye.

This rough visual appearance of the surface is confirmed by surface optical microscopy, as shown exemplarily in Figure 95. The surface shows many adhering powder particles as well as the melting paths of the laser beam in the form of vertical strings.

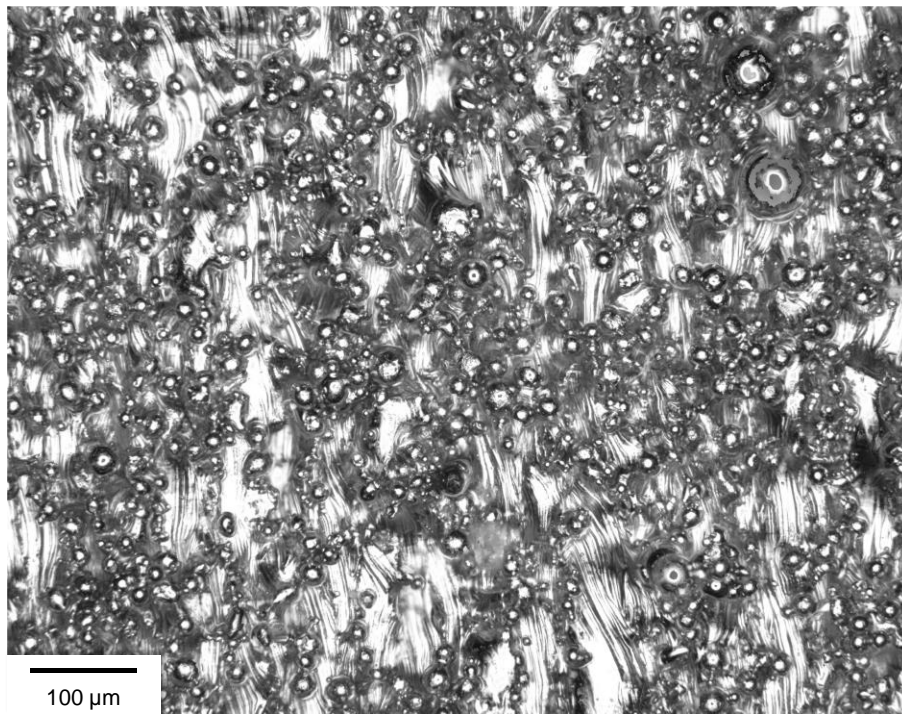
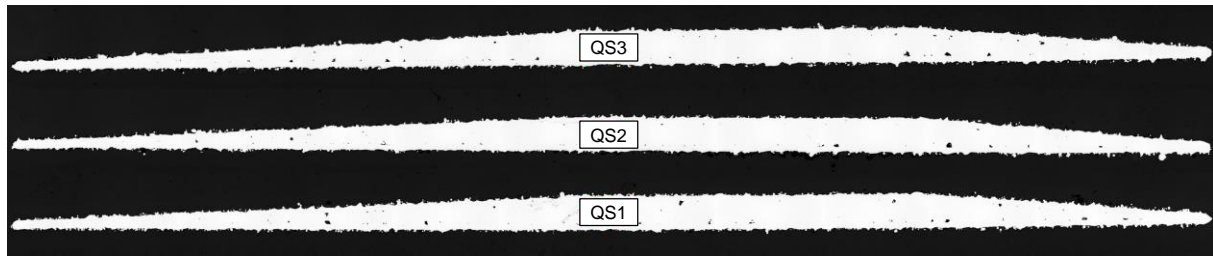


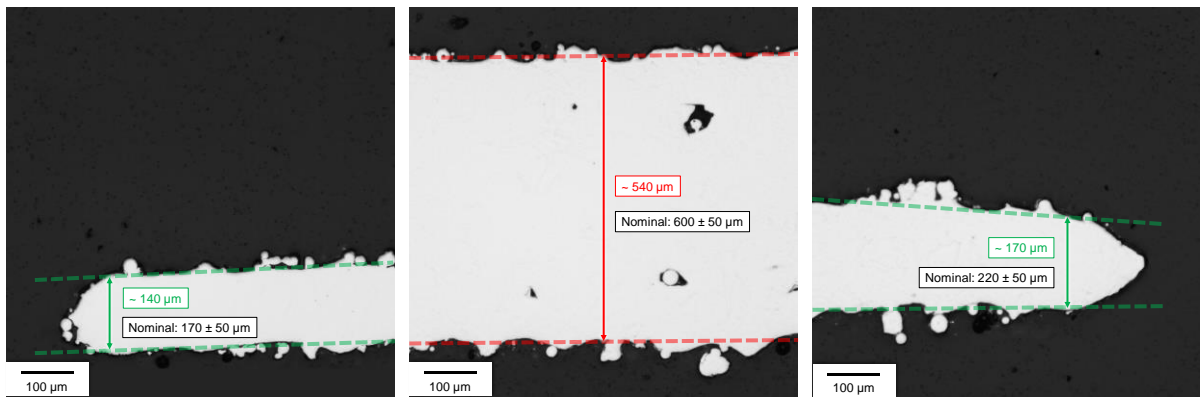
Figure 95: Exemplary surface optical micrograph of gradient mini-size stainless steel foils (SLM). The surface shows many adhering powder particles, and the melting paths of the laser beam are clearly visible.

Exemplary cross-sections were prepared and the geometrical quality of the foils, the shape of the edges as well as the microstructure were evaluated. Figure 96 shows the cross-sections QS1, QS2 and QS3 at different locations on the same foil. The overview micrographs look very similar and show a very rough and irregular surface as well as many inner porosities. The assumed systematic under-thickness in the order of $\sim 10\%$ (in the middle section) to $\sim 20\%$ (at the edges) is confirmed. As no notable differences were observed between the cross-sections QS1, QS2 and QS3 also in the further characterizations, only one representative micrograph is hereafter. By a Beraha II etching of another sample, depicted in Figure 97, a highly irregular and fine-grained austenitic microstructure is revealed throughout the entire cross-section. At higher magnification, the melting paths of the laser beam are also visible inside the foils. It is assumed that this microstructure originates from the rapid melting and cooling of the material during the SLM process, far away from thermal equilibrium conditions.

By a Vickers hardness measurement, the hardness of the gradient foils was measured to be 214 ± 5 HV1, thus significantly harder than the literature value of 152 HV.



a) Overview micrographs

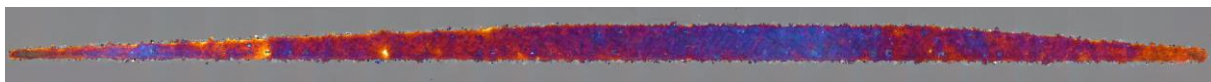


b) Representative left edge

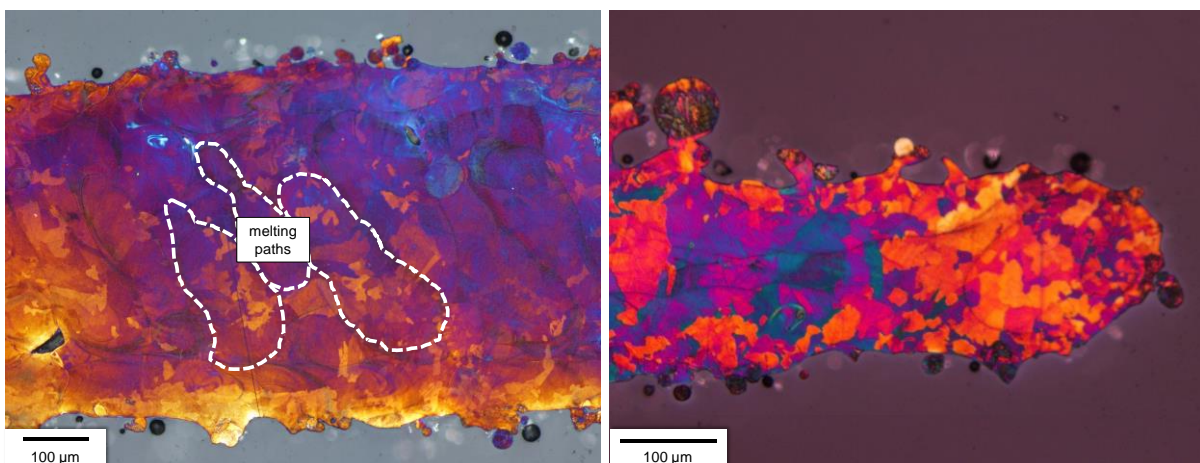
c) Representative middle section

d) Representative right edge

Figure 96: Exemplary cross-sectional optical micrographs of gradient mini-size stainless foils (SLM). The three overview micrographs appear very similar with a very rough and irregular surface and many inner porosities (a). At the gradient edges (b, d) as well as at the middle section (c), a small systematic under-thickness of the foils is confirmed.



a) Overview micrograph



b) Representative middle section

c) Representative edge section

Figure 97: Exemplary cross-sectional optical micrographs of gradient mini-size stainless foils (SLM), etched with Beraha II. A highly irregular and fine-grained austenitic microstructure is revealed throughout the entire cross-section. Furthermore, the melting paths of the laser beam are visible.

4.4.2 POST-PRODUCTION TREATMENTS

From the characterization results of the gradient mini-size stainless steel foils fabricated by SLM, it becomes clear that post-production treatments are necessary to make them usable for subsequent PVD coating and C2TWP cladding application experiments. Thus, the surface was first smoothed by shot peening. Afterwards, a hot isostatic pressing treatment was performed to close inner porosities, to recrystallize the microstructure and to remove inner stresses, which were potentially also introduced by the shot peening treatment.

Shot peening

A controlled shot peening treatment with glass spheres according to SAE-J2441 [200] was performed at Metal Improvement Company, LLC – Curtiss-Wright Surface Technologies (Unna, Germany). By using the smallest possible spheres and the lowest possible air pressure, the process was targeted at reducing the surface roughness while avoiding any macroscopic mechanical deformation of the foils. Figure 98 exemplarily shows a gradient mini-size stainless steel foil after shot peening. The surface of the foils appears more shiny and the thickness gradients become visible by eye. By weighing the foils before and after shot peening, an average material loss of $\sim 2.0\%$ was determined.



Figure 98: Gradient mini-size stainless steel foil (SLM, shot peening). After shot peening, the surface of the foils appears more shiny and the thickness gradients become visible by eye.

The smoother visual appearance of the surface is confirmed by surface optical microscopy, as shown exemplarily in Figure 99. The adhering powder particles are gone and the surface – while still being highly uneven – appears much smoother.

Again, an exemplary cross-section was prepared and Figure 100 shows the results. The adhering powder particles at the surface are removed and the surface is significantly smoothed. However, at some locations spallings can be observed, which are assumed to be deformed powder particles, which were only partially pressed into the surface by the impinging spheres. As expected, the inner porosities remain unchanged after shot peening.

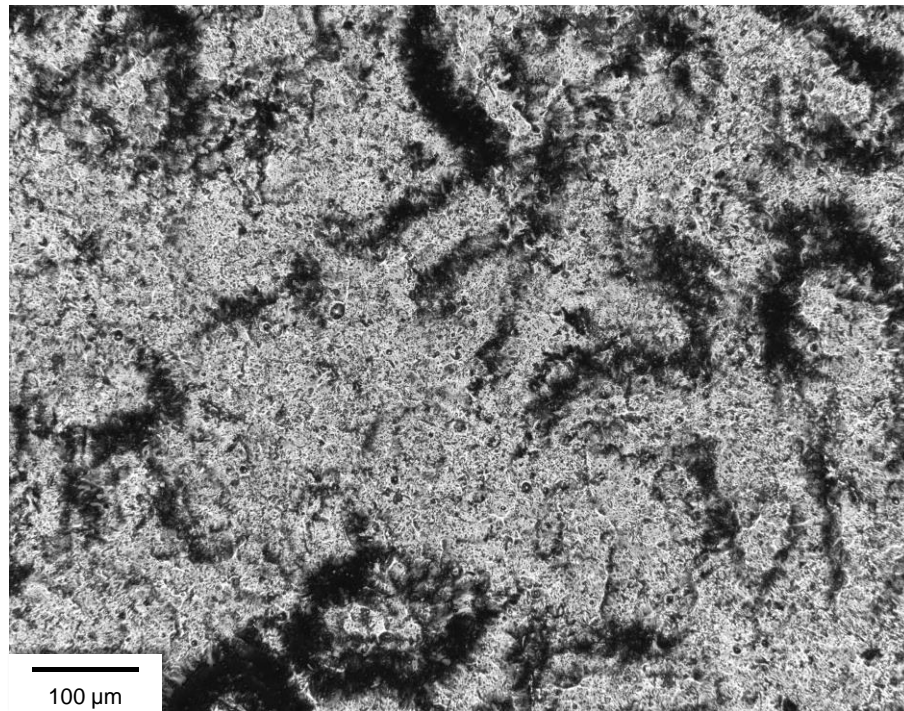


Figure 99: Exemplary surface optical micrograph of gradient mini-size stainless steel foils (SLM, shot peening). The adhering powder particles are gone and the surface appears much smoother.

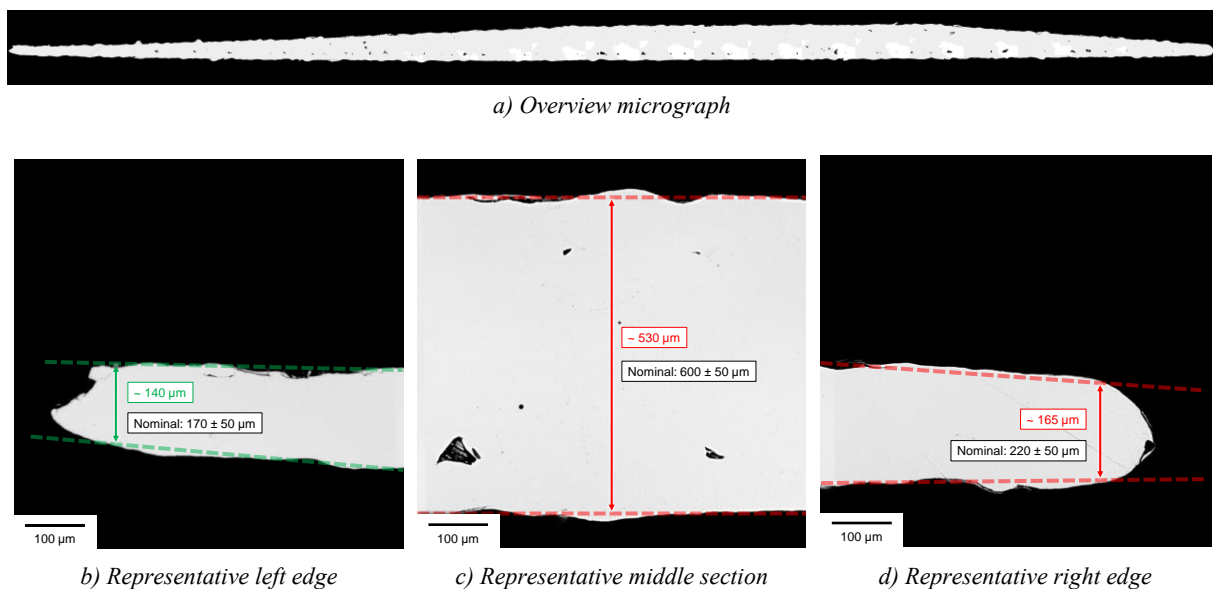


Figure 100: Exemplary cross-sectional optical micrographs of gradient mini-size stainless foils (SLM, shot peening). The adhering powder particles are removed, and the surface is significantly smoothed. However, some spallings can be observed at the surface.

Hot isostatic pressing

After shot peening, a HIP treatment was performed at Bodycote (Haag-Winden, Germany). Hereby, the foils were first double-wrapped in stainless steel foil to avoid any oxidation during the high-temperature process and then placed individually in ceramic containers inside the HIP vessel. As shown in the process diagram in Figure 101, the entire process lasted 14 hours, with 8 hours of heating and pressurization, 4 hours of holding at a temperature of 1150 °C and a pressure of 1000 bar argon, followed by 2 hours of cooling and depressurization. By weighing the foils before and after HIP, no material loss was measured.

Figure 102 exemplarily shows a gradient mini-size stainless steel foil after shot peening and HIP. The surface of the foils appears unchanged. By surface optical microscopy, as shown exemplarily in Figure 103, the surface is still found to be highly uneven. Many ~ 20 µm large islands of unknown origin, which were not found after shot peening, can now be observed.

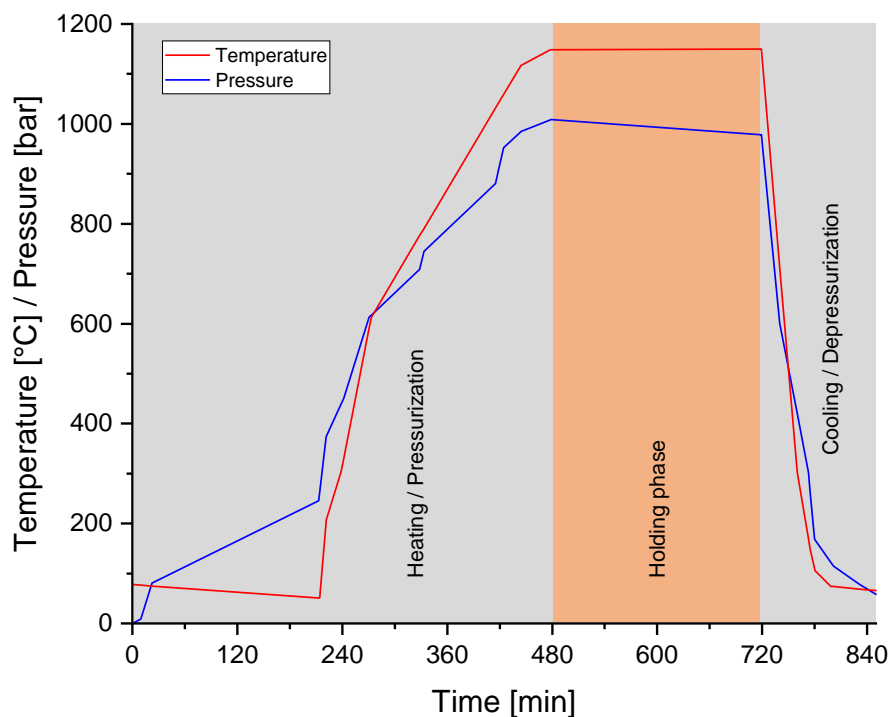


Figure 101: Process diagram of the HIP process. After 8 hours of heating and pressurization, the samples are kept at a temperature of 1150 °C and a pressure of 1000 bar argon for 4 hours, followed by 2 hours of cooling and depressurization.

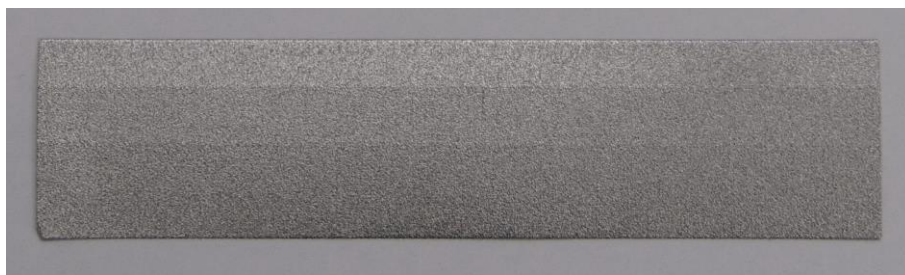


Figure 102: Gradient mini-size stainless steel foil (SLM, shot peening, HIP). After hot isostatic pressing, the surface of the foils appears unchanged.

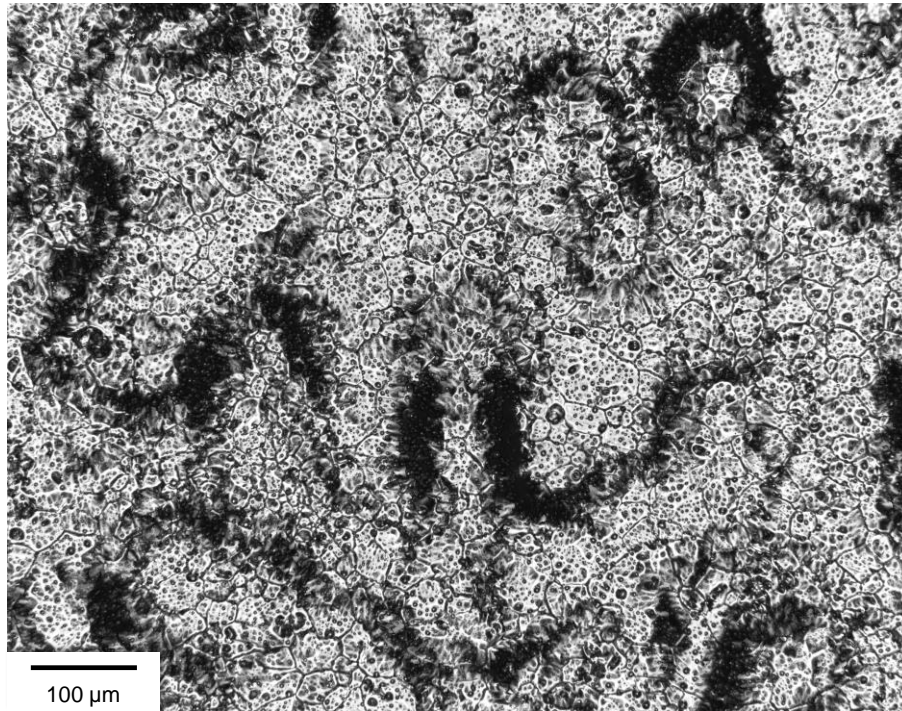


Figure 103: Exemplary surface optical micrograph of gradient mini-size stainless steel foils (SLM, shot peening, HIP). The surface shows many ~ 20 μm large islands of unknown origin.

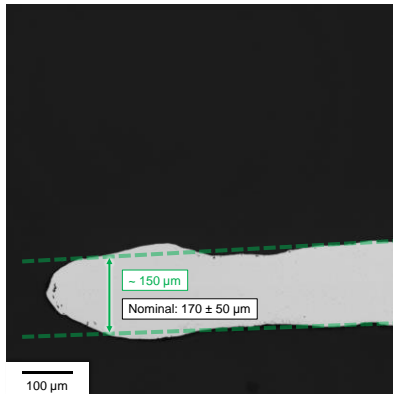
Also after the HIP treatment, an exemplary cross-section was prepared and Figure 104 shows the results. The inner porosities are closed and the surface appears again smoother than after shot peening. Presumably, the HIP process was able to press the remaining spallings, which were observed after shot peening, onto the surface. The slight bending of the sample, which is visible in the overview micrograph, may result from the relief of inner stresses due to the high temperatures during HIP.

By a Beraha II etching of another sample, depicted in Figure 105, a recrystallized austenitic microstructure is revealed, which does not show any melting paths or other irregularities anymore. The shadowing effects close to the surface of the foils result from a non-uniform etching due to the accumulation of the etching solution between the sample and the epoxy resin.

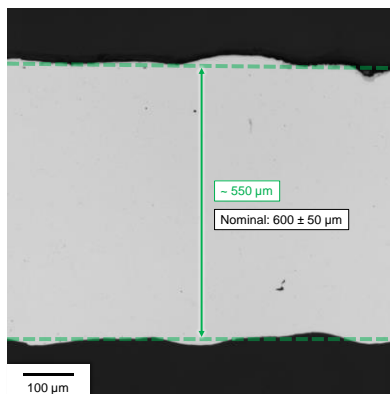
By a Vickers hardness measurement, the hardness of the gradient foils after shot peening and HIP was measured to be 157 ± 6 HV1, thus significantly softer than after SLM fabrication and in good agreement with the literature value of 152 HV.



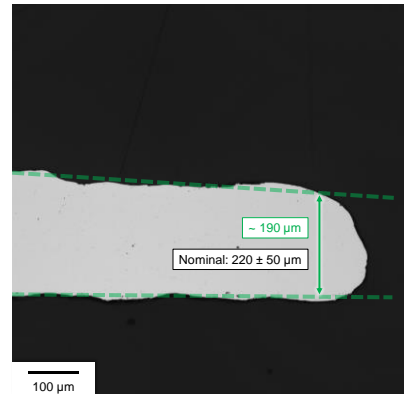
a) Overview micrograph



b) Representative left edge



c) Representative middle section

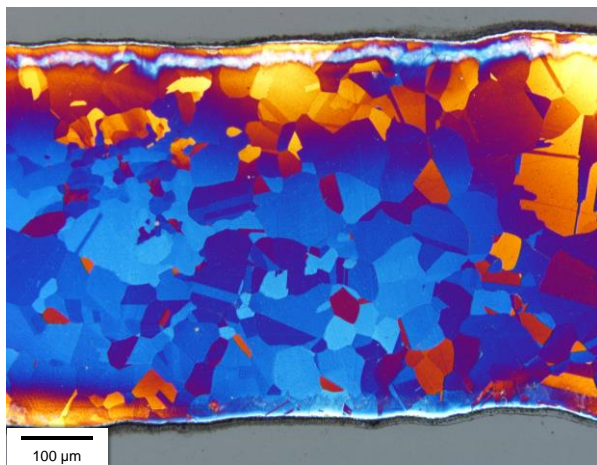


d) Representative right edge

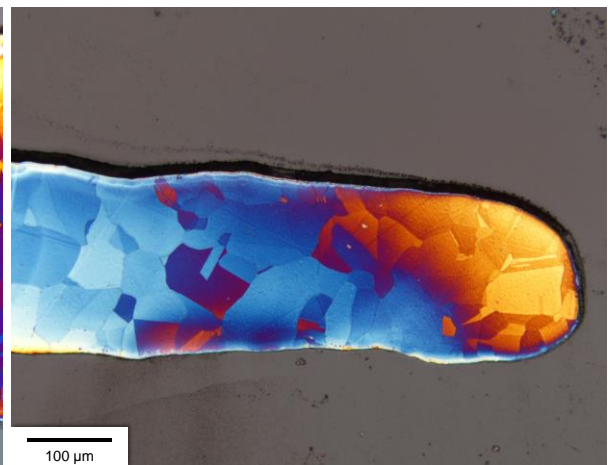
Figure 104: Exemplary cross-sectional optical micrographs of gradient mini-size stainless foils (SLM, shot peening, HIP). The inner porosities are fully closed and the surface is again smoothed. The HIP process presumably was able to press the spallings, which were observed after shot peening, onto the surface.



a) Overview micrograph



b) Representative middle section



c) Representative edge section

Figure 105: Exemplary cross-sectional optical micrographs of gradient mini-size stainless foils (SLM, shot peening, HIP), etched with Beraha II. The microstructure resembles a recrystallized austenitic structure. The laser melting paths are no more visible.

4.5 PVD COATING AND C2TWP CLADDING APPLICATION

Following the promising results of the fabrication of gradient mini-size stainless steel foils by milling and selective laser melting, PVD coating and C2TWP cladding application experiments were performed using representative samples. Hereby, the gradient foils fabricated by SLM were priorly subjected to shot peening and hot isostatic pressing as post-production treatments.

PVD coating

After chemical cleaning of the foils, the gradient foils were coated with $\sim 20 \mu\text{m}$ of Zr using the mini-size PVD coating device and the process parameters of the EMPIrE fabrication campaign. However, due to a technical failure at the time of this work, no plasma cleaning was performed on the samples.

After PVD coating, cross-sections were prepared from both samples. No adherence deficiencies were identified and the Zr coating was found to follow the surface topography of the foils very well, as depicted in Figure 106. On the foil fabricated by milling, no voids or layer defects were found. On the SLM sample, however, some small voids between the foil and the Zr layer were observed. These defects are believed to originate from the missing plasma cleaning step prior to PVD coating, which presumably would have been able to remove remaining surface contaminants from the fabrication processes, which could not be removed by the chemical cleaning process.

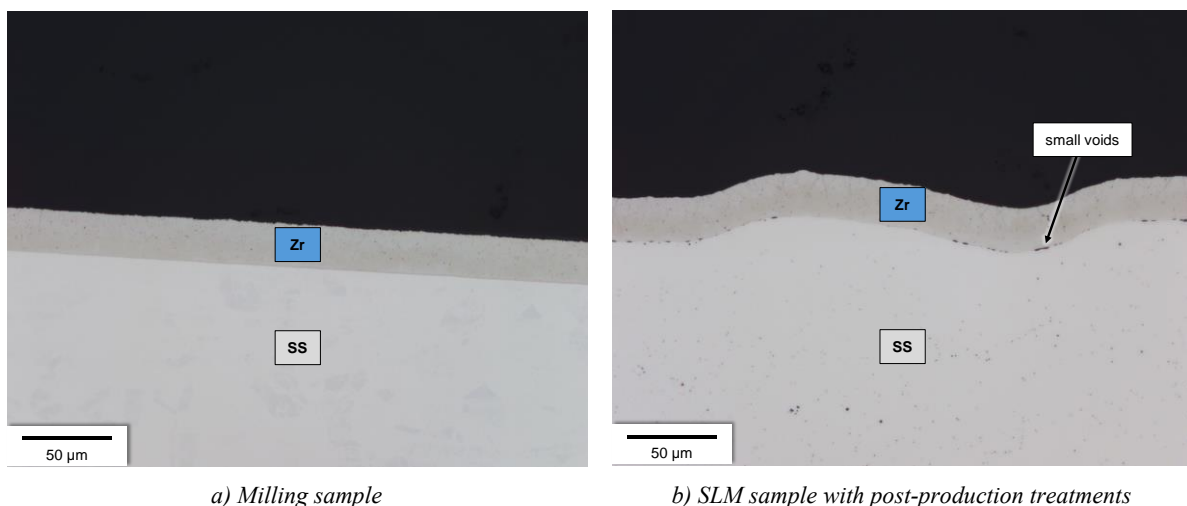


Figure 106: Exemplary cross-sectional optical micrographs of Zr-coated gradient mini-size foils. The Zr coating follows the surface topography of the foils very well. On the foil fabricated by milling (a), no voids or layer defects can be found. In contrast, some small voids between the foil and the Zr layer are observed at the SLM sample.

C2TWP cladding application

To evaluate the compatibility of the C2TWP cladding application process with gradient foils, a total of 13 samples were shipped to Framatome-CERCA for experiments. Within two process batches, various C2TWP parameters were tested using the two types of gradient foils [201]. All resulting mini-plates were subsequently inspected by ultrasonic testing and some were exemplarily cut for destructive examination.

As shown exemplarily in Figure 107, the surface of the gradient foils shows very good adherence with the cladding with no defects detectable by UT. But, similar to the previous results from the EMPIrE fabrication campaign, a large end gap between the foil and the cladding was observed on all samples. The occurrence of these gaps is assumed to be linked to the higher thickness of these foils compared to

previous C2TWP experiments. Via cross-sections prepared at Framatome-CERCA, the satisfactory bonding between the gradient foil surface and the cladding was confirmed, as depicted exemplarily in Figure 108 for an SLM sample. Hereby, the black line around the gradient foil is not considered a gap but an artifact from the sample polishing process.

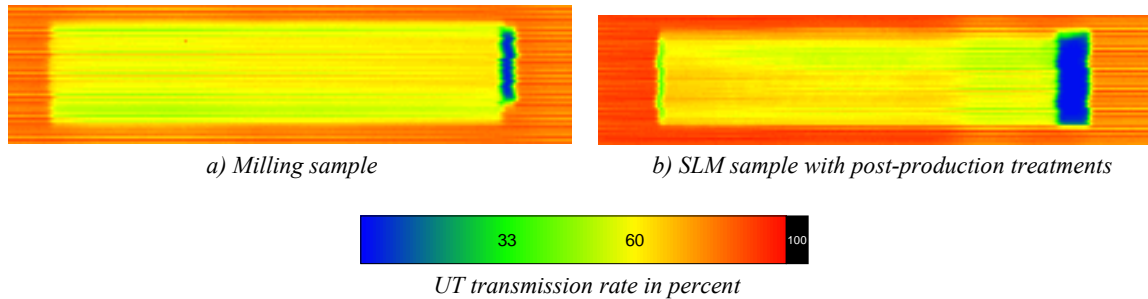


Figure 107: UT test results of mini-size plates with gradient stainless steel foils. Both the gradient foil fabricated by milling (a) and by SLM (b) show a good adherence with the cladding. The end gaps on the right side of the foils (blue areas) are not believed to be related to the gradient geometry. After [201].

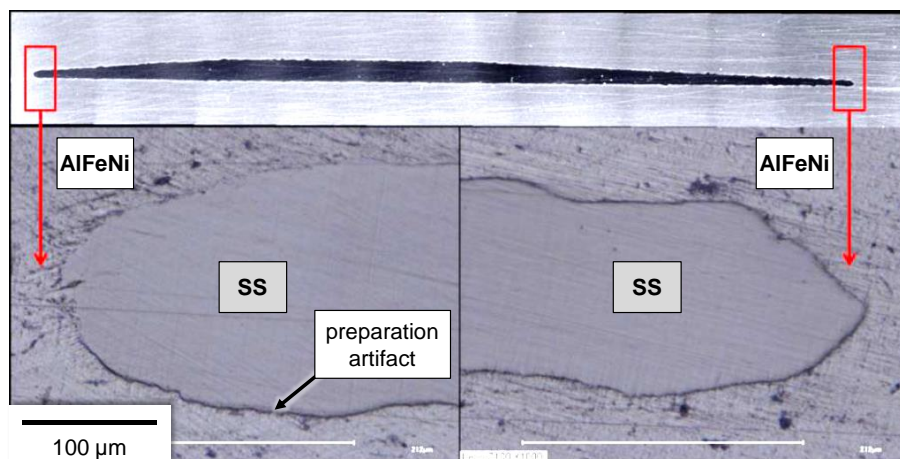


Figure 108: Exemplary cross-sectional optical micrograph of a mini-plate with a gradient stainless steel foil fabricated by SLM. The aluminum cladding follows the uneven but smooth surface topography of the gradient foil very well. The black line around the gradient foil is not considered a gap but an artifact from the sample polishing process. At the transversal edges (at higher magnification), no gap between the gradient foil and the cladding was observed. After [201].

5 DEVELOPMENT OF THE PILOT PVD COATING PROCESS

For the upcoming European irradiation test FUTURE-MONO-1, planned in 2023 in the BR2 material test reactor, LEU fuel plates shall be fabricated from flat full-size U-Mo foils and the Zr coating shall be applied by a pilot PVD coating process. After this irradiation test, the complete European fabrication process for monolithic U-Mo fuels can be industrialized for the conversion of the FRM II and potentially other research reactors.

Within this thesis, the necessary pilot PVD coating process is designed, realized and demonstrated using stainless steel substrates.

5.1 DESIGN FUNDAMENTALS FOR THE PILOT PVD COATING PROCESS

The pilot PVD coating process is the next iteration of TUM's efforts to apply an interdiffusion barrier onto U-Mo foils. It is an intermediate step between the experimental mini-size process and a future industrial process. Thus, the design of this pilot process shall be based on

- The experience gained from the mini-size process and the recommendations derived thereof, which are described in section 2.3.7
- The results of pre-experiments on an optimized substrate heating approach, which are given in section 5.2
- The results of pre-experiments on an optimized substrate biasing approach, which are given in section 5.3.
- A clear focus towards its future industrialization

5.1.1 REQUIREMENTS

The pilot PVD coating process shall be able to apply a Zr coating to full-size (762 mm x 45 mm) U-Mo foils. Due to a limited amount of full-size U-Mo foils available at TUM, the process shall also be compatible with *half-size* (380 mm x 45 mm) substrates, which can be produced from full-size substrates by cutting them in half, thus doubling the number of available substrates for experiments. For simplicity, the pilot PVD coating process will be referred to hereafter also as *full-size (PVD coating) process* and the device will be referred to as *full-size (PVD coating) device*.

From the design fundamentals described above, technical requirements for the new pilot process can be derived. The first and most obvious requirement is the specification-conformity of the U-Mo foils, which were coated with Zr in this process. This leads to the following basic requirements:

Full surface coverage. The surface coverage requirements of the mini-size process apply as well to the full-size process. Thus, no areas without Zr coating can be accepted on the entire U-Mo foil surface on both sides. If such areas exist after PVD coating, e.g. due to a necessary clamping of the substrate to the

substrate holder, these areas need to be trimmed off and the additional material loss needs to be considered.

Defect-free adherence. The adherence requirements of the mini-size process apply as well to the full-size process. Thus, no coating delaminations can be accepted on the entire U-Mo foil surface on both sides. If such delaminations appear after PVD coating, the corresponding areas of the foil need to be trimmed off as well and the additional material loss needs to be considered.

Minimum coating thickness at every location. The minimum Zr coating thickness requirement of the mini-size process was $\geq 25 \mu\text{m}$ on the entire U-Mo foil surface on both sides, to match with the technical capabilities of the alternative co-rolling process. For the full-size process, a reduction of this minimum thickness requirement to $8 \mu\text{m}$ is proposed, but no areas with lower thickness can be accepted. To avoid unnecessarily long process times to comply with this requirement, the coating thickness uniformity across the substrate surface shall be as good as possible.

Temperature control. After the C2TWP cladding application process, the U-Mo foils inside the fuel plates must still exist in their metastable γ phase. Therefore, the full-size process shall avoid the temperature range $\sim 400 - \sim 575 \text{ }^\circ\text{C}$, where fast γ phase decomposition occurs. Further, the formation of interaction layers between U-Mo and Zr shall be prevented, thus substrate temperatures $> 650 \text{ }^\circ\text{C}$ shall be avoided as well.

With its future industrialization in mind, the following additional requirements are laid down to the full-size PVD coating process:

Reduction of process parameter space. While the mini-size PVD coating device allowed the investigation of a large process parameter space to identify the most promising parameter set, this flexibility led to a strong increase in device complexity, defect frequency and cost. Therefore, only the most promising capabilities shall be implemented into the final full-size PVD coating device.

Reduction of process time. The mini-size process allowed the complete processing – including substrate cleaning, coating and packaging – of one U-Mo foil per working day. The full-size process shall be at least as fast, preferably faster. Therefore, all process steps shall be optimized towards short durations and possibilities to omit time-consuming steps shall be investigated.

Robustness and material efficiency. The pre-products for the PVD coating process – bare U-Mo foils, which will later be made from enriched uranium – are expensive and require complex safety and security measures during fabrication, handling and transport. The recycling of rejected U-Mo foils is complex, if at all possible, especially with Zr coating. Thus, the PVD coating process shall be as robust as possible to reduce the rate of non-specification-conform foils. Furthermore, areas of the U-Mo foils which need to be trimmed off shall be reduced to an absolute minimum to achieve a high material utilization efficiency. Also, the sputtering target utilization shall be as high as possible and the deposition profile shall be optimized to reduce the unwanted peripheral coating of the process chamber.

Two key issues have been previously identified in the mini-size PVD coating process and need to be resolved in the full-size process:

Cracking of the Zr layer during cladding application. Cracks in the Zr layer can deteriorate its effect as an interdiffusion barrier during irradiation. Thus, the ductility of the Zr layer shall be improved by an appropriate technical measure such as optimized substrate heating or biasing. Possible technical solutions for both approaches need to be studied with pre-experiments and the most promising solutions shall be implemented into the final full-size process.

Bending of the substrates after single-sided Zr coating application. This bending can deteriorate the coating uniformity, complicate the manual handling of the substrates, or even make the coating of large full-size substrates impossible. Thus, appropriate technical measures such as an optimization of the PVD process parameters, the reduction of the coating thickness, the fixing the substrate to the substrate holder or the simultaneous coating of both sides of the substrate shall be studied and the most promising solution shall be implemented into the final full-size process.

5.1.2 CONSTRAINTS

Due to the installation of the full-size PVD coating device in TUM's Nuclear Fuel Fabrication and Characterization Laboratory, several restrictions apply to the process and the design space is constrained as follows:

Radiation protection. Due to the licensing of the laboratory according to § 9 AtG, all installations and devices need to be fully compliant to the applicable radiation protection laws and regulations, especially the DIN 25425 [202]. The protection of the operators and the prevention of unintended release of radioactivity are important safety goals. Therefore, the full-size PVD coating process must be carried out inside a nuclear glovebox according to DIN 25412 [160], operating in negative pressure to prevent the release of open radioactivity into the laboratory. The existing HSK2 glovebox, described in section 3.1.2, shall be used for the implementation of the process.

Mass restriction. The laboratories' license limits the mass of enriched uranium handled at the same time to a total of 150 g U-235, which equals approximately three full-size U-Mo foils made from LEU. The process must comply with this limit and shall thus be designed in a way that no more than three U-Mo foils need to be handled at the same time.

Safety. Due to the laboratories' license, every device needs to be connected to the laboratories' emergency stop system, which is intended to automatically stop any ongoing process in the event of an emergency. Therefore, all components of the full-size PVD coating device must be inherently safe when currentless, e.g. by using NC valves. No manual operations must be necessary to put the device in a safe state, thus the process must be fully digitally controlled.

Infrastructure. The laboratory provides all experiments three-phase electrical power, cooling water with adjustable inlet temperature and pressure, pressurized air as well as argon, nitrogen and a gas mixture of 4 % hydrogen and 96 % argon. As the installation of additional media supplies is complex and cost-intensive in the nuclear environment, the process shall be designed to get along with the available media.

5.2 OPTIMIZED SUBSTRATE HEATING FOR PVD COATING

Substrate heating is a promising technique to increase the ductility of the deposited Zr layers. To develop an optimized substrate heating approach, two main tasks are followed:

- A detailed study on the U-Mo/Zr interaction behavior at different substrate temperatures during PVD coating was performed.
- Based on the results of this study, it is concluded if and how an optimized substrate heating approach, at an optimum substrate temperature and with better temperature control, could be implemented into the full-size PVD coating process.

The study on the U-Mo/Zr interaction behavior was performed within a B.Sc. thesis [203] and reference is made to this thesis wherever applicable. Since the mini-size PVD coating device is able to perform experiments with additionally heated substrates via the radiation heater element in its substrate holder, this device was used for the study.

5.2.1 MICRO-SIZE SAMPLE HOLDER

Models to simulate the substrate temperature in the mini-size device deliver uncertainties of more than ± 50 °C and therefore can not be used for the U-Mo/Zr interaction study, where the interesting temperature range is between ~ 575 °C and ~ 650 °C and thus only ~ 75 K wide. Instead, a special stainless steel sample holder for *micro-size* samples (10.3 mm x 9.5 mm) was built, which is intended to be placed on top of the high-temperature Mo plate of the substrate holder, as illustrated in Figure 109 a. Using this sample holder, the micro-size U-Mo sample in the left rectangular cut-out, as shown in Figure 109 b, is in direct line-of-sight of the radiation heating element below. To ensure fast heating and cooling rates of the micro-size samples as well as high reachable temperatures, the thermal contact between the Mo plate and the sample must be as weak as possible. Therefore, the entire micro-size sample holder stands solely on four stainless steel pins with 0.5 mm diameter.

The sample temperature during the process can not be measured directly, as the attachment of e.g. a thermocouple to it could influence its energy balance and therefore falsify the result. Thus, the temperature is measured indirectly via two type K thermocouples. The first one is a mantle thermocouple with 1 mm diameter, which is inserted into the central bar of the sample holder to monitor the temperature of the sample holder itself. The second thermocouple is a mantle thermocouple with 0.5 mm diameter, which is inserted into a boring in a Ti-6Al-4V reference sample in the right rectangular cut-out of the sample holder. The reference sample material Ti-6Al-4V was chosen due to its visual surface appearance, which is similar to freshly cleaned U-Mo foils. The thickness of the reference sample is set to 1 mm to achieve a similar weight of both samples. Thus, it is expected that both samples have similar absorbance for infrared radiation coming from the radiation heater and have similar thermal contact to the sample holder. Therefore, the micro-size sample temperature is defined via the direct measurement of the reference sample temperature.

5.2.2 PROCESS CHARACTERIZATION

Prior to the production of Zr-coated U-Mo samples at different temperatures, the experimental setup was characterized to determine the correct process parameters during the sample production. For these characterizations, a stainless steel dummy sample is placed in the left cut-out to protect the radiation heater element below from Zr coating. The distance between the sputtering target and the sample is set to 30 mm, which equals the standard operation point of the EMPIrE fabrication campaign [12].

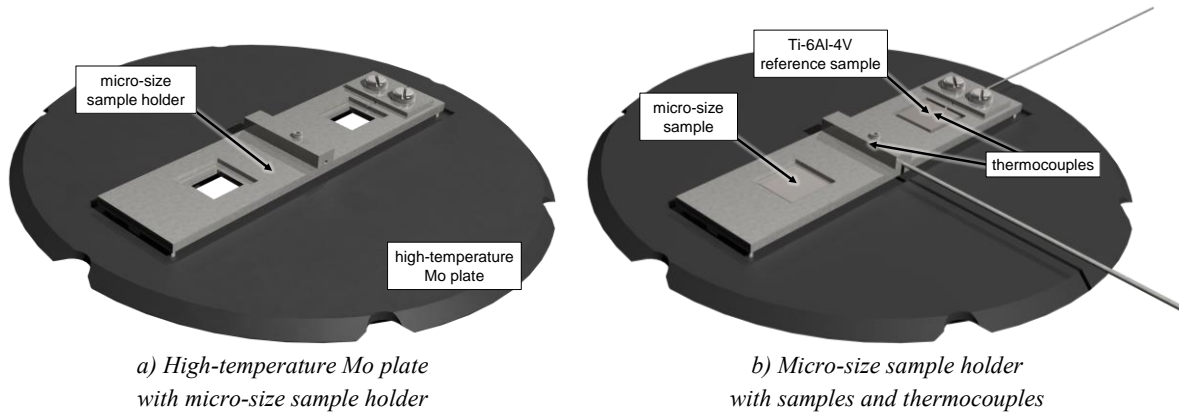


Figure 109: The micro-size sample holder. The sample holder is placed into the cut-out of the high-temperature Mo plate (a). The 10.3 mm x 9.5 mm micro-size sample is then placed loosely into the left cut-out of the sample holder, with a Ti-6Al-4V reference sample on a symmetrically identical position. The temperature of the sample holder and the reference sample is measured via two thermocouples (b).

No error bars are given in the following diagrams, since the uncertainty of the thermocouple measurement can be estimated to a few K only [204], similar to the uncertainty of the power measurement of less than 2 W [172].

Sample temperature with only heating

To pre-heat the samples to the correct temperature prior to PVD coating, the required electrical power of the radiation heater element (hereafter referred to as heating power) to reach the desired sample temperature needs to be known. Therefore, the heating power was first set to the lowest power of interest (25 W) and when thermal equilibrium at the thermocouples was reached, the temperatures were recorded and the power was increased. This was repeated until the power range up to 1000 W was covered. Figure 110 shows the results. The temperatures of the sample holder and the reference sample show a similar behavior and match very well in the considered heating power range. With a heating power of 1000 W, temperatures up to 900 °C can be reached.

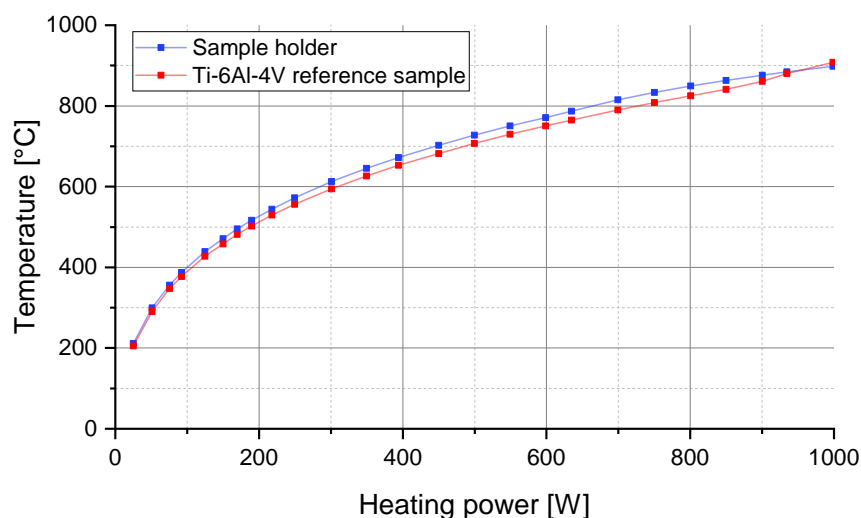


Figure 110: Temperature of the micro-size sample holder and the Ti-6Al-4V reference sample at various heating powers. The temperatures of the sample holder and the reference sample match very well and can reach up to 900 °C with 1000 W heating power. Data from [203].

Sample temperature with only sputtering

To know the influence of sputtering on the sample temperature independently, the thermal equilibrium temperature of the thermocouples was recorded for various sputtering powers from 200 W to 800 W without any additional heating. Figure 111 shows the results. It can be seen again that both temperatures show a similar behavior and match very well in the considered sputtering power range. With only sputtering, temperatures up to 540 °C can be reached at 800 W sputtering power. At 300 W sputtering power, the standard operation point of the EMPIrE fabrication campaign, which is also used for the sample production in this study, a sample temperature of 360 °C is reached.

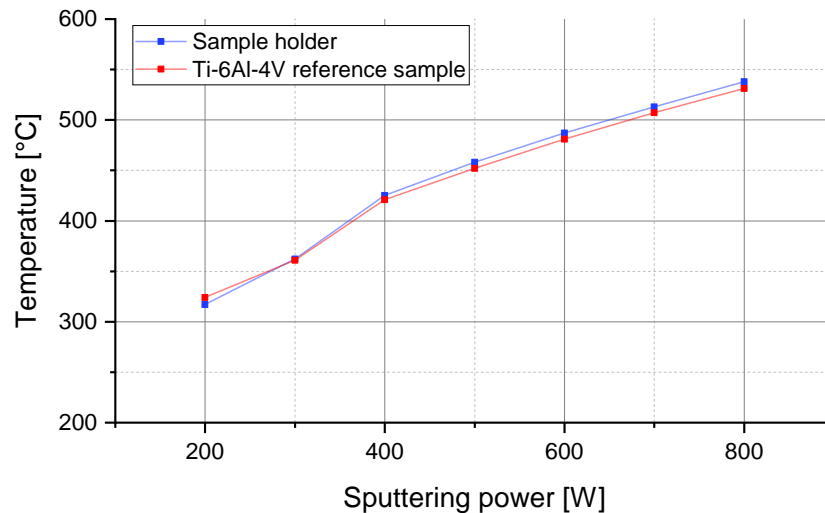


Figure 111: Temperature of the micro-size sample holder and the Ti-6Al-4V reference sample at various sputtering powers. The temperatures of the sample holder and the reference sample again match very well and can reach up to 540 °C with 800 W sputtering power. Data from [203].

Sample temperature with sputtering and heating

For the sample production, a sputtering power of 300 W is used. Therefore, the required heating power to reach the desired sample temperature during sputtering with 300 W needs to be known. Thus, the heating power was first set to the lowest power of interest (100 W) and when thermal equilibrium at the thermocouples was reached, the temperatures were recorded and the power was increased. This was repeated until the power range up to 800 W was covered. Figure 112 shows the results. Again, both temperatures show a similar behavior and match very well in the considered heating power range. At 800 W heating power and 300 W sputtering power, a sample temperature of up to 900 °C can be reached.

From these results, it is concluded that the experimental setup is suitable to produce the necessary Zr-coated U-Mo samples to investigate the effect of various substrate temperatures during PVD coating on the U-Mo/Zr interaction behavior and the resulting Zr layer properties. Both the temperature of the micro-size sample holder and of the Ti-6Al-4V reference sample are considered to be a good reference for the U-Mo sample temperature.

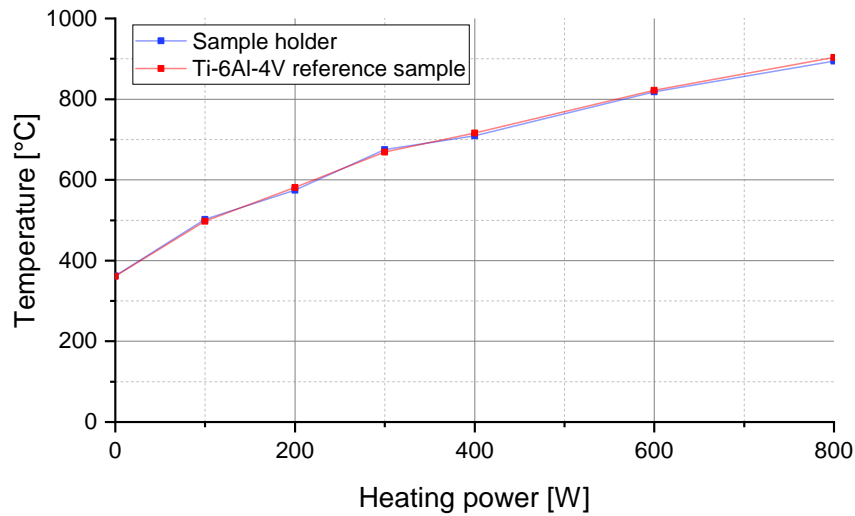


Figure 112: Temperature of the micro-size sample holder and the Ti-6Al-4V reference sample at various heating powers, while sputtering with 300W constantly. The temperatures of the sample holder and the reference sample again match very well and can reach up to 900 °C with 800 W heating power. Data from [203].

5.2.3 SAMPLE PRODUCTION

The temperature range of the micro-size samples to be covered by these experiments is 400 °C to 800 °C. Below 400 °C, no significant difference in the resulting layer grain structure is expected as shown in Figure 52. Since the micro-size sample holder is made of stainless steel, the eutectoid point at 928 °C in the binary Fe-Zr phase diagram, shown in Figure 113, must be avoided to not destroy the sample holder. To keep a safety margin to this point, the upper temperature limit is thus set to 800 °C.

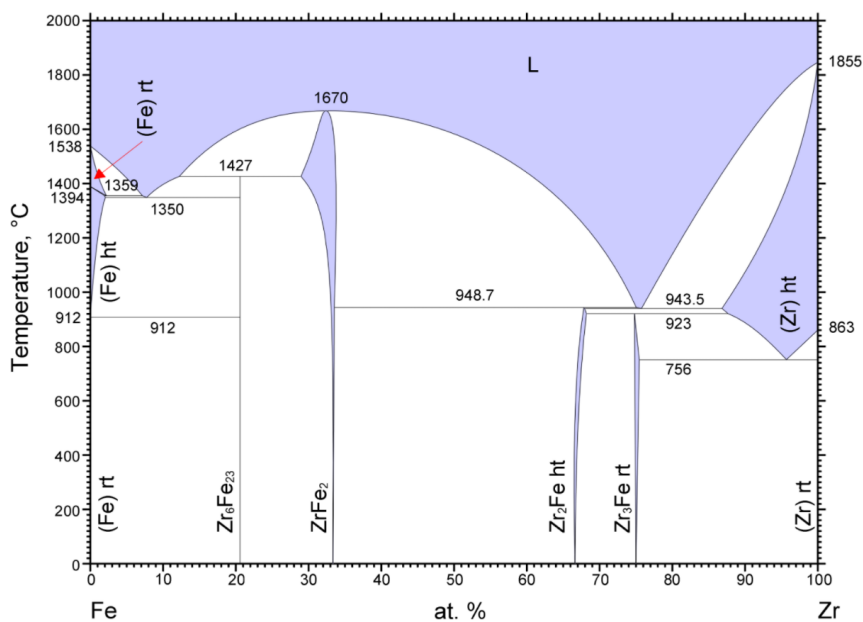


Figure 113: Binary Fe-Zr phase diagram. The eutectoid point at 928 °C must be avoided to not destroy the sample holder. Single-phase areas are drawn in purple, double-phase areas in white. From [205].

Table 10 explains the sample production process in this study. In addition to three stainless steel and eight U-Mo samples which were pre-heated before and heated during PVD coating, a reference U-Mo sample without any additional heating was produced. Figure 114 shows a photograph of the PVD coating process of a heated micro-size sample in the HSK3 device.

Table 10: Production process for Zr-coated samples with substrate heating. After the samples are prepared and installed into the PVD process chamber, the chamber is evacuated and the sputtering target is cleaned first. After a pre-heating step, the heating power is adjusted and the PVD coating process begins. Finally, sufficient time is given to allow cooling of the samples.

Step	Description
Cleaning	The sample is cleaned outside of the glovebox as described in section 3.2.1.
Weighing	The sample mass is determined by weighing with a precision scale inside the glovebox.
Installation	The sample is installed into the left position of the micro-size sample holder and the distance between sputtering target and sample is set to 30 mm.
Evacuation	The process chamber is evacuated down to base pressure.
Target cleaning	A process pressure of $\sim 4 \cdot 10^{-3}$ mbar argon is set. The sputtering target is cleaned by sputtering with 300 W for 5 minutes onto the closed substrate shutter. Afterwards, the sputtering power is shut down and the substrate shutter is opened.
Pre-heating	The sample is pre-heated by setting the heating power to the desired value until the thermal equilibrium is reached.
PVD coating	The sample is coated with Zr for 90 minutes at a sputtering power of 300 W. The heating power is adjusted to keep the temperature constant.
Cooling	All power supply units are shut down and the sample is allowed to cool down for at least 120 minutes.
Weighing	The sample is weighed again and the thickness of the deposited Zr layer is calculated.

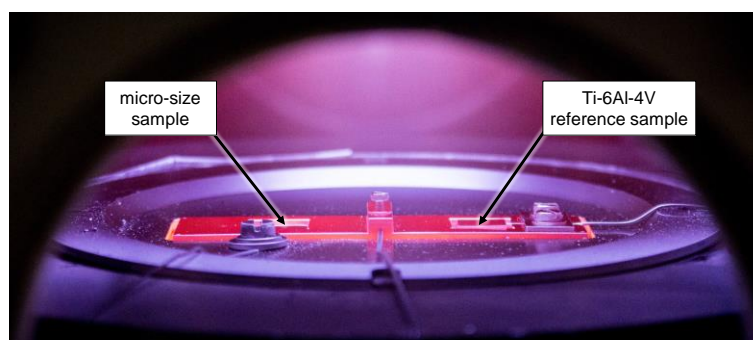


Figure 114: PVD coating of a heated micro-size sample in the HSK3 device. While the sample holder is glowing red due to the radiation heating from below, a Zr layer is deposited onto the samples from the sputtering source above (not depicted).

Two sample materials were used: stainless steel samples with 0.25 mm thickness and U-Mo samples with 0.33 mm thickness. The utilized Zr sputtering target was made from reactor-grade Zr, with an oxygen content of 340 ppm [206] and a hardness of 138 ± 9 HV1. Table 11 lists all samples produced in this study, together with the heating power set points.

Table 11: Overview of Zr-coated samples with substrate heating. Three stainless steel and nine U-Mo samples were produced in this study. All samples were produced with a sputtering power of 300 W.

Sample ID	Material	Desired temperature	Heating power during pre-heating	Heating power during sputtering
SS+Zr-500	SS	500 °C	192 W	101 W
SS+Zr-650	SS	650 °C	373 W	290 W
SS+Zr-800	SS	800 °C	639 W	550 W
U-Mo+Zr-cold	U-Mo	n/a*	0	0 W
U-Mo+Zr-400	U-Mo	400 °C	107 W	25 W
U-Mo+Zr-500	U-Mo	500 °C	192 W	90 W
U-Mo+Zr-550	U-Mo	550 °C	258 W	140 W
U-Mo+Zr-600	U-Mo	600 °C	309 W	198 W
U-Mo+Zr-650	U-Mo	650 °C	392 W	290 W
U-Mo+Zr-700	U-Mo	700 °C	492 W	375 W
U-Mo+Zr-750	U-Mo	750 °C	604 W	453 W
U-Mo+Zr-800	U-Mo	800 °C	738 W	600 W

*) measured temperature: 360 °C

Figure 115 shows a typical process diagram from the sample production, exemplarily for the U-Mo+Zr-700 sample. After approximately 60 minutes of evacuation of the process chamber, the sputtering target is cleaned for 5 minutes. Afterwards, the samples are pre-heated with the heating power predicted from Figure 110 until the thermal equilibrium is reached. When the sputtering power is enabled for PVD coating, the heating power is reduced to the value predicted from Figure 112. Discrepancies between the measured sample temperature and the expected temperature from the process characterization presumably result from differences in the sample surface structure and are compensated by small adjustments of the heating power during the process. After 90 minutes of PVD coating with a sputtering power of 300 W, all power supply units are shut down and the sample is left in the process chamber for at least 120 minutes, until the sample temperature is lower than 50 °C (not depicted).

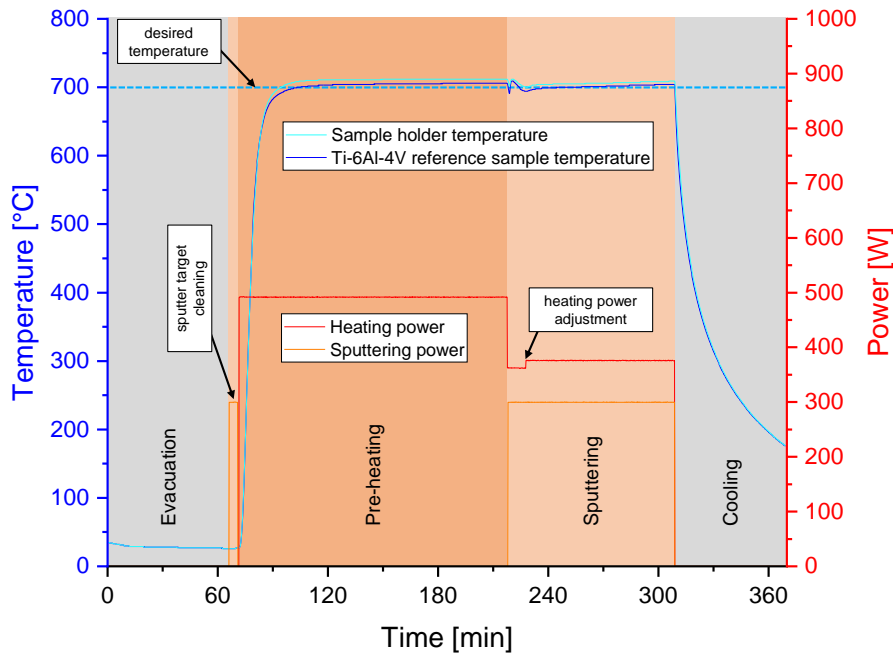


Figure 115: Process diagram of the U-Mo+Zr-700 sample production. After evacuation of the process chamber and cleaning of the sputtering target, the samples are pre-heated until thermal equilibrium is reached and the sputtering power is enabled for 90 minutes. As the process is monitored live by the operator, small adjustments of the heating power can be performed to keep the sample temperature as close as possible to the desired temperature.

5.2.4 SAMPLE CHARACTERIZATION

After their production, the samples were visually inspected and cross-sections were prepared for characterization with optical and scanning electron microscopy as well as hardness measurement of the deposited Zr layer. Ductility tests using the bending method could not be performed with micro-size samples, as the U-Mo substrate material usually cracks at the small bending radii needed.

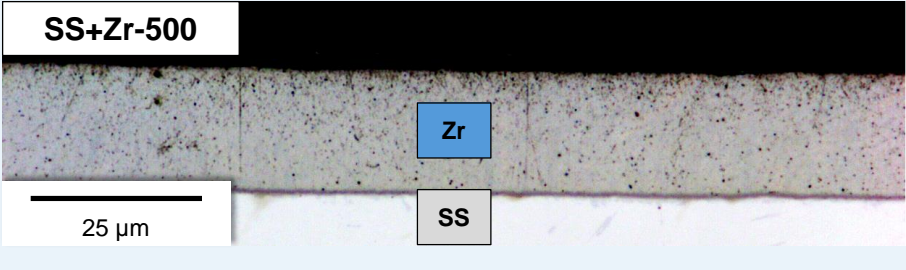
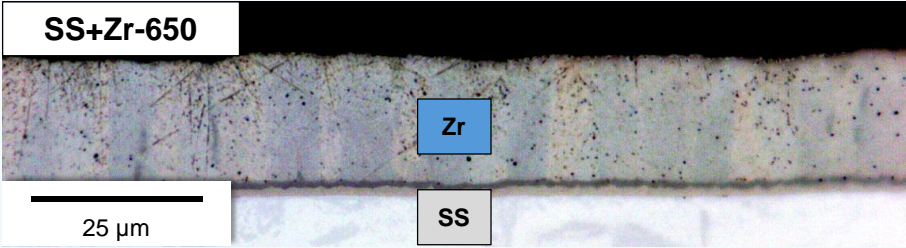
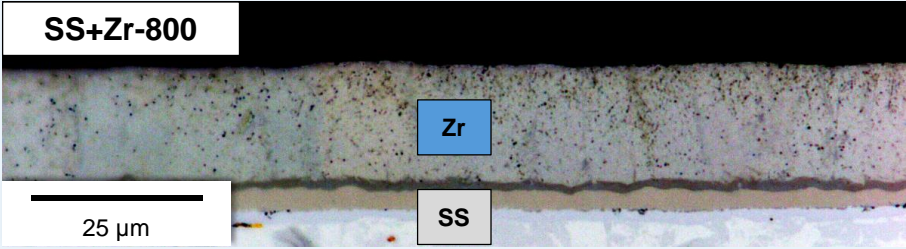
Due to the large hardness difference between the substrate and the Zr layer, the preparation of these samples is challenging. Often observed preparation artifacts, especially for soft Zr layers, are rounded edges at the surface of the Zr layer and diamonds impressed into the Zr layer during the final polishing steps. Both effects can be seen at the stainless steel samples in Table 12 and were mostly avoided for the U-Mo samples by lowering the sample pressing force during polishing and by choosing a firmer polishing cloth.

The visualization of the Zr grain structure by optical microscopy is challenging as well. With bright-field optical microscopy, which was used for the stainless steel samples, the grain structure is barely visible and can only be revealed by digital image processing. Therefore, polarized light microscopy with very narrow polarization angles was used for the U-Mo samples, leading to a significant improvement in grain visibility.

Stainless steel samples

Table 12 summarizes the optical microscopy and hardness measurement results of the three stainless steel samples heated to 500 °C, 650 °C and 800 °C, respectively.

Table 12: Micrographs of Zr-coated stainless steel samples with substrate heating. The Zr layer grain structure is barely observable and only a few grains are visible at the SS+Zr-650 and SS+Zr-800 samples. The layer hardness does not significantly change at various sample production temperatures.

Optical micrograph (polarized light)	Zr layer hardness
 <p>SS+Zr-500</p> <p>25 μm</p> <p>Zr</p> <p>SS</p>	<p>108 ± 8 HV0.01</p>
 <p>SS+Zr-650</p> <p>25 μm</p> <p>Zr</p> <p>SS</p>	<p>104 ± 17 HV0.01</p>
 <p>SS+Zr-800</p> <p>25 μm</p> <p>Zr</p> <p>SS</p>	<p>114 ± 15 HV0.01</p>

Even though the cleaning of the substrates was done at laboratory atmosphere and no plasma cleaning step was performed prior to the PVD coating, no Zr layer delaminations were observed at the stainless steel samples. By optical microscopy, the grain structure of the Zr layer is barely visible and numerous black dots can be found in the layer. Judging by the regularity and shape of these dots, they are not considered to be porosities but impressed diamonds from the last polishing step. By digital image processing, a few grains were made visible in the SS+Zr-650 and SS+Zr-800 samples.

The almost constant measured Zr layer hardness of ~ 110 HV0.01 for all three samples is remarkably lower than hardness of the sputtering target. Therefore, it is assumed that substrate heating promotes the formation of Zr layers with mechanical properties comparable to an annealed state. Due to these hardness values, the absence of growth defects, and by visually comparing the grain structures with the structures depicted in Figure 41, it is concluded that the preferred growth structure type C or higher is reached in these samples. This is also in accordance with the growth structures predicted for various process parameters in Figure 52.

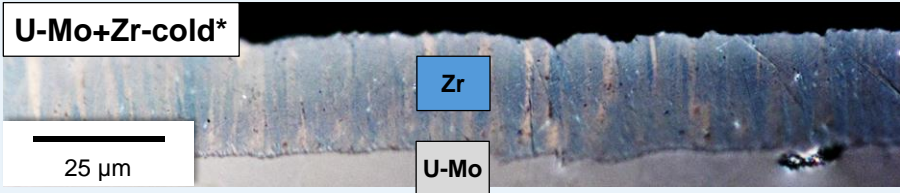
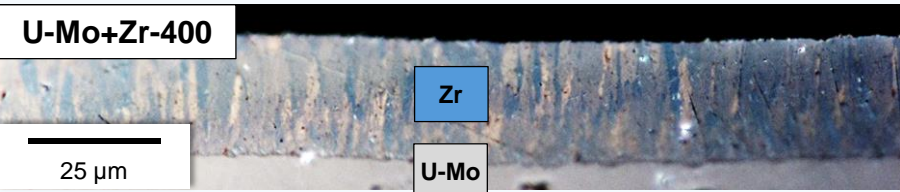
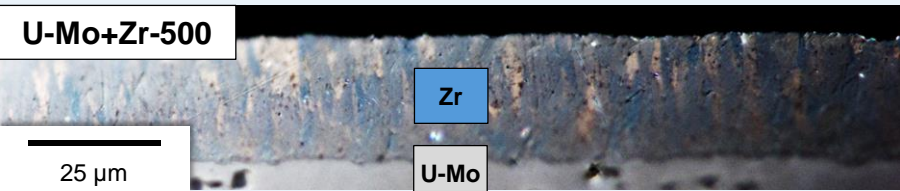
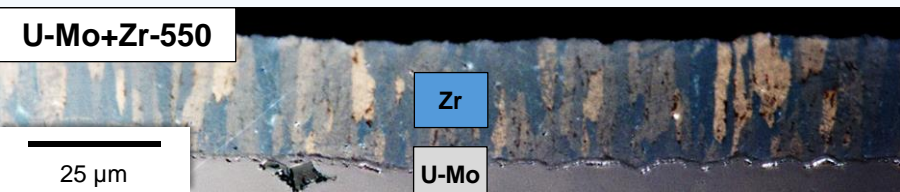
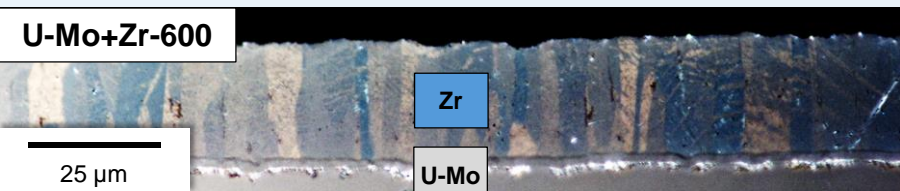
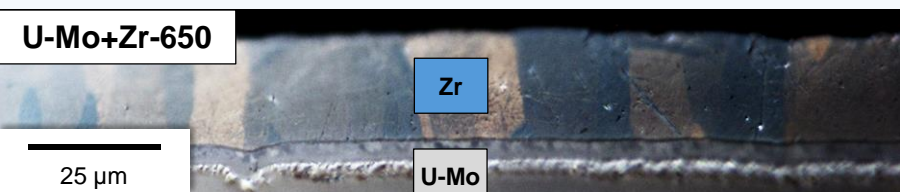
In the SS+Zr-650 and SS+Zr-800 samples, the formation of interaction layers between the stainless steel substrate and the Zr layer can be observed, with two intermetallic phases clearly distinguishable. Looking at the binary Fe-Zr phase diagram in Figure 113, several phases are possible to be formed at

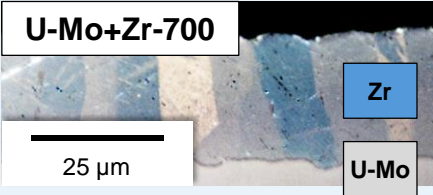
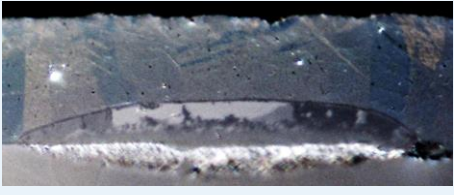
the respective temperatures. However, as the Fe-Zr interaction behavior is not the subject of this study, it is not further discussed here.

U-Mo samples

Table 13 summarizes the optical microscopy and hardness measurement results of the nine U-Mo samples with temperatures from 360 °C to 800 °C.

Table 13: Micrographs of Zr-coated U-Mo samples with substrate heating. Significant differences in the Zr layer grain structure can be seen between the various samples, while the hardness remains almost constant. At sample production temperatures > 700 °C, areas with (right pictures) and without (left pictures) U-Mo/Zr interaction were found.

Optical micrograph (polarized light)	Zr layer hardness
<p>U-Mo+Zr-cold*</p>  <p>*) measured temperature: 360 °C</p>	123 ± 15 HV0.01
<p>U-Mo+Zr-400</p> 	109 ± 6 HV0.01
<p>U-Mo+Zr-500</p> 	110 ± 8 HV0.01
<p>U-Mo+Zr-550</p> 	101 ± 6 HV0.01
<p>U-Mo+Zr-600</p> 	99 ± 9 HV0.01
<p>U-Mo+Zr-650</p> 	89 ± 2 HV0.01

 <p>U-Mo+Zr-700</p> <p>25 µm</p> <p>Zr</p> <p>U-Mo</p>		<p>94 ± 3 HV0.01</p>
 <p>U-Mo+Zr-750</p> <p>25 µm</p> <p>Zr</p> <p>U-Mo</p>		<p>101 ± 8 HV0.01</p>
 <p>U-Mo+Zr-800</p> <p>25 µm</p> <p>Zr</p> <p>U-Mo</p>		<p>99 ± 5 HV0.01</p>

Different to the process established for the EMPIRE fabrication campaign, all U-Mo samples were chemically cleaned at laboratory atmosphere and no plasma cleaning step was performed prior to PVD coating. It must thus be assumed that the sample surface is fully covered with adsorption and reaction layers from atmospheric contaminants such as O₂, N₂ and water vapor. However, no Zr layer delaminations were observed at any time, including the U-Mo+Zr-cold sample, even after several days of storage at laboratory atmosphere after coating. Obviously, the adsorption and reaction layers formed in the time period between chemical cleaning and transfer into the glovebox for PVD coating do not impair the layer adherence in the first place.

Due to improvements to the sample polishing process, edge rounding of the surface of the Zr layer as well as impressed diamonds inside the Zr layer were avoided to a large extent at the U-Mo+Zr samples. Judging from their irregular shape and distribution, the remaining large dark spots inside the Zr layer are mostly considered to be porosities – best visible at the U-Mo+Zr-550 sample – or scratches – best visible at the U-Mo+Zr-750 sample. Dark spots inside the U-Mo substrate typically are uranium carbide inclusions from the U-Mo foil fabrication process. Bright spots at the U-Mo/Zr interface – visible for sample production temperatures of 550 °C and above – are part of the U-Mo/Zr interaction layer.

Similar to the stainless steel samples, the Zr layer hardness on the U-Mo samples is remarkably lower than the hardness of the sputtering target, as long as additional substrate heating is applied. The U-Mo+Zr-cold sample without any additional substrate heating presents a slightly higher hardness, which is comparable to the sputtering target hardness. This confirms the assumption that substrate heating promotes the formation of Zr layers with mechanical properties comparable to an annealed state. Even though no bending tests were performed due to small sample size, bending tests performed previously on mini-size stainless steel samples showed a high ductility of the deposited Zr layers when heating the substrate [14]. However, the ductility of the formed U-Mo/Zr interaction layers remains unknown.

A general tendency can be observed when looking at the Zr layer grain structures: with increasing sample production temperature, the grains become significantly coarser. From the layer hardness values, the absence of growth defects, and by visually comparing the grain structures with the structures depicted in Figure 41, it is concluded that the preferred growth structure type C or higher is reached for all samples heated to 400 °C or more. Above 650 °C, the grain structure starts to resemble structure type D and at

800 °C, it even partly resembles a recrystallized structure of type E. The U-Mo+Zr-cold sample resembles a structure of type B to C. Again, this is in accordance with the growth structures predicted for various process parameters in Figure 52.

Starting at sample production temperatures of 550 °C, a thin interaction layer forms at the U-Mo/Zr interface, which gets thicker with increasing temperatures. Samples produced at 600 - 650 °C also very closely resemble the typical characteristics of co-rolled Zr coatings, as depicted in Figure 27. At 700 °C and above, the occurrence of a U-Mo/Zr interaction layer becomes continuously less with increasing sample production temperature. Only a few spots (at 700 °C) respectively a single spot (at 800 °C) with significant U-Mo/Zr interaction are found, as shown in the right pictures in Table 13. This unexpected behavior is assumed to originate from a few nm thick uranium oxide layer, which may form on the U-Mo substrate surface during the pre-heating step from the residual oxygen in the vacuum chamber atmosphere. Above a certain temperature, the thickness of this oxide layer may become sufficient to act as an interdiffusion barrier between the U-Mo substrate and the Zr layer. The remaining few interaction spots are believed to originate from small topography defects of the U-Mo substrate surface, which can disturb the formation of such a protective uranium oxide layer. When an interaction spot forms at such a location, the topography defect may not be visible by optical microscopy anymore due to the covering with interaction layers, which typically extend several μm into the U-Mo substrate. An example of a clear link between a defect in the U-Mo substrate and an interaction spot can be seen in in Figure 116. It was tried to confirm the presence of a uranium oxide layer by an EDX measurement, however this was not possible with the available equipment due to its resolution limitation.

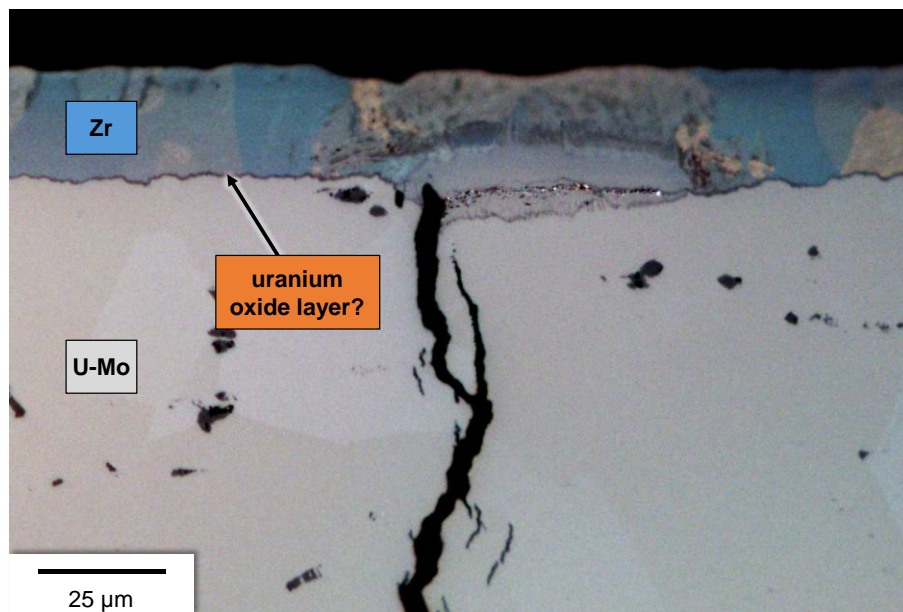


Figure 116: Optical micrograph (polarized light) of an interaction spot in sample U-Mo+Zr-800. While most of the U-Mo/Zr interface does not show any interaction layer above a sample production temperature of 700 °C, localized defects of the U-Mo substrate surface such as cracks may disturb the growth of a protective uranium oxide layer. At such locations, interaction spots are believed to form.

The U-Mo/Zr interaction behavior was subsequently investigated using SEM and EDX. As shown in Figure 117 c and e and further confirmed with EDX in Figure 118, the interaction layer consists of multiple distinct phases at the interface, in good accordance with the U-Mo/Zr interaction behavior predicted from literature. Starting from bulk U-Mo with the original composition, a several μm wide area lean in Mo is found, in which many Mo_2Zr crystals precipitate in the form of dark spots. At the

other side of the Matano plane, a several μm wide phase rich in U and Zr is found. Taking into account the binary U-Zr phase diagram in Figure 13 and looking at the continuous respective increase and decrease of Zr and U in this phase, it is likely to be the high-temperature Zr β phase (bcc), which is isostructural to the high-temperature U γ phase and the Mo α phase and therefore allows a significant incorporation of these elements.

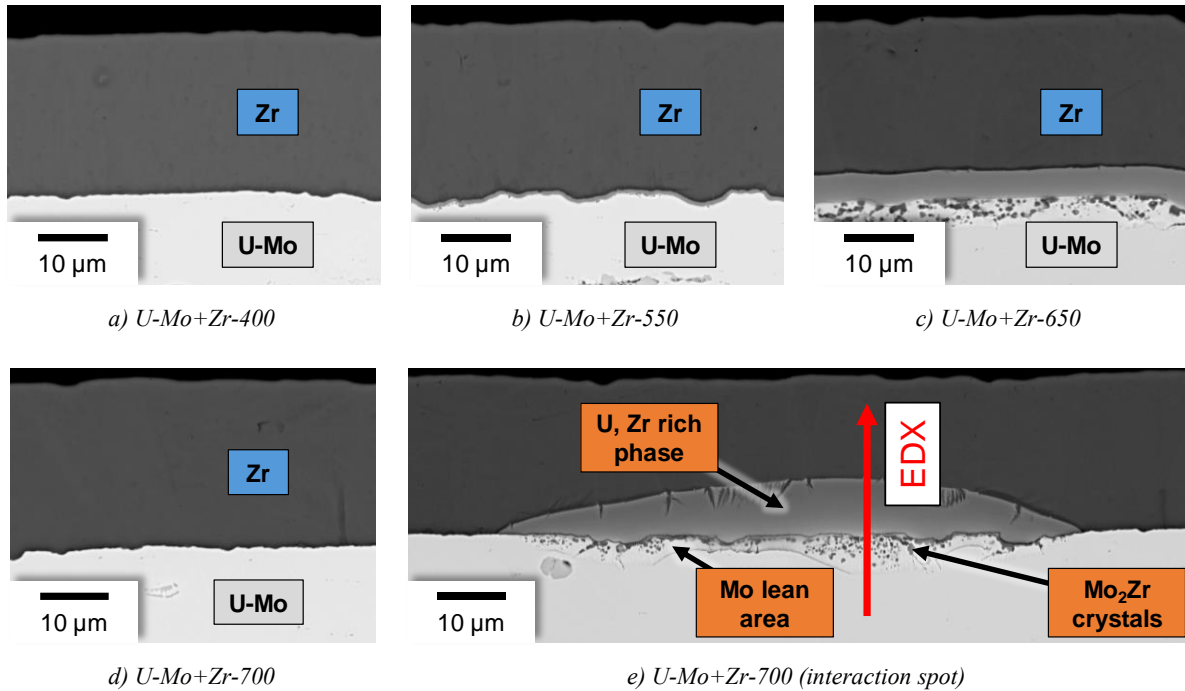


Figure 117: SEM micrographs (BSE detector) of U-Mo+Zr samples heated to various temperatures during PVD coating. While at 400 °C, no interaction layer is observed (a), a thin interaction layer starts to form at the U-Mo/Zr interface at 550 °C (b). At 650 °C, multiple distinct phases are found at the interface (c). At 700 °C, large parts of the interface do not exhibit interaction layers (d), whereas distinct interaction spots with phases similar to the 650 °C sample can be found at some locations (e). The red line indicates the path of the EDX line scan displayed in Figure 118.

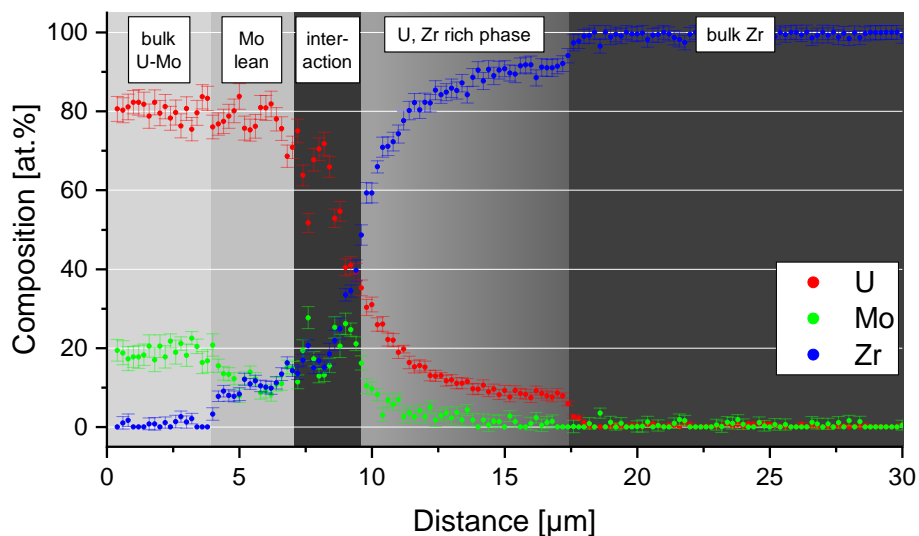


Figure 118: EDX line scan across a U-Mo/Zr interaction spot at the U-Mo+Zr-700 sample. After the bulk U-Mo, a several μm wide area lean in Mo is found. Near the Matano plane, strong interaction occurs with many Mo_2Zr precipitates. At the other side, a phase rich in U and Zr is found before the bulk Zr.

5.2.5 IMPLICATIONS ON THE FULL-SIZE PVD COATING PROCESS

An optimum substrate temperature for the PVD coating process, which delivers the desired dense and coarse-grained Zr layers, does not exist under the condition of no U-Mo/Zr interaction layer formation and the avoidance of the temperature range of 400 - 575 °C of fast U-Mo γ phase decomposition. A reliable reproduction of the seemingly promising interaction behavior at substrate temperatures above 700 °C, e.g. by the intentional oxidation of the U-Mo surface, seems hardly feasible due to the typically irregular U-Mo foil surface with many unavoidable topography defects.

Because of these results, and due to the increased complexity and longer processing times from pre-heating and cooling, the approach of substrate heating is not recommended as first choice for the full-size PVD coating process. Preferably, experiments on an optimized biasing approach should be performed instead. Nevertheless, the optical micrographs and hardness measurements of the Zr layers deposited at various sample temperatures gathered in these experiments allow a good assessment of other Zr-coated samples produced within this thesis.

In case the post-irradiation examination of EMPIrE LEU fuel plates with co-rolled Zr coating indicates a beneficial irradiation behavior of the U-Mo/Zr interaction layers, substrate heating should be still considered for the full-size PVD coating process. It was shown in this study that the typical co-rolled Zr layer characteristics can be reproduced with PVD by setting a substrate temperature of 600 - 650 °C. Thus, it is recommended to still envisage the potential later inclusion of a substrate heating option into the full-size PVD coating device. Ideally, this heating option shall not make use of a time-lagging and complex radiation heater element but other solutions to directly heat the substrate, e.g. by electrical current.

5.3 OPTIMIZED SUBSTRATE BIASING FOR PVD COATING

Similar to the optimized substrate heating approach studied in the previous section, optimizations to the substrate biasing technique are considered to be a promising approach to increase the ductility of the deposited Zr layer and therefore to eliminate its cracking during the cladding application process.

The experimental mini-size PVD coating process developed for the EMPIrE fabrication campaign [12,14] was carried out by DC magnetron sputtering with a sputtering power of 300 W and a substrate biasing voltage of -300 V at a target-substrate distance of 30 mm and a process pressure of $\sim 4.0 \cdot 10^{-3}$ mbar argon. Using these parameters, the required minimum layer thickness of $\geq 25 \mu\text{m}$ Zr on both sides of the substrate was reached after 105 minutes of PVD coating. The deposited layer, which is depicted exemplarily in Figure 119, is dense and exhibits a fine-grained microstructure with a measured hardness of $266 \pm 7 \text{ HV}0.01$, thus significantly harder than the sputtering target. However, due to the absence of porosities or other growth defects, the deposited layer is still classified as growth structure type C. With SEM imaging, no interaction between the Zr layer and the U-Mo substrate can be observed.

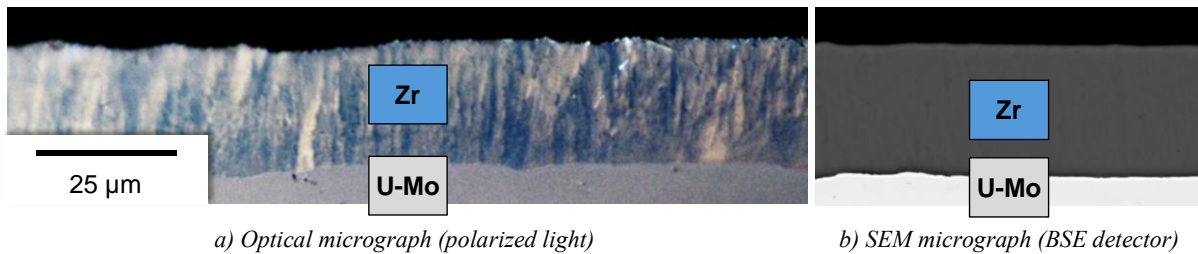


Figure 119: Micrographs of a U-Mo substrate with a Zr layer deposited with substrate biasing. The Zr layer is dense and exhibits a very fine-grained microstructure.

At these parameters, the process delivers an average effective layer growth rate of $0.237 \mu\text{m}/\text{min}$ on the substrate, which is $\sim 14\%$ lower than the average layer growth rate without substrate biasing due to the significant re-sputtering effect. Thus, the resulting Zr particle flux to the substrate is calculated to $1.97 \cdot 10^{16}$ atoms/ $\text{cm}^2 \text{ s}$. The average substrate current density achieved at a substrate biasing voltage of -300 V is $1.14 \text{ mA}/\text{cm}^2$, which equals an ion flux to the substrate of $7.13 \cdot 10^{15}$ ions/ $\text{cm}^2 \text{ s}$. Thus, the ratio R_i of impinging ions to Zr atoms on the substrate is ~ 0.36 and the average effective energy contribution of the ions $\langle E_{eff,i} \rangle$ is $\sim 92 \text{ eV}$ per deposited Zr atom.

As proposed before, the ductility of the deposited Zr layer could be improved by a reduction of the substrate biasing voltage to $\sim -100 \text{ V}$ or less. To maintain the energy contribution of the ions to the adatom mobility – while keeping the layer growth rate at the current value – the ion flux to the substrate consequentially must be increased by a factor of approximately three in return.

The possible techniques to do so generally aim for an increase in the plasma ionization density near the substrate. On one hand, this can be accomplished by extending the sputtering plasma from the sputtering source towards the substrate using unbalanced magnetrons of type 2. The existing sputtering source in the mini-size PVD coating device is a strongly balanced magnetron and extensive rebuilding work would be required to turn it into an unbalanced magnetron sputtering source, making the source unavailable for other experiments in the meantime. Thus, this possible solution can only be reasonably studied with a newly procured sputtering source in the full-size PVD coating device.

On the other hand, the ionization density can be increased by increasing the number of collisions between electrons and gas atoms near the substrate using one of the following methods:

-
- Similar to magnetron sputtering sources, the trajectories of the electrons in the plasma can be extended, e.g. with a static magnetic field parallel to the substrate surface.
 - Additional electrons can be inserted into the plasma near the substrate, e.g. from electron emitters such as glowing tungsten filaments.

Within an M.Sc. thesis [207], experimental studies on those two methods were carried out in the mini-size PVD coating device and reference is made to this thesis wherever applicable.

5.3.1 PLASMA ENHANCEMENT BY STATIC MAGNETIC FIELDS

Generating a static magnetic field near the surface of a sputtering target is a common technique to extend the trajectories of electrons in the plasma and thus to locally increase the plasma ionization density. This concept is as well applicable to substrate biasing. However, the common practice of placing permanent magnets below the surface would lead to a non-uniform magnetic field across the substrate, leading to a non-uniform ionization density distribution and thus a non-uniform erosion of the substrate surface. In contrast, the placement of permanent magnets at opposite sides above the substrate can deliver a more uniform static magnetic field and is thus studied with the following experiments.

Experimental setups

Two different geometrical arrangements of permanent magnets were tested, as depicted in Figure 120 a and Figure 121 a. For both cases, rectangular NdFeB permanent magnets with a remanence of 1.2 T were used. The stainless steel substrates with a size of 50 mm x 20 mm x 0.25 mm were positioned centrally on the biasing Mo plate of the substrate holder. The utilized Zr sputtering target was made from industrial-grade Zr 702, with an oxygen content of 1400 ppm [208] and a hardness of 234 ± 16 HV1.

In the first experimental setup, two permanent magnets with a size of 70 mm x 10 mm x 3 mm each were glued in flat orientation onto a copper frame. To vary the vertical distance d_{MS} between the magnets' mid-plane and the substrate surface, the copper frame can either be laid onto the aperture ring of the substrate holder ($d_{MS} = 6.5$ mm) or put onto ceramic blocks ($d_{MS} = 19$ mm). The results of a COMSOL simulation and of a verifying measurement of the magnetic field strength above the substrate for $d_{MS} = 6.5$ mm are shown in Figure 120 b. While the magnetic field direction shows a high uniformity above the substrate, the field strength parallel to the substrate varies from 44 mT centrally above the sample to 182 mT at the edges of the sample.

In the second experimental setup, four permanent magnets – two on each side of the sample – with a size of 60 mm x 10 mm x 2 mm each were glued in upright orientation onto a copper frame. To vary the vertical distance d_{MS} between the magnets' mid-plane and the substrate surface, the copper frame can again either be laid onto the aperture ring of the substrate holder ($d_{MS} = 10$ mm) or put onto ceramic blocks ($d_{MS} = 22.5$ mm). A COMSOL simulation of the magnetic field strength above the substrate for $d_{MS} = 10$ mm is shown in Figure 121 b. Compared to the flat magnet configuration, this magnet configuration shows an overall higher magnetic field strength and a higher uniformity in between the magnets. However, near the substrate the magnetic field becomes less uniform up to an extent where the magnetic field direction inverts at the edges of the sample.

Results

In pre-experiments, the ability of both magnet configurations to create a dedicated plasma near the substrate – with no plasma from the sputtering source being present – was compared to identify the most suitable setup for the PVD coating experiments.

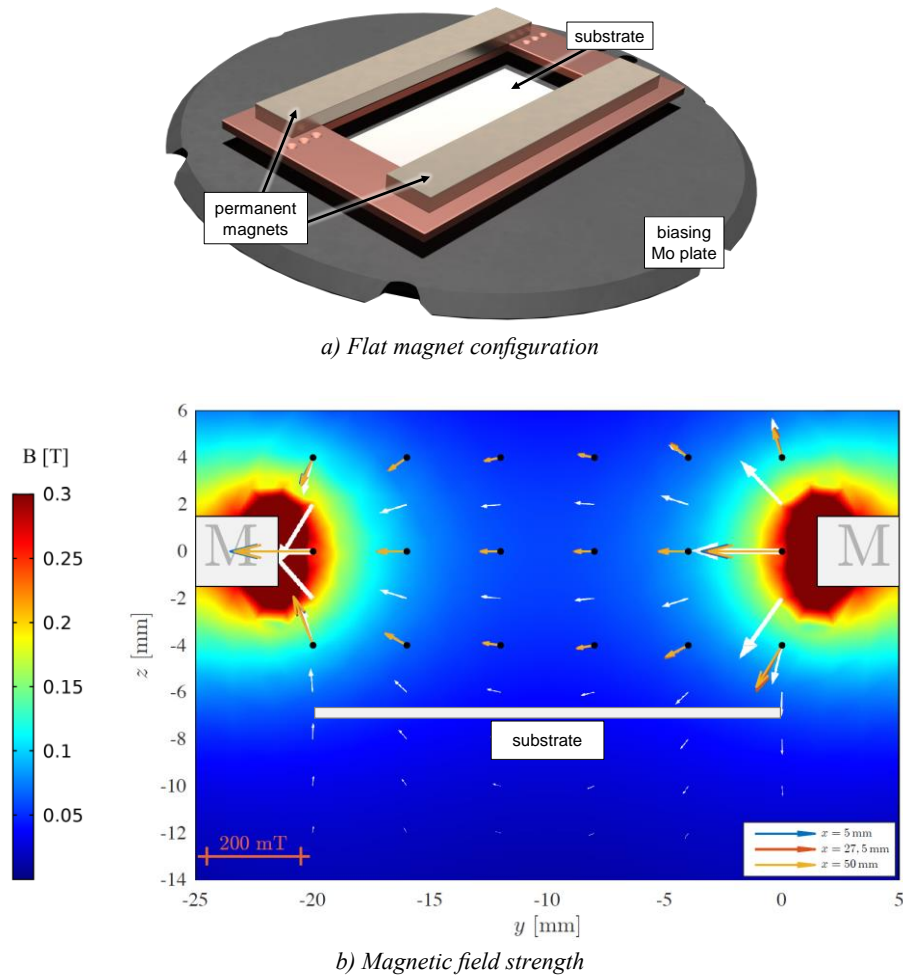
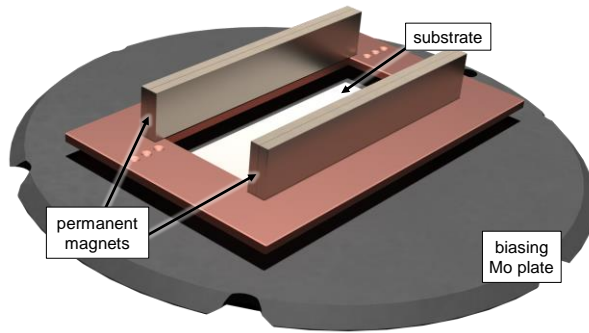


Figure 120: Experimental setup to establish a static magnetic field above the substrate (flat magnet configuration).

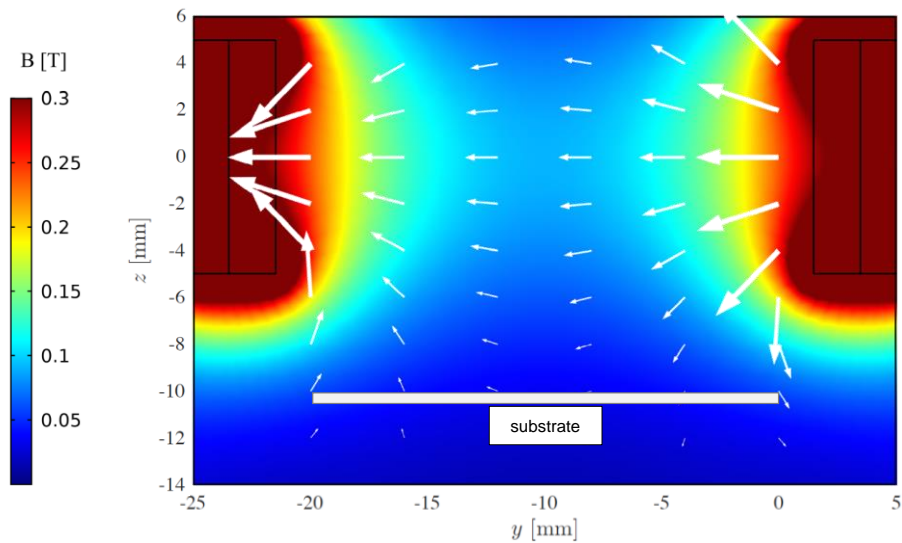
Two permanent magnets are glued flat onto a copper frame above the substrate (a). The magnetic field simulation (b, white arrows) is in good accordance with the measured values (blue, red, orange arrows). Simulation results after [207].

First, the necessary substrate voltage to ignite such a plasma was determined at various process pressures from 0.05 mbar to 0.5 mbar argon. Generally, both magnet configurations do not have a significant influence on the ignition voltage when placed directly on the aperture ring. However, when placed on ceramic blocks to increase the vertical distance d_{MS} between the magnets' mid-plane and the substrate surface, the ignition voltage is significantly reduced. For example, at a process pressure of 0.05 mbar argon, the ignition voltage is reduced from - 1000 V without magnetic field to - 700 V with the upright magnet configuration on ceramic blocks.

Subsequently, the substrate current density at the lowest possible process pressure of 0.05 mbar argon was measured with an active substrate plasma as a function of the substrate voltage. Based on the results of the previous experiment, both magnet configurations were placed on ceramic blocks and the substrate plasma was initiated first by applying the necessary ignition voltage before the substrate voltage was reduced. Figure 122 shows the results of this experiment. Up to a substrate voltage of - 200 V, no difference can be observed compared to the setup without magnets. At - 300 V, the substrate current density is increased from 0.1 mA/cm² to 0.2 mA/cm² using both magnet configurations. For higher substrate voltages, the increase remains in the order of 0.1 mA/cm² and thus the overall substrate current density remains small. As the flat magnet configuration delivers slightly higher values, the following PVD coating experiments with additional static magnetic fields are performed using this setup.



a) Upright magnet configuration



b) Magnetic field strength

Figure 121: Experimental setup to establish a static magnetic field above the substrate (upright magnet configuration). Four permanent magnets are glued upright onto a copper frame above the (a). The magnetic field simulation (b) shows a stronger and more uniform magnetic field than the flat configuration. Simulation results after [207].

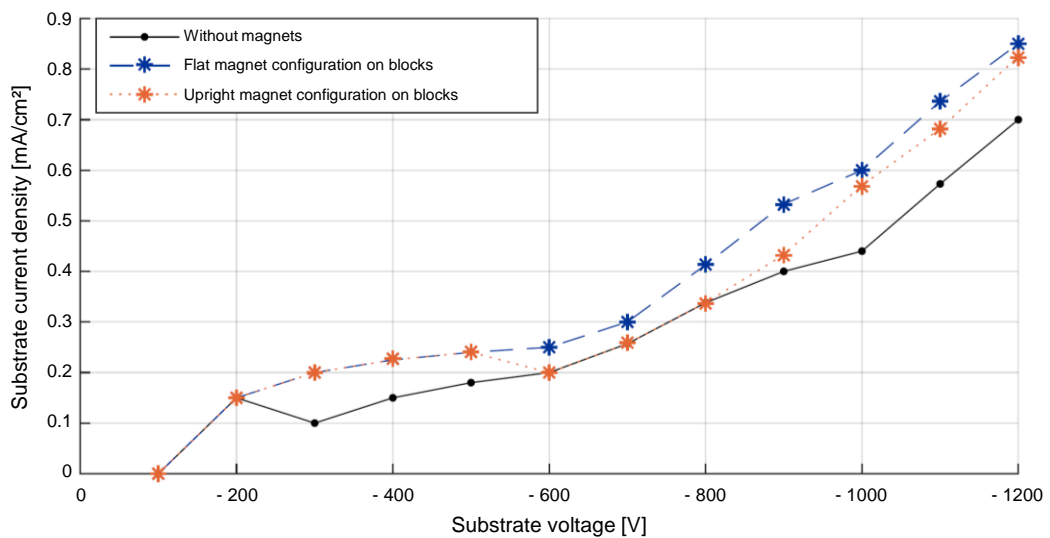


Figure 122: Achievable substrate current density with static magnetic fields without a sputtering plasma at 0.05 mbar process pressure. Up to a substrate voltage of - 200 V, no difference can be observed compared to the setup without magnets. At higher voltages, the substrate current density is increased by ~ 0.1 mA/cm². After [207].

Due to the positive results of the substrate current density measurement without any plasma from the sputtering source, the substrate current density was next measured with an active sputtering plasma as a function of the substrate biasing voltage. The process pressure was set to $7.8 \cdot 10^{-3}$ mbar argon and the sputtering power was set to 200 W. To reserve sufficient space for the magnet arrangements, the distance between the sputtering target and the substrate was set to 65 mm. Figure 123 shows the results of this experiment. Attention must be paid, as the substrate current density of 0.70 mA/cm^2 at a substrate biasing voltage of -300 V can not be directly compared to the value of 1.14 mA/cm^2 of the mini-size PVD coating process. Even though the same substrate biasing voltage was used, the mini-size process was carried out at higher sputtering power, lower process pressure and lower target-to-substrate distance – all these generally increasing the ion current to the substrate.

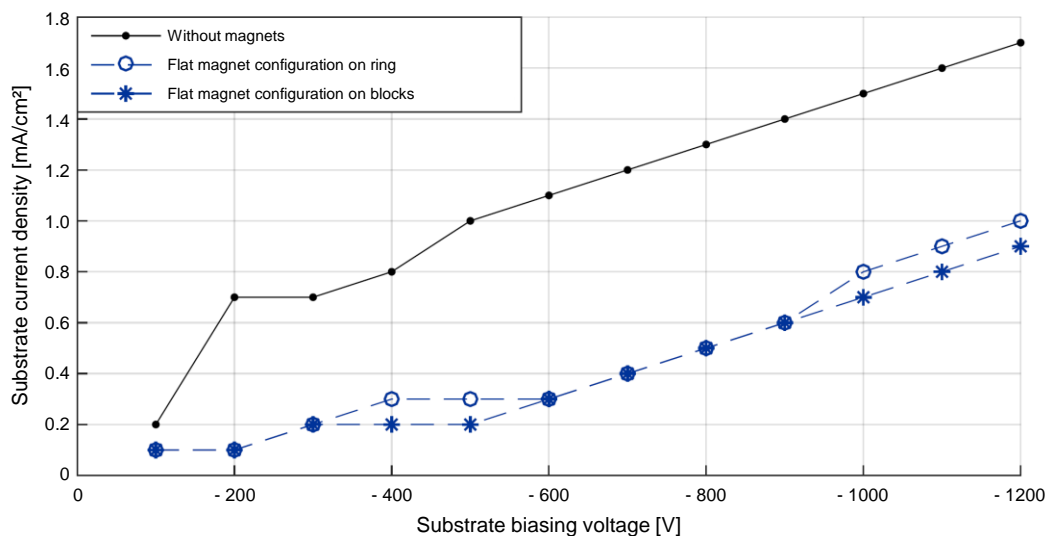


Figure 123: Achievable substrate current density with static magnetic field with a sputtering plasma at $7.8 \cdot 10^{-3}$ mbar process pressure. Compared to the experimental setup without magnets, the static magnetic fields generally decrease the substrate current density. After [207].

In contrast to the positive results of the pre-experiment without a sputtering plasma, the substrate current density is now unexpectedly decreased in the entire substrate biasing voltage range. It is assumed that the magnetic field – while being able to significantly enhance a dedicated substrate plasma – deflects the incoming ions from the sputtering plasma and thus undesirably reduces the ion flux to the substrate. To confirm this unfavorable result, three stainless steel samples with Zr coating were produced as summarized in Table 14. The general sample production procedure was similar to the one described in Table 10 for the optimized substrate heating studies, however a process pressure of $7.8 \cdot 10^{-3}$ mbar argon, a sputtering power of 200 W and a target-to-substrate distance of 65 mm were set. The substrate biasing voltage was set to -800 V to emphasize the effect of the different magnet configurations. During the deposition process, the substrate current was recorded and an average substrate current density was calculated afterwards. The average effective layer growth rate was determined by weighing the sample before and after the coating process, under the general assumption that any mass difference is due to the deposition or erosion of a Zr layer with bulk density of 6.5 g/cm^3 .

The substrate current densities in Table 14 confirm the measurement from Figure 123 and translate into ion fluxes to the substrate of $8.13 \cdot 10^{15} \text{ ions/cm}^2 \text{ s}$ (without magnets) and $3.13 \cdot 10^{15} \text{ ions/cm}^2 \text{ s}$ (with magnets). Due to the high substrate biasing voltage of -800 V , the energy of the impinging ions obviously was high enough to re-erode the sample surface up to the extent where the average effective

Table 14: Zr-coated stainless steel samples with substrate biasing and static magnetic fields. Three stainless steel samples were produced to study the effect of static magnetic fields on the PVD coating process with substrate biasing. All samples were produced with a sputtering power of 200 W and a substrate biasing voltage of - 800 V at a process pressure of $7.8 \cdot 10^{-3}$ mbar. Data from [207].

Sample ID	Magnet configuration	Average substrate current density	Average effective layer growth rate
SS+Zr-nomag	Without magnets	1.3 mA/cm ²	- 0.01 μm/min
SS+Zr-magflat_ring	Flat magnet configuration on aperture ring	0.5 mA/cm ²	0.05 μm/min
SS+Zr-magflat_blocks	Flat magnet configuration on ceramic blocks	0.5 mA/cm ²	0.03 μm/min

layer growth rate without magnets is negative. Therefore, the Zr particle flux, the impinging ion-to-atom ratio to the substrate and the energy contribution of the ions per deposited Zr atom could not be determined.

By visual inspection of the samples after the coating process, as shown in optical micrographs in Figure 124, a highly non-uniform surface texture is observed, which likely originates from the electrical field spikes at the edges of substrate due to the high substrate biasing voltage. In optical micrographs of cross-sections, the sample SS+Zr-nomag expectedly shows no deposited Zr layer at most locations – only at the outmost 1 mm width, a ~ 5 μm thick Zr layer can be found. The samples produced with magnetic field both present a few μm thin Zr layer, uniformly distributed across the surface. However, large areas of coating delamination can be observed at both samples produced with magnetic field after minutes (SS+Zr-magflat_blocks) to days (SS+Zr-magflat_ring) of storage in air.

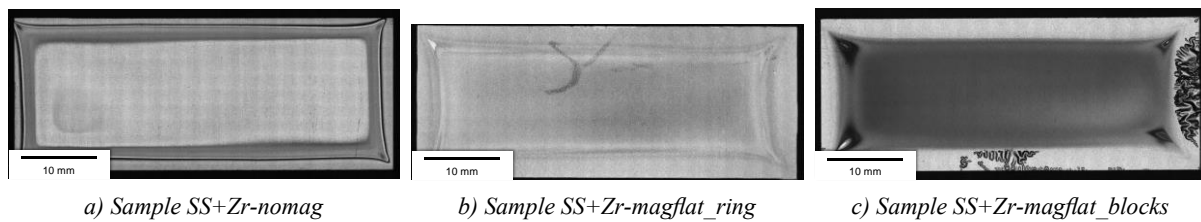


Figure 124: Optical micrographs of the sample surface after PVD coating with static magnetic fields. All samples show a non-uniform surface texture. While the sample produced without magnetic field (a) shows perfect coating adherence, the coating on the samples produced with magnetic field delaminates when stored in air. From [207].

5.3.2 PLASMA ENHANCEMENT BY ELECTRON EMISSION

As an alternative to the plasma enhancement by static magnetic fields, the ionization density near the substrate can also be increased by introducing additional electrons into the plasma. From various possible techniques to generate such electrons, the thermionic emission from glowing filaments can be implemented most easily into the mini-size PVD coating device and is thus studied with the experiments described hereafter.

To generate electrons, filaments need to be heated by the dissipation of electrical power P_{el} due to their electrical resistance $R(T_f)$:

$$P_{el} = \frac{U^2}{R(T_f)} \quad (51)$$

The most common materials for such filaments are tungsten and its alloys due to the high melting temperature of e.g. 3695 K [209] for pure tungsten. The electron emission current I_{el} from such a glowing filament can be estimated using the Richardson equation [210]:

$$I_{el} = a_R A T_f^2 e^{-\frac{W_A}{k_B T_f}} \quad (52)$$

Here, a_R is the Richardson constant, A is the surface area of the filament and W_A is the work function of the respective filament material. The temperature T_f of the filament can be calculated from the Stefan Boltzmann law:

$$P_{rad} = \sigma A \epsilon (T_f^4 - T_0^4) \quad (53)$$

Here, σ is the Stefan Boltzmann constant, ϵ is the filament's emissivity and T_0 is the ambient temperature. For pure tungsten, W_A is 4.55 eV [211] and ϵ can be estimated to 0.33 [212].

To select the ideal filament material and diameter regarding the electron emission current, mechanical stability and high-temperature resistance, a pre-experiment was performed. Here, pure tungsten filaments with different diameters were compared to a WLa20 filament (tungsten with 2.0 wt.% lanthanum oxide La_2O_3 added) with 0.70 mm diameter. WLa20 is often chosen for electron emitters due to its lower work function and improved high-temperature resistance compared to pure tungsten [213]. The filaments were heated with various heating powers using a DC heating PSU. The electron emission was stimulated by setting the entire filament to a negative voltage of - 30 V towards ground using a DC emission PSU, where the electron emission current was read. The results of this experiment are depicted in Figure 125. While very thin tungsten filaments generate high emission currents at low heating power, their poor mechanical stability at high temperature makes them unsuitable for this application. The WLa20 filament with 0.70 mm diameter represents the best compromise and was thus chosen for all further experiments.

Experimental setups

Two possibilities exist to bring electrons, which were generated by thermionic emission, into the plasma: (i) generating the electrons at a remote location and accelerating them into the plasma or (ii) generating the electrons directly inside the plasma. Both were tested with experimental setups in the mini-size PVD coating device, as depicted in Figure 126 a and Figure 127 a. The stainless steel substrates with a size of 50 mm x 20 mm x 0.25 mm were positioned centrally on the biasing Mo plate of the substrate holder.

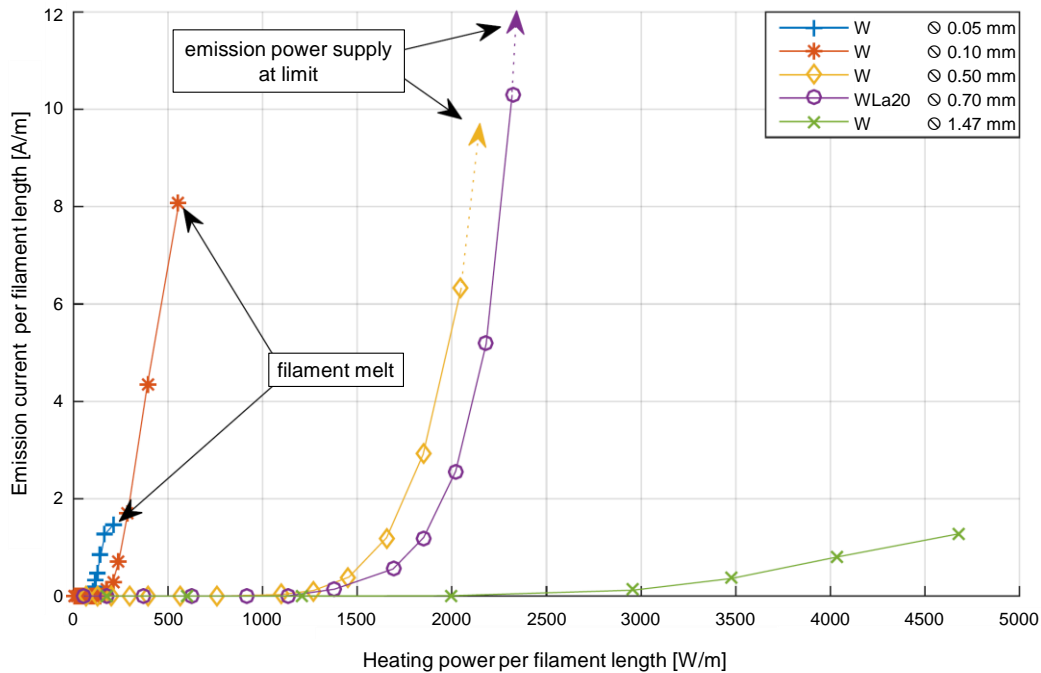


Figure 125: Measured electron emission currents of various tungsten filaments. While very thin tungsten filaments generate high emission currents at low heating power, their poor mechanical stability at high temperature makes them unsuitable for this application. The WLa20 filament with 0.70 mm diameter represents the best compromise. After [207].

The utilized Zr sputtering target was made from industrial-grade Zr 702, with an oxygen content of 1400 ppm [208] and a hardness of 234 ± 16 HV1.

The first experimental setup consists of a spiral WLa20 filament and an opposing 10 mm x 30 mm copper anode, both placed 20 mm sideways and 20 mm above the substrate. The electrical wiring is laid out so that the electrons are generated by heating the spiral filament using a DC heating PSU and are accelerated into the plasma by an electrical potential between the filament and the anode from a DC acceleration PSU. As alternatives to the wiring shown in Figure 126 b, two other electrical setups were tested:

- Positive terminal of the heating PSU and negative terminal of the acceleration PSU connected to ground.
- Positive terminal of the heating PSU and negative terminal of the acceleration PSU connected to ground. Spiral filament placed inside a stainless steel tube with 30 mm diameter at positive potential against ground.

The second experimental setup consists of a WLa20 filament loop with 150 mm total length, which is mounted directly above the substrate at approximately 15 mm vertical distance. The electrical wiring shown in Figure 127 b is simplified compared to the previous setup: the electrons are generated by heating the filament loop using a DC heating PSU and emitted into the plasma by a DC emission PSU, which sets the filament loop to a negative potential against ground.

Results

Similar to the experiments on plasma enhancement by static magnetic fields, the ability of both experimental setups to create a dedicated plasma close to the substrate – with no plasma from the sputtering source being present – was compared to identify the most suitable setup for the PVD coating experiments.

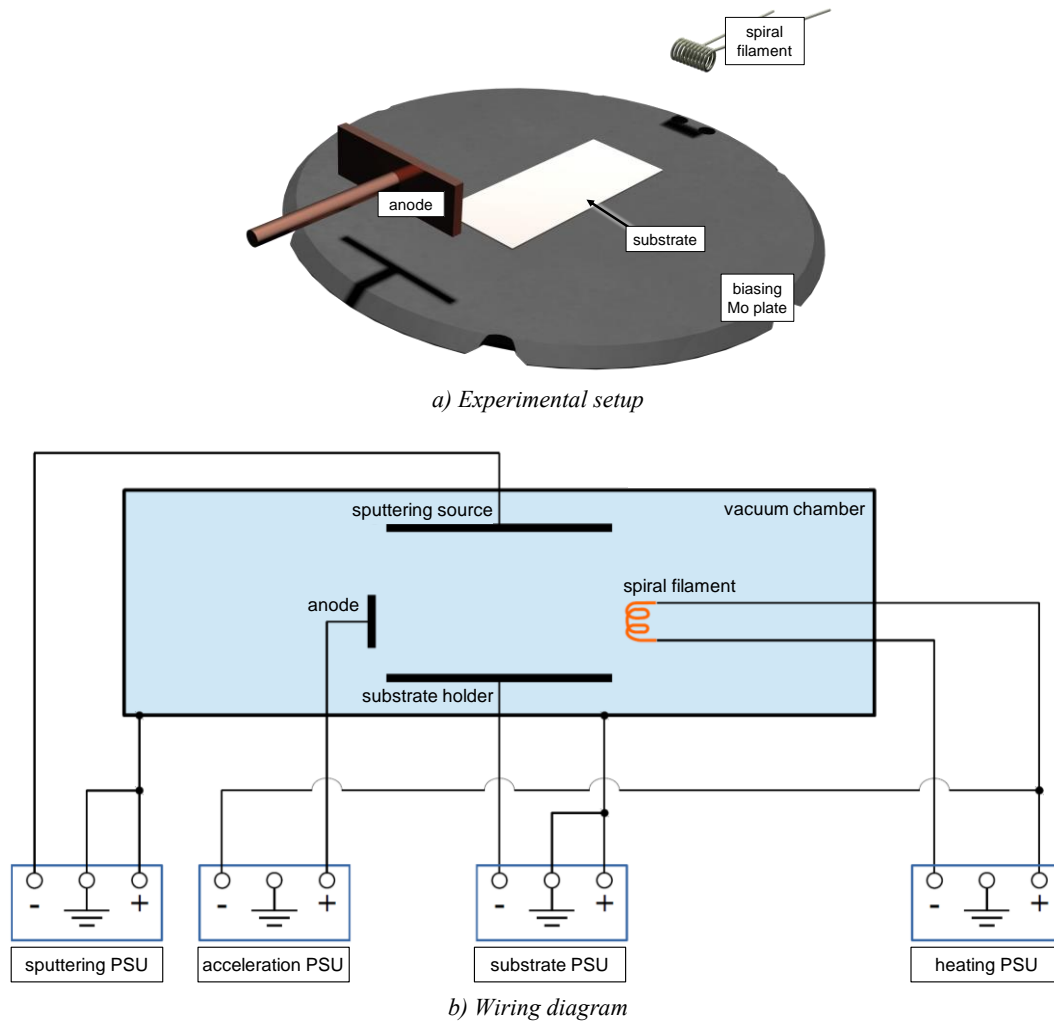


Figure 126: Experimental setup for electron emission through spiral filament and anode. A spiral filament and an anode are placed 20 mm sideways and 20 mm above the substrate, which is laid onto the biasing Mo plate of the substrate holder (a). The filament is heated by a heating PSU and the emitted electrons are accelerated into the plasma by an acceleration PSU (b). After [207].

The experimental setup with a bare spiral filament and an anode allowed the ignition of a weak substrate plasma at a process pressure of $1.3 \cdot 10^{-3}$ mbar argon, using a substrate voltage of - 800 V and an anode voltage of 70 V. However, this setup was quickly discarded prior to any detailed characterization due to the occurrence of many unwanted sparks and flashes at the entire substrate holder, no matter if the positive terminal of the heating PSU and the negative terminal of the acceleration PSU were connected to ground or not.

Placing the spiral filament inside a stainless steel tube at positive potential against ground while also connecting the positive terminal of the heating PSU and the negative terminal of the acceleration PSU to ground showed better results. The ignition of a substrate plasma was possible at a process pressure of $7.8 \cdot 10^{-3}$ mbar argon and a substrate voltage of - 300 V. With an anode voltage of 75 V and a tube voltage of 5 V, a substrate current density of 1.8 mA/cm^2 was reached. However, this setup was also discarded due to a highly unsteady and flickering plasma, which was mostly located in front of the tube and the anode, and not above the substrate as wanted.

In contrast, the experimental setup with a filament loop above the substrate showed very promising results. With a filament heating power of 1566 W/m, the filament glowed intensively and a strong

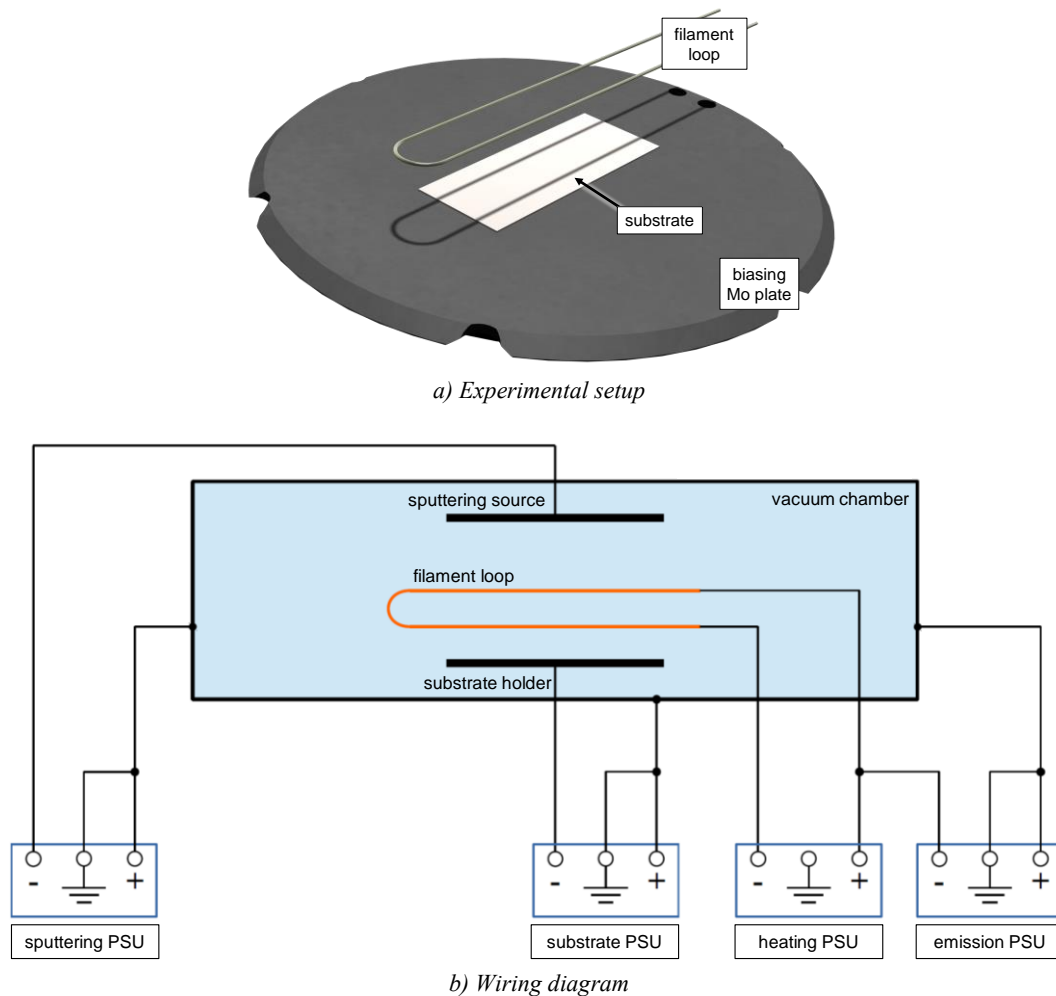


Figure 127: Experimental setup for electron emission through filament loop. A filament loop is installed 15 mm above the substrate, which is laid onto the biasing Mo plate of the substrate holder (a). The filament is heated by a heating PSU and the electrons are emitted by an emission PSU (b). After [207].

substrate plasma with a substrate current density of 4.8 mA/cm^2 could be ignited at a process pressure of $7.9 \cdot 10^{-3} \text{ mbar}$ argon, an emission voltage of -41 V and a substrate voltage of only -150 V . The plasma burned uniformly and consistent above the entire substrate and thus, this setup was chosen for the subsequent PVD coating studies.

The substrate current density was next measured with an active sputtering plasma at various sputtering powers and emission voltages as a function of the substrate biasing voltage. The process pressure was set to $7.8 \cdot 10^{-3} \text{ mbar}$ argon, the filament heating power was set to 1566 W/m and the distance between the sputtering target and the substrate was set to 42 mm , to reserve sufficient space for the filament loop. Figure 128 shows the results of this experiment. As can be seen, the electron emission from the filament loop increases the achievable substrate current density by up to one order of magnitude. Generally, higher sputtering powers and higher emission voltages lead to higher substrate current density values, which reach saturation typically at a substrate voltage of -100 V . Attention has to be paid, as the substrate current densities at a substrate biasing voltage of -300 V can not be directly compared to the value of 1.14 mA/cm^2 of the mini-size PVD coating process. Even though the same substrate biasing voltage was used, the mini-size process was carried out at 300 W sputtering power, lower process pressure and lower target-to-substrate distance – all these generally influencing the ion flux to the substrate.

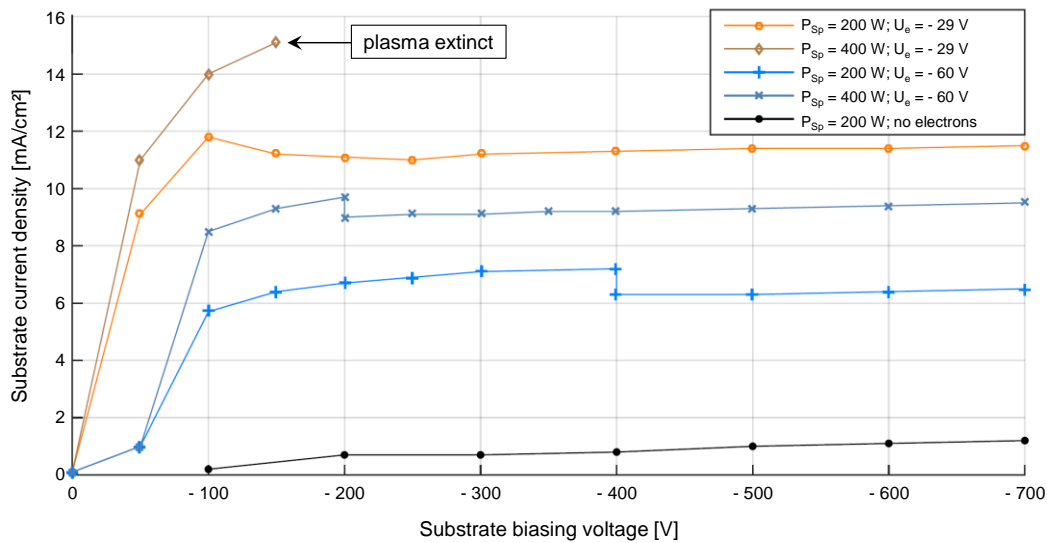


Figure 128: Achievable substrate current density by electron emission from a filament loop heated with 1566 W/m with a sputtering plasma at $7.8 \cdot 10^{-3}$ mbar process pressure. The additional electrons emitted from the filament loop increase the substrate current density by up to one order of magnitude. After [207].

To confirm these promising results, three stainless-steel samples with Zr coating were produced, as summarized in Table 15. The aim was to identify an optimum operation point with low substrate biasing voltage but high average substrate current density and high average effective layer growth rate. The general sample production procedure was similar to the one described in Table 10 for the optimized substrate heating studies, however a process pressure of $7.8 \cdot 10^{-3}$ mbar argon, a sputtering power of 400 W and a target-to-substrate distance of 42 mm were set. During the deposition process, the substrate current was recorded and an average substrate current density was calculated afterwards. The average effective layer growth rate was determined by weighing the sample before and after the coating process, under the general assumption that any mass difference is due to the deposition or erosion of a Zr layer with bulk density of 6.5 g/cm^3 .

Table 15: Zr-coated stainless steel samples with substrate biasing and electron emission. Three stainless steel samples were produced to study the effect of the emission of additional electrons on the PVD coating process with substrate biasing. All samples were produced with a sputtering power of 400 W at a process pressure of $7.8 \cdot 10^{-3}$ mbar. Data from [207].

Sample ID	Substrate voltage	Emission voltage	Heating power	Average substrate current density	Average effective layer growth rate
SS+Zr-el1	- 500 V	- 50 V	411 W/m	2 mA/cm ²	0.04 $\mu\text{m}/\text{min}$
SS+Zr-el2	- 150 V	- 41 V	1536 W/m	24 mA/cm ²	- 0.17 $\mu\text{m}/\text{min}$
SS+Zr-el3	- 50 V	- 30 V	1115 W/m	15 mA/cm ²	0.25 $\mu\text{m}/\text{min}$

Apart from sample SS+Zr-el1, where the filament heating power was set too low, remarkably high average substrate current densities were recorded, which translate into ion fluxes to the substrate ranging from $9.38 \cdot 10^{16}$ ions/cm² s (sample SS+Zr-el3) to $1.50 \cdot 10^{17}$ ions/cm² s (sample SS+Zr-el2). At sample SS+Zr-el2, the extremely high substrate current density in combination with a comparably high substrate voltage led to the immediate re-sputtering of any deposited Zr atom as well as of the underlying substrate

material, thus no Zr layer was deposited. As a result, the electron emission parameters as well as the substrate biasing voltage were reduced for sample SS+Zr-e13, so that no substrate material was eroded anymore and an approximately 30 μm thick Zr layer was deposited. Assuming no re-erosion of the deposited Zr atoms, this yields a Zr particle flux to the substrate of approximately $1.79 \cdot 10^{16}$ atoms/ cm^2 s, an impinging ion-to-atom ratio to the substrate of 5.24 and an average effective energy contribution of the ions of ~ 222 eV per deposited Zr atom. Hence, the goals for an optimized substrate biasing approach were overfulfilled. By visual inspection of the sample SS+Zr-e13 after coating, as shown in Figure 129, no coating delaminations are found and the surface appears metallic-shiny. Due to the 30 μm thick Zr coating, a strong central upwards bending of the sample of several mm can be observed.

By repeating the production of sample SS+Zr-e13 with a thermocouple directly attached to the sample, the maximum sample temperature during PVD coating was measured to be 655 $^{\circ}\text{C}$, even though the substrate holders' biasing Mo plate with good thermal contact to the cooling water was used. For comparison, the temperature of a substrate produced identical to sample SS+Zr-e13 – but without additional electron emission and heating from a glowing filament – was measured to be ~ 400 $^{\circ}\text{C}$.

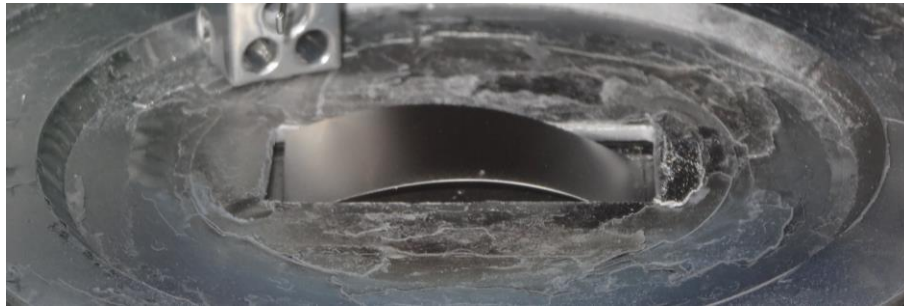


Figure 129: Sample SS+Zr-e13 after production. The sample appears metallic-shiny but is strongly bent due to the high Zr coating thickness of 30 μm .

A cross-section from sample SS+Zr-e13 was prepared and characterized by optical microscopy, as depicted in Figure 130. Expectedly, the sample shows a 30 μm thick deposited Zr layer, uniformly distributed across the surface. The thickness of the stainless steel substrate is unchanged at ~ 250 μm , thus no erosion of the substrate took place. Similar to the stainless steel samples from the substrate heating study, the individual grains in the Zr layer as well as numerous black spots inside are visible, which are not considered to be porosities but impressed diamonds from the last polishing step. The interaction layer formed between the substrate and the Zr layer – which is comparable to the one found in sample SS+Zr-650 in the substrate heating study – confirms a substrate temperature during PVD coating of approximately 650 $^{\circ}\text{C}$. However, the Zr layer microstructure presents significantly finer grains as expected from this substrate temperature. Still, the layer is dense and free of growth defects and is thus classified as growth structure type C. In contrast to the expectations, the ion bombardment obviously still hinders the formation of larger grains.

The hardness of the deposited Zr layer was measured to be 175 ± 11 HV0.01. It has to be noted that, due to the use of an industrial-grade Zr sputtering target with high oxygen content, this hardness value can not be directly compared with the samples from the substrate heating study, which were produced using a significantly softer reactor-grade Zr sputtering target. However, the measured Zr layer hardness is again remarkably lower than the hardness of the sputtering target. To evaluate also the ductility of the Zr coating, a bending test was performed. The optical micrographs in Figure 131 indicate a very ductile layer with excellent adherence, as no cracks were found on the outward and inward (not depicted) bends.

After multiple PVD coating experiments, the WLa20 filament loop was removed from the PVD coating device and visually inspected as shown in Figure 132. In areas in line-of-sight of the sputtering target, deposits of Zr were found. These deposits appeared partially re-molten, as the filament's temperature was calculated to be higher than 2500 K, thus well above the melting point of Zr. This imposes the risk of the formation of macroscopic Zr droplets during PVD coating, which could undesirably attach to the substrate surface. In uncoated areas, no apparent changes of the filaments' appearance were observed.

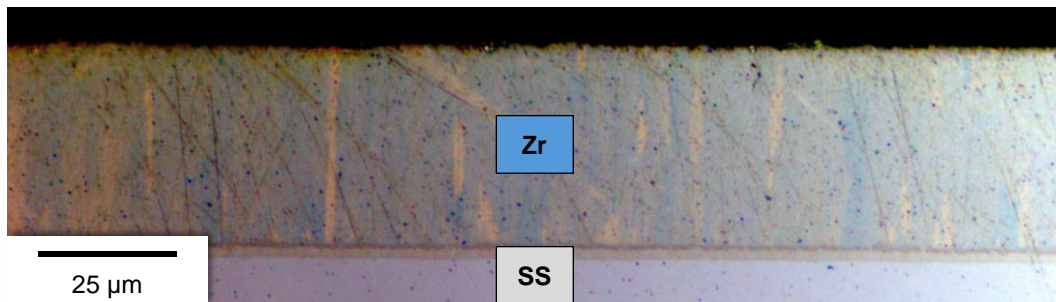


Figure 130: Optical micrograph (polarized light) of a cross-section of sample SS+Zr-el3. The Zr layer is dense and exhibits a columnar microstructure of growth structure type C. An interaction layer has formed between the stainless steel substrate and the Zr coating, which corresponds to a sample temperature of approximately 650 °C.

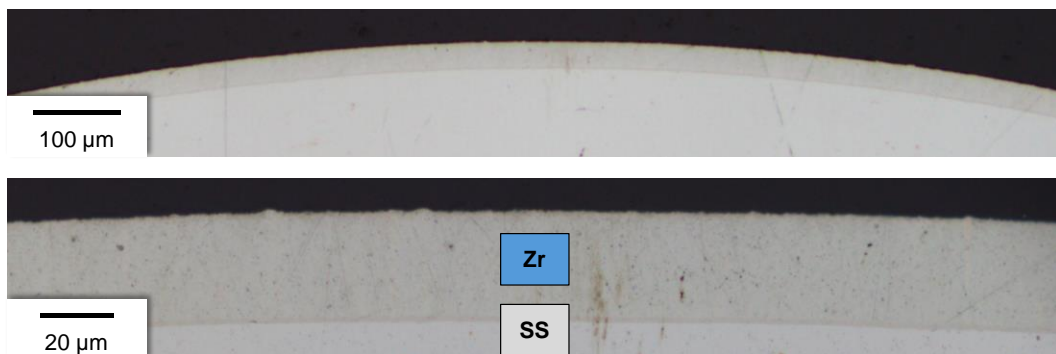


Figure 131: Bending test results of sample SS+Zr-el3. The Zr layer does not exhibit any cracks on the outward bend and shows excellent adherence throughout the entire bending.



Figure 132: WLa20 filament loop after being used for several PVD coating experiments. Where the filament is in line-of-sight of the sputtering target, partially re-molten Zr deposits are found (red circle). In uncoated areas, the filament appears matte grey.

5.3.3 IMPLICATIONS ON THE FULL-SIZE PVD COATING PROCESS

Due to the undesirable results, the technique of plasma enhancement by static magnetic fields is not recommended for an optimized substrate biasing approach for the full-size PVD coating process.

In contrast, plasma enhancement by electron emission has shown positive effects on substrate biasing and is thus considered to be a promising option for such an optimized substrate biasing approach. However, due to its technical complexity, its inherent risks such as high-current short circuits between the substrate and the filament as well as the danger of Zr droplet formation from the Zr-coated filament, this technique is only seen as a backup solution for the full-size PVD coating process.

Instead, the pursuance of an optimized substrate biasing approach shall be continued by realizing the full-size PVD coating process with a sputtering source with interchangeable magnet configurations, including an unbalanced magnetron of type 2. Due to the nevertheless promising results of plasma enhancement by electron emission, it is recommended to still envisage the potential later inclusion of this technique into the full-size PVD coating device.

5.4 THE FULL-SIZE PVD COATING DEVICE

Based on the design fundamentals laid out in section 5.1, the full-size PVD coating device was designed and built.

5.4.1 CHEMICAL CLEANING EQUIPMENT

A chemical cleaning step is necessary and the method of first choice to remove the oxide layer and other unwanted contaminants from the U-Mo foil surface prior to PVD coating. While mini-size or smaller U-Mo substrates can be cleaned in the chemistry glovebox of the HSK3 device, the handling of larger substrates such as full-size foils is only reasonably possible at the laboratory workbench. As standard laboratory glassware is not available in a size suitable for full-size foils, custom cleaning equipment was built as shown in Figure 133. The U-Mo substrate is first put inside a custom stainless steel cage produced by Conpex GmbH. The cage is then immersed into the cleaning solution in custom-made acrylic glass vessel. A constant circulation is ensured by pumping the liquid in a circle using a stainless steel GEO-INOX in-line pump from COMET-Pumpen Systemtechnik GmbH & Co. KG [214], which is connected to the outlet and inlet connections of the vessel, respectively. A drain outlet allows the safe disposal of the cleaning liquid after the cleaning process.

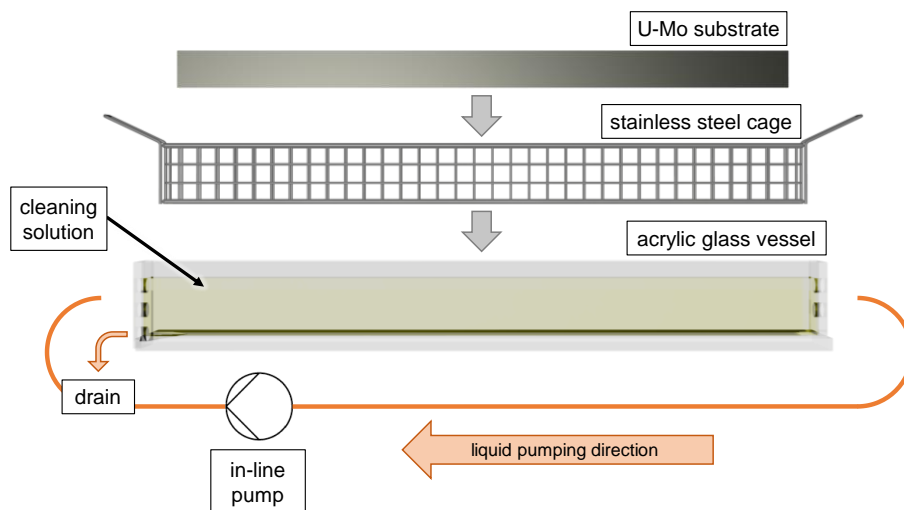


Figure 133: Chemical cleaning setup for full-size U-Mo foils. At the laboratory workbench, the U-Mo substrate is inserted into a stainless steel cage and immersed into the cleaning solution. A continuous circulation is ensured by pumping the liquid in a circle in the acrylic glass vessel.

5.4.2 VACUUM CHAMBER INTERIOR DESIGN

The full-size PVD coating device is designed as a top-down device – meaning that the sputtering source is installed above the substrate to be coated. Therefore, no obstructive clamping of the substrate is required, but the unwanted falling down of flakes from spalling layers deposited to the inner vacuum chamber walls to the substrate must be prevented. This is accomplished by a sputtering target larger than the substrate, a short target-substrate distance and by sandblasting of all surfaces inside the vacuum chamber, which are subject to undesired sputter deposition. Also, the sputter deposition onto any cables, tubes, threaded holes and other sensitive components inside the vacuum chamber shall be avoided. Therefore, as depicted in Figure 134, sandblasted stainless steel cover plates are installed into the vacuum chamber. At the top and rear wall, these cover plates are made of two parts, where the outer part can easily be removed for cleaning. To limit the downwards sputter deposition solely to the substrate,

height-adjustable cover plates with a central gap for the substrate holder are installed at the height of the substrate. The necessary cables and tubes for the substrate holder are routed from the top KF40 flanges of the vacuum chamber behind the rear wall plates through the vertical channel to the bottom area. Additionally, two eyebolts are installed at the top for carrying heavy items using tension belts.

Because the sputtering source, as described in section 5.4.4, allows the adjustment of the sputtering direction, e.g. during the initial sputtering target cleaning step, no movable protective shutter between the sputtering target and the substrate is installed. This allows a short target-substrate distance, which reduces the number of collisions of sputtered atoms and therefore increases their energy contribution to the adatom mobility.

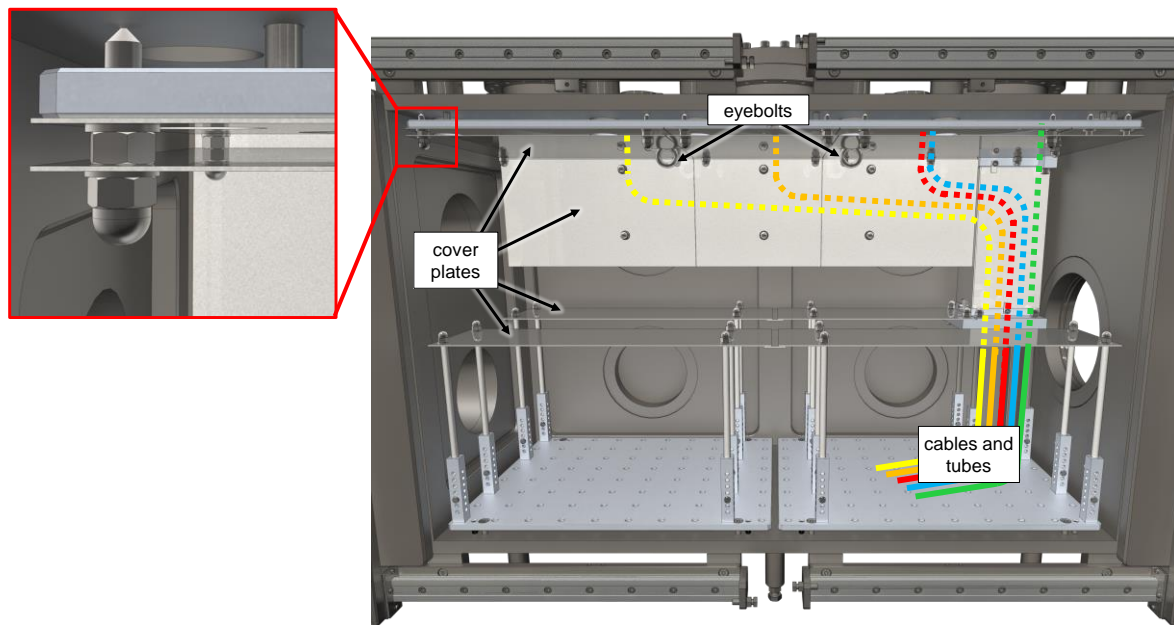


Figure 134: Interior design of the vacuum chamber of the full-size PVD coating device. To protect the walls and installations from sputter deposition, cover plates are installed at the top, the rear wall and at the height of the substrate. Cables and tubes are routed through the vertical channel from the top flanges to the substrate holder. When varying the target-substrate distance, the height of the lower cover plates can be adjusted manually. For carrying heavy items, tension belts can be attached to the eyebolts on top.

5.4.3 SUBSTRATE HOLDER

The interior design of the vacuum chamber allows the installation of different substrate holders in the central gap of the lower cover plates. The following media supplies and electrical connections are available to the substrate holders:

- Four type K thermocouple connectors
- A cooling water circuit with adjustable inlet temperature (16 - 22 °C), 5 bar inlet pressure and an adjustable flow rate (max. 2 l/min)
- An electrical high voltage line for substrate biasing from a biasing power supply unit (max. 1200 V DC, 10 kW)
- An electrical high current line for substrate heating from a heating power supply unit (max. 170 A DC, 5 kW)

In this thesis, two different substrate holders with different capabilities are used:

Flat support half-size substrate holder

The flat support half-size substrate holder, depicted in Figure 135 and Figure 136, was developed and built within an M.Sc. thesis [207] and is briefly described hereafter.

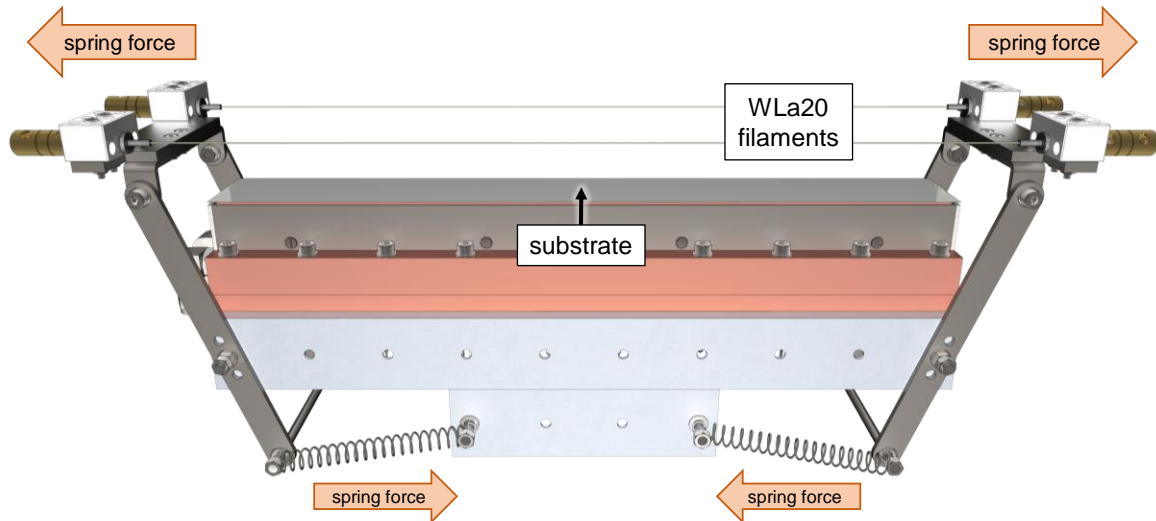


Figure 135: Flat support half-size substrate holder. The substrate is typically installed by laying it flat onto the support surface, which is thermally connected to a water-cooled copper block. Optionally, an electron emission system consisting of two WLa20 filament wires can be installed. The filament wires are held in place via spring-loaded mounting brackets.

It can hold half-size substrates with a fixed size of 380 mm x 45 mm. The substrate holder generally consists of two copper blocks, which are screwed against each other using electrically insulating PEEK (Polyether ether ketone) [215] screws and separated by an electrically insulating KERAFOIL Softtherm U281 [216] heat conducting film. The lower block is made of two parts and can be water-cooled by a machined circular cooling water channel with a cross-sectional area of 0.6 cm². The upper block serves as the substrate support surface and is connected to the substrate biasing voltage supply via a copper connector rod, which again is electrically insulated from the grounded lower block using a ceramic tube. To avoid the ignition of an undesired plasma at the sides of the upper block, stainless steel dark space shielding plates with a distance of 1 mm to voltaged parts are attached to the lower block. Via a scissor table below the substrate holder, the target-substrate distance can be adjusted between 30 mm and 70 mm.

Similar to the substrate holder of the mini-size device, the substrate is typically installed by laying it centrally onto the support surface of the upper copper block without any further attachment. For experiments on the substrate bending effect, it can alternatively be screwed to the support surface via three M3 threaded holes each on the left and right side of the upper block. Optionally, an adhesive heat conducting film can be placed between the substrate and the support surface and the electrical contact of the substrate can be ensured by screwing it to the M3 threaded holes.

To measure the temperature of the substrate and the substrate holder during the coating process, two type K mantle thermocouples with 0.5 mm diameter are installed through borings in the PEEK screws. The measuring point of the first thermocouple is located inside an Alunit® AlN [217] mantle which is only in direct contact with the flat lying substrate, thus aiming at measuring the substrate temperature itself. The measuring point of the second thermocouple is again located inside an AlN mantle, which is in contact with the upper copper block, thus aiming at measuring the substrate holder temperature. AlN

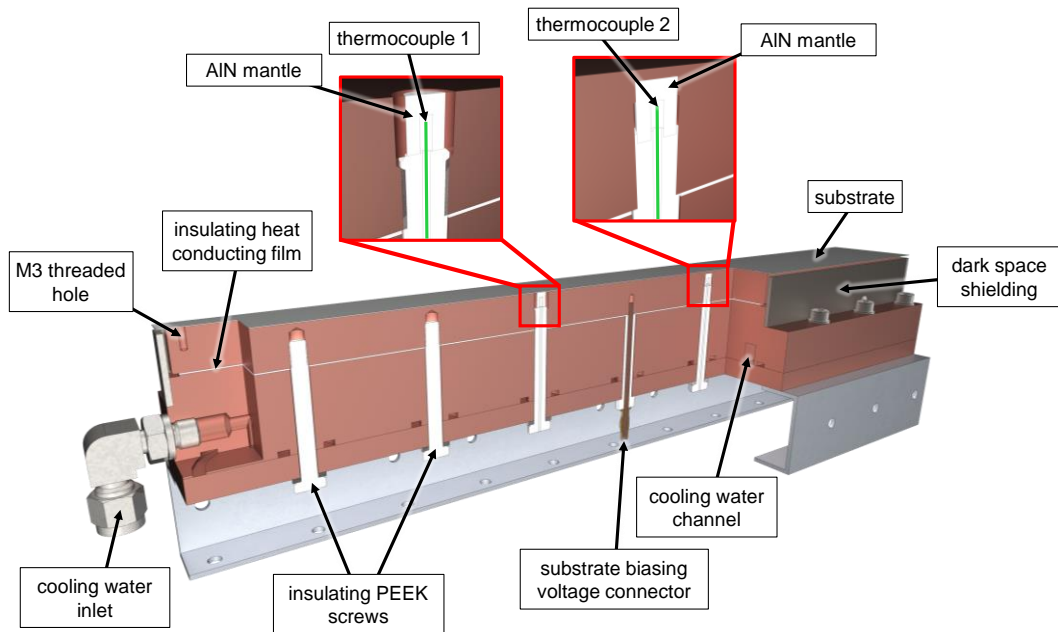


Figure 136: Cross-cut view of the flat support half-size substrate holder. The substrate support surface is thermally connected and electrically insulated from the water-cooled block via a heat conducting film and PEEK screws. Via borings in the PEEK screws, two type K thermocouples are guided to the substrate, where they are encapsulated in AlN mantles for electrical insulation and good thermal contact.

was chosen as material for the mantles due to its high thermal conductivity and good electrical insulation properties. Attention needs to be paid, as the so-measured substrate temperature is subject to great uncertainties, because thermal contact of the thermocouple to the water-cooled surrounding copper block can not be fully avoided and because the thermal contact to the substrate is generally considered weak, especially when the substrate bends upwards during the coating process. Thus, a calibration of the measured temperatures shall be performed using true values from another direct measurement method.

Optionally, the substrate holder can be equipped with an electron emission system for further experiments on plasma enhancement by electron emission. This system consists of two WLa20 filament wires which are placed 35 mm above the substrate at a horizontal distance to the substrate of 21 mm. These filament wires are connected to the power supply using electrically insulating porcelain contact clamps screwed onto the lateral mounting brackets. To prevent sagging of the filament wires due to thermal expansion, the mounting brackets are spring-loaded against the substrate holder.

Clamping full-size substrate holder

Based on the experience gained from experiments with the half-size substrate holder, the clamping full-size substrate holder, as depicted in Figure 137 and Figure 138, was designed and built. This substrate holder mainly consists of two clamping blocks, in between which the substrate is installed via fixing it using two fixation pins on each side, which connect to corresponding bores inside the substrate. The clamping blocks are mounted on two slide axles and a threaded rod to adjust their distance, thus holding substrates of various length up to 800 mm. The target-substrate distance can be adjusted between 30 mm and 70 mm by vertically shifting the slide axles and the threaded rod via a height adjustment system in the pedestals. Via two springs and finger screws on the threaded rod, a spring force is applied to the clamping blocks. This force pushes the blocks outwards, aiming at keeping the substrate flat even though thermal expansion and bending may occur during the coating process.

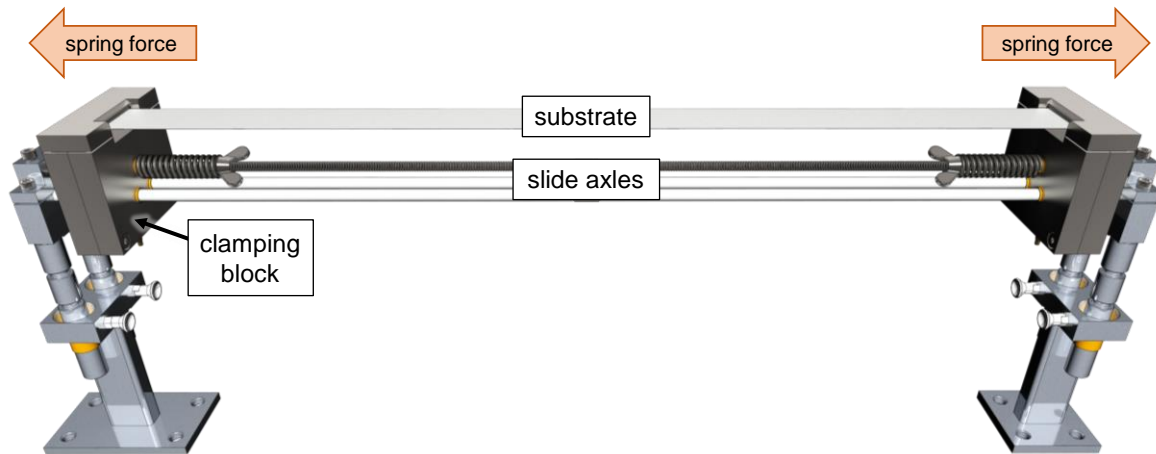


Figure 137: Clamping full-size substrate holder. The substrate is held flat by spring force in between two clamping blocks, which are mounted on slide axes and a threaded rod.

The clamping blocks themselves consist of two parts: (i) the inner part at the substrate's electrical potential and (ii) the outer housing at ground potential. Both parts are electrically insulated from each other using an Al_2O_3 (aluminum oxide) plate at the bottom and a constant 1 mm gap all-around. The removable top cover shields the sensitive inner part and prevents coating or contamination thereof. Via electrical connectors on both clamping blocks, a biasing voltage can be applied to the substrate. Optionally, the substrate can be heated by electrical current from a separate heating power supply unit.

In contrast to the half-size substrate holder, no more water cooling or temperature measurement is possible with this substrate holder. Therefore, control measurements need to be performed for each specific set of process parameters to determine the substrate temperature during the coating process.

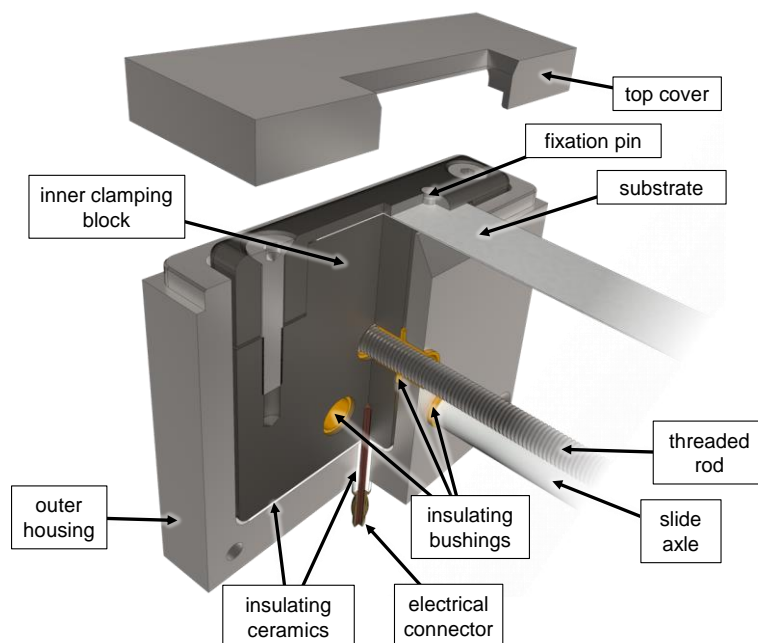


Figure 138: Cross-cut view of a clamping block of the clamping full-size substrate holder. The inner clamping block is electrically insulated from the grounded outer housing, slide axes and the threaded rod via insulating ceramics and bushings. Via an electrical connector, a substrate biasing voltage and/or heating current can be applied to the inner clamping block and thus to the substrate, which is attached via a fixation pin.

5.4.4 SPUTTERING SOURCE

The existing sputtering source in the mini-size PVD coating device has shown very good results in the EMPIRE fabrication campaign. At a compact target size of 122 mm x 54 mm, it allows sputtering power densities of 15 W/cm² and above. However, it is not able to coat large substrates up to full-size geometry uniformly in reasonable time. Therefore, a sputtering source using a significantly larger sputtering target is needed for the full-size PVD coating device. As a rule of thumb, the effectively used target length l_t and width w_t shall correspond to the substrate length l_s and width w_s (762 mm x 45 mm for full-size substrates) as follows:

$$l_t \geq l_s + 2 w_t \quad (54)$$

$$w_t \geq w_s \quad (55)$$

By these effectively used target dimensions, the usually uneroded borders are taken into account and therefore they are typically ~ 10 mm shorter than the target's physical size. When using a cylindrical tube as target, the effectively used width corresponds to the width of the erosion zone. For full-size substrates, the effectively used target size shall thus be at least 852 mm x 45 mm.

As planar sputtering sources usually have a low material utilization of less than 30 % and are hard to integrate into existing vacuum chambers at the required size, the decision was made to use a compact cylindrical sputtering source. Based on a market study, the CM series external-mount end block [218] from the commercial supplier Sputtering Components was chosen. As depicted in Figure 139, it consists of an external end block mounted to an external flange of the vacuum chamber, an internal mount, and a cylindrical sputtering target with an interchangeable magnet bar inside (not depicted). The external end block, as depicted in Figure 140, contains all the media connectors and motors necessary to operate the sputtering source.

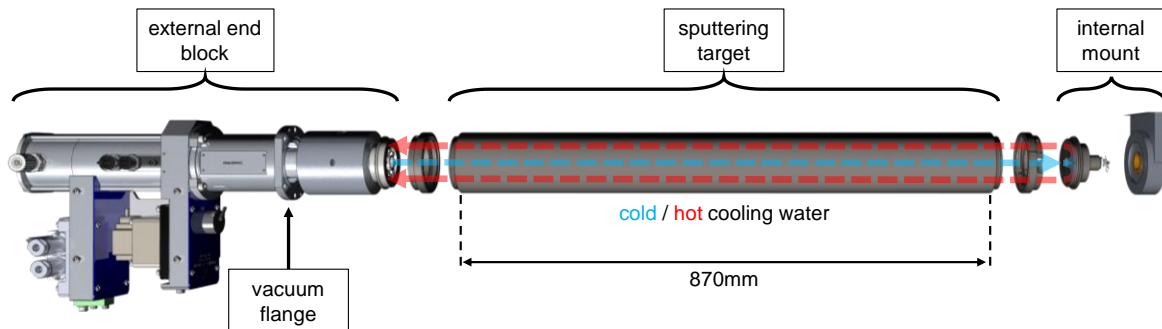


Figure 139: Overview of the cylindrical sputtering source used in the full-size PVD coating device. The sputtering source generally consists of an externally mounted end block, a sputtering target, and an internal mount.

For a top-down sputtering process, the external end block is installed at the upper CF160 flange on the front door of the vacuum chamber and the sputtering target protrudes into the vacuum chamber concentrically from the inside of the flange. The internal mount, which is necessary to compensate the weight of the sputtering target, is screwed to the top of the vacuum chamber. By design, any conductive parts in contact to the sputtering target such as clamps, shaft, end plug and cooling water are at the same electrical potential, i.e. several hundred volts against ground. The internal mount and the dark space shielding ring on the shaft are kept at floating potential.

For zirconium, the sputtering source is rated up to a sputtering power of 10 kW. To ensure good cooling of the sputtering target and to prevent de-magnetization of the permanent magnets due to over-heating

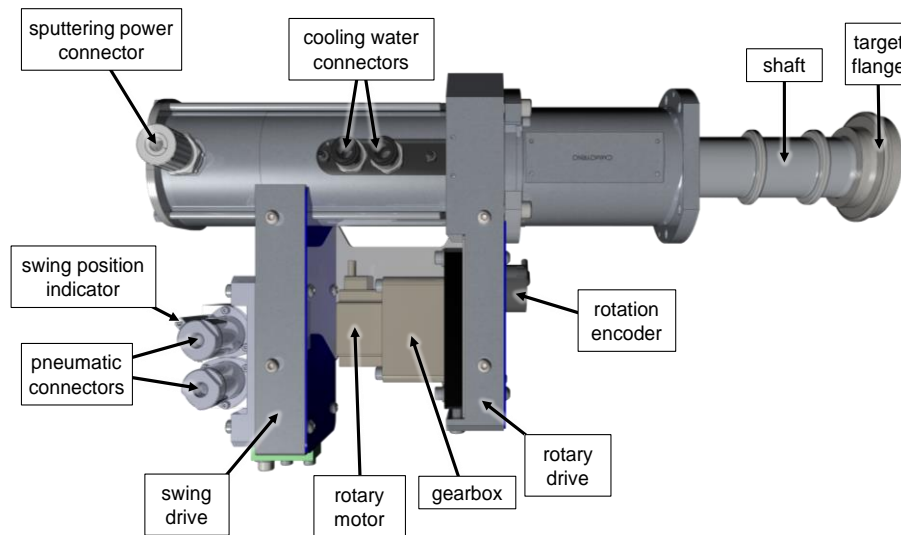


Figure 140: External end block of the cylindrical sputtering source. All media connectors and motors are located on the external side of the end block and are routed through the glovebox to the outside.

above their Curie temperature, an effective water cooling system is thus necessary. This is achieved by guiding the cold inlet cooling water through the central tube of the magnet bar to the end plug of the sputtering target, where the cooling water flow is deflected so that the water is guided back on the inner surface of the sputtering target towards the cooling water outlet. By design, the minimum cooling water flow shall be 1 l/min kW to ensure a sufficient heat removal.

To maximize the effectively used target length, the available space in the vacuum chamber is used as efficiently as possible. Therefore, the shaft length is reduced compared to the stock configuration and the remaining space between the internal mount and the vacuum chamber wall is reduced to the minimum required for target installation and removal. This allows the installation of sputtering targets with a length of 870 mm. By design of the magnet bar inside the sputtering target, its effectively used length is approximately 850 mm and therefore just meets the length requirement. The outer diameter of the sputtering target is 100 mm and the wall thickness is 10 mm, so that a zirconium sputtering target weighs approximately 16.3 kg. To install and remove the heavy sputtering target without opening the glovebox, the target can be hooked to the eyebolts at the top of the vacuum chamber for manual handling. The remaining cooling water inside the sputtering target can be blown out by connecting pressurized argon gas to the cooling water inlet connector.

To efficiently utilize the sputtering target material, the target is put under continuous rotation with a typical speed of 10 rotations per minute. The rotational movement is generated by a brushless DC motor and a gearbox at the external end block and transferred to the target axis via a non-conductive tooth belt. Via an encoder, the rotational movement of the motor is recorded and can be read-out by a device control system.

Two different 860 mm long magnet bars with different magnet configurations can be alternatively installed into the sputtering target:

- The standard single-row SRM80 magnet bar with one row of magnets sitting on an iron yoke, aiming to deliver a balanced magnetic field configuration
- The custom-designed triple-row uTRM80 magnet bar with two rows of magnets and a central iron yoke, aiming to deliver an unbalanced magnetic field configuration of type 2.

Figure 142 and Figure 142 illustrate the magnet configurations and the resulting magnetic field lines of the magnet bars, according to a simulation from the supplier [219]. As it can be seen, the SRM80 magnet bar leads to a strong confinement of electrons close to the target surface. In contrast, the uTRM80 magnet bar allows electrons to escape from the plasma and thus, at a distance of 30 mm greater to the target surface, a high ion bombardment of the substrate can be expected.

The effectively used target width can be estimated by the distance between the two erosion zones, thus ~ 55 mm for the SRM80 magnet bar and ~ 45 mm for the uTRM80 magnet bar, leading to reachable sputtering power densities $\geq 20 \text{ kW/cm}^2$ at 10 kW sputtering power. The magnet bars can be swiveled by 135° into a cleaning position, inside and independent of the sputtering target rotation. If ignited in this position, the burning plasma and therefore the flux of sputtered target atoms is not directed towards the substrate but towards the cover plates of the vacuum chamber. This can be used to clean the sputtering target prior to the substrate coating process. The swiveling movement is generated by a pneumatic rotary actuator driven by pressurized argon gas at the end block and transferred to the magnet bar axis via another non-conductive tooth belt. Via two reed switches at the actuator, the position of the magnet bar can be read-out by a device control system.

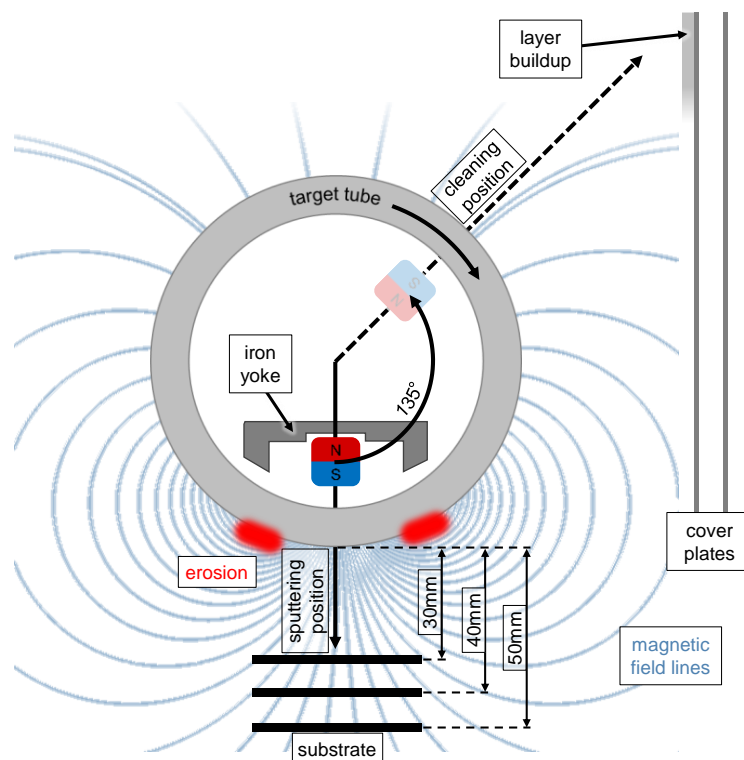


Figure 141: Magnetic configuration and field lines of the SRM80 magnet bar. The SRM80 magnet bar shows a strongly balanced magnetic field configuration due to only a single row of magnets. Magnetic field simulation from [219].

5.4.5 POWER SUPPLY UNITS

Several power supply units are available for the full-size PVD coating device. Depending on the way how the process shall be conducted, a sputtering PSU, a substrate PSU, a heating PSU, and/or an emission PSU may need to be connected. Figure 143 shows the possible power supply configurations for the different operation modes:

- The substrate heating mode – sputtering with substrate heating – requires a sputtering PSU connected to the sputtering target and a heating PSU connected to both ends of the substrate.

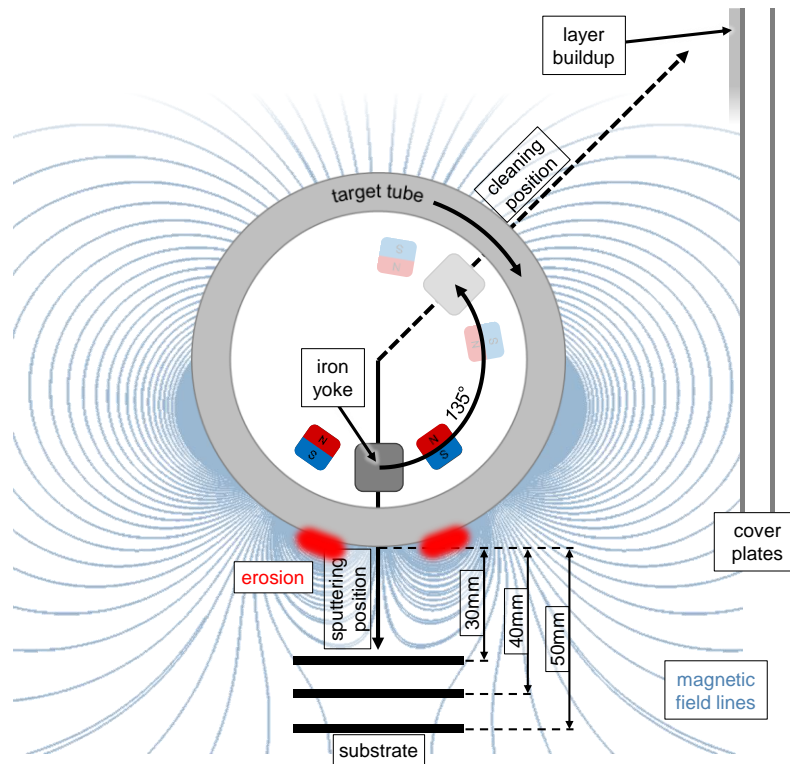


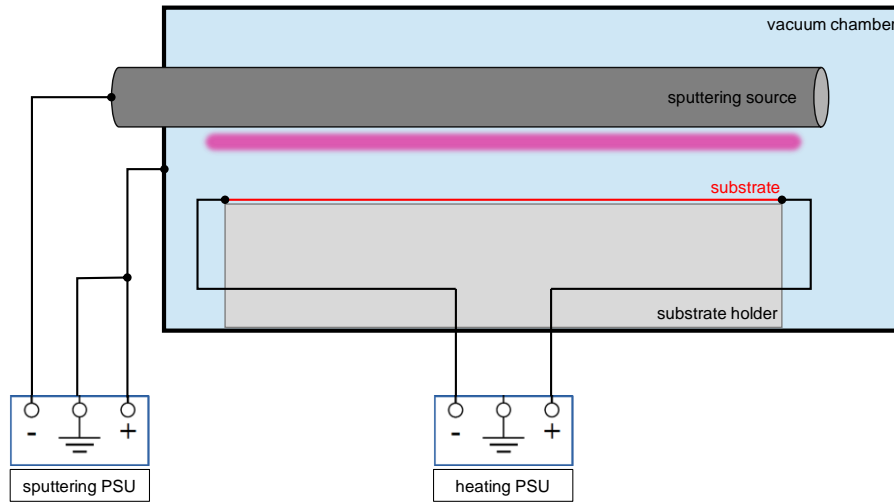
Figure 142: Magnetic configuration and field lines of the uTRM80 magnet bar. The uTRM80 bar aims at an unbalanced magnetic field configuration of type 2. Magnetic field simulation from [219].

- The substrate biasing mode – sputtering with substrate biasing – requires a sputtering PSU connected to the sputtering target and a substrate PSU connected to the substrate.
- The electron emission mode – sputtering with substrate biasing and electron emission from glowing WLa20 filament wires – requires a sputtering PSU connected to the sputtering target, a substrate PSU connected to the substrate as well as a heating PSU connected to the filament wires and an emission PSU which puts both filament wires on a negative potential against the grounded vacuum chamber.

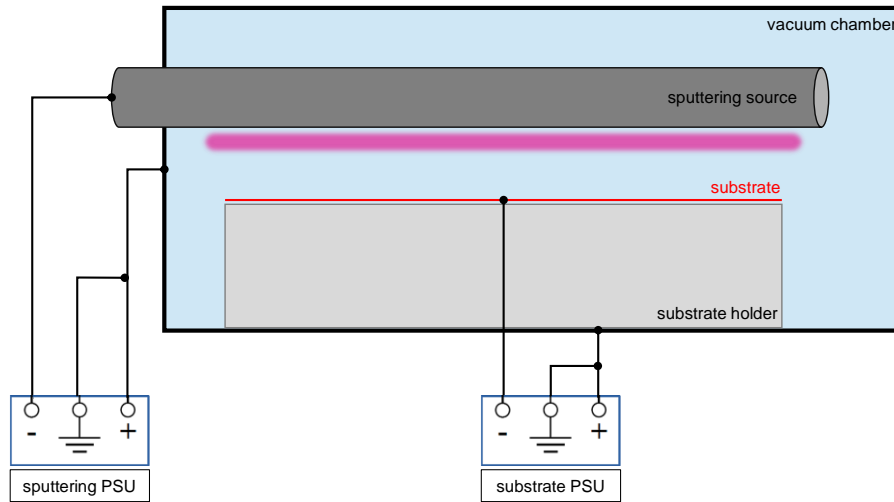
Therefore, the sputtering and substrate power supply units shall be dedicated DC plasma PSUs, optimized towards either magnetron sputtering or substrate biasing applications, with nominal output values of at least 1000 V and 10 kW. They shall further incorporate an arc management system able to suppress or compensate the typically occurring arcs in a sputtering plasma. As the positive terminals are connected to ground, these PSUs do not necessarily need to be free-of-ground.

To be able to heat WLa20 filament wires to a temperature where glow emission occurs, and to be able to heat a full-size U-Mo substrate by electrical current to a temperature of several hundred °C, the heating power supply unit shall be a high current DC PSU with a nominal output current of more than 100 A. For electron emission, an additional DC emission PSU with nominal output values of approximately 20 A and 80 V is required. For maximum flexibility, the outputs of both units shall be free-of-ground.

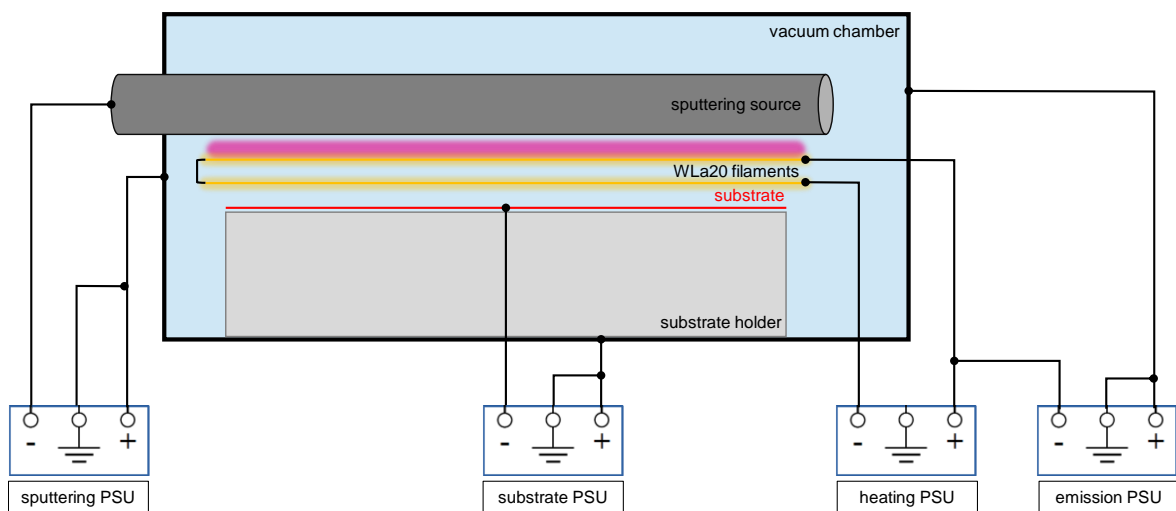
Table 16 lists the available power supply units and their respective capabilities and characteristics.



a) Substrate heating



b) Substrate biasing



c) Electron emission

Figure 143: Possible power supply configurations of the full-size PVD coating device. Using sputtering, substrate, heating and emission PSUs, the device can be operated either in substrate heating mode (a), substrate biasing mode (b) or electron emission mode (c).

Table 16: Power supply units of the full-size PVD coating device. Four PSUs with different capabilities and output characteristics are available. Data from [172,220–222].

	Sputtering PSU	Substrate PSU	Heating PSU	Emission PSU
Manufacturer	TRUMPF Hüttinger GmbH	TRUMPF Hüttinger GmbH	HEIDEN power GmbH	EA Elektro- Automatik GmbH
Device name	TruPlasma DC 3020 G2	TruPlasma DC 4010 G2 Ext.	PSI9080-170 3U	PSI5080-20 A
Device type	Magnetron plasma PSU	Magnetron plasma PSU with biasing and pulsed-DC mode	High current PSU	Laboratory PSU
Nominal output values (U/I/P)	1000 V / 50 A / 20 kW	1200 V / 33 A / 10 kW	80 V / 170 A / 5 kW	80 V / 20 A / 640 W
Arc management	Yes, up to 2000 arcs/sec	Yes, up to 2000 arcs/sec	No	No
Water cooling required	Yes	Yes	No	No
Footprint	19 inch rack, 3 U*	19 inch rack, 4 U*	19 inch rack, 3 U*	200 mm x 87 mm x 320 mm
Control interface	EtherCAT	EtherCAT	Analog/Digital I/O	Analog/Digital I/O

*) Height Units, approximately 133 mm per U

5.4.6 PLC SYSTEM

The full-size PVD coating device needs to be connected to the laboratory emergency stop system and all its components must be inherently safe when currentless. The PVD coating process must be fully digitally controlled and no manual operations shall be necessary. Therefore, the process is controlled by a BECKHOFF TwinCAT *PLC* (Programmable Logic Controller) system, as depicted in Figure 144. Complex components with various input/output parameters like the turbomolecular pump, the mass flow controllers and the sputtering and substrate power supply units are connected via digital bus systems like EtherCAT and ProfiBus. All other actuators, sensors and PSUs are connected via analog and digital I/O terminals. The laboratory emergency stop system is connected via a separate EtherCAT bus line and is able to safely stop any ongoing process, e.g. in the event of a water leakage, the failure of the laboratory cooling water supply or of the glovebox gas purification system. By a GUI running on a dedicated user control PC, the operator can electronically set and read all device parameters. At any point in the process, the system monitors critical process parameters like the flow of cooling water and the pressure in the vacuum chamber and can prohibit the execution of process steps which may be harmful to the device or the operator.

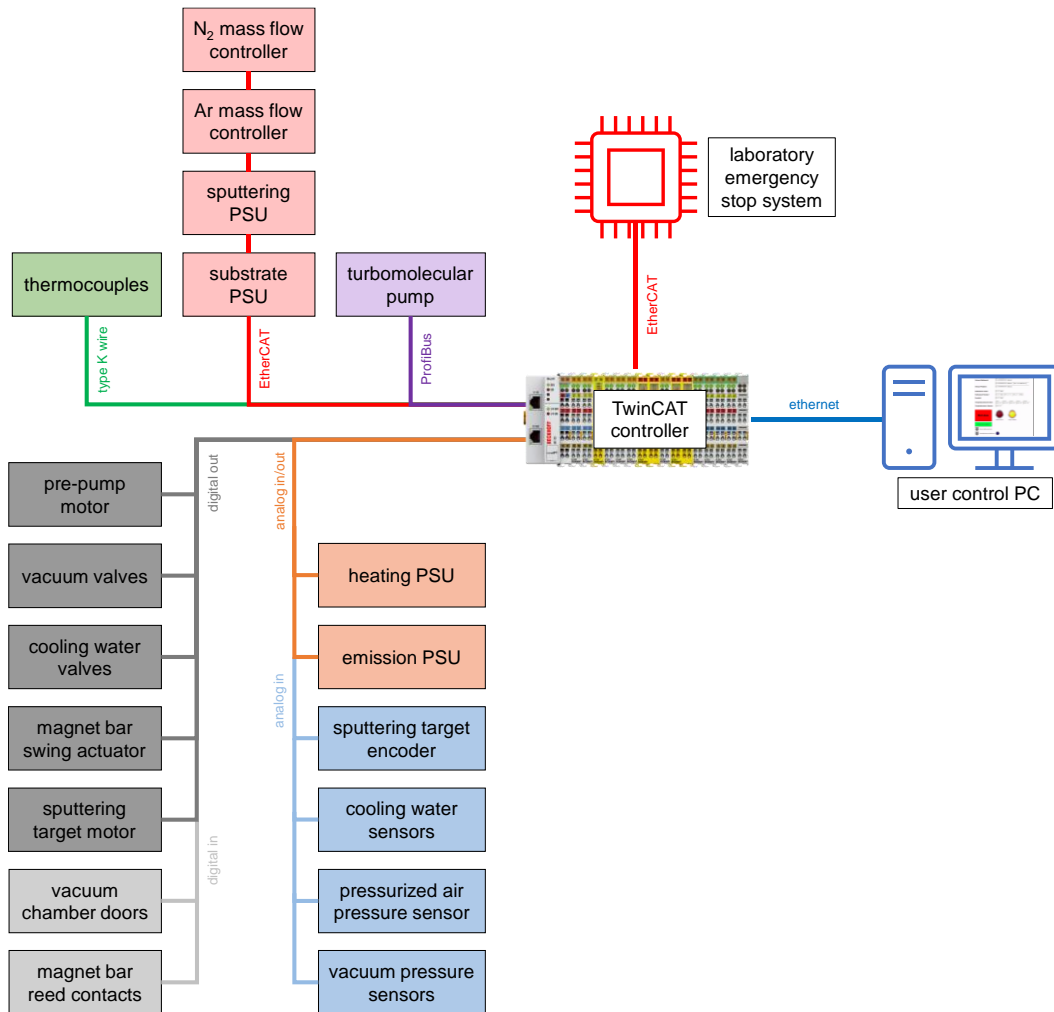


Figure 144: PLC system of the full-size PVD coating device. The heart of the system is a TwinCAT controller, where all sensors and actuators are connected to either via analog and digital I/O terminals, Profibus or EtherCAT bus lines or type K thermocouple wire. All values can be read and set via a user control PC, connected via ethernet. The system is connected to the laboratory emergency stop system, which is able to safely stop any ongoing PVD coating process.

5.4.7 WEIGHING EQUIPMENT

To follow the uranium accounting requirements from the laboratories' license, and to be able to estimate the coating thickness on the substrate, it is necessary to weigh all substrates before and after PVD coating with a precision of 1 mg. Therefore, a Cubis MSE1203S precision scale [223] from Sartorius Lab Instruments GmbH & Co. KG is installed inside the glovebox, as depicted in Figure 145. It has a weighing range of 1200 g with a readability of 1 mg and a reproducibility of ± 0.7 mg. To weigh large full-size substrates without vibration-induced inaccuracies, the scale is installed onto an elevated platform and the substrates are vertically attached to a hook at the bottom of the scale.

5.4.8 TRIMMING EQUIPMENT

Any areas of the substrate with no coating or weak coating adherence must be trimmed off prior to cladding application. When the clamping full-size substrate holder is used, an uncoated area at both ends of the substrate is unavoidable due to the clamping. Also, an area with weak coating adherence typically develops close to the uncoated area. In total, less than 15 mm therefore need to be trimmed off from both ends of the substrate, as depicted in Figure 146.

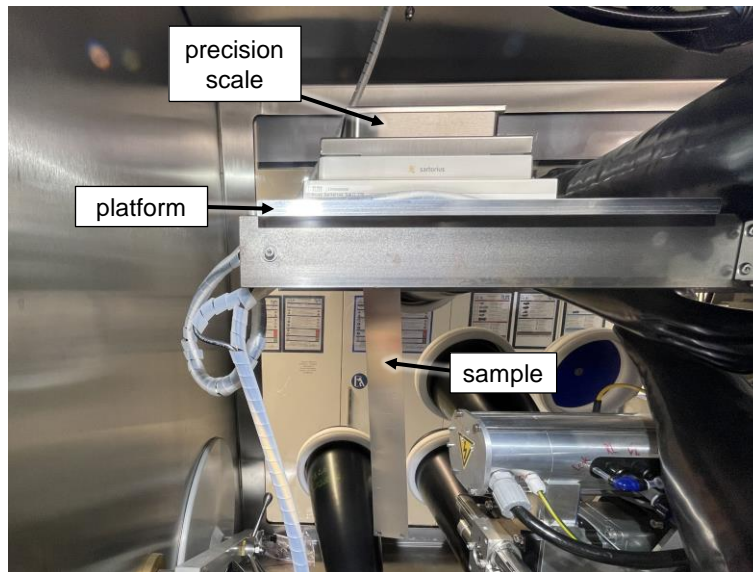


Figure 145: The precision scale inside the glovebox. To weigh full-size substrates, the scale is installed onto an elevated platform and the substrates are vertically attached to a hook at the bottom of the scale.

To perform this trimming operation, a hand-operated Dahle 580 workshop guillotine [224] with a maximum cut length of 815 mm and a cutting capacity of up to 4 mm is available in the laboratory. The material and shape of its cutting blade are optimized towards cutting of various materials such as metals and a laser indicator helps positioning the sample prior to cutting. Due to the size of the guillotine, the trimming process can only be performed outside of the glovebox at laboratory atmosphere and thus, the Zr coating is inevitably exposed to air. To avoid any potential oxidation of the coating and to achieve a better edge quality with higher geometric precision in the future, a laser-cutting device inside a glovebox with inert atmosphere will be available at Framatome-CERCA starting early 2022. It is planned to perform the trimming process then directly before the cladding application process.

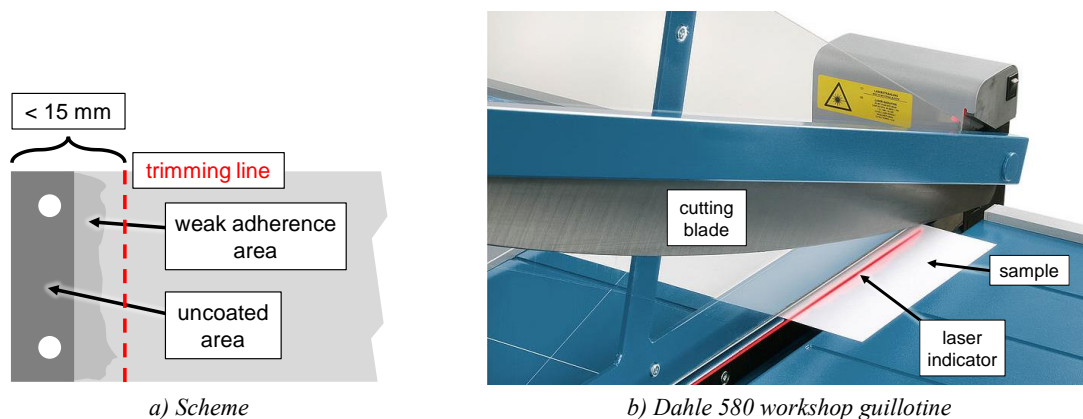


Figure 146: Trimming of substrates coated with the clamping full-size substrate holder. Due to the clamping of the substrates at the two borings at the ends of the substrate, uncoated areas as well as areas with weak coating adherence exist at both ends and need to be trimmed off prior to cladding application. After [224].

5.4.9 PACKAGING AND SEALING EQUIPMENT

Before the coated substrates can be shipped to Framatome-CERCA for the C2TWP cladding application process, they need to be packaged to protect them from mechanical stress, oxidation and contamination.

Therefore, the substrates are placed inside bags made from 123 μm thick A30 T PETP-Al-LDPE composite material [225], which can be sealed leak-tight using a Polystar 120 GE impulse generator with attached welding tongs [226], as displayed in Figure 147. The welding tongs are placed inside the glovebox, so that the substrates can be packaged under high-purity argon atmosphere. To save space inside the glovebox, the impulse generator is located outside and connected to the welding tongs via a feedthrough.



Figure 147: Polystar 120 GE impulse generator with attached welding tongs. The welding tongs is placed inside the glovebox to allow the packaging of the coated substrates under high-purity argon atmosphere. After [226].

5.5 PROCESS REALIZATION AND FIRST RESULTS

Using the equipment described in the previous section, the full-size PVD coating device was commissioned in TUM's Nuclear Fuel Fabrication and Characterization Laboratory and connected to the laboratory infrastructure and media supply. In December 2020, the notified expert of the laboratories' regulatory authority – the TÜV Süd Industrie Service GmbH – has approved the handling of uranium within the device. Figure 148 shows the entire device including the external equipment attached to the glovebox.

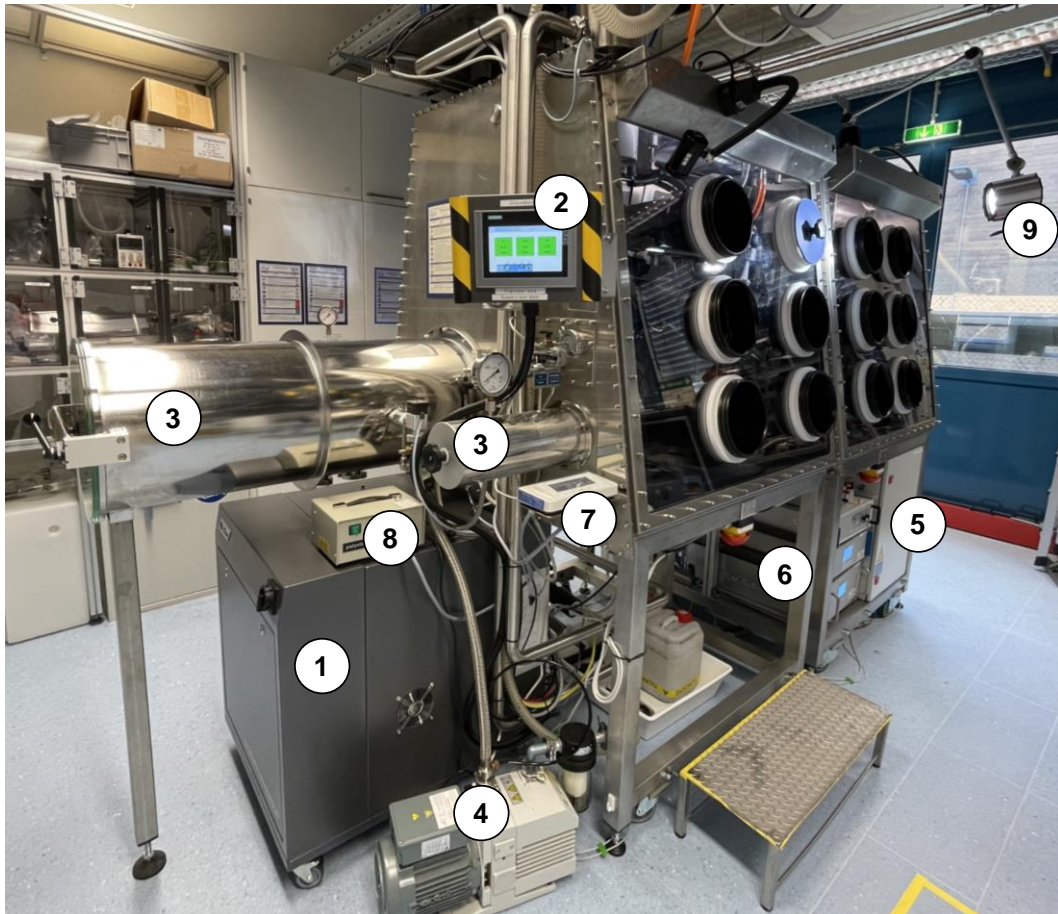
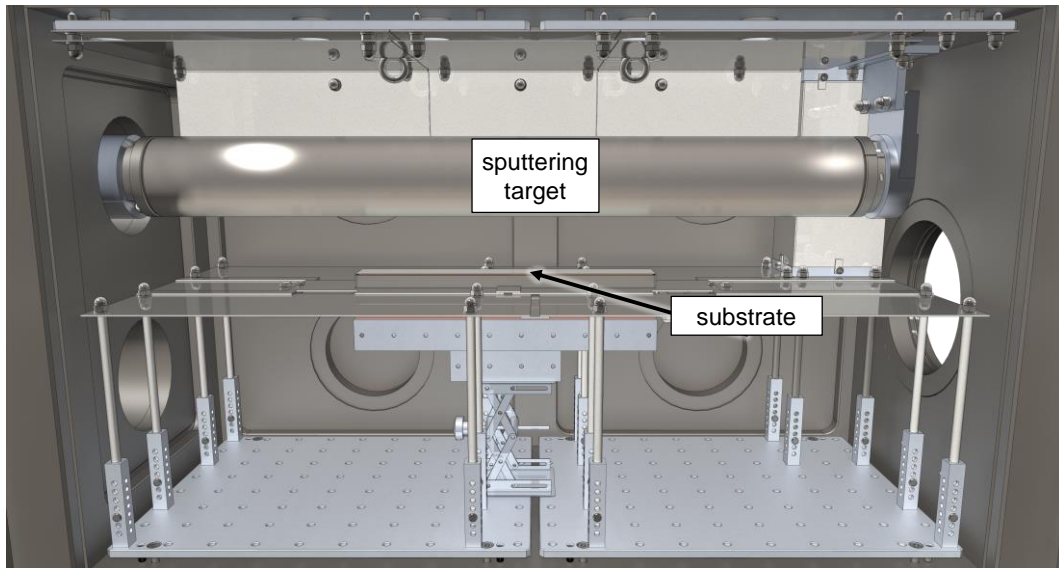


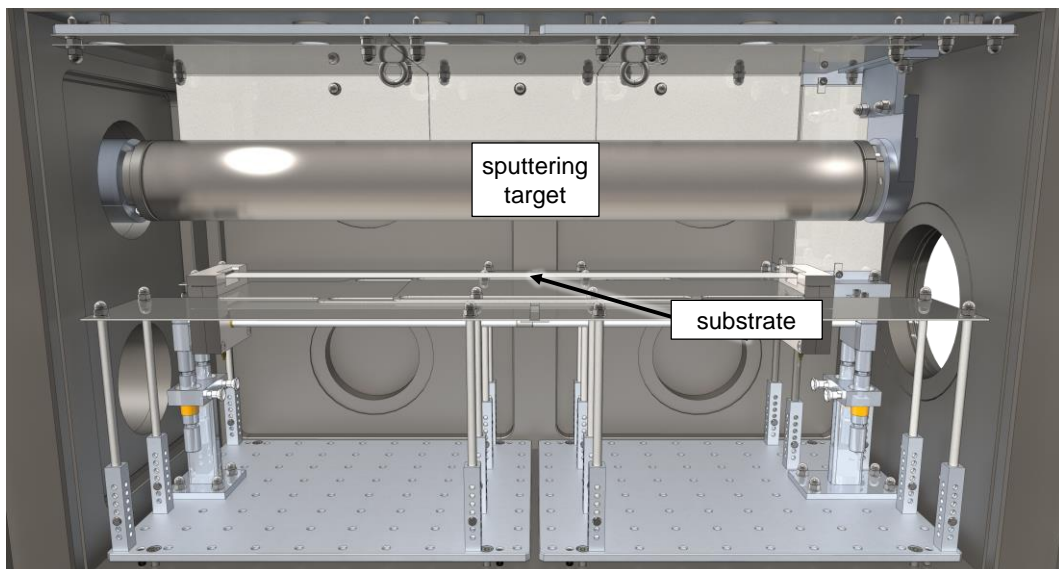
Figure 148: The complete full-size PVD coating device from the outside. The glovebox is equipped with a gas purification system (1) with touch-screen interface (2), two transfer locks (3) and a suitable vacuum pump (4). For the electrical supply of the PVD device, the electrical cabinet (5) and the power supply units (6) are installed under the glovebox. The control panel of the precision scale (7), the impulse generator for the welding tongs (8) as well as a lightning system (9) are installed externally.

For the initial commissioning, characterization and parametrization as well as for the first sample production campaign, the flat support half-size substrate holder was mostly used to study the effect of substrate bending, and the unbalanced uTRM80 magnet bar was installed in the sputtering source to study its effect on substrate biasing. The utilized sputtering target was made from industrial-grade Zr 702, with an oxygen content of 1200 ppm [227]. Because only one sputtering target is available, its hardness could not be measured. However, due to the similar oxygen content, the hardness is assumed to be comparable to the previously used Zr 702 sputtering target of the mini-size device (1400 ppm , $234 \pm 16 \text{ HV1}$). The device was operated in the biasing mode, i.e. solely with the substrate power supply unit connected to the substrate and without the optional electron emission system. Based on these experiments, the clamping full-size substrate holder was designed, built and installed later on. Figure

149 a and b show an inside view of the full-size PVD coating device with the two different substrate holders installed.



a) with flat support half-size substrate holder



b) with clamping full-size substrate holder

Figure 149: The full-size PVD coating device equipped with the sputtering source and two different substrate holders. The initial commissioning, characterization and first sample production was performed mostly using the flat support half-size substrate holder (a). Based on these experiments, the clamping full-size substrate holder was designed, built and installed later on (b). For better visibility, the target-substrate distance depicted is 70 mm.

5.5.1 PROCESS FLOW

The process flow for the PVD coating of a substrate with Zr in the full-size PVD coating device in total consists of 18 steps. All relevant steps and set parameters are documented in written form in a dedicated sample production book and furthermore stored digitally in a Microsoft Excel sheet. All process parameters, which can be collected digitally by the PLC system, are furthermore recorded and saved in CSV (comma-separated values) files.

In the following process flow description, all parameters which are studied during the device characterization and parametrization in section 5.5.2, are printed in *italics*.

1. **Quality control.** Prior to any processing of a stainless steel or U-Mo substrate, it is visually inspected by eye to detect surface anomalies or obvious geometrical deviations.
2. **Initial weighing.** Each substrate is then weighed with mg precision using a suitable scale in the laboratory.
3. **Drilling of fixation borings (optional).** If the substrate is to be installed into the clamping full-size substrate holder, two borings need to be drilled at each end of the substrate. The position of the borings is marked and the drilling is performed using a hand-operated rechargeable driller, equipped with a drill bit suitable for hard metals.
4. **Chemical cleaning.** Depending on the substrate material, it is cleaned on the laboratory workbench using one of the methods described in section 3.2.1.
5. **Transfer into glovebox.** The freshly cleaned substrate is transferred into the glovebox, together with suitable packaging material.
6. **Post-cleaning weighing.** To determine the mass loss due to chemical cleaning, the substrate is weighed again using the precision scale inside the glovebox. While for stainless steel substrates, only insignificant mass losses can be expected, the mass loss of U-Mo substrates can reach > 1 wt.% and therefore must be recorded.
7. **Installation.** The vertical height of the substrate holder is adjusted to the desired *target-substrate distance* before the substrate is installed. When the flat support half-size substrate holder is used, the substrate is laid centrally onto the substrate support surface. To install the substrate into the clamping full-size substrate holder, the springs are loosened first and the top covers of both clamping blocks are removed. Afterwards, the top parts of the inner clamping blocks are removed and the substrate borings are aligned with the fixation pins. Then, the inner clamping blocks are re-assembled, the top covers are mounted again on both clamping blocks and the springs are loaded so that the substrate is held straight and flat centrally below the sputtering target.
8. **Short-circuit test.** During plasma cleaning and substrate biasing, high voltage is applied to the substrate and thus, short-circuits between the substrate and the grounded surroundings must be avoided. Thus, the electrical insulation of the substrate is confirmed using a multimeter.
9. **Evacuation.** The vacuum chamber is closed and evacuated using the vacuum pumping system. Once a vacuum of less than 0.5 mbar is reached by the backing pump, the regulation valve and the exhaust valve are opened and the turbomolecular pump is activated. Once a vacuum of less than $2 \cdot 10^{-6}$ mbar is reached, typically after 30 - 60 minutes, the process is continued with step 10.
10. **Plasma cleaning.** In addition to chemical cleaning, plasma cleaning ensures a clean substrate surface prior to the coating process. Thus, the desired *plasma cleaning process pressure* is first set using the mass flow controllers and by using the regulation valve. Then, the sputtering target rotation is set on and the cooling water valves are opened. Finally, the substrate PSU is switched on with its power and current set points set to maximum, before the voltage set point is slowly increased from 100 V to the desired *plasma cleaning voltage* and the ignition of a substrate plasma is watched. Once the substrate voltage has stably reached the desired voltage, the plasma cleaning process is kept running for the desired *plasma cleaning time*. Then, the substrate PSU and the argon mass flow controller are switched off and the vacuum chamber is again evacuated to less than $2 \cdot 10^{-6}$ mbar by the turbomolecular pump.
11. **Sputtering target cleaning.** The sputtering target is cleaned from any contaminants deposited by the substrate plasma cleaning process via sputtering towards the cover plates. Thus, the desired *sputtering process pressure* is first set using the mass flow controllers and by using the regulation

valve and the magnet bar inside the sputtering target is swiveled into the cleaning position. Once the cleaning position is reached, the sputtering PSU is switched on with its voltage and current set points set to maximum, and its power set point is set to 5 kW. After 5 minutes of sputtering, the power set point of the sputtering PSU is set to the desired *sputtering power* and the magnet bar is swiveled back into the sputtering position.

- 12. Sputter deposition.** Before the magnet bar has reached the sputtering position, the substrate PSU is switched on with its power and current set points set to maximum, and its voltage set point is set to the desired *substrate biasing voltage*. After the desired *sputtering time* has passed, all power supply units, the argon mass flow controller and the sputtering target rotation are switched off and the vacuum chamber is evacuated again using the turbomolecular pump.
- 13. Cooling and venting.** After the sputter deposition is finished, the substrate is kept in the vacuum chamber for at least 30 minutes to allow it to cool down to less than 50 °C. After this time has passed, the cooling water and vacuum valves are closed, the vacuum pumps are switched off and the vacuum chamber is vented by manually opening the venting valves.
- 14. Turning and re-installation (optional).** If also the second side of the substrate needs to be coated, the substrate is turned and re-installed into the substrate holder, as described in step 7. Steps 8 - 13 are repeated.
- 15. Post-coating weighing.** The substrate is removed from the vacuum chamber and weighed again using the precision scale inside the glovebox.
- 16. Transfer out of glovebox and trimming (optional).** If the clamping full-size substrate holder is used, both ends of the substrate need to be trimmed off after PVD coating. While the possibility to perform this step by laser cutting is not yet available at Framatome-CERCA, the substrate needs to be transferred out of the glovebox for this step. Then, the trimming is performed using the workshop guillotine and the substrate is transferred back into the glovebox.
- 17. Packaging.** Before the substrates can be shipped to Framatome-CERCA for cladding application, they are packaged in the high-purity argon atmosphere of the glovebox. They are first inserted into a smaller A30 T bag (“inner bag”), which is sealed leak-tight using the welding tongs. Then, the inner bag together with an RP-A oxygen absorber [228] and an ageless-eye oxygen indicator [229] is inserted into a larger A30 T bag (“outer bag”), which is again sealed leak-tight using the welding tongs.
- 18. Transfer out of glovebox.** Finally, the packaged substrates are transferred out of the glovebox. They are mounted on rigid plastic boards to prevent mechanical deformation during transport.

An exemplary process diagram, showing the steps 9 to 13 of the PVD coating process, can be seen in Figure 150. By two operators, the entire process flow on a single substrate can be executed in typically six hours. As large parts of the process can be performed parallelized for multiple substrates, typically two substrates can be finished per standard working day.

5.5.2 PROCESS CHARACTERIZATION AND PARAMETRIZATION

The initial characterization and parametrization of the full-size PVD coating process was partly carried out within a B.Sc. thesis [230] and reference is made to this thesis wherever applicable. These experiments were performed in the biasing mode using mostly the flat support half-size substrate holder and the unbalanced uTRM80 magnet bar inside an industrial-grade Zr 702 sputtering target. For all experiments presented in this section, stainless steel substrates with 0.40 mm thickness were used, which were cut to size by laser cutting. Figure 151 shows a photograph of the PVD coating process of a half-size stainless steel substrate inside the device.

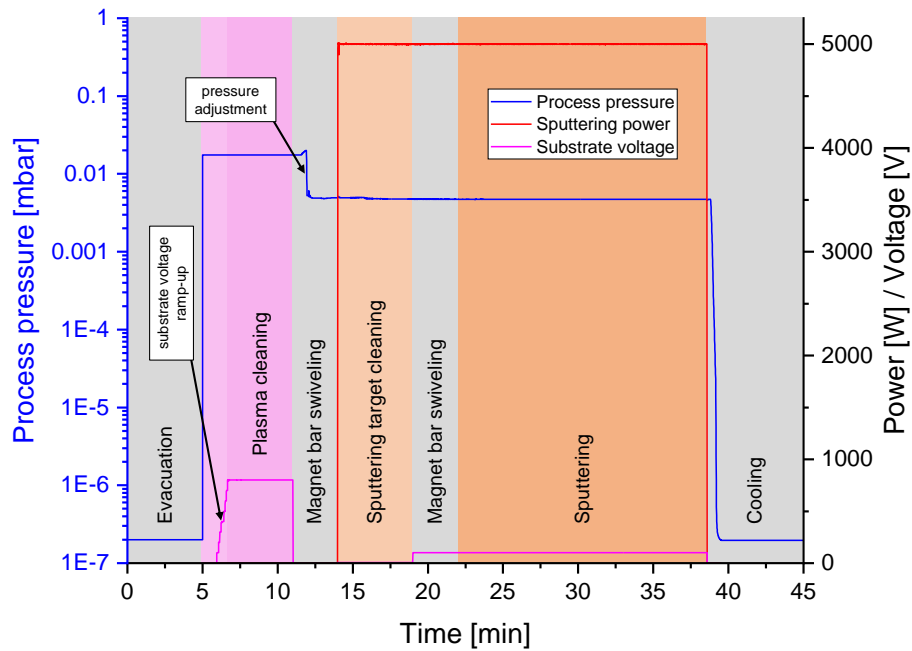


Figure 150: Exemplary process diagram of the full-size PVD coating process. After evacuation of the process chamber (not displayed in full length), the substrate is plasma cleaned. To remove the deposited layer from the sputtering target afterwards, it is cleaned with the magnet bar in cleaning position. Then, the magnet bar is swiveled back into sputtering position and the substrate is coated with a substrate biasing voltage applied. After the process is finished, the substrate cools down (not displayed in full length).

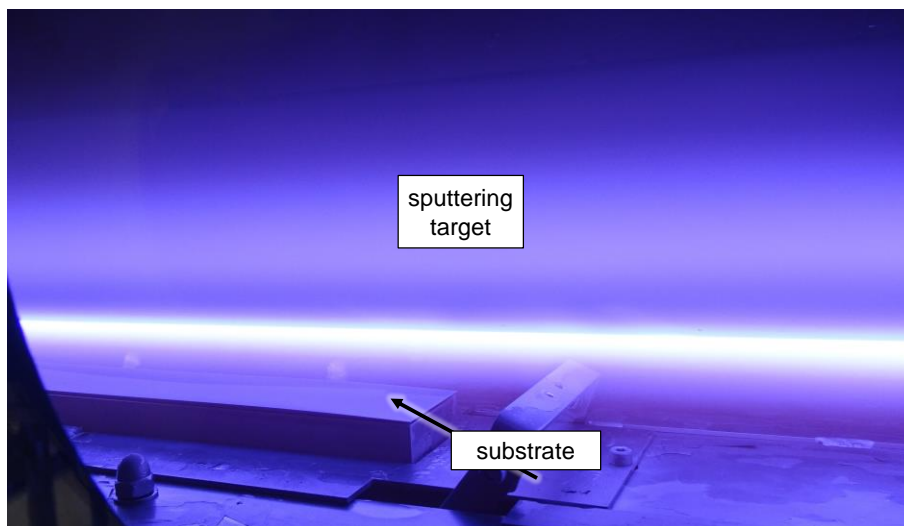


Figure 151: PVD coating of a half-size stainless steel substrate. A sputtering plasma is ignited below the sputtering target, which is under continuous rotation. The sputtered Zr atoms are deposited onto the substrate below.

Plasma cleaning

It was shown previously that plasma cleaning is an important factor to ensure proper adherence of the Zr coating [12]. For the EMPIrE fabrication campaign, this process step was performed on mini-size substrates for 15 minutes per substrate side at a process pressure of ~ 0.4 mbar argon and a substrate voltage of -800 V. While this plasma cleaning step has contributed to the excellent adherence of the

coating, it has shown several disadvantages which shall be improved in the full-size process. Due to the high process pressure and high substrate voltage, the average surface abrasion rate was measured to be approximately 93 nm/min, leading to a significant radioactive contamination of the vacuum chamber walls when the process is performed several times. If performed similarly on half-size substrates, these process conditions can further lead to a severe warping of the substrate due to thermal expansion and thus make the process not reproducible. Also, such high process pressures in combination with such high voltages can lead to the occurrence of many unwanted electrical arcs at the substrate.

The pre-experiments on an optimized substrate heating approach have shown no layer adherence problems on samples produced without plasma cleaning, presumably due to a sufficient removal of residual water and volatile contaminants during substrate pre-heating. Therefore, it is aimed to reduce both the intensity and the duration of the plasma cleaning step in the full-size process. Residual water and volatile contaminants shall still be removed, but the underlying substrate material does not necessarily need be substantially eroded anymore.

Via numerous experiments carried out in a B.Sc. thesis [230], an optimum parameter set for such a mild plasma cleaning step was found. Most importantly, the plasma cleaning process pressure is reduced to $2.0 \cdot 10^{-2}$ mbar argon in order to reduce the plasma intensity. To be able to still ignite a stable substrate plasma, the magnet bar inside the sputtering source is swiveled downwards into the coating position also for plasma cleaning and the plasma cleaning voltage is maintained at - 800 V. The plasma cleaning time is reduced to 5 min. Using these parameters, the plasma ignites across the entire substrate surface while leading only to an insignificant average surface abrasion rate of 0.45 nm/min. As shown later, no harmful warming of the substrate to temperatures greater than 400 °C can be expected during this process step.

The adherence of the Zr coating deposited after such a mild plasma cleaning process was evaluated visually after several hours of storage at air. Figure 152 a shows extensive coating delaminations at the edges of a substrate, which has not undergone plasma cleaning prior to PVD coating. In contrast, the mildly plasma-cleaned substrate in Figure 152 b does not show any delaminations at all.

It is thus concluded that plasma cleaning remains a key factor to ensure proper adherence of the Zr coating. The developed mild plasma cleaning step has shown to be still sufficient to remove surface adsorbates such as residual water and volatile contaminants. In parallel, the undesired abrasion of substantial amounts of substrate material was reduced to insignificant values.

PVD coating

To keep the parameter space for the initial characterization small, the sputtering process pressure was kept at $4.0 \cdot 10^{-3}$ mbar argon, which is in the range commonly found in the literature. Hereby, the ignition and continuous operation of a sputtering plasma is reliably possible for sputtering powers up to 7500 W at target-substrate distances between 30 mm and 70 mm for several hours. Depending on the sputtering power set point, a sputtering voltage in the range of - 300 to - 500 V is typically necessary to maintain the plasma. Apart from the phase of the first plasma ignition after the vacuum chamber was opened, usually less than 0.01 arcs/s occur after 5 minutes of sputtering target cleaning.

Usually, plasma parameters like the floating potential and the substrate current density at various substrate potentials are first measured when characterizing a new PVD coating device. Due to the unavailability of a typically used *Langmuir probe* [231] and a suitable four-quadrant substrate power supply unit, able to apply negative or positive substrate voltages and to measure positive or negative substrate currents without re-wiring, only the floating potential and the substrate earth current density

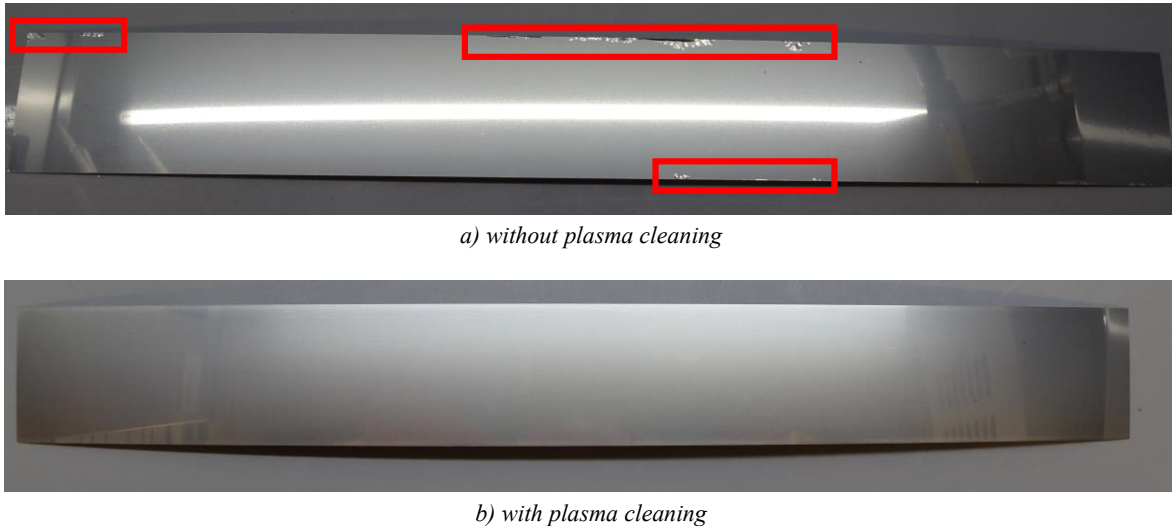


Figure 152: Half-size substrates after PVD coating without (a) and with (b) prior plasma cleaning. The substrate which has not undergone plasma cleaning prior to PVD coating shows extensive delaminations at the edges (marked in red). In contrast, the plasma-cleaned substrate shows no delaminations at all. From [230].

were measured using a half-size substrate lying on the substrate holder. Thus, the size of the probe (here: a half-size substrate with a surface area of 171 cm²) can not be considered minor and the measured values are only average values. Because unlike in the mini-size device, the target-substrate distance can not be adjusted during a running process, the measurements were performed only for the two extreme values of 30 mm and 70 mm.

The floating potential of the substrate was measured at various sputtering powers between 100 W and 7500 W by disconnecting the substrate power supply unit and connecting a multimeter in voltage mode to the substrate voltage connector and the grounded substrate holder, respectively. Between 2000 W and 3000 W sputtering power, the floating potential could not be determined since the plasma was unstable in this range, the reason for this behavior being not yet known. Figure 153 shows the result of these measurements. Generally, the floating potential becomes less negative with increasing sputtering power and almost reaches saturation around - 9 V at a sputtering power of 3000 W and above. Except for very low sputtering powers below 500 W, no significant difference was observed between 30 mm and 70 mm target-substrate distance. Due to the large probe size, this result likely is not suitable for the exact determination of further plasma parameters. The similar floating potential at the target-substrate distances 30 mm and 70 mm however indicates that the plasma characteristics are similar at both distances.

To measure the substrate earth current density, the substrate power supply unit was kept disconnected and the substrate voltage connector was connected to ground via a multimeter in current mode. Hereby, the substrate potential is artificially set to ground potential and the measured earth current equals the sum of the impinging ion and electron currents to the substrate. Similar to the floating potential, the earth current density could not be determined between 2000 W and 3000 W sputtering power since the plasma was unstable in this range. Figure 154 shows the result of these measurements. Generally, the earth current density increases almost linearly with increasing sputtering power. Above a sputtering power of 6000 W, however, no significant increase is observed anymore. No significant difference of the substrate earth current density can be observed between 30 mm and 70 mm target-substrate distance. The similar substrate earth current density at the target-substrate distances 30 mm and 70 mm again indicates that the plasma characteristics are similar at both distances.

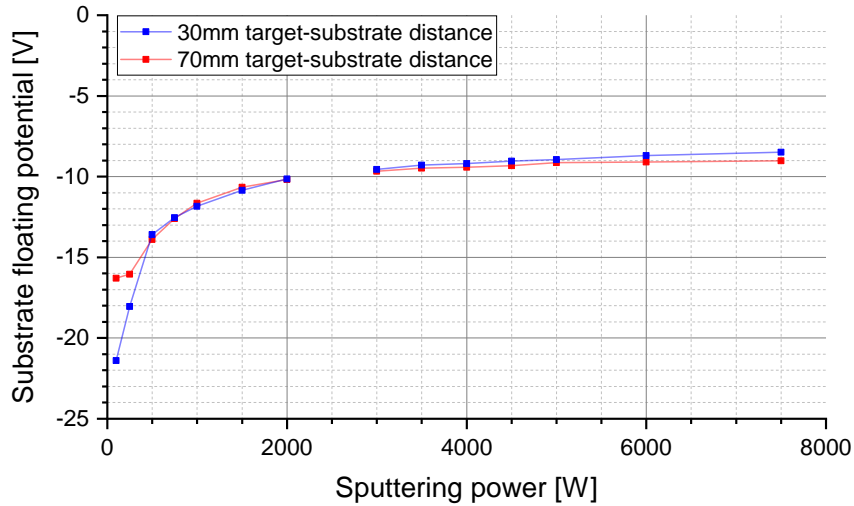


Figure 153: Floating potential of a half-size substrate at various sputtering powers at 30 mm and 70 mm target-substrate distance. At sputtering powers of 3000 W and more, the floating potential remains almost constant. Between 2000 W and 3000 W, the floating potential could not be determined since the plasma was unstable in this range. Data from [230].

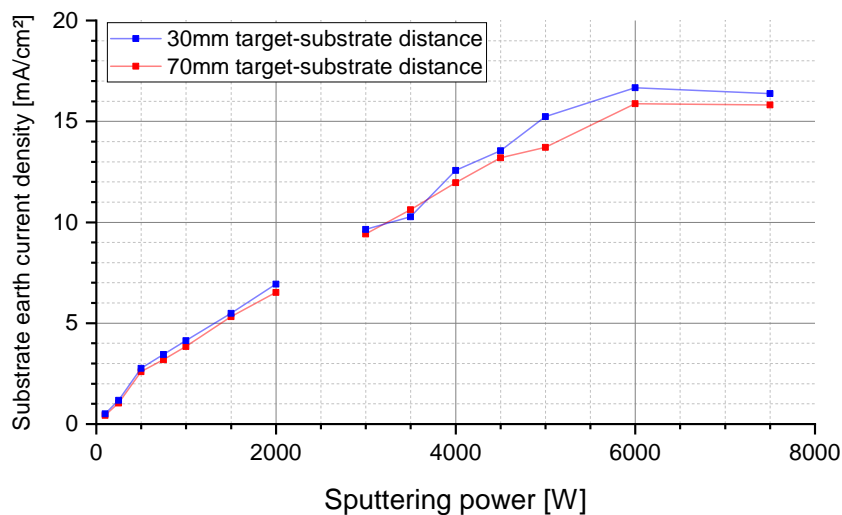


Figure 154: Earth current density at various sputtering powers at 30 mm and 70 mm target-substrate distance. The earth current density increases with increasing sputtering power. Above 6000 W, no significant increase was measured anymore. Between 2000 W and 3000 W, the earth current density could not be determined since the plasma was unstable in this range. Data from [230].

These measurements do not indicate any major difference in the general plasma characteristics at different target-substrate distances. The sputtering power – once set higher than the instability range of 2000 - 3000 W – also has almost no influence on the substrate floating potential and only the expected linear influence on the substrate earth current density up to 6000 W. Considering the mean free path of sputtered Zr atoms of approximately 6 mm at the process pressure of $4.0 \cdot 10^{-3}$ mbar argon, the average number of collisions between sputtered and gas atoms increases from 5 to 11.67 when increasing the target-substrate distance from 30 mm to 70 mm, under the assumption of solely forward scattering. As the sputtered Zr atoms lose a part of their kinetic energy at each collision, the target-substrate distance is thus expected to have a significant impact on the energy contribution of sputtered atoms to the adatom

mobility. Also, due to the additional scattering and for simple geometric reasons, the average effective growth rate of the deposited Zr layer is expected to be lower at higher target-substrate distances. This was confirmed by measurements: the average effective layer growth rate was determined to be $0.317 \mu\text{m}/\text{min}$ at 30 mm target-substrate distance and $0.190 \mu\text{m}/\text{min}$ at 70 mm target substrate distance at $4.0 \cdot 10^{-3}$ mbar process pressure and 5000 W sputtering power [230]. Therefore, with the goal of short process times and high adatom mobility in mind, the characterization and parametrization were continued using the lowest possible target-substrate distance of 30 mm and a fixed sputtering power of 5000 W.

The upcoming results in section 5.5.3 will confirm that these process parameters are suitable for the successful PVD coating of half-size stainless steel substrates with Zr and the subsequent C2TWP cladding application. Therefore, a further determination and discussion of plasma parameters, as it was performed for the mini-size process, will not take place within this thesis and is left for future theses, if necessary.

Substrate bending

To study the effect of substrate bending, several half-size substrates were coated with Zr on a single side using the flat support half-size substrate holder and the process parameters defined before: $4.0 \cdot 10^{-3}$ mbar process pressure, 5000 W sputtering power and 30 mm target-substrate distance. While during the actual PVD coating process, almost no bending of the substrate was observed, a strong bending developed during the cooling phase, while the substrate was still installed in the vacuum chamber. A central upwards bending of the substrates, when laid flat onto the laboratory workbench as shown in Figure 155, indicates the existence of tensile stresses in the deposited layer – similar to the results obtained in the EMPIRE fabrication campaign [12]. Depending on the average coating thickness, the extent of bending is almost linear, as shown in Figure 156. Hereby, the average coating thickness was determined by weighing the sample before and after the coating process, under the general assumption that any mass difference is due to the deposition of a Zr layer with bulk density of $6.5 \text{ g}/\text{cm}^3$.

The thermocouples integrated into the flat support half-size substrate holder are designed and calibrated [207] to indicate the substrate temperature only if it lays flat on the support surface. Therefore, no substrate temperature measurements can be reasonably performed when the substrate is developing only a slight upwards bending during the PVD coating process. Such measurements were instead performed using the clamping full-size substrate holder and will be presented later.

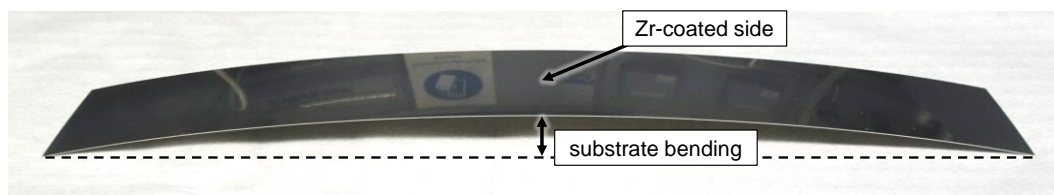


Figure 155: Bent half-size substrate with single-sided Zr coating. The central upwards bending – when laid flat onto the laboratory workbench – indicates the existence of tensile stresses in the deposited Zr layer.

Optimization of PVD process parameters. To adjust the form and level of stresses in the layer, the literature commonly recommends an adjustment of the process parameters [132,158,159,232,233]. For example, the process pressure is said to have an influence on the development of tensile or compressive stresses. Because the previously selected process pressure of $4.0 \cdot 10^{-3}$ mbar argon already is comparably low and the operation of a sputtering plasma is not stably possible at significantly lower process pressures, only an increased process pressure is investigated. It is further suggested to reduce the

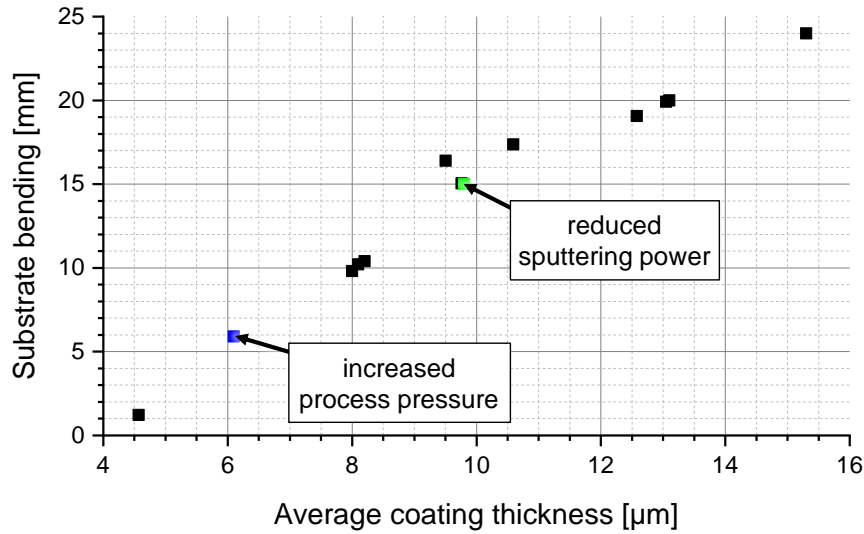


Figure 156: Measured bending of half-size substrates with single-sided Zr coating. The measured substrate bending increases with increasing average coating thickness. The colored data points from experiments using an increased process pressure (blue) or a reduced sputtering power (green) are in good agreement with the general trend.

sputtering power to decrease the amount of stresses in the deposited layer. Table 17 shows the process parameters and the results of representative experiments with increased process pressure and with reduced sputtering power, respectively. As it can be seen, both approaches significantly decrease the layer growth rate and therefore are in strong contradiction to the goal of short process times. It was furthermore not possible to reduce the substrate bending by these measures, as the bending is still in good agreement with the general trend visualized in Figure 156.

Table 17: Process parameter variations to study the substrate bending effect. While both approaches –increased process pressure as well as reduced sputtering power – significantly reduce the average effective layer growth rate, the resulting substrate bending is still in good agreement with the results using standard parameters.

	Standard parameters	Increased process pressure	Reduced sputtering power
Target-substrate distance	30 mm	30 mm	30 mm
Sputtering process pressure	$4.0 \cdot 10^{-3}$ mbar	$2.0 \cdot 10^{-2}$ mbar	$4.0 \cdot 10^{-3}$ mbar
Sputtering power	5000 W	5000 W	1000 W
Sputtering time	30 min	50 min*	200 min*
Average coating thickness	9.5 μm	6.1 μm	9.8 μm
Average effective layer growth rate	0.317 μm/min	0.122 μm/min	0.05 μm/min
Substrate bending	16.3 mm	5.9 mm	15.0 mm

*) Sputtering time adjusted to partially compensate the higher process pressure or lower sputtering power

Reduction of the coating thickness. Because the Zr coating is applied to the substrate one side after the other, the application of a 25 μm thick Zr coating on both sides – the requirement from the EMPIRE fabrication campaign – is obviously not possible, even in half-size geometry. However, the application of a proposed 8 μm Zr coating on both sides seems feasible for the production of half-size stainless steel samples for subsequent cladding application experiments. While the resulting substrate bending after cooling is approximately 10 mm, the bending does not exceed 5 mm during the PVD coating process and the resulting layer thickness non-uniformity due to a non-uniform target-substrate distance is thus considered acceptable. For coating the second side, the installation of the substrate centrally onto the substrate holder is still manageable and the upwards bending of the ends of the substrate usually disappears when the substrate has warmed up after some minutes of PVD coating. When both sides are finally coated with the same thickness, the substrates are entirely flat again and are thus suitable for the cladding application process. However, for the future PVD coating of full-size substrates – even with only 8 μm Zr coating on both sides – the substrate needs to be forcefully kept flat and straight on the substrate holder during the process.

Fixing of the substrate to the substrate holder. The flat support half-size substrate holder offers two possibilities to fix the substrate to the support surface, which were studied in experiments [207]: the substrate can be either (i) screwed to the support surface at the ends or (ii) adhered to the support surface using an adhesive heat conducting film. In experiments, both approaches were not able to keep the substrate reliably flat during and after the PVD coating process. When screwed to the support surface at one or both ends, the substrate still developed a central upwards bending. When adhered to the support surface, the tensile stresses in the Zr layer as well as the thermal expansion of the substrate still were able to locally tear off the substrate and cause an upwards bending. Depending on the manual force applied while adhering the substrate to the heat conducting film, the substrate occasionally was too tightly glued to the film, so that it could not be removed non-destructively after PVD coating

Clamping full-size substrate holder. The clamping full-size substrate holder is designed to keep the substrate straight and flat during PVD coating by fixing it at borings at both ends and pulling it straight by spring force. In several experiments using stainless steel full-size substrates and the same process parameters developed before, the deposition of 30 μm Zr and more did not lead to any notable bending of the substrates when installed into this substrate holder. The spring force was able to compensate the thermal expansion of the substrate as well as the tensile stresses inside the deposited Zr layer. When removed from the substrate holder after single-sided coating, the substrates exhibit the typical central upwards bending which is in good agreement with the trend visualized in Figure 156. The re-installation into the substrate holder for coating the second side is still manageable, and after coating of both sides, the substrates are entirely flat again. As Figure 157 shows, a small area with weak coating adherence typically develops near the uncoated area where the substrates are clamped. The occurrence of this area is assumed to be linked to the proximity to the outer housings of the clamping blocks, which are at ground potential and thus can locally disturb the plasma. To achieve specification-conform substrates without delaminations, less than 15 mm need to be trimmed off from both ends.

As a result, this substrate holder will be used for future experiments on PVD coating and C2TWP cladding application using half-size and full-size U-Mo substrates, which are beyond the scope of this thesis.

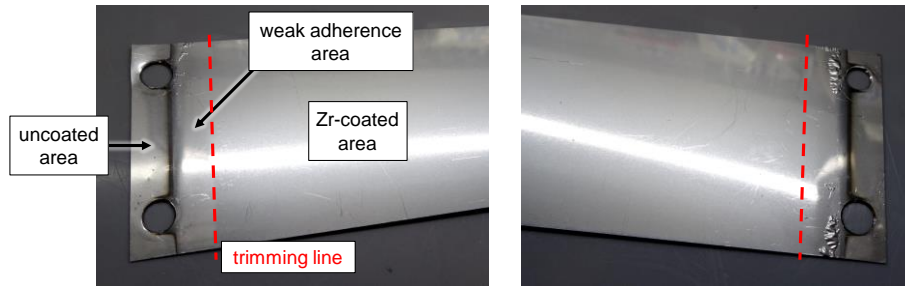


Figure 157: Example of substrate ends to be trimmed off. When using the clamping full-size substrate holder, the uncoated and weak adherence areas at both ends need to be trimmed off after PVD coating.

Substrate biasing

As a result of the pre-experiments, an optimized substrate biasing approach using a sputtering source with an unbalanced magnetron of type 2 is seen as the technique of first choice to improve the ductility of the Zr coating. Hereby, it should be possible to decrease the substrate biasing voltage to ~ -100 V or less while significantly increasing the ion flux to the substrate, with the goal of maintaining the energy contribution of impinging ions to the adatom mobility.

Thus, the achievable substrate current density was first measured at various sputtering powers under the previously described standard operation conditions. This measurement, whose results are shown in Figure 158, expectedly shows an increase of the substrate current density with increasing sputtering power. Furthermore, the substrate current density reaches a saturation level at certain substrate biasing voltages. For example, at 5000 W sputtering power, the saturation level is reached at -100 V substrate biasing voltage. This leads to the assumption that, if a certain substrate biasing voltage is exceeded, all available ions from the plasma are effectively dragged towards the substrate. The measured substrate current then corresponds to the ion saturation current. If the substrate biasing voltage is increased further, the energy of impinging ions is increased but no more additional ions are attracted.

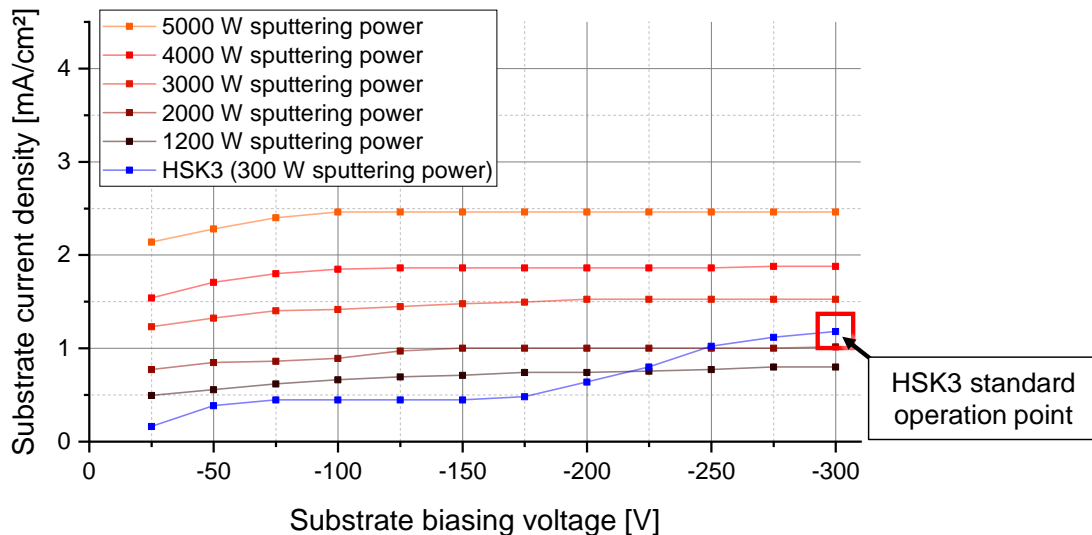


Figure 158: Achievable substrate current density at various sputtering powers in comparison to the mini-size device (HSK3). Especially for higher sputtering powers, the substrate current density reaches a saturation level at a substrate biasing voltage of not more than -100 V. For comparison, the substrate current density at the standard operation conditions of the mini-size device continues to increase with increasing substrate biasing voltage.

When comparing the results with 5000 W sputtering power to the results from the mini-size PVD coating device at its standard operation conditions [14], the substrate current density is increased by a factor of two at a substrate biasing voltage of - 300 V and even by a factor of five at - 100 V. At 5000 W sputtering power and - 100 V substrate biasing voltage, an ion flux to the substrate of $1.54 \cdot 10^{16}$ ions/cm² s can be achieved. This leads to an impinging ion-to-atom ratio to the substrate of 0.68 and an average effective energy contribution of the ions of ~ 58 eV per deposited Zr atom. Hence, it was possible to achieve the desired increase of the ion flux to the substrate even at a lower substrate biasing voltage. However, the energy contribution of the ions to the adatom mobility is ~ 37 % lower than at the standard operation point of the mini-size device.

Even though the energy contribution of the ions to the substrate is lower than expected, the results appear promising due to the significantly lower necessary substrate biasing voltage. Therefore, four half-size stainless steel samples were produced with different substrate biasing voltages from 0 V to - 200 V to study its effect on the main properties of the deposited Zr layer: grain structure, hardness and ductility. The other process parameters were kept at the previously described standard values. To reach a deposited layer thickness of approximately 10 μm , which is considered sufficient to evaluate the layer's grain structure and hardness, the sputtering time was increased from 30 minutes for 0 V substrate biasing voltage to 40 minutes for the other samples, to compensate the potential re-sputtering of the deposited layer. Table 18 summarizes the produced samples. The average effective layer growth rate was determined by weighing the sample before and after the coating process, under the general assumption that any mass difference is due to the deposition of a Zr layer with bulk density of 6.5 g/cm³.

Table 18: Zr-coated stainless steel samples with substrate biasing. Four stainless steel samples were produced to study the effect of different substrate biasing voltages.

Sample ID	Substrate voltage	Average substrate current density	Average effective layer growth rate	Impinging ion-to-atom ratio*	Ion energy per Zr atom*
SS+Zr-0V	0 V	n/a	0.317 $\mu\text{m}/\text{min}$	n/a	n/a
SS+Zr-50V	- 50 V	2.28 mA/cm ²	0.315 $\mu\text{m}/\text{min}$	0.63	27 eV
SS+Zr-100V	- 100 V	2.46 mA/cm ²	0.315 $\mu\text{m}/\text{min}$	0.68	58 eV
SS+Zr-200V	- 200 V	2.46 mA/cm ²	0.265 $\mu\text{m}/\text{min}$	0.68	115 eV

*) With a negative substrate biasing voltage, the average effective layer growth rate may be reduced due to the re-sputtering of the deposited layer by impinging ions. Thus, the Zr particle flux was calculated using the undisturbed growth rate of 0.317 $\mu\text{m}/\text{min}$.

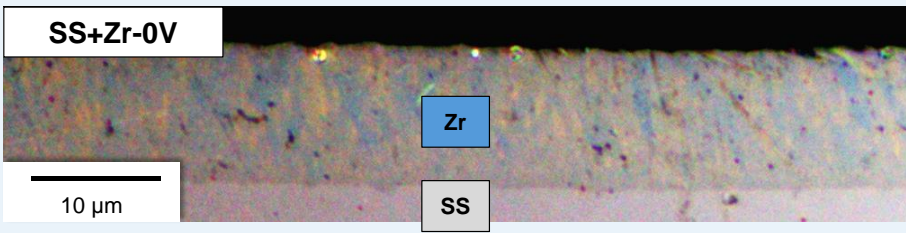
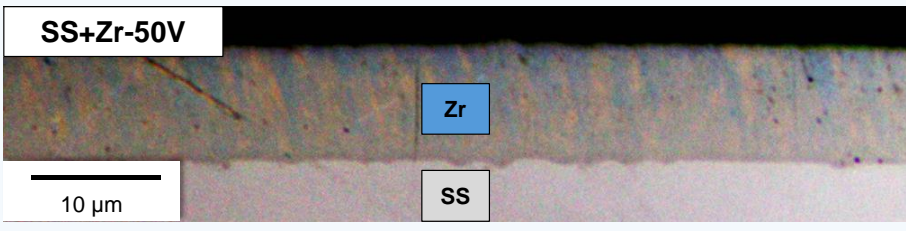
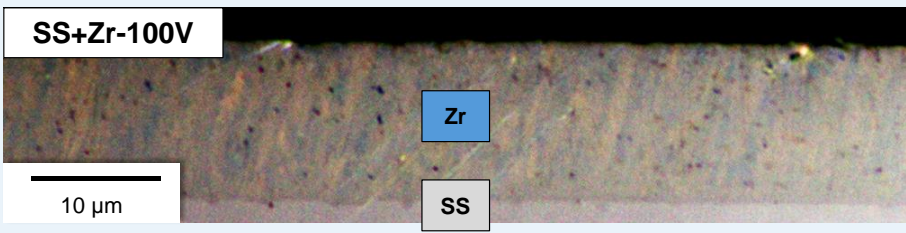
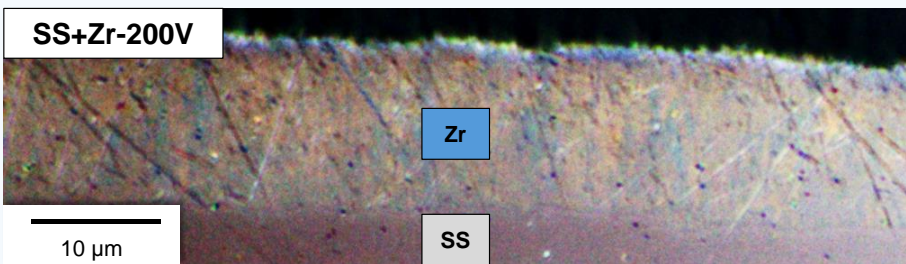
During the coating process, the samples expectedly exhibited a slight central upwards bending of not more than 5 mm while installed onto the substrate holder. After cooling, the measured bending of the substrates was in line with the general trend visualized in Figure 156 and it is thus concluded that substrate biasing does not significantly influence substrate bending. By visual inspection of the samples after coating at air, no delaminations were found on any sample and the coated surfaces appeared metallic-shiny with no obvious irregularities.

While the average effective layer growth rates of the samples with 0 V, - 50 V and - 100 V substrate biasing voltage are equal within the achievable measurement precision, the rate is reduced by approximately 16 % at - 200 V substrate biasing voltage. Obviously, impinging ions with such energy are able to re-erode the deposited layer to a significant extent. From an assumed undisturbed growth rate

of 0.317 $\mu\text{m}/\text{min}$, a Zr particle flux to the substrate of approximately $2.27 \cdot 10^{16}$ atoms/ $\text{cm}^2 \text{ s}$ is thus calculated. From the average substrate current densities, ion fluxes to the substrate of 1.42 ions/ $\text{cm}^2 \text{ s}$ to 1.54 ions/ $\text{cm}^2 \text{ s}$ are calculated, leading to impinging ion-to-atom ratios to the substrate of 0.63 - 0.68. The energy contribution of the ions to the adatom mobility ranges from ~ 27 eV per deposited Zr atom to ~ 115 eV.

Table 19 shows the results from optical microscopy and hardness measurement of the samples. Numerous black spots are visible within the deposited Zr layer, which are not considered to be porosities but impressed diamonds from the last polishing step. While individual grains are barely visible in the deposited layer, the fine and dense structure appears similar on all samples. Due to the absence of porosities or other growth defects, it is concluded that the preferred growth structure type C can be reached independently of the application of a substrate biasing voltage. Also, the hardness of the Zr layer is similar on all samples and slightly lower than the assumed hardness of the sputtering target of 234 ± 16 HV1.

Table 19: Micrographs of Zr-coated stainless steel samples with substrate biasing. The different samples show a similarly fine and dense Zr layer grain structure with comparable hardness.

Optical micrograph (polarized light)	Zr layer hardness
	182 ± 9 HV0.01
	209 ± 17 HV0.01
	186 ± 7 HV0.01
	204 ± 13 HV0.01

To evaluate the ductility of the Zr coating, a bending test was performed on all samples and the results are shown in Figure 159. The ductility is significantly influenced by the substrate biasing voltage. If no or a low voltage is set, the outward bend shows many irregular cracks. With an increased voltage of - 100 V, the ductility increases significantly so that only a single crack is found. At - 200 V substrate biasing voltage, the coating becomes more brittle and the outward bend again shows many irregular cracks. On the inward bends, no cracks were found at all. It is thus assumed that an optimum operation point at - 100 V substrate biasing voltage exists, which delivers the most ductile Zr coating. On all samples, the coating shows excellent adherence, since even cracked parts stick to the substrate surface.

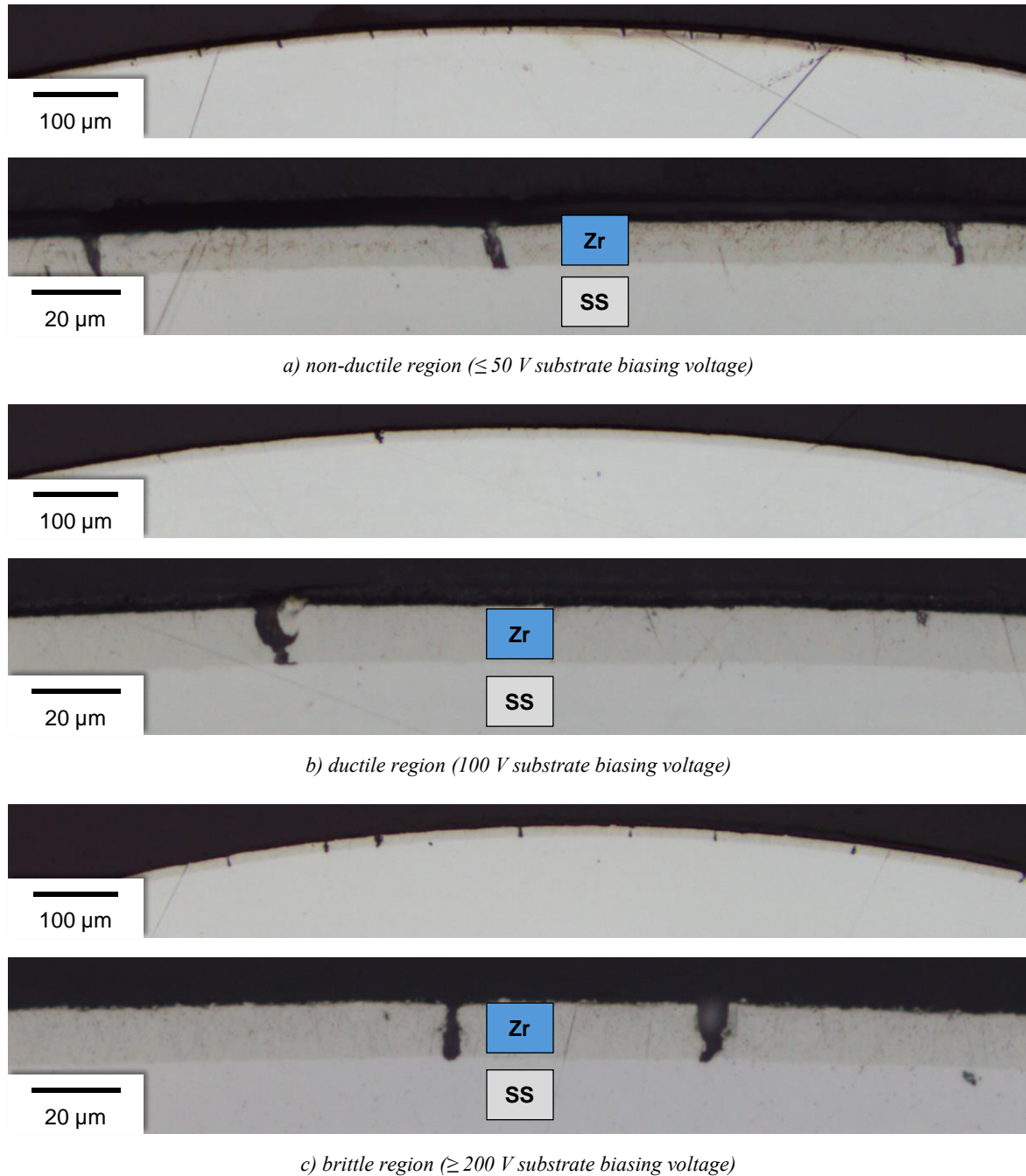


Figure 159: Bending test results for Zr layers deposited at various substrate biasing voltages. The Zr coating is prone to cracking on the outward bends if the substrate biasing voltage is kept too low (non-ductile region, a) or too high (brittle region, c). In the ductile region, only a single crack close to the top of the bend could be found. In any case, the coating shows excellent adherence, since even cracked parts stick to the substrate surface.

It is thus concluded that the full-size PVD coating process with an optimized substrate biasing approach using the unbalanced uTRM80 magnet bar is suitable for the deposition of dense, defect-free and comparably soft Zr layers in growth structure type C. By the application of a substrate biasing voltage of - 100 V, the ion flux to the substrate is significantly increased compared to the standard operation point of the mini-size device. As a result, the coating shows a high ductility with only a single crack found in the bending test, even though the desired larger grains could not be achieved.

Due to these promising results, no further experiments on an optimized substrate biasing approach using an electron emission system or on an optimized substrate heating approach were performed within this thesis. Also, no experiments using the balanced SRM80 magnet bar were performed. Such experiments are left for future theses if necessary.

Substrate temperature

Due to the strong bending of the substrates on the flat support half-size substrate holder during and after the PVD coating process, the measurement of the substrate temperature using the built-in thermocouples of the substrate holder as proposed by [207] is not appropriate. Therefore, the temperature can not be contactlessly measured on each sample during the process. Instead, reference measurements for various process steps were performed within a B.Sc. thesis [234] by attaching two type K mantle thermocouples to the bottom of a half-size substrate in the clamping full-size substrate holder using thermal adhesive. One of the thermocouples was attached at the middle of the substrate while the other was placed approximately 30 mm next to the trimming line at one end of the substrate. The results of these measurements are briefly summarized hereafter.

Figure 160 shows the measured equilibrium substrate temperature at various sputtering powers from 500 W to 7000 W after typically 20 minutes of sputtering. All other process parameters were set to the previously described standard operation conditions. Generally, the substrate temperature increases with increasing sputtering power but does not exceed 350 °C even at a sputtering power of 7000 W. The standard sputtering power of 5000 W leads to a substrate temperature of less than 300 °C. The temperature in the middle of the substrate is typically higher than at the end, presumably due to the good thermal contact of the substrate with the massive clamping blocks made of stainless steel.

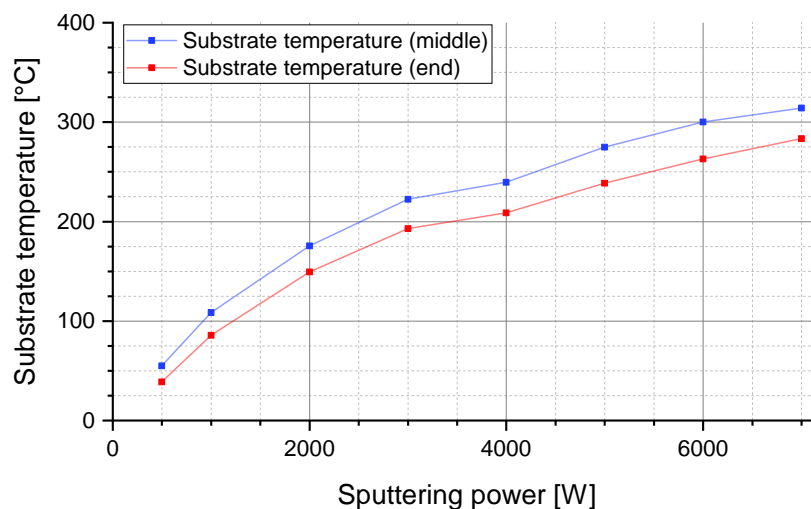


Figure 160: Measured equilibrium substrate temperature at various sputtering powers. The substrate temperature generally increases with increasing sputtering power but does not exceed 350 °C even at a sputtering power of 7000 W. Data from [234].

Figure 161 shows the measured equilibrium substrate temperature at various substrate biasing voltages from 0 V to - 300 V after typically 20 minutes of sputtering. All other process parameters were set to the standard operation conditions. The substrate temperature generally increases with increasing substrate biasing voltage but does not exceed 400 °C even at a substrate biasing voltage of - 300 V. The standard substrate biasing voltage of - 100 V leads to a substrate temperature of less than 300 °C. Again, the temperature in the middle of the substrate is typically higher than at the end.

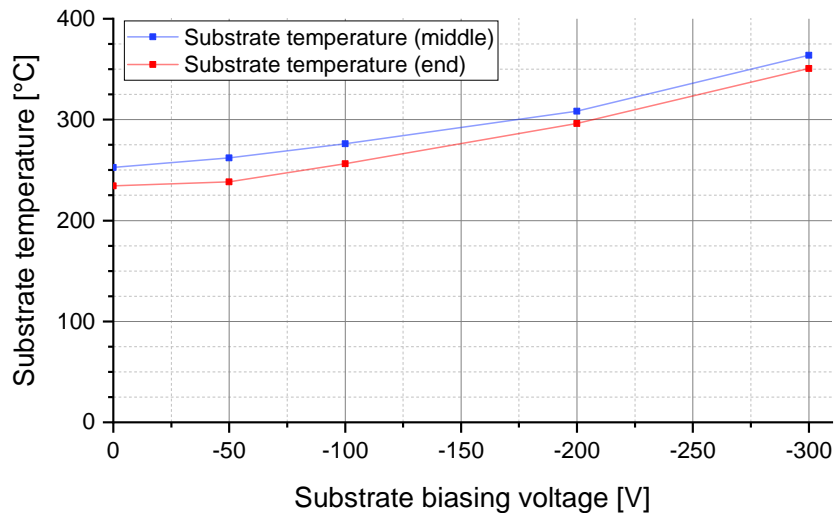


Figure 161: Measured equilibrium substrate temperature at various substrate biasing voltages. The substrate temperature generally increases with increasing substrate biasing voltage but does not exceed 400 °C even at a substrate biasing voltage of - 300 V. Data from [234].

Figure 162 shows the measured equilibrium substrate temperature at various plasma cleaning pressures from 0.05 mbar to 0.15 mbar argon after typically 5 minutes of plasma cleaning. The plasma cleaning voltage was set to the standard operation point of - 800 V. Because higher plasma cleaning pressures generally lead to a higher ion bombardment of the substrate, the substrate temperature increases as well. During the measurement at 0.15 mbar plasma cleaning pressure, both thermocouples failed and the data points serve only for the orientation. Above 0.05 mbar plasma cleaning pressure, the substrate temperature exceeds 400 °C and therefore, the unwanted temperature range of fast U-Mo γ phase decomposition can not be safely avoided. At the standard plasma cleaning pressure of 0.02 mbar, however, no potentially harmful warming of the substrate is expected. Except for the lowest investigated plasma cleaning pressure of 0.05 mbar, the temperature in the middle of the substrate is higher than at the end, potentially due to a slightly non-uniform substrate plasma, which tends to be more intense close to edges.

These measurements confirm that the standard operation points defined for the production of samples for cladding application experiments do not lead to a warming of the substrate above 400 °C. Therefore, the unwanted temperature ranges of fast U-Mo γ phase decomposition and U-Mo/Zr interaction layer formation are safely avoided at any time during the process.

Coating thickness uniformity

A coating thickness profile across the substrate surface must be known for each specific set of process parameters to be able to comply with the minimum thickness requirement. Once this thickness profile is known, the sputtering time can be adjusted to ensure that every location of the substrate is coated with at least the minimum required thickness. Areas with a higher thickness than the minimum requirement

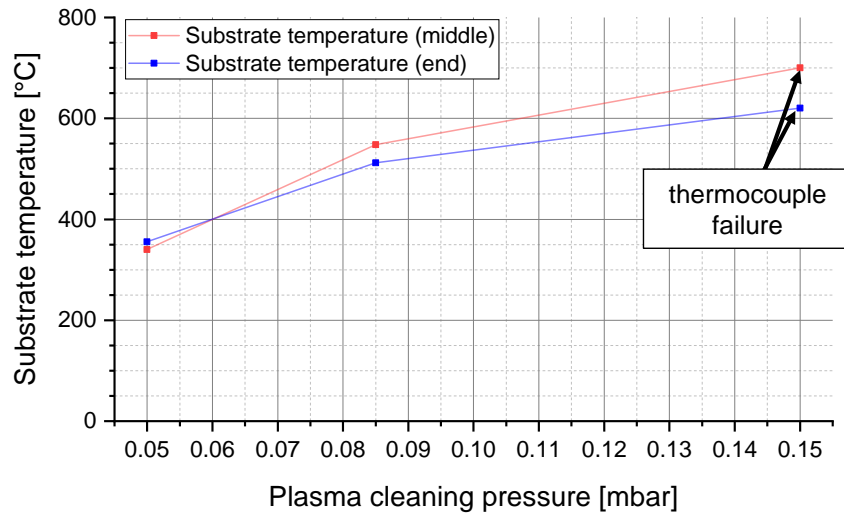


Figure 162: Measured equilibrium substrate temperature at various plasma cleaning pressures. The substrate temperature generally increases with increasing plasma cleaning pressure. During the measurement at 0.15 mbar plasma cleaning pressure, both thermocouples failed and the data points serve only for the orientation. Data from [234].

are not generally unfavored, as long as the deviations do not necessitate extremely long sputtering times to fulfill the minimum thickness requirement at each location. For half-size substrates placed centrally below the sputtering target, no significant thickness deviations are expected along the length of the substrate due to the significantly longer active area of the sputtering target. However, due to the intentionally narrow angular deposition profile of the sputtering source, especially when using the uTRM80 unbalanced magnet bar, the coating thickness profile along the width of the substrate needs to be known.

To determine such a transverse thickness profile under the previously described standard operation conditions, destructive characterization of reference samples using optical microscopy on cross-sections was performed. To cover substrate widths of more than 80 mm, four 82.5 mm wide mini-size substrates were laid perpendicularly and equidistantly to each other onto a flat 45 mm wide substrate mounted in the clamping full-size substrate holder, as shown in Figure 163.

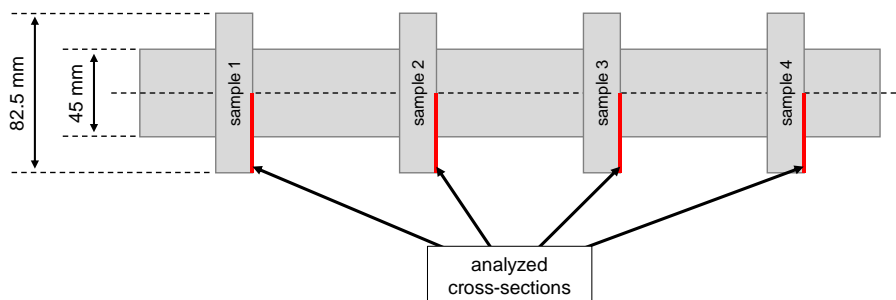


Figure 163: Analyzed cross-sections for the determination of the transverse coating thickness profile. The data was obtained from four 82.5 mm wide mini-size substrates, which were laid perpendicularly and equidistantly to each other onto a flat 45 mm wide substrate in the full-size substrate holder. For symmetry reasons, a cross-section was prepared only of the half width of each substrate.

The sputtering time was adjusted to reach an average coating thickness of approximately 30 μm , which is sufficient to precisely measure the thickness using optical microscopy. For symmetry reasons, only a cross-section of the half width of each substrate was prepared after coating. Along this section, marked in red in Figure 163, the thickness of the deposited layer was measured at ten equidistant measurement locations using the layer thickness measurement tool of the optical microscope software. At each $\sim 100 \mu\text{m}$ wide measurement location, the thickness was automatically measured at 100 equidistant points. The coating thickness profile of the other half width of the substrates was extrapolated by mirroring the measured data due to the expected symmetry. The final coating thickness profile, which is shown in Figure 164, was obtained first by averaging the 100 measurement points at each measurement location, followed by averaging the measurements on all four substrates.

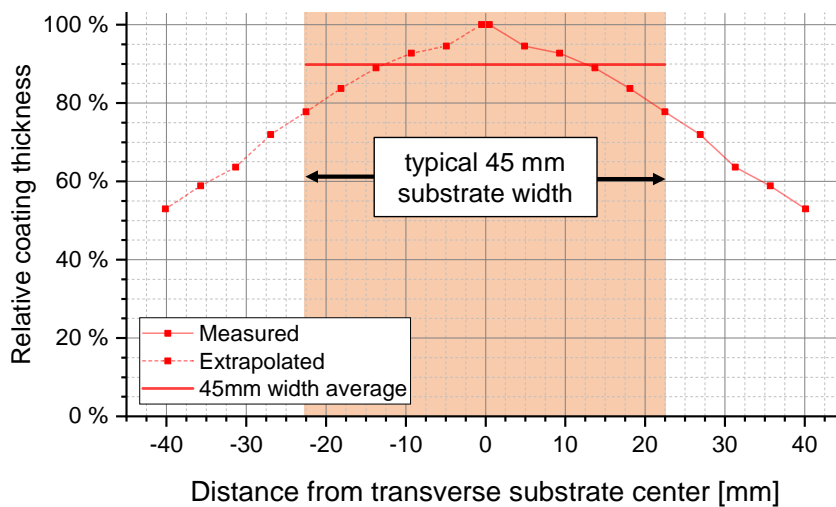


Figure 164: Measured transverse coating thickness profile. The data left of the origin was extrapolated by mirroring the measured data due to the expected symmetry. The orange area marks the width of half-size and full-size substrates.

As can be seen, the maximum of the coating thickness profile is located in the transverse center of the substrate and the relative coating thickness decreases with increasing distance from the center. At the outmost edge of a 45 mm wide half-size or full-size substrate, the thickness is $\sim 22\%$ lower than in the center. The average coating thickness on such a substrate is $\sim 89.8\%$ of the thickness in the center, as represented by the horizontal red line in Figure 164. To ensure the deposition of the minimum required coating thickness across the entire substrate width, the average thickness, which is typically determined by weighing the sample before and after the coating process, must therefore be $\sim 10.2\%$ higher than the minimum required thickness and the sputtering time can be adjusted accordingly. These uniformity values are comparable to the mini-size PVD coating process at 30 mm target-substrate distance, where the coating thickness on the outmost side of a mini-size substrate is approximately 21% lower than in the center.

For the PVD coating of full-size U-Mo substrates in preparation of the FUTURE-MONO-1 irradiation test, which will be subject of future theses, the coating thickness profile shall also be determined along the length of a substrate. Such full-size substrates with 762 mm length are only slightly shorter than the active length of the sputtering target and thus, edge effects must be considered and quantified.

5.5.3 FIRST RESULTS AFTER C2TWP CLADDING APPLICATION

Following the development of the pilot PVD coating process and its successful characterization and parametrization, a common study was performed by TUM and Framatome-CERCA. The aim of this study was to test the new PVD coating process in combination with the C2TWP cladding application process. For this study, a total of four half-size stainless steel substrates (380 mm x 45 mm x 0.40 mm) were coated identically with Zr on both sides and shipped to Framatome-CERCA. After the successful cladding application, non-destructive examination of the resulting half-size plates was conducted at Framatome-CERCA, followed by detailed destructive examination back at TUM.

Sample production parameters

During the characterization and parametrization of the PVD coating process, an optimized parameter set for the production of samples was identified. This set includes general device conditions and specific PVD process parameters and is shown in Table 20. After PVD coating, the produced substrates with double-sided Zr coating meet all defined requirements. Figure 165 exemplarily shows a photograph of such a substrate, ready for cladding application. The substrate is fully coated on both sides, the surface appears metallic-shiny without notable defects or delaminations, and the substrate is entirely flat.



Figure 165: Half-size stainless steel substrate with double-sided Zr coating ready for cladding application. Using the parameter set described in Table 20, four substrates were produced identically.

Table 20: PVD sample production parameters for subsequent C2TWP cladding application. While the device conditions were defined earlier, the PVD process parameters were identified during the process characterization and parametrization experiments.

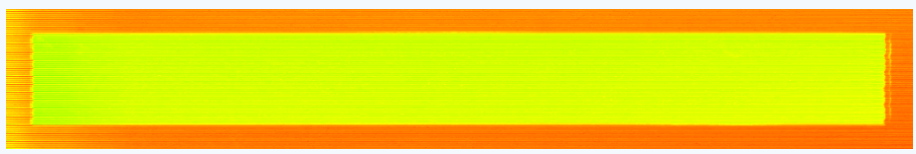
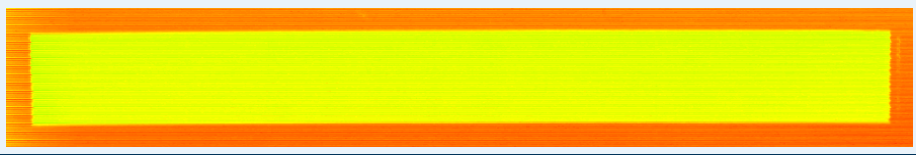
PVD process parameter	Operation point
Target-substrate distance	30 mm
Plasma cleaning process pressure	$2.0 \cdot 10^{-2}$ mbar
Plasma cleaning voltage	- 800 V
Plasma cleaning time	5 min
Sputtering process pressure	$4.0 \cdot 10^{-3}$ mbar
Substrate biasing voltage	- 100 V
Sputtering power	5000 W
Sputtering time	22 min*

Device condition	Operation point
Device operation mode	Biasing mode
Substrate holder	Flat support half-size substrate holder
Magnetron configuration	Unbalanced uTRM80 magnet bar
Sputtering target	Industrial-grade Zr 702

C2TWP results

After C2TWP, the resulting half-size plates were examined non-destructively using UT testing at Framatome-CERCA. The results shown in Table 21 do not indicate any areas of delamination or large end gaps on the final half-size plates.

Table 21: UT test results of half-size plates with Zr-coated stainless steel substrates. The dashed line at sample 101H-SS316L-Zr8 (not drawn for the other samples) shows the position of the half-size substrates inside the plates. No areas of delamination or large end gaps were found on the final half-size plates. From [235].

Sample ID	Ultrasonic transmission test result
101H-SS316L-Zr8	 half-size substrate
102H-SS316L-Zr8	
103H-SS316L-Zr8	
104H-SS316L-Zr8	



UT transmission rate in percent

Destructive examination results

Following the positive results from C2TWP and subsequent UT testing, the half-size plates were shipped back to TUM for destructive examination. Hereby, the plates were first sectioned according to the sectioning plan shown in Figure 166 and cross-section samples were prepared from each section. To

analyze the behavior of the Zr coating in longitudinal and transverse plate direction, and to examine potential end gaps between the substrate and the cladding, a total of nine samples were taken from each plate and examined by optical microscopy. Samples x.21, x.22, x.42, x.62 and x.63 are longitudinal cross-sections and samples x.23, x.41, x.43 and x.61 are transverse cross-sections. Here, the letter x must be replaced by the corresponding sample ID.

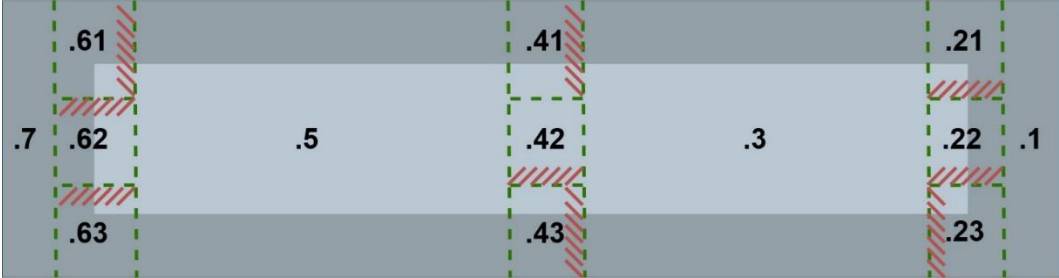


Figure 166: Sectioning plan for the half-size plates with Zr-coated stainless steel substrates. A total of nine samples were taken from each plate. The cross-sections (red lines) were prepared in longitudinal (.21, .22, .42, .62, .63) and transverse (.23, .41, .43, .61) plate direction.

Longitudinal middle sections (x.42). To analyze the behavior of the Zr coating, i.e. to identify potential cracks due to the mechanical stresses during C2TWP, the longitudinal middle sections x.42 were examined. Figure 167 exemplarily shows an optical micrograph of the sample 102H-SS316L-Zr8.42. The Zr coating on all four samples follows the surface topography of the substrate very well and no cracks, interaction layers or other irregularities were found. The black spots inside the cladding are typical non-harmful effects from the C2TWP cladding application process.

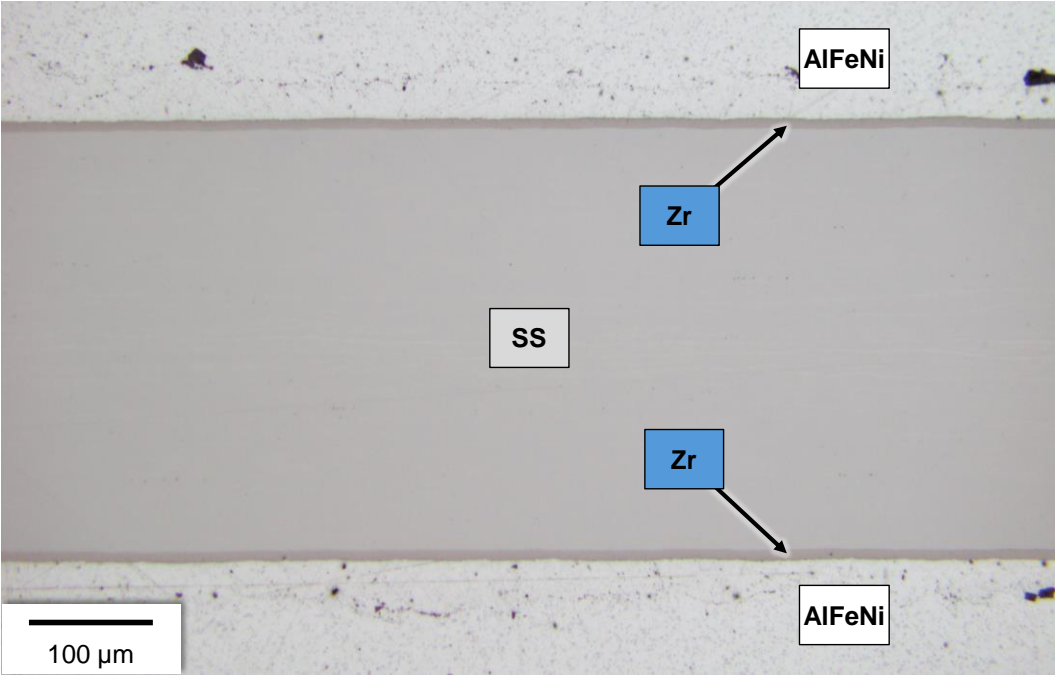
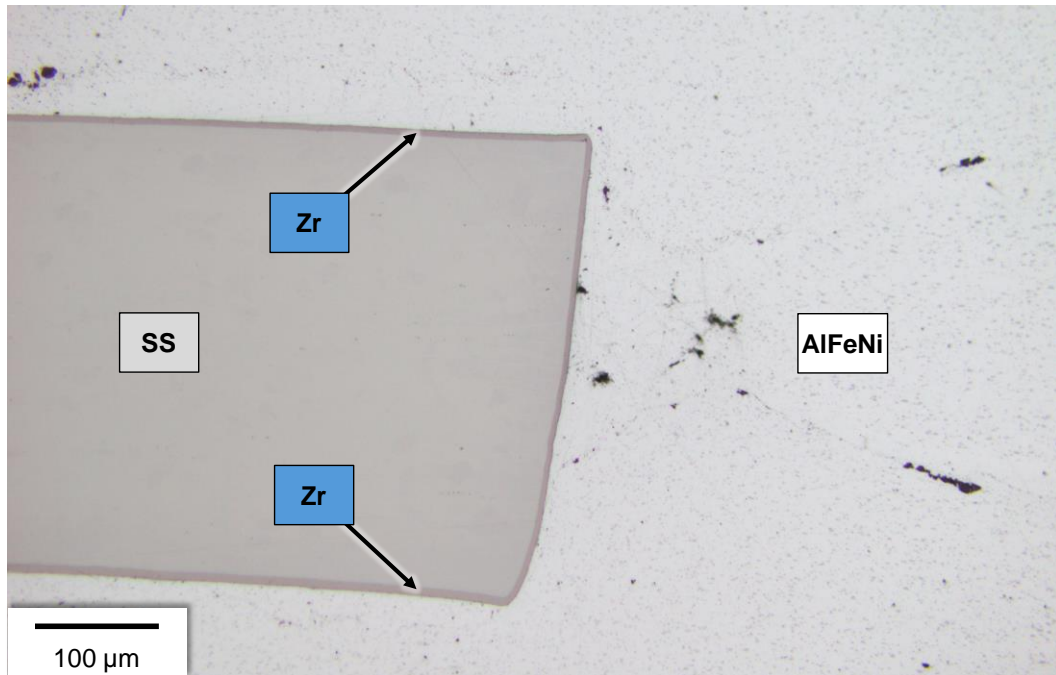
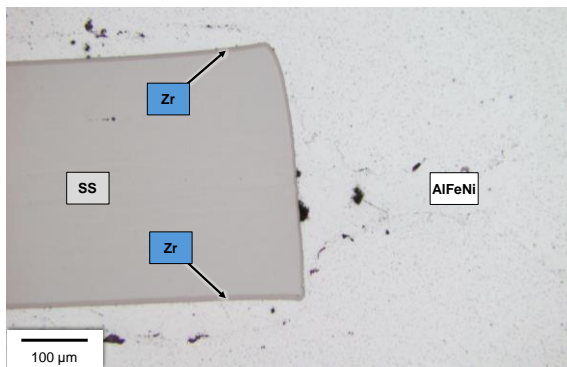


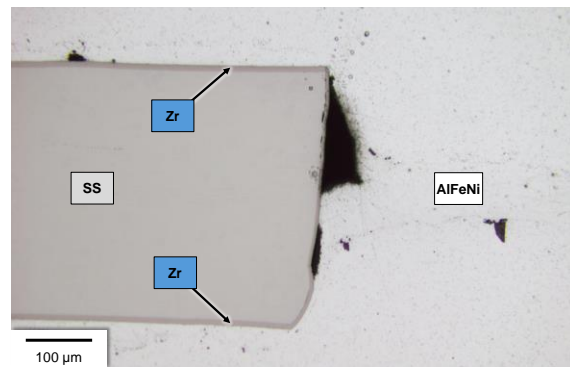
Figure 167: Exemplary optical micrograph of the longitudinal middle section 102H-SS316L-Zr8.42. No cracks or other irregularities were found in the Zr coating. The black spots inside the cladding are typical non-harmful effects from the C2TWP cladding application process.



a) No gap



b) Small gap (< 100 μm)

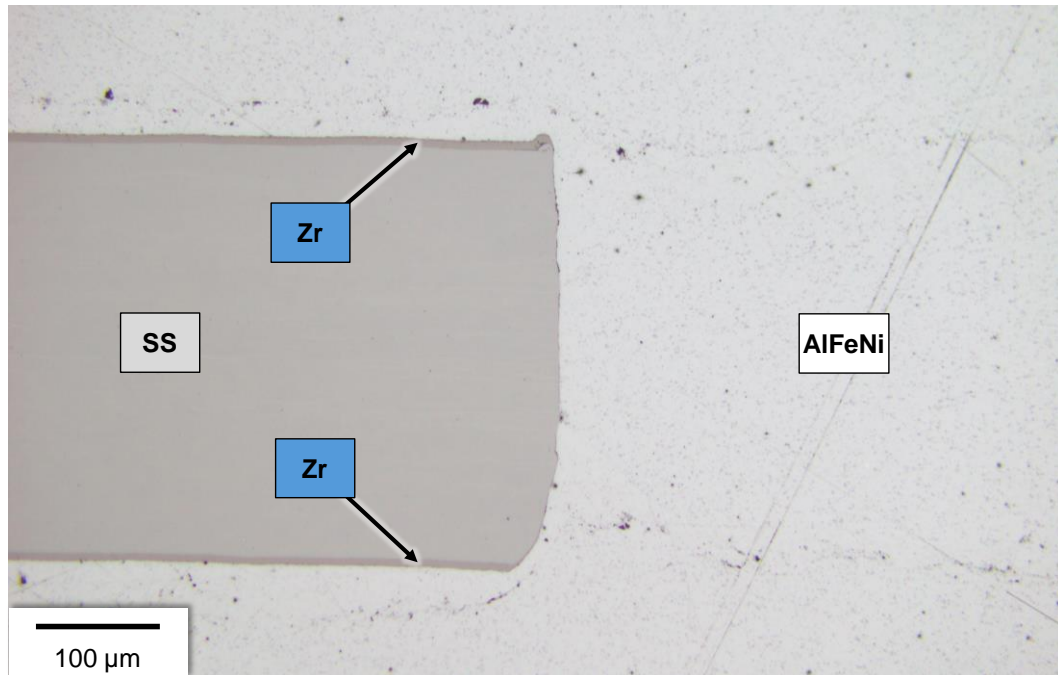


c) Large gap (> 100 μm)

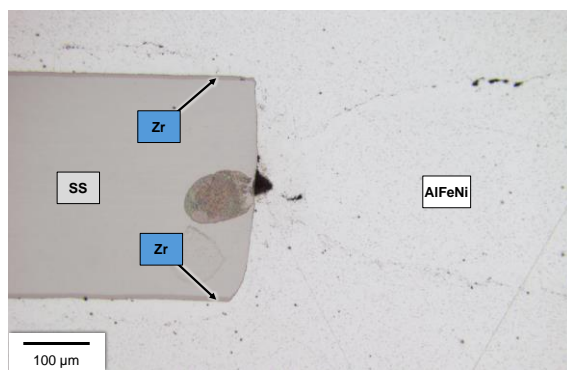
Figure 168: Exemplary optical micrographs of the longitudinal end sections 103H-SS316L-Zr8.21 (a), 102H-SS316L-Zr8.21 (b) and 102H-SS316L-Zr8.62 (c). From the eight longitudinal end samples, four samples did not show any gap at all (a). Two samples showed a gap smaller than 100 μm (b). Two samples showed a gap larger than 100 μm (c). The Zr coating is free from defects and entirely covers also the sides of the substrates.

Longitudinal end sections (x.62, x.21). To identify potential gaps between the substrate and the cladding at the short ends of the substrate, the longitudinal end sections x.62 and x.21 were examined. Figure 168 exemplarily shows optical micrographs of the samples 103H-SS316L-Zr8.21, 102H-SS316L-Zr8.21 and 102H-SS316L-Zr8.62. From a total of eight samples, four samples (101H-SS316L-Zr8.62, 103H-SS316L-Zr8.21, 104H-SS316L-Zr8.62 and 104H-SS316L-Zr8.21) did not show any gap at all. Two samples (101H-SS316L-Zr8.21 and 102H-SS316L-Zr8.21) showed a small gap with a maximum extent of 100 μm. Two samples (102H-SS316L-Zr8.62 and 103H-SS316L-Zr8.62) showed a gap larger than 100 μm.

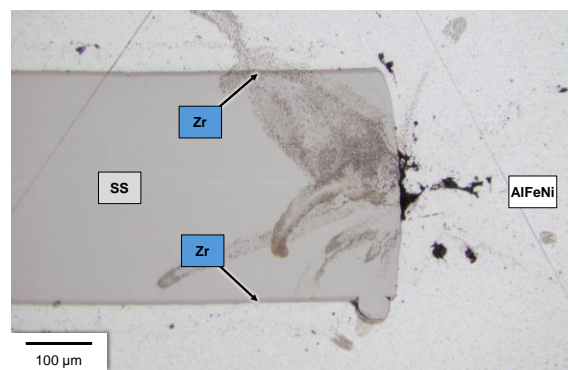
The Zr coating also entirely covers the sides of the substrates, presumably because the 380 mm long half-size substrates were positioned centrally in the plasma below the sputtering target, which is more than twice as long. Similar to the longitudinal middle sections, the coating is intact without any cracks or irregularities on all samples.



a) No gap



b) Small gap (< 100 μm)



c) Large gap (> 100 μm)

Figure 169: Exemplary optical micrographs of the transverse end sections 104H-SS316L-Zr8.61 (a), 104H-SS316L-Zr8.41 (b) and 102H-SS316L-Zr8.41 (c). From the twelve transverse end samples, seven samples did not show any gap at all (a). Two samples showed a gap smaller than 100 μm (b). Three samples showed a gap larger than 100 μm (c). Stains near the gaps result from debris, which has accumulated in the gaps during the sample polishing steps. The Zr coating shows some defects close to the edges and does not cover the sides of the substrates.

Transverse end sections (x.61, x.41, x.23). To identify potential gaps between the substrate and the cladding at the long sides of the substrate, the transverse end sections x.61, x.41 and x.23 were examined. Figure 169 exemplarily shows optical micrographs of the samples 104H-SS316L-Zr8.61, 104H-SS316L-Zr8.41 and 102H-SS316L-Zr8.41. From a total of twelve samples, seven samples (101H-SS316L-Zr8.61, 101H-SS316L-Zr8.23, 102H-SS316L-Zr8.61, 102H-SS316L-Zr8.23, 103H-SS316L-Zr8.23, 104H-SS316L-Zr8.61 and 104H-SS316L-Zr8.23) did not show any gap at all. Two samples (103H-SS316L-Zr8.61 and 104H-SS316L-Zr8.41) showed a small gap with a maximum extent of 100 μm. Three samples (101H-SS316L-Zr8.41, 102H-SS316L-Zr8.41 and 103H-SS316L-Zr8.41) showed a gap larger than 100 μm.

Different to the longitudinal end sections, the sides of the transverse end sections do not show a significant Zr coating, presumably due to the narrow deposition profile of the sputtering source. On some

of the transverse end sections, defects were found in the Zr coating, as shown exemplarily in Figure 170. These defects were found only at the edges of the substrates and are always associated with burrs of the substrate material. Thus, they are not linked to the coating or cladding application processes themselves, but to the substrate sizing process by laser cutting, which obviously resulted in significant burrs at the length direction of the substrates. The necessary deburring step at the supplier was either omitted or performed insufficiently.

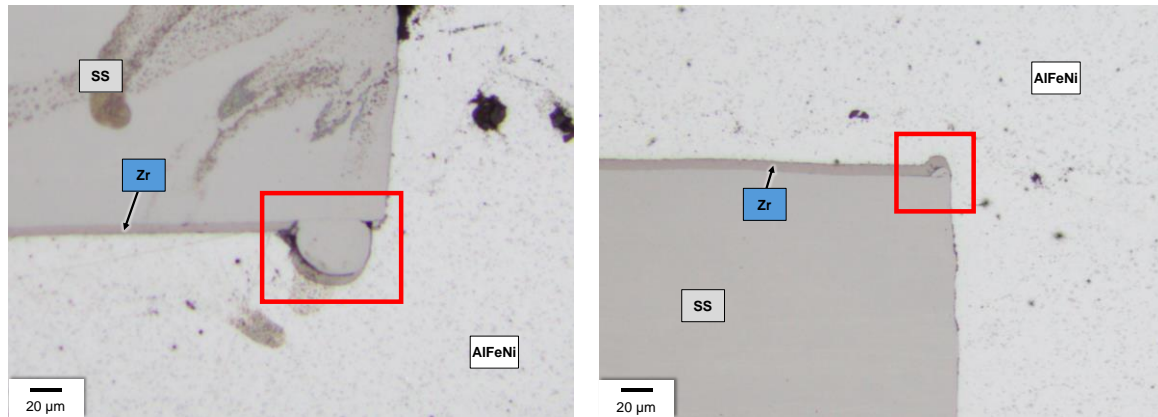


Figure 170: Exemplary optical micrographs of Zr coating defects close to the transverse edges of the substrates. The coating defects are associated with burrs of the substrate edges, which presumably originate from the substrate cutting process by laser.

6 CONCLUSION

This section concludes this PhD thesis, which aimed at bringing forward the European fabrication process for monolithic U-Mo fuels for research reactors.

By first-of-a-kind demonstration experiments on the fabrication of fuel foils with thickness gradient (gradient foils), an important foundation is laid for the further development of such techniques, which might become necessary for the conversion of research reactors like the FRM II to a lower enrichment.

By successfully establishing a pilot PVD process for the application of Zr interdiffusion barriers onto U-Mo foils, an important part in the pilot process chain for the fabrication of monolithic U-Mo fuel plates in Europe is now available and will be ready for the fabrication campaign of the upcoming European irradiation test FUTURE MONO-1, planned in 2023.

6.1 FABRICATION DEMONSTRATION OF GRADIENT FOILS

Within this thesis, the fabrication of gradient U-Mo foils using subtractive and additive manufacturing processes was investigated for the first time in Europe. Therefore, mini-size and full-size gradient foil geometries were derived from earlier neutronic and thermal-hydraulic calculations for the conversion of FRM II to a lower enrichment using monolithic U-Mo. Based on these designs, the following requirements for fabrication processes for such foils were defined:

- Ability to reach the geometrical tolerances
- Compatibility with subsequent PVD coating and C2TWP cladding application processes
- Reduction of material losses
- Re-usability and recyclability of fabrication scraps
- Protection of the environment and the operators from radiological contamination
- Exclusion of criticality hazards

Subsequently, milling (subtractive manufacturing) and selective laser melting (SLM, additive manufacturing) were selected as processes of choice for first-of-a-kind fabrication demonstrations. For these experiments, potential surrogate materials for U-Mo were evaluated and stainless steel AISI 316L and titanium alloy Ti-6Al-4V were selected. These materials present a good compromise between close resemblance of the material parameters of U-Mo and other criteria, such as commercial availability and industrial fabrication experience.

Milling (subtractive manufacturing)

The fabrication of specification-conform gradient mini-size foils of stainless steel AISI 316L was successfully demonstrated using commercial milling equipment at an industrial partner. Hereby, flat foils with an exact and uniform thickness within tight tolerances are crucial to obtain gradient foils within the geometrical tolerances. In a detailed characterization, the gradient foils did show a high surface and geometrical quality as well as the desired austenitic microstructure, with only little precipitates of deformation martensite at the machined surfaces. The compatibility of such gradient mini-size foils with

the PVD coating and the C2TWP cladding application process was further demonstrated together with Framatome-CERCA. No adherence deficiencies of the Zr coating or the AlFeNi cladding with the gradient foils were identified.

In a subsequent fabrication study, it was confirmed that the fabrication of gradient foils by milling is technically feasible also in the full-size geometry and with the more challenging material titanium alloy Ti-6Al-4V. In this study, the collection of the fabrication scraps was successfully demonstrated and high collection rates of > 98 % were achieved in the first attempt.

Selective laser melting (additive manufacturing)

The fabrication of gradient mini-size foils of stainless steel AISI 316L was successfully demonstrated using commercial SLM equipment at a research partner. A combination of shot peening and hot isostatic pressing as post-production treatments was found to be necessary to obtain foils with a smooth surface, no inner porosities and a regular austenitic microstructure. Such foils as well have shown to be compatible with the PVD coating and the C2TWP cladding application process.

The fabrication of gradient full-size foils by SLM still presents a significant challenge. In a scoping experiment, fabrication failures of wider geometries were reproducibly observed due to inner stresses. Furthermore, only few commercial SLM devices exist which offer a sufficiently large build space for the full-size geometry.

6.1.1 OUTLOOK

Based on the previously defined process requirements and the results from the fabrication demonstration experiments, an industrial fabrication of gradient foils can be established using either milling or SLM. However, both processes need to be further adapted and optimized for the final material U-Mo in full-size geometry.

For the industrial fabrication by milling, the following technical and safety challenges are identified:

- To achieve specification-conform gradient foils within the geometrical tolerances, the use of commercial CNC machining centers is sufficient, but the thickness of the original flat foils needs to be exact and uniform within tight tolerances.
- The milling parameters must be optimized towards high precision, uniformity and surface quality of the milled gradients. Furthermore, a suitable cutting wedge material shall be chosen for good surface quality of the gradient foils and low wear of the cutting tool.
- To collect the cutting chips and to ensure their recyclability, the use of a cooling lubricant shall be omitted, a suitable chip collection enclosure shall be used and all parts in contact with the cutting chips shall be cleaned prior to each use. The milling parameters shall also be optimized towards large cutting chips and little warming of the material. Furthermore, the execution of the milling process at inert atmosphere, e.g. in a nuclear glovebox or a modified sealed CNC machining center operating in negative pressure, is necessary to safely prevent the ignition or oxidation of the cutting chips and to protect the operators from radiological contamination.
- To safely exclude any criticality hazards, the use of water must be minimized and the cutting chips must be collected completely. The accumulation of cutting chips outside of the collection enclosure must be avoided by design.

In comparison, the industrial fabrication by SLM presents more and greater technical and safety challenges:

- A reliable source of pure, fine and spherical U-Mo powder, e.g. by an atomization process, must be available for the fabrication of gradient U-Mo foils with high precision and purity.
- Suitable SLM process parameters for U-Mo must first be identified and subsequently optimized towards low surface roughness, few inner porosities and a regular microstructure in the U-Mo γ phase. Potentially occurring systematic geometrical deviations shall be compensated. The necessity of post-production treatments like shot peening and hot isostatic pressing shall be investigated again with U-Mo foils and suitable process parameters shall be identified.
- To reliably allow the fabrication of gradient U-Mo foils in full-size geometry, inner stresses in the built parts need to be reduced via appropriate measures, e.g. optimized process parameters or a heated powder bed. Furthermore, different orientations of the foils and the addition of adequate massive support structures shall be investigated.
- The SLM process as well as all post-production treatments need to be adapted towards high material efficiency. For example, the ventilation system and the filters in the SLM device shall be optimized and the re-usability and recyclability of powder residues must be tested. Special care needs to be taken of the shot peening process, if necessary, since the separation of μm -sized eroded U-Mo particles from the peening spheres is assumed to require significant filtering efforts.
- All process steps shall be carried out at inert atmosphere, e.g. in a nuclear glovebox or modified sealed devices operating in negative pressure, to safely prevent the ignition or oxidation of the U-Mo powder and to protect the operators from radiological contamination.
- To safely exclude any criticality hazards, the utilized amounts of U-Mo powder must be reduced as far as possible, e.g. by a reduction of the powder cartridge and build plate size. The accumulation of powder in any of the devices must be avoided by design and the use of water (e.g. for device cooling) shall be minimized.

These challenges are also confirmed by a safety assessment made by Framatome-CERCA [236]. From a technical standpoint, the realization of an industrial fabrication process for gradient full-size U-Mo foils by milling seems less challenging. However, the decision on which process will be industrialized will be made not only based on technical and safety considerations, but also economical aspects which have not yet been covered. Therefore, a dedicated economical study to evaluate the costs and the potential fabrication yield associated with each process shall be performed by the fuel fabricator.

6.2 DEVELOPMENT OF THE PILOT PVD COATING PROCESS

Within this thesis, a pilot PVD coating process for the application of Zr interdiffusion barriers onto full-size (762 mm x 45 mm) and half-size (380 mm x 45 mm) foils was developed. This process follows the experimental process for mini-size foils (82.5 mm x 19 mm), which was successfully demonstrated in the fabrication campaign of the EMPIrE irradiation test. Thus, the pilot process must meet the same general requirements as the mini-size process:

- Full coating coverage of the entire substrate surface on both sides
- Defect-free coating adherence on the entire substrate surface on both sides
- Deposition of the minimum required coating thickness at every location on the substrate
- Avoidance of temperature ranges, where fast U-Mo γ phase decomposition ($\sim 400 - \sim 575$ °C) or U-Mo/Zr interaction layer formation (> 650 °C) occurs
- Compatibility with the infrastructure, radiation protection and safety constraints of TUM's Nuclear Fuel Fabrication and Characterization Laboratory

As the pilot process will be followed by an industrial process as the next iteration step, the following additional requirements must be met to prepare the industrialization:

- Reduction of process parameter space
- Reduction of process time
- Improved robustness
- Higher material efficiency

Prior to the development of the pilot process, the previous work on PVD coating processes for monolithic U-Mo foils at TUM was thoroughly analyzed and the results from the fabrication campaign of the EMPIrE irradiation test were reviewed. Two key issues of the mini-size process were identified, which were successfully resolved within the new process:

Cracking of the Zr coating. Cracks in the Zr coating can deteriorate its effect as an interdiffusion barrier between the U-Mo foil and the aluminum cladding during irradiation. Thus, the tendency of the coating to crack during the C2TWP cladding application process was eliminated in this thesis by improving its ductility through an optimized substrate biasing approach. This approach is based on a reduction of the substrate biasing voltage to reduce the re-sputtering effect and structural damages in the deposited layer. To still achieve dense and defect-free Zr layers in the preferred growth structure type C, the adatom mobility is maintained in return by an increase of the ion flux to the substrate. While keeping the other PVD process parameters similar to the mini-size process, this is accomplished by the use of a cylindrical full-size sputtering source with an unbalanced magnetron type 2 configuration. This magnet configuration allows plasma electrons to escape from their confinement, leading to an extension of the sputtering plasma towards the substrate. By the application of a substrate biasing voltage of only - 100 V, up to $1.54 \cdot 10^{16}$ ions/cm² s are attracted by the substrate, which means an increase by a factor of two compared to the standard operation point of the previous mini-size PVD coating device.

As an alternative, an optimized substrate heating approach was studied, aiming at identifying an optimum substrate temperature which promotes the deposition of dense and ductile Zr layers while avoiding the unwanted temperature ranges of fast U-Mo γ phase decomposition and U-Mo/Zr interaction layer formation. By this study, it was proven that heating the substrates to 400 °C and more delivers defect-free Zr layers in growth structure type C or higher, with large grains and good mechanical properties. However, significant U-Mo/Zr interaction layers were found at substrate temperatures of 550 °C and above. Hence, substrate heating is considered only as a backup solution for the full-size PVD coating process. It could still be implemented, if the post-irradiation examination of EMPIrE LEU

fuel plates with co-rolled Zr coating – which have shown notable U-Mo/Zr interaction layers – would indicate a beneficial irradiation behavior thereof.

Substrate bending. The bending of the substrates after single-sided Zr coating application can deteriorate the coating uniformity, complicate the manual handling of the substrates, or even make the coating of large full-size substrates impossible. While this issue could not be resolved by changing relevant PVD process parameters as suggested by the literature, a reduction of the Zr coating thickness from 25 μm to the recently proposed 8 μm led to a manageable bending for half-size substrates. For larger substrates up to 800 mm length, a new substrate holder with biasing and heating capability was built and successfully tested. By mechanically fixing the substrates to spring-loaded clamping blocks, this substrate holder is able to forcefully keep the substrates flat during the PVD coating process.

Within this thesis, the full-size PVD coating device was designed, constructed and commissioned in TUM's Nuclear Fuel Fabrication and Characterization Laboratory. A complete 18-step process for the Zr coating of half-size and full-size substrates was developed, characterized and parametrized using stainless steel substrates. The process starts from bare, as-received substrates and ends with substrates fully coated with Zr without adherence deficiencies and readily packaged for transport. It includes, among other steps, initial substrate quality control, chemical cleaning, pre- and post-coating weighing, plasma cleaning, PVD coating and airtight packaging. Typically, two substrates can be finished per standard working day by two operators.

In the first common fabrication study between TUM and Framatome-CERCA for plates larger than mini-size geometry, this new pilot PVD coating process was successfully demonstrated in combination with the C2TWP cladding application process using half-size stainless steel substrates. By the identification of an optimized PVD process parameter set, targeted towards the deposition of at least 8 μm of Zr with defect-free adherence and high layer ductility at a high deposition rate, the reproducible production of Zr-coated samples was made possible at TUM. Out of such Zr-coated samples, the C2TWP process was able to successfully produce specification-conform half-size plates, without any delaminations or large end gaps detectable by UT testing. By destructive examination at TUM, no cracks or other severe defects were found in the Zr coating and the extent of the remaining few end gaps was found to be significantly smaller than in the EMPIrE fabrication campaign for mini-size plates. At the edges of the substrates, a few minor defects in the Zr coating were found, which are clearly linked to the substrate edge quality and can be simply avoided in the future by implementing an appropriate substrate deburring step.

6.2.1 OUTLOOK

By this thesis, the pilot PVD coating process is now established at TUM's Nuclear Fuel Fabrication and Characterization Laboratory and thus, an important part in the pilot process chain for the fabrication of full-size monolithic U-Mo fuel plates in Europe is available. However, several advancements still need to be accomplished for the upcoming FUTURE-MONO-1 fabrication campaign and for the industrial fuel fabrication for FRM II and other research reactors

FUTURE-MONO-1

As part of the FUTURE-MONO-1 fabrication campaign, the following steps shall be accomplished and dealt with in future work:

- Additional PVD coating experiments shall be performed on full-size substrates. In particular, a layer thickness uniformity measurement along the length of a full-size substrate is required to quantify the thickness variation of the deposited layer at the longitudinal edges.
- The pilot PVD coating process needs to be tested on U-Mo substrates made from depleted uranium. In particular, half-size and full-size U-Mo substrates shall be coated with Zr using the previously defined sample production parameter set and shipped to Framatome-CERCA for cladding application in multiple subsequent batches. By non-destructive and destructive examination of the resulting plates, both processes shall be further optimized.
- Based on the results from these experiments, a parameter set for the production of full-size LEU fuel plates needs to be developed and the fuel plates for the FUTURE-MONO-1 irradiation test must be fabricated.

Process industrialization

For the industrial fabrication of monolithic U-Mo fuel for FRM II, approximately 500 specification-conform fuel plates are required per year. Thus, the process time and the required number of operators for the PVD coating process need to be further reduced and the production yield shall become comparable to the current fuel fabrication process (> 90 %). To follow these provisions, it is proposed to set up the industrial PVD coating process for U-Mo foils as a semi-automatic in-line process, similar to the PVD coating process developed for neutron supermirrors by FRM II's neutron optics group:

- Via input and output gloveboxes under argon atmosphere, the U-Mo foils shall be installed into and out of a continuous conveyor system, which slowly moves the foils through the process chamber. To avoid the need for venting and re-evacuating the chamber after each foil, a load-lock transfer system shall be implemented at the input and output sides.
- Both sides of the U-Mo foils shall be coated simultaneously, finally eliminating also the issue of substrate bending. Therefore, the foils shall be clamped at their short ends and moved by the conveyor system in between two continuously operating identical cylindrical sputtering sources. To keep the footprint of the device small, the foils shall be orientated parallel to the cylindrical sputtering targets.
- To achieve a defect-free coating adherence and similar or better properties of the deposited layer, the parameters for the industrial process shall be derived from the parameter set developed in this thesis.

Scientific advancements

Moreover, the following scientific questions can be studied within future academic theses at TUM:

- The SRM80 magnet bar with balanced magnetron configuration can be installed into the sputtering target and its influence on the substrate biasing, especially the achievable ion flux to the substrate and the necessary substrate biasing voltage, can be studied with experiments.
- Using a four-quadrant power supply unit and a Langmuir probe, additional plasma parameters of the full-size PVD coating process can be measured and compared with the mini-size process.
- The Zr layers deposited using various PVD process parameters can be characterized in more detail using microstructural analysis, e.g. by *XRD* (X-ray diffraction), *EBS*D (Electron backscatter diffraction) or *(S)TEM* ((Scanning) Transmission electron microscopy).
- To further improve the ductility and reduce the hardness of the Zr coating, a cylindrical sputtering target made from reactor-grade Zr, with significantly less oxygen and other impurities, can be procured, installed and tested.
- Using sputtering targets from other materials, the mini-size and full-size PVD coating processes can be tested with other interdiffusion barrier materials such as Mo or W.

SCIENTIFIC CONTRIBUTIONS

Journal publications

B. Baumeister, A. Robinson, W. A. Hanson, A. Leenaers, J. Wight, W. Petry, Results of the Non-Destructive Post-Irradiation examination of the Monolithic U-Mo Plates in the EMPIrE Irradiation Test. *Submission to Journal of Nuclear Materials in preparation*.

B. Baumeister, C. Reiter, W. Petry: The EMPIrE Irradiation Test: Lower-Enriched Fuel For High-Performance Research Reactors, *Atw International Journal for Nuclear Power* (11/12), S. 571–574.

X. Iltis, D. Drouan, T. Blay, I. Zacharie, C. Sabathier, C. Onofri, C. Steyer, C. Schwarz,

B. Baumeister, J. Allenou, B. Stepnik, W. Petry, Microstructural characteristics of a fresh U(Mo) monolithic mini-plate: Focus on the Zr coating deposited by PVD, *Nuclear Engineering and Technology* 53 (2021) 2629–2639. <https://doi.org/10.1016/j.net.2021.02.026>.

D. Salvato, J. Shi, H. Breitzkreutz, W. van Renterghem, **B. Baumeister**, C. Schwarz, A. Leenaers, S. van den Berghe, C. Detavernier, W. Petry, U(Mo) grain refinement induced by irradiation with high energy iodine, *Journal of Nuclear Materials* 548 (2021) 152850. <https://doi.org/10.1016/j.jnucmat.2021.152850>.

Conference contributions (only first-authored contributions)

B. Baumeister, TUM Fuel Fabrication Efforts. International Meeting on Reduced Enrichment for Research and Test Reactors RERTR, 2021.

B. Baumeister, EMPIrE: First Results from the Monolithic PIE. European Research Reactor Conference RRFM, 2020.

B. Baumeister, C. Schwarz, C. Steyer, H. Breitzkreutz, W. Petry, J. Allenou, B. Stepnik, Production of Surrogate Fuel Plates with Monolithic Gradient Foils. International Meeting on Reduced Enrichment for Research and Test Reactors RERTR, Edinburgh, 2018.

B. Baumeister, C. Schwarz, C. Steyer, H. Breitzkreutz, W. Petry, Manufacturing Processes for Inert Monolithic Mini-Size Fuel Foils with Thickness Gradient. European Research Reactor Conference RRFM, Munich, 2018.

B. Baumeister, C. Steyer, M. Hölzel, H. Breitzkreutz, W. Petry, Development options for the TUM PVD Zr Application Process for Monolithic U-Mo Fuel. International Meeting on Reduced Enrichment for Research and Test Reactors RERTR, Chicago, 2017.

B. Baumeister, W. Schmid, F. Kraus, W. Petry, An Alternative Chemical Cleaning Procedure for Blank Monolithic U-Mo Foils. European Research Reactor Conference RRFM, Prague, 2012.

Supervised degree theses

J. Mausz, Characterization of U7.8Mo Layers deposited with Physical Vapour Deposition via X-ray Diffraction and Differential Scanning Calorimetry. M.Sc. thesis, München, 2021.

N. Plößner, Commissioning and Parametrization of an Upscaled Sputtering Device for Nuclear Fuel Development. B.Sc. thesis, München, 2019.

S. lo Muzio, Property Studies of Sputtered Zr Layers on Monolithic Uranium-Molybdenum Nuclear Fuels. B.Sc. thesis, München, 2018.

A. Grimm, Untersuchung von Verbesserungsmethoden für einen Sputterprozeß in der Kernbrennstoffentwicklung und Entwicklung eines dafür geeigneten Meßprobenhalters. M.Sc. thesis, München, 2016.

S. Oswald, Herstellung und Untersuchung eines Spaltproduktsurrogats zur Erprobung eines 99Mo-Extraktionsverfahrens. B.Sc. thesis, München, 2014.

BIBLIOGRAPHY

- [1] Technische Universität München, Forschungs-Neutronenquelle Heinz Maier-Leibnitz (FRM II). <http://www.frm2.tum.de> (accessed 24 January 2022).
- [2] H. Breitzkreutz, Coupled Neutronics and Thermal Hydraulics of High Density Cores for FRM II. PhD thesis, München, 2011.
- [3] B. Rabin, M. Meyer, J. Cole, I. Glagolenko, G. Hofman, W. Jones, J. F. Jue, D. Keiser, Y. S. Kim, C. Miller, G. Moore, H. Ozaltun, F. Rice, A. Robinson, J. Smith, D. Wachs, W. Williams, N. Woolstenhulme, Preliminary Report on U Mo Monolithic Fuel for Research Reactors. INL/EXT-17-40975, 2017.
- [4] U.S. Nuclear Regulatory Commission, Safety Evaluation Report Related to the Evaluation of Low-Enriched Uranium Silicide-Aluminum Dispersion Fuel for Use in Non-Power Reactors. NUREG-1313, 1988.
- [5] P. Lemoine, D. Wachs, High Density Fuel Development for Research Reactors. IAEA International Conference on Research Reactors, Sydney, 2007.
- [6] HERACLES Consortium, The European HERACLES consortium. <https://heracles-consortium.eu> (accessed 16 December 2021).
- [7] J. Rest, Y. S. Kim, G. L. Hofman, M. K. Meyer, S.L. Hayes, U-Mo Fuels Handbook. ANL-09/31, 2009.
- [8] W. Schmid, Construction of a sputtering reactor for the coating and processing of monolithic U-Mo nuclear fuel. PhD thesis, München, 2011.
- [9] B. Stepnik, C. Jarousse, J. C. Houplain, ALPS program - U-Mo monolithic plate manufacturing - Final report. DCR/12-466/BS, 2012.
- [10] B. Baumeister, W. Schmid, F. Kraus, W. Petry, An alternative chemical cleaning procedure for blank monolithic U-Mo foils. European Research Reactor Conference RRFM, Prague, 2012.
- [11] C. Schwarz, T. Dirks, B. Baumeister, C. Steyer, W. Petry, All-In-One chemical cleaning and deoxidation process for monolithic uranium-molybdenum foils. European Research Reactor Conference RRFM, Berlin, 2016.
- [12] C. Steyer, B. Baumeister, C. Schwarz, M.W. McCollough, C. Reiter, F. Alder, D. Bach, T. Dirks, T. K. Huber, H. Breitzkreutz, W. Petry, Production of monolithic UMo plates for the EMPIrE irradiation experiment. International Meeting on Reduced Enrichment for Research and Test Reactors RERTR, Antwerp, 2016.
- [13] C. Steyer, B. Baumeister, H. Breitzkreutz, W. Petry, B. Stepnik, M. Grasse, C. Moyroud, Characterization of monolithic U-Mo foils and Zr coatings for the EMPIrE irradiation experiment. European Research Reactor Conference RRFM, Rotterdam, 2017.

-
- [14] C. Steyer, Plasma- und festkörperphysikalische Optimierung eines Beschichtungsverfahrens für monolithische UMo-Kernbrennstoffe. PhD thesis, München, 2019.
- [15] S. Lorand, B. Stepnik, J. Allenou, C. Rontard, F. Gauché, B. Baumeister, C. Steyer, W. Petry, European Developments for Monolithic UMo Fuel: UMo Foil Manufacturing Project. International Meeting on Reduced Enrichment for Research and Test Reactors RERTR, Zagreb, 2019.
- [16] C.R. Clark, N.P. Hallinan, J.F. Jue, D. Keiser, J. Wight, Monolithic Fuel Fabrication Process Development. INL/CON-06-01370, 2006.
- [17] G. Moore, F.J. Rice, N. Woolstenhulme, W.D. Swank, D.C. Haggard, J.F. Jue, B.H. Park, S.E. Steffler, N.P. Hallinan, M.D. Chapple, D. Burkes, Monolithic Fuel Fabrication Process Development at the Idaho National Laboratory. INL/CON-08-14550, 2008.
- [18] G. Moore, F.J. Rice, N. Woolstenhulme, J.F. Jue, B.H. Park, S.E. Steffler, N.P. Hallinan, M.D. Chapple, M.C. Marshall, B.I. Mackowiak, C.R. Clark, B. Rabin, Monolithic Fuel Fabrication Process Development at the Idaho National Laboratory. INL/CON-09-17298, 2009.
- [19] M.J. Nilles, J. Wight, Recent Babcock & Wilcox UMo Plate Fabrication Experience. International Meeting on Reduced Enrichment for Research and Test Reactors RERTR, Lisbon, 2010.
- [20] E. Perez, B. Yao, D. Keiser, Y. Sohn, Microstructural analysis of as-processed U–10wt.%Mo monolithic fuel plate in AA6061 matrix with Zr diffusion barrier, *Journal of Nuclear Materials* 402 (2010) 8–14. <https://doi.org/10.1016/j.jnucmat.2010.04.016>.
- [21] L. Jollay, A. Moore, J. Gooch, H. Longmire, M. Gambrell, A. DeMint, Low Enriched Uranium-Molybdenum Coupon Fabrication at the Y-12 National Security Complex. International Meeting on Reduced Enrichment for Research and Test Reactors RERTR, Warsaw, 2012.
- [22] K.J. Hollis, Plasma Spraying of Diffusion Barrier Coatings for LEU Monolithic Fuel. International Meeting on Reduced Enrichment for Research and Test Reactors RERTR, Warsaw, 2012.
- [23] A. DeMint, J. Henkel, H.A. Longmire, M. Gambrell, C. Langham, A. Moore, Y-12 National Security Complex U-Mo Fabrication. International Meeting on Reduced Enrichment for Research and Test Reactors RERTR, Vienna, 2014.
- [24] B. Rabin, J. Cole, I. Glagolenko, N. Woolstenhulme, G. Moore, A. Robinson, U.S. Progress in U-Mo Monolithic Fuel Development. International Meeting on Reduced Enrichment for Research and Test Reactors RERTR, Seoul, 2015.
- [25] G.W. Coffey, K.D. Meinhardt, V. Joshi, L.R. Pederson, C. Lavender, D. Burkes, Concept Feasibility Report for Electroplating Zirconium onto Uranium Foil. PNNL-24106, 2015.
- [26] R. Johnson, R. Mayfield, D. Navolio, Progress of the U-Mo Foil Rolling Demonstration Line at BWX Technologies. European Research Reactor Conference RRFM, Berlin, 2016.
- [27] J. Wight, USHPRR Fuel Fabrication Pillar Baseline Process and Alternatives. European Research Reactor Conference RRFM, Rotterdam, 2017.
- [28] L. Hubbard, C. Arendt, D. Dye, C. Clayton, M. Lerchen, N. Lombardo, C. Lavender, A. Zacher, U-10Mo Baseline Fuel Fabrication Process Description. PNNL-26880, 2017.

- [29] A. Röhrmoser, Smallest thinkable LEU elements for FRM II with most progressive and also most conservative fuel options. International Meeting on Reduced Enrichment for Research and Test Reactors RERTR, Edinburgh, 2018.
- [30] H. Breitzkreutz, A. Röhrmoser, W. Petry, Monolithic UMo based fuel element designs for FRM II. European Research Reactor Conference RRFM, St. Petersburg, 2013.
- [31] D. Senior, D. Burkes, Fuel Fabrication Capability Research and Development Plan: Global Threat Reduction Initiative - Convert Program. PNNL-22528, 2017.
- [32] M. K. Meyer, G. L. Hofman, R.V. Strain, C.R. Clark, J.R. Stuart, Metallographic Analysis of Irradiated RERTR-3 Fuel Test Specimens. International Meeting on Reduced Enrichment for Research and Test Reactors RERTR, Las Vegas, 2000.
- [33] M. K. Meyer, G. L. Hofman, J. L. Snelgrove, C.R. Clark, S.L. Hayes, R.V. Strain, J.M. Park, K.H. Kim, Irradiation Behavior of Uranium-Molybdenum Dispersion Fuel: Fuel Performance Data from RERTR-1 and RERTR-2. International Meeting on Reduced Enrichment for Research and Test Reactors RERTR, Budapest, 1999.
- [34] G. L. Hofman, M. Finlay, Y. S. Kim, Post-Irradiation Analysis of Low Enriched U-Mo/Al Dispersions Fuel Miniplate Tests, RERTR 4 & 5. International Meeting on Reduced Enrichment for Research and Test Reactors RERTR, Vienna, 2004.
- [35] M. K. Meyer, J. GAN, J.F. Jue, D. Keiser, E. Perez, A. Robinson, D. Wachs, N. Woolstenhulme, G. L. Hofman, Y. S. Kim, Irradiation Performance of U-Mo Monolithic Fuel, Nuclear Engineering and Technology 46 (2014) 169–182. <https://doi.org/10.5516/NET.07.2014.706>.
- [36] A. Robinson, D.M. Perez, D.L. Porter, G.L. Chang, D. Keiser, D. Wachs, G. L. Hofman, Irradiation Performance of U–Mo Alloy Based ‘Monolithic’ Plate-Type - Design Selection Update. INL/EXT-09-16807, 2013.
- [37] D.M. Perez, M. Lillo, G.S. Chang, G.A. Roth, N. Woolstenhulme, D. Wachs, RERTR-10 Irradiation Summary Report. INL/EXT-10-18456, 2011.
- [38] D.M. Perez, M. Lillo, G.S. Chang, G.A. Roth, N. Woolstenhulme, D. Wachs, RERTR-9 Irradiation Summary Report. INL/EXT-10-18421, 2011.
- [39] A. Izhutov, V. Alexandrov, A. Novosyolov, V. Starkov, A. Sheldyakov, V. Shishin, V. Iakovlev, I. Dobrikova, A. Vatulin, G. Kulakov, V. Suprun, The Main Results of Investigation of Modified Dispersion LEU U-Mo Fuel Tested in the MIR Reactor. International Meeting on Reduced Enrichment for Research and Test Reactors RERTR, Lisbon, 2010.
- [40] H.-Y. Chiang, Material Selection of UMo Fuel for Research Reactors: Swift Heavy Ion Irradiation Studies. PhD thesis, München, 2014.
- [41] R. Jungwirth, Irradiation behavior of modified high-performance nuclear fuels. PhD thesis, München, 2011.
- [42] J. Shi, Qualification of U-Mo Fuel for Research Reactors: Characterisation of the Interfaces Between U-Mo Kernel, Diffusion Barrier and Al Matrix Under Heavy Ion Irradiation. PhD thesis, München, 2021.
- [43] J. Shi, C. Onofri, H. Palancher, X. Iltis, D. Drouan, H. Breitzkreutz, W. Petry, Microstructure evolution and phase transformation of heavy-ion irradiated U–Mo/Al fuels, Journal of Nuclear Materials 541 (2020) 152399. <https://doi.org/10.1016/j.jnucmat.2020.152399>.

-
- [44] K. Johnson, L. Owsley, J. Tucker, M. Dahl, K. Mattlin, M. Rhodes, C. Clayton, C. Lavender, V. Joshi, K. Brooks, A Trade Study of Pilgering Versus Rolling, U-10Mo Fuel Foils. PNNL-29930, 2020.
- [45] C. Lavender, D. Paxton, M. Smith, A. Soulami, V. Joshi, D. Burkes, Concept Feasibility Report for Using Co-Extrusion to Bond Metals to Complex Shapes of U-10Mo. PNNL-23045, 2013.
- [46] D. Chandler, B. R. Betzler, J.W. Bae., D. H. Cook, G. Ilas, Conceptual Fuel Element Design Candidates for Conversion of High Flux Isotope Reactor with Low-Enriched Uranium Silicide Dispersion Fuel, EPJ Web Conf. 247 (2021) 8017. <https://doi.org/10.1051/epjconf/202124708017>.
- [47] N. Woolstenhulme, I. Glagolenko, Design of Irradiation Tests for Monolithic Fuel Qualification. International Meeting on Reduced Enrichment for Research and Test Reactors RERTR, Seoul, 2015.
- [48] I. Glagolenko, N. Woolstenhulme, M. Lillo, J. Nielsen, C. Jensen, D. Crawford, W. Jones, S. Snow, B. Hawkes, J. Wiest, M. Sprenger, K. Holdaway, B. Rabin, J. Schulthess, D. Keiser, Design of Miniplate Experiments for Irradiation in the Advanced Test Reactor. International Meeting on Reduced Enrichment for Research and Test Reactors RERTR, Seoul, 2015.
- [49] I. Glagolenko, G. Housley, J. Nielsen, D. Crawford, B. Hawks, J. Wiest, European Mini-Plate Irradiation Experiment Status Update. European Research Reactor Conference RRFM, Rotterdam, 2017.
- [50] I. Glagolenko, D. Wachs, D. Keiser, M. Pope, N. Woolstenhulme, J. Nielsen, D. Crawford, W. Jones, M. Sprenger, K. Holdaway, J. Schulthess, Design of EMPIRE Experiment for Irradiation in ATR. European Research Reactor Conference RRFM, Bukarest, 2015.
- [51] HERACLES Consortium, EU-QUALIFY: EUropean QUalification Approach for Low Enriched Fuel sYstems for secure production supply of medical isotopes. <https://heracles-consortium.eu/euqualify.php> (accessed 19 January 2022).
- [52] G.J. Lauth, J. Kowalczyk, Einführung in die Physik und Chemie der Grenzflächen und Kolloide, Springer Berlin Heidelberg, Berlin, Heidelberg, 2016.
- [53] M. Kizilyalli, J. Corish, R. Metselaar, Definitions of Terms for Diffusion in the Solid State, Pure and Applied Chemistry 71 (1999) 1307–1325. <https://doi.org/10.1351/pac199971071307>.
- [54] G.V. Kidson, Some aspects of the growth of diffusion layers in binary systems, Journal of Nuclear Materials 3 (1961) 21–29. [https://doi.org/10.1016/0022-3115\(61\)90175-1](https://doi.org/10.1016/0022-3115(61)90175-1).
- [55] H. Mehrer, Diffusion in Intermetallics, Mater. Trans., JIM 37 (1996) 1259–1280. <https://doi.org/10.2320/matertrans1989.37.1259>.
- [56] K.N. Kulkarni, A.A. Luo, Interdiffusion and Phase Growth Kinetics in Magnesium-Aluminum Binary System, J. Phase Equilib. Diffus. 34 (2013) 104–115. <https://doi.org/10.1007/s11669-013-0189-2>.
- [57] D.A. Young, Phase diagrams of the elements, 1975.
- [58] H. L. Yakel, A Review of X-Ray Diffraction Studies in Uranium Alloys, 1974.
- [59] P. Villars, K. Cenzual (Eds.), Pauling File: Inorganic Materials Database. in SpringerMaterials, Springer-Verlag; Material Phases Data System (MPDS), Switzerland & (NIMS), Japan, Berlin, Heidelberg, Zürich, Tokyo, 2012.

- [60] P.E. Repas, R.H. Goodenow, R.F. Hehemann, Transformation Characteristics of U-Mo and U-Mo-Ti alloys, *Transactions of the American Society for Metals* 57 (1964) 150–163.
- [61] S. Säubert, Isothermal Transformation Kinetics in Uranium Molybdenum Alloys. M.Sc. thesis, München, 2017.
- [62] Y. Park, N. Eriksson, R. Newell, D. Keiser, Y. Sohn, Phase decomposition of γ -U (bcc) in U-10 wt% Mo fuel alloy during hot isostatic pressing of monolithic fuel plate, *Journal of Nuclear Materials* 480 (2016) 271–280. <https://doi.org/10.1016/j.jnucmat.2016.08.022>.
- [63] V. Joshi, D.M. Paxton, C. Lavender, D. Burkes, The Effect of Rolling As-Cast and Homogenized U-10Mo Samples on the Microstructure Development and Recovery Curves. PNNL-25781, 2016.
- [64] V. Joshi, E.A. Nyberg, C. Lavender, D. Paxton, D. Burkes, Thermomechanical process optimization of U-10wt% Mo – Part 2: The effect of homogenization on the mechanical properties and microstructure, *Journal of Nuclear Materials* 465 (2015) 710–718. <https://doi.org/10.1016/j.jnucmat.2015.07.005>.
- [65] V. Joshi, E.A. Nyberg, C. Lavender, D. Paxton, H. Garmestani, D. Burkes, Thermomechanical process optimization of U-10 wt% Mo – Part 1: High-temperature compressive properties and microstructure, *Journal of Nuclear Materials* 465 (2015) 805–813. <https://doi.org/10.1016/j.jnucmat.2013.10.065>.
- [66] Z. Xu, V. Joshi, S. Hu, D. Paxton, C. Lavender, D. Burkes, Modeling the homogenization kinetics of as-cast U-10wt% Mo alloys, *Journal of Nuclear Materials* 471 (2016) 154–164. <https://doi.org/10.1016/j.jnucmat.2015.11.026>.
- [67] B. Baumeister, Reinigungsverfahren für metallische Uran-Molybdän-Kernbrennstoffe. B.Sc. thesis, München, 2011.
- [68] D. Burkes, C.A. Papesch, A.P. Maddison, T. Hartmann, F.J. Rice, Thermo-physical properties of DU-10wt.% Mo alloys, *Journal of Nuclear Materials* 403 (2010) 160–166. <https://doi.org/10.1016/j.jnucmat.2010.06.018>.
- [69] J. T. Mihalezo, Reactivity calibrations and fission rate distributions in an un-moderated un-reflected Uranium Molybdenum alloy research reactor. ORNL-TM-189, 1962.
- [70] M. S. Farkas, Mechanical and physical properties of fuels and cladding materials with potential for use in Brookhaven's pulsed fast reactor. Mechanical and physical properties of fuels and cladding materials with potential for use in Brookhaven's pulsed fast reactor. BMI-X-455, 1967.
- [71] T. K. Huber, Thermal Conductivity of High-Density Uranium-Molybdenum Fuels for Research Reactors. PhD thesis, München, 2015.
- [72] B. Ye, Y. Miao, J. Shi, D. Salvato, K. Mo, L. Jamison, A. Bergeron, G. L. Hofman, A. Leenaers, A. Oaks, A. Yacout, S. van den Berghe, W. Petry, Y. S. Kim, Temperature Effects on Interdiffusion of Al and U-Mo under Irradiation, *Journal of Nuclear Materials* 544 (2021) 152684. <https://doi.org/10.1016/j.jnucmat.2020.152684>.
- [73] G.B. Fedorov, E.A. Smirnov, F.I. Zhomov, V.N. Gusev, S.A. Paraev, Diffusion of Uranium in Refractory Body-Center-Cubic Metals, *Atomic Energy* (1971) 1280.
- [74] K. Huang, C.C. Kammerer, D. Keiser, Y. Sohn, Diffusion Barrier Selection from Refractory Metals (Zr, Mo and Nb) Via Interdiffusion Investigation for U-Mo RERTR Fuel Alloy, *J. Phase Equilib. Diffus.* 35 (2014) 146–156. <https://doi.org/10.1007/s11669-013-0270-x>.

-
- [75] L. Pavlinov, A. Nakonechnikov, V. Bykov, Diffusion of Uranium in Molybdenum, Niobium, Zirconium, and Titanium, Atomic Energy (1965) 1495.
- [76] A. Buch, Pure metals properties: A scientific-technical handbook, ASM International; Freund Publishing House, Materials Park, Ohio, London, 1999.
- [77] H.-Y. Chiang, T. Wiss, S.-H. Park, O. Dieste-Blanco, W. Petry, TEM analysis of irradiation-induced interaction layers in coated UMo/X/Al trilayer systems (X= Ti, Nb, Zr, and Mo), Journal of Nuclear Materials 499 (2018) 558–566. <https://doi.org/10.1016/j.jnucmat.2017.12.015>.
- [78] H. Palancher, Comprehension phase final report (HERACLES-CP D2.02). DES/IRESNE/DEC/CP NT 2020-003, 2020.
- [79] S. Kim, Y. S. Kim, Y.J. Jeong, K. Mo, Y. Miao, B. Ye, A. Oaks, S. Bhattacharya, K.H. Lee, K.N. Kim, J.M. Park, A. Yacout, Effectiveness of the metal coating on U–7Mo dispersion fuel in Al during irradiation, Journal of Nuclear Materials 529 (2020) 151945. <https://doi.org/10.1016/j.jnucmat.2019.151945>.
- [80] S. Matuschik, Production and Heavy-Ion Irradiation of Tungsten Coatings as Diffusion Barrier in the U-Mo/Al Fuel System. B.Sc. thesis, München, 2020.
- [81] G. Chiarotti, 1.6 Crystal structures and bulk lattice parameters of materials quoted in the volume: Datasheet from Landolt-Börnstein - Group III Condensed Matter \textperiodcentered Volume 24B: “Electronic and Vibrational Properties” in SpringerMaterials (https://doi.org/10.1007/10086058_6), Springer-Verlag Berlin Heidelberg. https://materials.springer.com/lb/docs/sm_lbs_978-3-540-47399-2_6.
- [82] G.B. Skinner, H.L. Johnston, Thermal Expansion of Zirconium between 298 K and 1600 K, The Journal of Chemical Physics 21 (1953) 1383–1384. <https://doi.org/10.1063/1.1699227>.
- [83] L. Xu, Y. Xiao, A. van Sandwijk, Q. Xu, Y. Yang, Separation of Zirconium and Hafnium: A Review, in: Energy Materials 2014, Springer International Publishing, Cham, 2016, pp. 451–457.
- [84] Firmetal, Zirconium 702 Data Sheet. <https://www.firmetal.com/zirconium/zirconium-702.html> (accessed 16 April 2020).
- [85] Sandvik AB, Zr 702 Datasheet. <https://www.materials.sandvik/en/materials-center/material-datasheets/tube-and-pipe-seamless/sandvik-zr-702/> (accessed 16 April 2020).
- [86] J. Dai, H. Guan, L. Chai, K. Xiang, Y. Zhu, R. Qiu, N. Guo, Y. Liu, Comparative Study of Microstructural Characteristics and Hardness of β -Quenched Zr702 and Zr-2.5Nb Alloys, Materials (Basel) 12 (2019). <https://doi.org/10.3390/ma12223752>.
- [87] R.I. Sheldon, D.E. Peterson, The U-Zr (Uranium-Zirconium) system, Bulletin of Alloy Phase Diagrams 10 (1989) 165–171.
- [88] K. Huang, Y. Park, D. Keiser, Y. Sohn, Interdiffusion Between Zr Diffusion Barrier and U-Mo Alloy, J. Phase Equilib. Diffus. 33 (2012) 443–449. <https://doi.org/10.1007/s11669-012-0106-0>.
- [89] International Atomic Energy Agency, Research reactor core conversion guidebook: Volume 4: Fuels, Wien, 1992.
- [90] B. Kapusta, J. Garnier, L. Allais, C. Janis, B. Maugard, P. Lemoine, Irradiation Effects on 6061-T6 Aluminium Alloy Used for JHR Internal Structures, Saclay, 2007.
- [91] A. Laik, K. Bhanumurthy, G. Kale, Intermetallics in the Zr–Al diffusion zone, Intermetallics 12 (2004) 69–74. <https://doi.org/10.1016/j.intermet.2003.09.002>.

- [92] J.C.M. Farrar, *The alloy tree: A guide to low-alloy steels, stainless steels and nickel-base alloys*, CRC Press; Woodhead Publ, Boca Raton, Cambridge, 2004.
- [93] A. Bandyopadhyay, S. Bose, *Additive Manufacturing*, Second Edition, secondnd ed., CRC Press LLC, Milton, 2019.
- [94] P. D. Harvey, *Engineering Properties of Steels*, American Society for Metals, 1982.
- [95] D. Peckner, I. M. Bernstein, *Handbook of Stainless Steels*, McGraw-Hill Book Company, 1977.
- [96] *Metals Handbook: Vol.1 - Properties and Selection: Irons, Steels, and High-Performance Alloys*, American Society for Metals, 1990.
- [97] H. E. Boyer, T. L. Gall, *Metals Handbook*, American Society for Metals, 1985.
- [98] N.K. Tolochko, Y.V. Khlopkov, S.E. Mozzharov, M.B. Ignatiev, T. Laoui, V.I. Titov, Absorptance of powder materials suitable for laser sintering, *Rapid Prototyping Journal* 6 (2000) 155–161. <https://doi.org/10.1108/13552540010337029>.
- [99] R. Boyer, G. Welsch, E. W. Collings, *Materials Properties Handbook: Titanium Alloys*, ASM International, 1994.
- [100] *Metals Handbook: Vol. 3, Properties and Selection: Stainless Steels, Tool Materials and Special-Purpose Metals*, American Society for Metals, 1980.
- [101] *Metals Handbook: Vol.2 - Properties and Selection: Nonferrous Alloys and Special-Purpose Materials*, American Society for Metals, 1990.
- [102] J. M. Holt, C. Y. Ho, *Structural Alloys Handbook*, 1996.
- [103] F. Cardarelli, *Materials Handbook*, Springer-Verlag, 2008.
- [104] P. Felbinger, B. Baumeister, C. Schwarz, C. Reiter, T. Chemnitz, W. Petry, F. Kraus, Measurement of the emissivity of U-Mo at different tarnish colours and temperatures. International Meeting on Reduced Enrichment for Research and Test Reactors RERTR, 2021.
- [105] British Stainless Steel Association, *Magnetic Properties of Stainless Steel*. <https://www.bssa.org.uk/cms/File/SSAS2.81-Magnetic%20Properties.pdf> (accessed 27 May 2020).
- [106] A. L. Schaeffler, Constitution diagram for stainless steel, *Metal Progress* 11 (1949) 680.
- [107] W. Bleck, X. Guo, Y. Ma, The TRIP Effect and Its Application in Cold Formable Sheet Steels, *steel research int.* 88 (2017) 1700218. <https://doi.org/10.1002/srin.201700218>.
- [108] D. Samantaray, A. Chaudhuri, U. Borah, A.K. Bhaduri, P. Dutta, Role of grain boundary ferrite layer in dynamic recrystallization of semi-solid processed type 304L austenitic stainless steel, *Materials Letters* 179 (2016) 65–68. <https://doi.org/10.1016/j.matlet.2016.05.049>.
- [109] Sandvik AB, Schaeffler Diagram. <https://www.materials.sandvik/en/products/welding-products/welding-handbook3/ferrite-content-diagrams/> (accessed 18 January 2018).
- [110] thyssenkrupp Materials Ltd, *Stainless Steel 1.4404 Material Data Sheet*. <https://www.thyssenkrupp-materials.co.uk/stainless-steel-316l-14404.html> (accessed 27 May 2020).
- [111] DIN Deutsches Institut für Normung e.V., *EN 10088-2: Nichtrostende Stähle - Teil 2: Technische Lieferbedingungen für Blech und Band aus korrosionsbeständigen Stählen für allgemeine Verwendung*, 2014th ed.

-
- [112] S.S. Da Rocha, G. L. Adabo, G.E.P. Henriques, M.A.d.A. Nóbilo, Vickers hardness of cast commercially pure titanium and Ti-6Al-4V alloy submitted to heat treatments, *Braz. Dent. J.* 17 (2006) 126–129. <https://doi.org/10.1590/S0103-64402006000200008>.
- [113] R.B. Osman, M.V. Swain, A Critical Review of Dental Implant Materials with an Emphasis on Titanium versus Zirconia, *Materials (Basel)* 8 (2015) 932–958. <https://doi.org/10.3390/ma8030932>.
- [114] P. Barriobero Vila, Phase transformation kinetics during continuous heating of $\alpha+\beta$ and metastable β titanium alloys, 2015.
- [115] P. Barriobero Vila, Effect of heat treatments on the microstructure of deformed Ti-6Al-4V. Diplomarbeit, Wien, 2010.
- [116] A. Heldmann, Diffraction Based Investigation of Elastic and Plastic Deformation on Multiphase Alloys. PhD thesis, München, 2021.
- [117] A. Heldmann, M. Hoelzel, M. Hofmann, W. Gan, W. Schmahl, E. Griesshaber, T. Hansen, N. Schell, W. Petry, Diffraction-based determination of single-crystal elastic constants of polycrystalline titanium alloys, *J. Appl. Crystallogr.* 52 (2019) 1144–1156. <https://doi.org/10.1107/S1600576719010720>.
- [118] B. Bab, Physically Based Model for Plasticity and Creep of Ti-6Al-4V. Licentiate Thesis, 2008.
- [119] T. Weyhmüller, Fertigungstechnische und tribologische Wirkmechanismen beim Polymerlappen am Beispiel der Werkstoffpaarung einer Nockenwellenlagerung. Dissertation, Karlsruhe, Karlsruhe, 2016.
- [120] J. Shi, C. Schwarz, N. Rehms, C. Steyer, B. Baumeister, W. Petry, Evaluation of the thickness of PVD-deposited Mo, Zr coatings as diffusion barriers between U-Mo and Al using heavy ion irradiation. International Meeting on Reduced Enrichment for Research and Test Reactors RERTR, Zagreb, 2019.
- [121] G.G. Raju, Electron-atom collision cross sections in argon: an analysis and comments, *IEEE Trans. Dielect. Electr. Insul.* 11 (2004) 649–673. <https://doi.org/10.1109/TDEI.2004.1324355>.
- [122] Pfeiffer Vacuum GmbH, Vacuum Technology: Know How, Asslar, 2009.
- [123] B.N. Chapman, Glow discharge processes: Sputtering and plasma etching, Wiley, New York, 1980.
- [124] P.M. Martin (Ed.), Handbook of deposition technologies for films and coatings: Science, applications and technology, 3rd ed., Elsevier, Amsterdam, Boston, 2010.
- [125] U. Stroth, Plasmaphysik: Phänomene, Grundlagen, Anwendungen, Vieweg+Teubner Verlag / Springer Fachmedien Wiesbaden GmbH, Wiesbaden, 2011.
- [126] J. Musil, M. Jaroš, Plasma and floating potentials in magnetron discharges, *Journal of Vacuum Science & Technology A: Vacuum, Surfaces, and Films* 35 (2017) 60605. <https://doi.org/10.1116/1.4992054>.
- [127] D.J. Ball, Plasma Diagnostics and Energy Transport of a dc Discharge Used for Sputtering, *Journal of Applied Physics* 43 (1972) 3047–3057. <https://doi.org/10.1063/1.1661657>.

- [128] R. Marquardt, J. Cipo, F. Schlichting, G. Kolhatkar, H. Kohlstedt, H. Kersten, Correlation between properties of direct current magnetron sputtered thin niobium nitride films and plasma parameters, *Thin Solid Films* 742 (2022) 139046. <https://doi.org/10.1016/j.tsf.2021.139046>.
- [129] A. Piel, *Plasma Physics: An introduction to laboratory, space, and fusion plasmas*, Springer, Berlin, 2010.
- [130] R. Hippler, H. Kersten, M. Schmidt, K.H. Schoenbach (Eds.), *Low temperature plasmas: Fundamentals, Technologies, and Techniques*, 2nd ed., Wiley-VCH, Weinheim, 2008.
- [131] H. Frey (Ed.), *Plasmaphysik, Plasmadiagnostik, Analytik*, 1st ed., VDI-Verlag, Düsseldorf, 1995.
- [132] G. Kienel, K. Röhl (Eds.), *Verfahren und Anlagen*, 1st ed., VDI-Verlag, Düsseldorf, 1995.
- [133] S. Arumugam, P. Alex, S.K. Sinha, Effective secondary electron emission coefficient in DC abnormal glow discharge plasmas, *Physics of Plasmas* 24 (2017) 112106. <https://doi.org/10.1063/1.4997622>.
- [134] M. Schmid, A Simple Sputter Yield Calculator. Based on empirical equations for sputter yields at normal incidence, 2009. <https://www.iap.tuwien.ac.at/www/surface/sputteryield> (accessed 9 October 2017).
- [135] G.K. Wehner, D. Rosenberg, Angular Distribution of Sputtered Material, *Journal of Applied Physics* 31 (1960) 177–179. <https://doi.org/10.1063/1.1735395>.
- [136] M. Stepanova, S.K. Dew, Estimates of differential sputtering yields for deposition applications, *J. Vac. Sci. Technol. A* 19 (2001) 2805. <https://doi.org/10.1116/1.1405515>.
- [137] S. Mahieu, K. van Aeken, D. Depla, Transport of Sputtered Particles Through the Gas Phase, in: R. Hull, R.M. Osgood, J. Parisi, H. Warlimont, D. Depla, S. Mahieu (Eds.), *Reactive Sputter Deposition*, Springer Berlin Heidelberg, Berlin, Heidelberg, 2008, pp. 199–227.
- [138] J.T. Gudmundsson, Physics and technology of magnetron sputtering discharges, *Plasma Sources Sci. Technol.* 29 (2020) 113001. <https://doi.org/10.1088/1361-6595/abb7bd>.
- [139] R. Brown, V. Bellido-Gonzalez, Comparison of balanced and unbalanced array designs. <https://www.genco.com/resources/documents/comparison-balanced-unbalanced-array-designs.pdf> (accessed 12 October 2021).
- [140] Materials Science, Inc., MSI SunSource GEN II Linear Planar Magnetron Sputtering Sources. <http://www.msi-pse.com/> (accessed 18 January 2021).
- [141] PLATIT AG, ARC Rotierende Kathoden. <https://www.platit.com/de/beschichtungs-know-how/beschichtungstechnologien/arc-mit-rotierenden-kathoden/> (accessed 18 January 2021).
- [142] S. Mahieu, *Biaxial Alignment in Sputter Deposited Thin Films*. Dissertation, Gent, 2006.
- [143] P. Ghekiere, *Structure Evolution of Biaxially Aligned Thin Films Deposited by Sputtering*. Dissertation, Gent, 2007.
- [144] B.A. Movchan, A.V. Demchishin, Study of the Structure and Properties of Thick Vacuum Condensates of Nickel, Titanium, Tungsten, Aluminum Oxide and Zirconium Dioxide, *Fizika metallov i metallovedenie* 28 (1969) 653.
- [145] J.A. Thornton, The microstructure of sputter-deposited coatings, *J. Vac. Sci. Technol. A* 4 (1986) 3059–3065. <https://doi.org/10.1116/1.573628>.

-
- [146] A. Anders, A structure zone diagram including plasma-based deposition and ion etching, *Thin Solid Films* 518 (2010) 4087–4090. <https://doi.org/10.1016/j.tsf.2009.10.145>.
- [147] A. Belkind, S. Gershman, *Plasma Cleaning of Surfaces, VT&C (Vacuum Technology & Coating)* 9 (2008) 47–57.
- [148] Diener electronic GmbH, *Plasmatechnik: Plasma-Surface-Technology*, fourth ed., Ebhausen, 2011.
- [149] U. Vorhrer, C. Oehr, *Plasma-Feinreinigung von Metalloberflächen. Abschlußbericht*, Heidelberg, 1994.
- [150] D.M. Mattox, *Handbook of physical vapor deposition (PVD) processing*, second. ed., William Andrew, Amsterdam, 2010.
- [151] T. K. Huber, T. Zweifel, H. Breitreutz, C. Coullomb, Sputter coated and INL coated samples for the CERCA C2TWP process: Zy4, Zr and Ti coatings on DU - UMo mini-foils SEM/EDX analysis. TUM/HDF-ALPS/131201-Rev1, 2013.
- [152] J. A. Smith, A. L. Crawford, D. L. Cottle, Grading of AREVA Plates. Private communication, 2017.
- [153] P. Felbinger, *Präparation und Charakterisierung von monolithischen Uran-Molybdän-Brennstoffen mit Zr-Diffusionsbarriere und AlFeNi-Cladding*. B. Sc. thesis, München, 2018.
- [154] C. Coullomb, M. Grasse, B. Stepnik, EMPIRE manufacturing project- UT indication analysis Metallographic analysis of LEU monolithic plates (SPL/17-111/CC). Private communication, 2017.
- [155] G. Bourdat, M. Grasse, B. Stepnik, HERACLES-CP – Monolithic manufacturing of UMo mini-size plates: Inert test and 1st DU test samples Destructive examination (SEM - EDX). SPL/16-302/GB, 2016.
- [156] G. Bourdat, M. Grasse, B. Stepnik, HERACLES-CP – Monolithic manufacturing of UMo mini-size plates: 2nd DU test samples Results. SPL/16-323/MG, 2016.
- [157] X. Iltis, D. Drouan, T. Blay, I. Zacharie, C. Sabathier, C. Onofri, C. Steyer, C. Schwarz, B. Baumeister, J. Allenou, B. Stepnik, W. Petry, Microstructural characteristics of a fresh U(Mo) monolithic mini-plate: Focus on the Zr coating deposited by PVD, *Nuclear Engineering and Technology* 53 (2021) 2629–2639. <https://doi.org/10.1016/j.net.2021.02.026>.
- [158] R.J. Drese, M. Wuttig, In situ stress measurements in zirconium and zirconium oxide films prepared by direct current sputtering, *Journal of Applied Physics* 99 (2006) 123517. <https://doi.org/10.1063/1.2208733>.
- [159] D.W. Hoffman, J.A. Thornton, Compressive stress and inert gas in Mo films sputtered from a cylindrical-post magnetron with Ne, Ar, Kr, and Xe, *Journal of Vacuum Science and Technology* 17 (1980) 380–383. <https://doi.org/10.1116/1.570394>.
- [160] DIN Deutsches Institut für Normung e.V., DIN 25412-1:2015-12: *Laboreinrichtungen - Handschuhkästen - Teil 1: Maße und Anforderungen*, 2015th ed., Beuth Verlag. <https://www.beuth.de/de/norm/din-25412-1/240285142> (accessed 13 June 2021).
- [161] M. Braun Inertgas-Systeme GmbH, *Inerte Gasreinigungssysteme Datenblätter*. <https://www.mbraun.com/de/produkte/gasreinigungssysteme.html> (accessed 14 June 2021).

- [162] T. Chemnitz, Inbetriebnahme und Parametrisierung einer Sputteranlage in der Kernbrennstoffentwicklung. B.Sc. thesis, München, 2014.
- [163] Leybold GmbH, TRIVAC D 65 B Datenblatt: Zweistufige Drehschieber-Vakuumpumpe. <https://www.leyboldproducts.de/produkte/oelgedichtete-vakuumpumpen/trivac/trivac-b/pumpen/607/trivac-d-65-b> (accessed 13 June 2021).
- [164] Leybold GmbH, TURBOVAC MAG W 1300 iP Datenblatt: Magnetisch gelagerte Turbo-Molekularpumpe. <https://www.leyboldproducts.de/produkte/hochvakuumpumpenkryotechnik/turbovac-turbovac-mag/turbovac-magintegra/pumpen/672/turbovac-mag-w-1300-ip> (accessed 13 June 2021).
- [165] Bronkhorst Deutschland Nord GmbH, EL-FLOW Select F-201CS Datenblatt: Thermischer Massenflussregler mit integriertem Absperrventil. <https://www.bronkhorst.com/de-de/produkte/gas-durchfluss/el-flow-select/f-201cs/> (accessed 13 June 2021).
- [166] Leybold GmbH, CERAVAC CTR 100 N Datenblatt: Drucksensor. <https://www.leyboldproducts.de/produkte/vakuum-mess-und-analysegeraete/druckmessung-und-anzeigegeeraete/aktive-sensoren/ceravac-transmitter/transmitter/1806/ceravac-ctr-100-n> (accessed 13 June 2021).
- [167] Leybold GmbH, PENNINGVAC PTR 90 N Datenblatt. <https://www.leyboldproducts.de/produkte/vakuum-mess-und-analysegeraete/druckmessung-und-anzeigegeeraete/aktive-sensoren/penningvac-transmitter/penningvac-ptr-90-n/1348/penningvac-ptr-90-n?c=571> (accessed 13 June 2021).
- [168] TRUMPF Huettinger GmbH, TruPlasma DC Serie 3000: Technische Daten. https://www.trumpf.com/filestorage/TRUMPF_Master/Products/Power_Electronics/DC_plasma_excitations/TruPlasma_DC_Serie_3000/TRUMPF_TruPlasma_DC_Serie_3000-DE.pdf (accessed 21 December 2021).
- [169] TRUMPF Huettinger GmbH, TruPlasma RF Serie 1000: Technische Daten. https://www.trumpf.com/no_cache/de_DE/produkte/leistungselektronik/plasmageneratoren/truplasma-rf-serie-1000-3000-g213/product_data_sheet/download/TRUMPF-technical-data-sheet-TruPlasma-RF-Serie-1000---3000-%28G2-13%29.pdf (accessed 21 December 2021).
- [170] UHV Design Ltd., EpiCentre deposition stage: Brochure. <https://d2129m0g0hc1fl.cloudfront.net/uhvdesign/media/literature-downloads/etd-040-epicentre-brochure.pdf> (accessed 21 December 2021).
- [171] TRUMPF Huettinger GmbH, TruPlasma Bias Serie 3000: Technische Daten. <https://docplayer.org/133830110-Truplasma-bias-serie-3000-grosse-dinge-unterstuetzen.html> (accessed 21 December 2021).
- [172] EA Elektro-Automatik GmbH & Co. KG, EA-PS 8000 2U 640W - 3000W Datenblatt: DC-Labornetzgeräte. https://elektroautomatik.com/shop/media/pdf/e8/06/d0/datasheet_ps8000-2u.pdf (accessed 5 July 2021).
- [173] GS Glovebox Systemtechnik GmbH, GS Glovebox Systemtechnik Gasreinigungen. <http://www.glovebox-systemtechnik.de/GS-Glovebox-Gasreinigung.php> (accessed 12 October 2021).

-
- [174] DIN Deutsches Institut für Normung e.V., DIN EN 1822-1:2011-01: Schwebstofffilter (EPA, HEPA und ULPA) - Teil 1: Klassifikation, Leistungsprüfung, Kennzeichnung, 2011st ed., Beuth Verlag. <https://www.beuth.de/de/norm/din-en-1822-1/133628826> (accessed 13 June 2021).
- [175] DIN Deutsches Institut für Normung e.V., DIN EN ISO 21420:2020-06: Schutzhandschuhe - Allgemeine Anforderungen und Prüfverfahren, 2020th ed., Beuth Verlag. <https://www.beuth.de/de/norm/din-en-iso-21420/299314747> (accessed 13 June 2021).
- [176] ifm electronic gmbh, IE5390 Datenblatt: Induktiver Sensor IEK31,5-BPKG/V4A/K1/AS. <https://www.ifm.com/de/de/product/IE5390> (accessed 13 June 2021).
- [177] SurTec Deutschland GmbH, SurTec® 138 Datenblatt.
- [178] SurTec Deutschland GmbH, SurTec® 089 Datenblatt.
- [179] C.A. Laue, D. Gates-Anderson, T.E. Fitch, Dissolution of metallic uranium and its alloys, *Journal of Radioanalytical and Nuclear Chemistry* 261 (2004) 709–717. <https://doi.org/10.1023/B:JRNC.0000037117.01721.f1>.
- [180] Struers ApS, Etching: Applikations Know-how. <https://www.struers.com/de-DE/Knowledge/Etching#etchinghowto> (accessed 9 September 2021).
- [181] Wegerhoff R. et. al., Basics of Light Microscopy & Imaging, *Imaging & Microscopy*.
- [182] JEOL GmbH, Scanning Electron Microscope A To Z: Basic Knowledge for Using The SEM. https://www.jeol.co.jp/en/applications/pdf/sm/sem_atoz_all.pdf (accessed 22 July 2021).
- [183] DIN Deutsches Institut für Normung e.V., DIN EN ISO 6507-1:2018-07: Metallische Werkstoffe - Härteprüfung nach Vickers - Teil 1: Prüfverfahren (ISO 6507-1:2018), 2018th ed., Beuth Verlag. <https://www.beuth.de/de/norm/din-en-iso-6507-1/280959455> (accessed 13 June 2021).
- [184] Struers ApS, Härteprüfung und Probenpräparation: Application Note. <http://www.struers.com/-/media/Library/Brochures/German/Harteprüfung-und-Probenpräparation.pdf> (accessed 22 July 2021).
- [185] U. Heisel, F. Klocke, E. Uhlmann, G. Spur (Eds.), *Handbuch Spanen*, 2nd ed., Hanser, München, 2014.
- [186] Ingersoll Werkzeuge GmbH, *Technisches Handbuch Fräsen und Bohren*, 2016.
- [187] Machinery Trade International Magazine, Latest Face Mill Cuts Interference Issues. <https://mtimagazine.com/latest-face-mill-cuts-interference-issues/> (accessed 5 January 2022).
- [188] Y. Zhu, Lecture 13: Machining I: Processing of Metallic Materials. <https://www.slideserve.com/emmett/mse-440-540-processing-of-metallic-materials> (accessed 4 January 2022).
- [189] I. Gibson, D. Rosen, B. Stucker, M. Khorasani, *Additive manufacturing technologies*, Third edition, Springer, Cham, Switzerland, 2021.
- [190] E. Liboutet, J. Allenou, B. Stepnik, S. Costil, C. Verdy, *Additive Manufacturing of Nuclear Component in Framatome CERCA. International Meeting on Reduced Enrichment for Research and Test Reactors RERTR*, 2021.
- [191] J.O. Milewski, *Additive Manufacturing of Metals*, Springer International Publishing, Cham, 2017.

- [192] S. Di Cataldo, S. Vinco, G. Urgese, F. Calignano, E. Ficarra, A. Macii, E. Macii, Optimizing Quality Inspection and Control in Powder Bed Metal Additive Manufacturing: Challenges and Research Directions, *Proc. IEEE* 109 (2021) 326–346.
<https://doi.org/10.1109/JPROC.2021.3054628>.
- [193] Metal Improvement Company, Controlled shot peening. <https://www.kugelstrahlen-shotpeening-mic.de/downloads.html> (accessed 7 January 2022).
- [194] Metal Improvement Company, SLM Bauteiloberflächen effektiv verbessern und stärken. https://metall-brandenburg.de/sites/default/files/2020-02/vorstellung_kontrolliertes_kugelstrahlen_mic_0.pdf (accessed 7 January 2022).
- [195] E. Liverani, A.H.A. Lutey, A. Ascari, A. Fortunato, The effects of hot isostatic pressing (HIP) and solubilization heat treatment on the density, mechanical properties, and microstructure of austenitic stainless steel parts produced by selective laser melting (SLM), *Int J Adv Manuf Technol* 107 (2020) 109–122. <https://doi.org/10.1007/s00170-020-05072-9>.
- [196] Metal Additive Manufacturing magazine, Hot Isostatic Pressing: Improving quality and performance in AM parts production. <https://www.metal-am.com/articles/hot-isostatic-pressing-improving-quality-and-performance-in-3d-printing/> (accessed 5 January 2022).
- [197] M. Lutter-Günther, A. Hofmann, C. Hauck, C. Seidel, G. Reinhart, Quantifying Powder Losses and Analyzing Powder Conditions in order to Determine Material Efficiency in Laser Beam Melting, *AMM* 856 (2016) 231–237.
<https://doi.org/10.4028/www.scientific.net/AMM.856.231>.
- [198] Concept Laser GmbH, M2 cusing Datenblatt: Metall-Laserschmelzanlage. <https://pdf.directindustry.de/pdf/concept-laser/m2-cusing/15662-646608.html> (accessed 14 January 2022).
- [199] Concept Laser GmbH, CL20ES material data: Edelstahl. https://www.fkm.net/wp-content/uploads/2018/06/Edelstahl_1.4404_Deutsch.pdf (accessed 14 January 2022).
- [200] SAE International, SAE-J2441: Shot Peening - engineering requirements for peening surfaces of parts by impingement of metallic shot, glass beads, or ceramic shot, 201506th ed. https://www.sae.org/standards/content/j2441_201506/ (accessed 14 January 2022).
- [201] S. Lorand, J. Allenou, M. Grasse, B. Stepnik, C. Rontard, F. Gauché, B. Baumeister, C. Schwarz, C. Steyer, C. Reiter, W. Petry, Development of U-Mo Monolithic Plates with Gradient Foils. International Meeting on Reduced Enrichment for Research and Test Reactors RERTR, 2021.
- [202] DIN Deutsches Institut für Normung e.V., DIN 25425-1:2013-05: Radionuklidlaboratorien - Teil 1: Regeln für die Auslegung, 2013rd ed., Beuth Verlag. <https://www.beuth.de/de/norm/din-25425-1/172100654> (accessed 13 June 2021).
- [203] S. Lo Muzio, Property Studies of Sputtered Zr Layers on Monolithic Uranium-Molybdenum Nuclear Fuels. B.Sc. thesis, München, 2018.
- [204] G. Scheller, Messunsicherheit einer Temperaturmesskette: Mit Beispielrechnungen, first. Aufl., Juchheim, Fulda, 2003.
- [205] P. Villars, H. Okamoto, Fe-Zr Binary Phase Diagram 0-100 at.% Zr: Datasheet from “PAULING FILE Multinaries Edition - 2012” in SpringerMaterials (https://materials.springer.com/isp/phase-diagram/docs/c_0101139), Springer-Verlag Berlin

-
- Heidelberg & Material Phases Data System (MPDS), Switzerland & National Institute for Materials Science (NIMS), Japan. https://materials.springer.com/isp/phase-diagram/docs/c_0101139.
- [206] revierlabor GmbH, Prüfbericht 16-01589: 16/0055/1 816181 ZDOA 35 P1. Private communication.
- [207] A. Grimm, Untersuchung von Verbesserungsmethoden für einen Sputterprozeß in der Kernbrennstoffentwicklung und Entwicklung eines dafür geeigneten Meßprobenhalters. M.Sc. thesis, München, 2016.
- [208] Alfa Aesar GmbH, Certificate of Analysis for Lot no. 61200020, Product number 802211. Private communication.
- [209] W.M. Haynes, CRC Handbook of Chemistry and Physics, 95th Edition, ninthfifthth ed., CRC Press, Hoboken, 2015.
- [210] H. Lindner, W. Siebke, Physik für Ingenieure: Mit Tabellen und Beispielen, seventeenth. Aufl., Fachbuchverl. Leipzig im Carl-Hanser-Verl., München, 2006.
- [211] H. Fricke, H. Frohne, P. Vaske, F. Moeller, Grundlagen der Elektrotechnik: Mit 25 Tafeln und 239 Beispielen, sixteenth., neubearb. und erw. Aufl., Teubner, Stuttgart, 1976.
- [212] viZaar industrial imaging AG, Emissionsgradtabelle. <http://www.thermografie-xtra.de/tippstricks/> (accessed 20 April 2016).
- [213] Plansee SE, Wolfram. <https://www.plansee.com/de/werkstoffe/wolfram.html> (accessed 30 July 2021).
- [214] COMET-Pumpen Systemtechnik GmbH & Co. KG, GEO-INOX-INLINE Datenblatt: Inline-Pumpen. https://www.comet-pumpen.de/fileadmin/pdf/pumpen_datenblaetter/Datenblatt_GEO-INOX-INLINE_7701.21.01.pdf (accessed 12 October 2021).
- [215] Direct Plastics Ltd, PEEK Material Data Sheet. <https://www.directplastics.co.uk/pdf/datasheets/PEEK%20Data%20Sheet.pdf> (accessed 7 October 2021).
- [216] KERAFOL Keramische Folien GmbH & Co. KG, Softtherm U 281 Datenblatt: Silikonfreie Wärmeleitfolie. https://www.kerafol.com/_wpframe_custom/downloads/files/Kerafol_WLF_Datenblatt_U-281__082159-28082020.pdf (accessed 7 October 2021).
- [217] CeramTec GmbH, Advanced Ceramics for Electronic Applications: Material properties of Rubalit®, Alunit® and Zirkolit®. https://www.ceramtec-industrial.com/fileadmin/user_upload/Corporate/11_Downloads/06_Electronic_Heatsinks/CeramTec_Material_Properties_Electronic_Applications_r1.pdf (accessed 7 October 2021).
- [218] Sputtering Components, CM-Series: External-Mount End Block. <https://www.sputteringcomponents.com/products/rotary-cathodes/external-mount-end-blocks/cm-series-end-block> (accessed 7 October 2021).
- [219] Ethan Arendt, TRM80UB & SRM80 Magnet Bar Simulation. Private communication, 2021.
- [220] HEIDEN power GmbH, HEA-PSI 9000 3U Datenblatt: Programmierbare Hochleistungs-DC-Netzgeräte. https://www.heidenpower.com/wp-content/uploads/2021/01/HEA-PSI9000_3U_de_en.pdf (accessed 12 October 2021).

- [221] TRUMPF Huettinger GmbH, TruPlasma DC Serie 3000 (G2): Technische Daten. https://www.trumpf.com/no_cache/de_DE/produkte/leistungselektronik/plasmageneratoren/truplasma-dc-serie-3000-g2/product_data_sheet/download/TRUMPF-technical-data-sheet-TruPlasma-DC-Serie-3000-%28G2%29.pdf (accessed 12 October 2021).
- [222] TRUMPF Huettinger GmbH, TruPlasma DC Serie 4000 (G2): Technische Daten. https://www.trumpf.com/no_cache/de_DE/produkte/leistungselektronik/plasmageneratoren/truplasma-dc-serie-4000-g2/product_data_sheet/download/TRUMPF-technical-data-sheet-TruPlasma-DC-Serie-4000-%28G2%29.pdf (accessed 12 October 2021).
- [223] Sartorius Lab Instruments GmbH & Co. KG, Sartorius Cubis® Serie: Broschüre.
- [224] Novus Dahle GmbH, Guillotine 580 Technical Data. https://www.dahle-office.com/pim/media/Dahle_00580_AS_815MM_RAL5009_eng_GLO_20210913193909_178438.PDF (accessed 12 October 2021).
- [225] Long Life for Art, Aluminium-Verbundfolie A30 T Technisches Datenblatt. <https://llfa.de/mwdownloads/download/link/id/118/> (accessed 12 October 2021).
- [226] Rische + Herfurth GmbH Maschinen- und Apparatebau, polystar® impulse generator 120 GE Manual. <https://llfa.de/mwdownloads/download/link/id/374/> (accessed 12 October 2021).
- [227] robeko GmbH & Co. KG, Materialzeugnis 2.2 nach EN 10204; Rohrtarget Zr 702 121.000102.0000. Private communication.
- [228] Mitsubishi Gas Chemical Co., Inc., RP System Brochure. <https://llfa.de/mwdownloads/download/link/id/92/> (accessed 12 October 2021).
- [229] Long Life for Art, Ageless Eye data sheet. <https://llfa.de/mwdownloads/download/link/id/133/> (accessed 12 October 2021).
- [230] N. Plößner, Inbetriebnahme und Parametrisierung einer hochskalierten Sputteranlage für die Kernbrennstoffentwicklung. B.Sc. thesis, München, 2019.
- [231] L. Conde, An introduction to Langmuir probe diagnostics of plasmas, Madrid, 2011.
- [232] T.J. Vink, M.A.J. Somers, J.L.C. Daams, A.G. Dirks, Stress, strain, and microstructure of sputter-deposited Mo thin films, *Journal of Applied Physics* 70 (1991) 4301–4308. <https://doi.org/10.1063/1.349108>.
- [233] A. Al-masha'al, A. Bunting, R. Cheung, Evaluation of residual stress in sputtered tantalum thin-film, *Applied Surface Science* 371 (2016) 571–575. <https://doi.org/10.1016/j.apsusc.2016.02.236>.
- [234] E. Fuchs, Vergleich zweier PVD-Anlagen über die Charakterisierung von hergestellten Zirkonium-Schichten. B.Sc. thesis, München, 2021.
- [235] S. Lorand, High-Resolution UT and X-Ray Pictures of the 1st half-size SS+Zr run. Private communication.
- [236] S. Lorand, Report on the assessment of inert graded foil process: LEU-FOREvER Deliverable D2.6 (confidential). 70R&D0005ETU0001 DRAFT, 2022.

LIST OF FIGURES

Figure 1: Cut view of the FRM II core installations	1
Figure 2: Inner view of the current FRM II fuel element	2
Figure 3: Cut view of a current FRM II fuel plate before involute shaping	3
Figure 4: Power deposition in MW/l at the end of life of a current FRM II fuel element	3
Figure 5: Fuel candidates for the conversion of FRM II	4
Figure 6: Proposed European fabrication process for monolithic U-Mo fuel plates	5
Figure 7: Cut view of a potential gradient monolithic fuel plate before involute shaping	5
Figure 8: Micrographs of disperse (a) and monolithic (b) U-Mo fuel after irradiation in RERTR-4 and RERTR-8, respectively	6
Figure 9: Multi-phase diffusion of elements A and B	11
Figure 10: Phase diagram of pure uranium	12
Figure 11: Binary phase diagram of the U-Mo system	13
Figure 12: TTT diagram of the U-10wt.%Mo system	14
Figure 13: Binary phase diagram of the U-Zr system	17
Figure 14: Binary phase diagram of the Mo-Zr system	18
Figure 15: Ternary phase diagrams of the U-Mo-Zr system at 500 °C (a), 600 °C (b), 700 °C (c) and 1000 °C (d)	19
Figure 16: Interaction between clamped bulk U-Mo and Zr samples at various temperatures	20
Figure 17: Phase diagram of the Al-Fe-Ni system at room temperature	21
Figure 18: Phase diagram of the Al-Zr system	21
Figure 19: Microstructures of stainless steels	25
Figure 20: Schaeffler diagram of stainless steels	25
Figure 21: Pseudo-binary phase diagram of Ti-6Al alloys with V addition	27
Figure 22: General microstructures of titanium $\alpha+\beta$ alloys	27
Figure 23: Homogenization of U-Mo ingots	29
Figure 24: Canning process	30
Figure 25: Hot-Rolling process	31
Figure 26: Typical surface structure of untreated metallic parts	33
Figure 27: Electron micrograph of a U-Mo foil co-rolled with Zr	35

Figure 28: Electron micrograph of a U-Mo foil PVD-coated with Zr.....	35
Figure 29: Basic principle of the sputtering process	36
Figure 30: Single-ionization cross-section for collisions of argon atoms with electrons.....	37
Figure 31: Electrical potential curve for different substrate conditions	39
Figure 32: Exemplary measurement of the substrate current at various substrate potentials.....	41
Figure 33: Sputter yield for selected elements and bombardment with argon ions.....	43
Figure 34: Sketch of the angular distribution of sputtered particles.....	43
Figure 35: Mean free path of selected atom species in argon atmosphere	44
Figure 36: Magnetron configurations.....	46
Figure 37: Scheme and example of planar sputtering sources	47
Figure 38: Scheme and example of cylindrical sputtering sources	47
Figure 39: Condensation	48
Figure 40: Nucleation.....	49
Figure 41: Grain growth structures	49
Figure 42: Anders structure zone diagram.....	51
Figure 43: Schematic views of the HSK1 PVD coating device	53
Figure 44: Zr-coated U-Mo foils from HSK1	54
Figure 45: UT test results of Zr-coated U-Mo foils from HSK1 after C2TWP cladding application ...	54
Figure 46: Schematic view of the HSK3 PVD coating device.....	55
Figure 47: Zr-coated mini-size U-Mo foils from HSK3.....	55
Figure 48: UT test results of rejected EMPIrE fuel plates	56
Figure 49: Cracks in the Zr coating introduced by the C2TWP process	57
Figure 50: Typical destructive examination results of monolithic U-Mo fuel plates	57
Figure 51: Bending of a mini-size stainless steel substrate with 50 μm single-sided Zr coating.....	58
Figure 52: Optimized substrate heating and biasing approaches	59
Figure 53: The HSK3 chemistry glovebox.....	62
Figure 54: The HSK3 sputtering glovebox	62
Figure 55: The HSK3 vacuum chamber.....	63
Figure 56: The HSK3 vacuum and gas supply system.....	64
Figure 57: Sectional view of the sputtering source of HSK3 with magnetic field lines	64
Figure 58: Sectional view of the substrate holder of HSK3	66
Figure 59: The HSK2 glovebox	67
Figure 60: The HSK2 vacuum chamber.....	68
Figure 61: The HSK2 vacuum and gas supply system.....	69
Figure 62: Preparation of Zr-coated samples	71

Figure 63: Preparation of gradient foil samples	73
Figure 64: High-alloy steel etched with Beraha II	73
Figure 65: Exemplary optical micrographs of a Zr-coated U-Mo sample with AlFeNi cladding	74
Figure 66: Exemplary SEM micrographs of a Zr-coated U-Mo sample with AlFeNi cladding.....	75
Figure 67: Vickers hardness test of a Zr layer deposited by PVD.....	76
Figure 68: Preparation of bending test samples	76
Figure 69: Preliminary gradient full-size geometry	78
Figure 70: Preliminary gradient mini-size geometry.....	79
Figure 71: Categories and examples of fabrication processes for gradient foils.....	81
Figure 72: Sketch of subtractive manufacturing processes	81
Figure 73: Scheme and example of the milling process of steel parts	82
Figure 74: Schematic view of the two most common general forms of milling	83
Figure 75: Sketch of additive manufacturing processes.....	83
Figure 76: Scheme and example of the SLM process	84
Figure 77: Schematic view of the laser melting process	85
Figure 78: Schematic views of abrasive blasting and shot peening	86
Figure 79: Schematic view of a HIP device	86
Figure 80: Substrate holder for milling of gradient mini-size foils.....	88
Figure 81: Mass distribution of the gradient mini-size stainless steel foils (milling)	89
Figure 82: Graphical explanation for the gradient widths being out of tolerance	89
Figure 83: Gradient mini-size stainless steel foil (milling).....	90
Figure 84: Exemplary surface optical micrographs of gradient mini-size stainless steel foils (milling)	90
Figure 85: Exemplary cross-sectional optical micrographs of gradient mini-size stainless foils (milling)	91
Figure 86: Exemplary cross-sectional optical micrographs of gradient mini-size stainless foils (milling), etched with Beraha II	91
Figure 87: Substrate holder for milling of gradient full-size foils.....	92
Figure 88: Mass distribution of the gradient full-size stainless steel foils (milling)	93
Figure 89: Gradient full-size stainless steel foil (milling).....	93
Figure 90: Mass distribution of the gradient full-size titanium alloy foils (milling).....	94
Figure 91: Gradient full-size titanium alloy foil (milling)	95
Figure 92: Results of the SLM fabrication experiments	97
Figure 93: Mass distribution of the gradient mini-size stainless steel foils (SLM).....	97
Figure 94: Gradient mini-size stainless steel foil (SLM)	97
Figure 95: Exemplary surface optical micrograph of gradient mini-size stainless steel foils (SLM) ...	98

Figure 96: Exemplary cross-sectional optical micrographs of gradient mini-size stainless foils (SLM)	99
Figure 97: Exemplary cross-sectional optical micrographs of gradient mini-size stainless foils (SLM), etched with Beraha II	99
Figure 98: Gradient mini-size stainless steel foil (SLM, shot peening)	100
Figure 99: Exemplary surface optical micrograph of gradient mini-size stainless steel foils (SLM, shot peening)	101
Figure 100: Exemplary cross-sectional optical micrographs of gradient mini-size stainless foils (SLM, shot peening)	101
Figure 101: Process diagram of the HIP process	102
Figure 102: Gradient mini-size stainless steel foil (SLM, shot peening, HIP)	102
Figure 103: Exemplary surface optical micrograph of gradient mini-size stainless steel foils (SLM, shot peening, HIP)	103
Figure 104: Exemplary cross-sectional optical micrographs of gradient mini-size stainless foils (SLM, shot peening, HIP)	104
Figure 105: Exemplary cross-sectional optical micrographs of gradient mini-size stainless foils (SLM, shot peening, HIP), etched with Beraha II	104
Figure 106: Exemplary cross-sectional optical micrographs of Zr-coated gradient mini-size foils	105
Figure 107: UT test results of mini-size plates with gradient stainless steel foils	106
Figure 108: Exemplary cross-sectional optical micrograph of a mini-plate with a gradient stainless steel foil fabricated by SLM	106
Figure 109: The micro-size sample holder	111
Figure 110: Temperature of the micro-size sample holder and the Ti-6Al-4V reference sample at various heating powers	111
Figure 111: Temperature of the micro-size sample holder and the Ti-6Al-4V reference sample at various sputtering powers	112
Figure 112: Temperature of the micro-size sample holder and the Ti-6Al-4V reference sample at various heating powers, while sputtering with 300W constantly	113
Figure 113: Binary Fe-Zr phase diagram	113
Figure 114: PVD coating of a heated micro-size sample in the HSK3 device	114
Figure 115: Process diagram of the U-Mo+Zr-700 sample production	116
Figure 116: Optical micrograph (polarized light) of an interaction spot in sample U-Mo+Zr-800	120
Figure 117: SEM micrographs (BSE detector) of U-Mo+Zr samples heated to various temperatures during PVD coating	121
Figure 118: EDX line scan across a U-Mo/Zr interaction spot at the U-Mo+Zr-700 sample	121
Figure 119: Micrographs of a U-Mo substrate with a Zr layer deposited with substrate biasing	123
Figure 120: Experimental setup to establish a static magnetic field above the substrate (flat magnet configuration)	125

Figure 121: Experimental setup to establish a static magnetic field above the substrate (upright magnet configuration).....	126
Figure 122: Achievable substrate current density with static magnetic fields without a sputtering plasma at 0.05 mbar process pressure.....	126
Figure 123: Achievable substrate current density with static magnetic field with a sputtering plasma at $7.8 \cdot 10^{-3}$ mbar process pressure	127
Figure 124: Optical micrographs of the sample surface after PVD coating with static magnetic fields	128
Figure 125: Measured electron emission currents of various tungsten filaments	130
Figure 126: Experimental setup for electron emission through spiral filament and anode	131
Figure 127: Experimental setup for electron emission through filament loop	132
Figure 128: Achievable substrate current density by electron emission from a filament loop heated with 1566 W/m with a sputtering plasma at $7.8 \cdot 10^{-3}$ mbar process pressure	133
Figure 129: Sample SS+Zr-e13 after production	134
Figure 130: Optical micrograph (polarized light) of a cross-section of sample SS+Zr-e13	135
Figure 131: Bending test results of sample SS+Zr-e13.....	135
Figure 132: WLa20 filament loop after being used for several PVD coating experiments.....	135
Figure 133: Chemical cleaning setup for full-size U-Mo foils.....	137
Figure 134: Interior design of the vacuum chamber of the full-size PVD coating device	138
Figure 135: Flat support half-size substrate holder	139
Figure 136: Cross-cut view of the flat support half-size substrate holder.....	140
Figure 137: Clamping full-size substrate holder	141
Figure 138: Cross-cut view of a clamping block of the clamping full-size substrate holder	141
Figure 139: Overview of the cylindrical sputtering source used in the full-size PVD coating device	142
Figure 140: External end block of the cylindrical sputtering source.....	143
Figure 141: Magnetic configuration and field lines of the SRM80 magnet bar.....	144
Figure 142: Magnetic configuration and field lines of the uTRM80 magnet bar.....	145
Figure 143: Possible power supply configurations of the full-size PVD coating device	146
Figure 144: PLC system of the full-size PVD coating device.....	148
Figure 145: The precision scale inside the glovebox	149
Figure 146: Trimming of substrates coated with the clamping full-size substrate holder.....	149
Figure 147: Polystar 120 GE impulse generator with attached welding tongs.....	150
Figure 148: The complete full-size PVD coating device from the outside	151
Figure 149: The full-size PVD coating device equipped with the sputtering source and two different substrate holders.....	152
Figure 150: Exemplary process diagram of the full-size PVD coating process.....	155

Figure 151: PVD coating of a half-size stainless steel substrate	155
Figure 152: Half-size substrates after PVD coating without (a) and with (b) prior plasma cleaning .	157
Figure 153: Floating potential of a half-size substrate at various sputtering powers at 30 mm and 70 mm target-substrate distance	158
Figure 154: Earth current density at various sputtering powers at 30 mm and 70 mm target-substrate distance.....	158
Figure 155: Bent half-size substrate with single-sided Zr coating	159
Figure 156: Measured bending of half-size substrates with single-sided Zr coating	160
Figure 157: Example of substrate ends to be trimmed off	162
Figure 158: Achievable substrate current density at various sputtering powers in comparison to the mini-size device (HSK3).....	162
Figure 159: Bending test results for Zr layers deposited at various substrate biasing voltages	165
Figure 160: Measured equilibrium substrate temperature at various sputtering powers.....	166
Figure 161: Measured equilibrium substrate temperature at various substrate biasing voltages	167
Figure 162: Measured equilibrium substrate temperature at various plasma cleaning pressures.....	168
Figure 163: Analyzed cross-sections for the determination of the transverse coating thickness profile	168
Figure 164: Measured transverse coating thickness profile	169
Figure 165: Half-size stainless steel substrate with double-sided Zr coating ready for cladding application	170
Figure 166: Sectioning plan for the half-size plates with Zr-coated stainless steel substrates	172
Figure 167: Exemplary optical micrograph of the longitudinal middle section 102H-SS316L-Zr8.42	172
Figure 168: Exemplary optical micrographs of the longitudinal end sections 103H-SS316L-Zr8.21 (a), 102H-SS316L-Zr8.21 (b) and 102H-SS316L-Zr8.62 (c).....	173
Figure 169: Exemplary optical micrographs of the transverse end sections 104H-SS316L-Zr8.61 (a), 104H-SS316L-Zr8.41 (b) and 102H-SS316L-Zr8.41 (c).....	174
Figure 170: Exemplary optical micrographs of Zr coating defects close to the transverse edges of the substrates	175

LIST OF TABLES

Table 1: Phases of uranium	13
Table 2: Material properties of the U-10wt.%Mo alloy	15
Table 3: Phases of zirconium.....	16
Table 4: Material properties of Zr 702	17
Table 5: Chemical compositions of selected aluminum cladding alloys.....	22
Table 6: Results of the U-Mo surrogate material study.....	24
Table 7: Chemical composition of stainless steel AISI 316L.....	26
Table 8: Grinding and polishing recipe for Zr-coated samples	72
Table 9: Material loss calculation for the gradient full-size and mini-size foil geometries.....	78
Table 10: Production process for Zr-coated samples with substrate heating.....	114
Table 11: Overview of Zr-coated samples with substrate heating.....	115
Table 12: Micrographs of Zr-coated stainless steel samples with substrate heating	117
Table 13: Micrographs of Zr-coated U-Mo samples with substrate heating	118
Table 14: Zr-coated stainless steel samples with substrate biasing and static magnetic fields.....	128
Table 15: Zr-coated stainless steel samples with substrate biasing and electron emission	133
Table 16: Power supply units of the full-size PVD coating device	147
Table 17: Process parameter variations to study the substrate bending effect.....	160
Table 18: Zr-coated stainless steel samples with substrate biasing	163
Table 19: Micrographs of Zr-coated stainless steel samples with substrate biasing	164
Table 20: PVD sample production parameters for subsequent C2TWP cladding application	170
Table 21: UT test results of half-size plates with Zr-coated stainless steel substrates	171

DANKSAGUNG

Am Ende dieser Arbeit möchte ich mich bei all denen bedanken, die mich auf meinem Weg zur Promotion begleitet und unterstützt haben.

Zunächst geht ein herzlicher Dank an meinen Doktorvater **Herrn Prof. Petry** für die Möglichkeit, dieses spannende Thema im Rahmen einer Promotion bearbeiten zu können, für die ausgezeichnete Betreuung und das immerwährende in mich gesetzte Vertrauen. Ebenfalls möchte ich mich für die Übertragung der Aufgaben als Arbeitsgruppenleiter und Projektmanager im Jahr 2018 bedanken. Diese verantwortungsvollen Aufgaben haben mich Erfahrungen sammeln lassen, die mein Arbeitsleben noch lange prägen werden, auch wenn sie mit Sicherheit nicht zur Beschleunigung dieser Promotion beigetragen haben.

Auch an **Herrn Prof. Böni** geht ein herzlicher Dank für die Bereitschaft der Übernahme der Zweitbegutachtung dieser Arbeit.

Meinen Mitstreitern **Dr. Christian Steyer, Dr. Christian Reiter und Dr. Tobias Chemnitz** gebührt Dank für die zahlreichen Jahre kollegialer und freundschaftlicher Zusammenarbeit auf dem Weg zur Promotion. Auch wenn ich etwas länger gebraucht habe als ihr, so haben wir uns doch immer gegenseitig bei der Erreichung unserer Ziele unterstützt.

Auch allen anderen aktiven und ehemaligen Mitgliedern der Arbeitsgruppe, insbesondere **Christian Schwarz, Jingyi Shi, Julia Mausz, Kevin Buducan und Kaltrina Shehu** sowie **Dr. Harald Breitzkreutz, Dr. Wolfgang Schmid und Dr. Rainer Jungwirth** möchte ich für das freundschaftliche Miteinander und die vielfältige Unterstützung danken. Ein herzlicher Dank auch an die zahlreichen Werk-, Bachelor- und Masterstudenten der Arbeitsgruppe, insbesondere **Arnulf Grimm, Silvia lo Muzio und Nikolas Plößner**, für ihren unermüdlichen Einsatz und die tolle Arbeit.

Mein großer Dank gilt auch meinem Laborbetriebs-Team **Thomas Kersch, Serhat Polat, Nicholas Rehms und Viktor Schweigert**. Ihr betreibt mit eurem unermüdlichen Einsatz das Kernbrennstofflabor jederzeit fabelhaft, und ermöglicht so erst die Ergebnisse von Arbeiten wie dieser.

Meinen Partnern aus Forschung und Industrie, **Markus Kaupe (H-TEC Präzisionstechnik GmbH), Johannes Schütz (Laserzentrum Nord) sowie Bertrand Stepnik, Sylvain Lorand und Jérôme Allenou (Framatome-CERCA)** möchte ich für die ausgezeichnete Zusammenarbeit bei den zahlreichen Projekten in dieser Arbeit danken.

Meinen Eltern **Inge Baumeister und Ernst Stenger** sowie meiner Schwester **Julia Müller** danke ich für die jahrelange, geduldige moralische Unterstützung während meines Studiums und dieser Arbeit.

Zuletzt gilt ein tausendfacher Dank meiner wundervollen Frau **Alexandra**, die ich im Laufe dieser Arbeit kennen und lieben lernen und schließlich heiraten durfte, und die mir mit unseren beiden wunderbaren Töchtern **Laura und Emilia** das größte Geschenk auf Erden gemacht hat. Du warst immer geduldig mit mir, hast mich zu jeder Zeit mit voller Kraft unterstützt, und hast mir gemeinsam mit unseren Kindern jeden Tag aufs Neue gezeigt, was wirklich wichtig ist im Leben.